

1991

A study of high speed flows in an aircraft transition duct

Bruce A. Reichert
Iowa State University

Follow this and additional works at: <https://lib.dr.iastate.edu/rtd>

 Part of the [Mechanical Engineering Commons](#)

Recommended Citation

Reichert, Bruce A., "A study of high speed flows in an aircraft transition duct " (1991). *Retrospective Theses and Dissertations*. 9573.
<https://lib.dr.iastate.edu/rtd/9573>

This Dissertation is brought to you for free and open access by the Iowa State University Capstones, Theses and Dissertations at Iowa State University Digital Repository. It has been accepted for inclusion in Retrospective Theses and Dissertations by an authorized administrator of Iowa State University Digital Repository. For more information, please contact digirep@iastate.edu.

INFORMATION TO USERS

This manuscript has been reproduced from the microfilm master. UMI films the text directly from the original or copy submitted. Thus, some thesis and dissertation copies are in typewriter face, while others may be from any type of computer printer.

The quality of this reproduction is dependent upon the quality of the copy submitted. Broken or indistinct print, colored or poor quality illustrations and photographs, print bleedthrough, substandard margins, and improper alignment can adversely affect reproduction.

In the unlikely event that the author did not send UMI a complete manuscript and there are missing pages, these will be noted. Also, if unauthorized copyright material had to be removed, a note will indicate the deletion.

Oversize materials (e.g., maps, drawings, charts) are reproduced by sectioning the original, beginning at the upper left-hand corner and continuing from left to right in equal sections with small overlaps. Each original is also photographed in one exposure and is included in reduced form at the back of the book.

Photographs included in the original manuscript have been reproduced xerographically in this copy. Higher quality 6" x 9" black and white photographic prints are available for any photographs or illustrations appearing in this copy for an additional charge. Contact UMI directly to order.

U·M·I

University Microfilms International
A Bell & Howell Information Company
300 North Zeeb Road, Ann Arbor, MI 48106-1346 USA
313/761-4700 800/521-0600



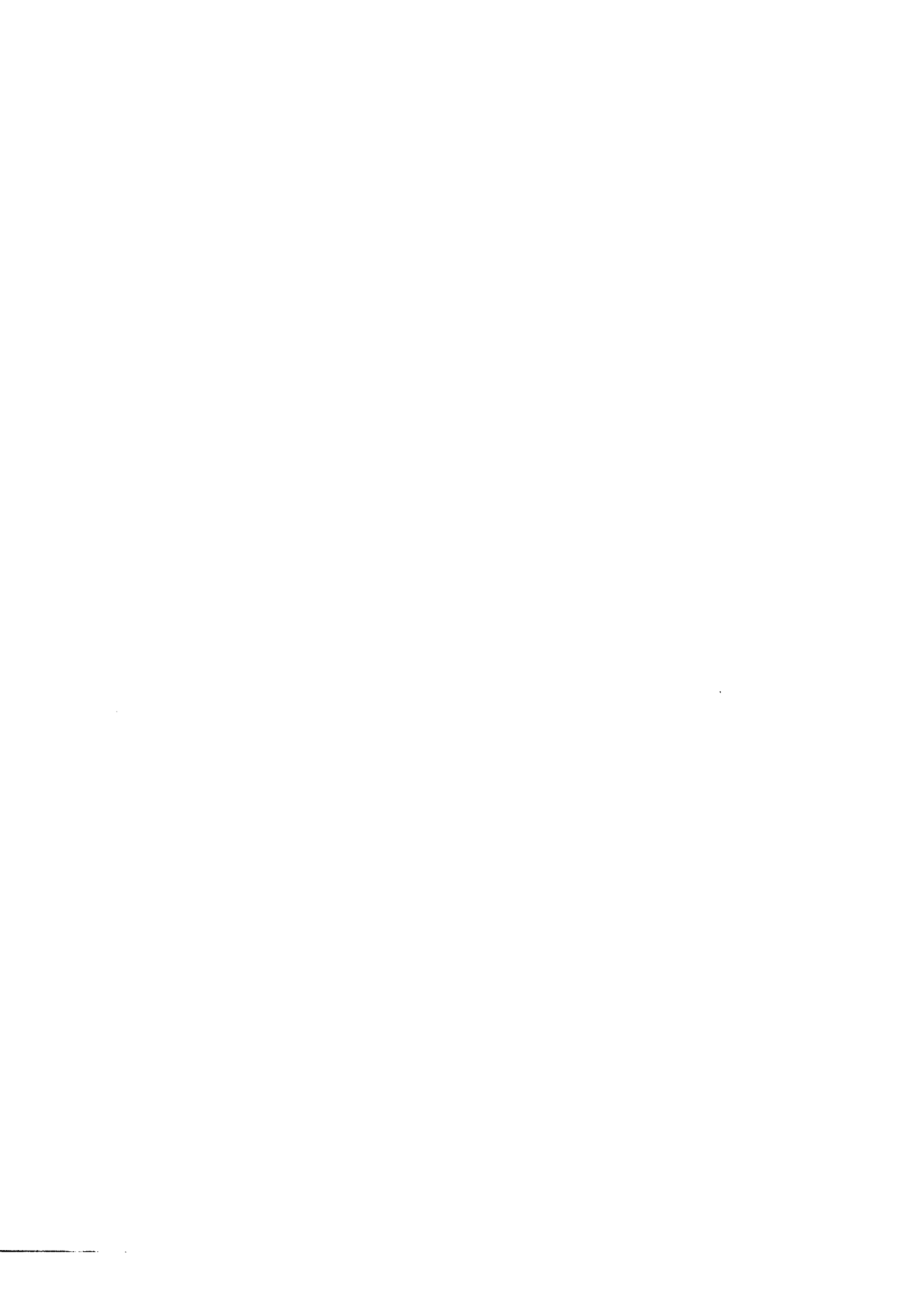
Order Number 9126241

A study of high speed flows in an aircraft transition duct

Reichert, Bruce A., Ph.D.

Iowa State University, 1991

U·M·I
300 N. Zeeb Rd.
Ann Arbor, MI 48106



NOTE TO USERS

**THE ORIGINAL DOCUMENT RECEIVED BY U.M.I. CONTAINED PAGES
WITH SLANTED PRINT. PAGES WERE FILMED AS RECEIVED.**

THIS REPRODUCTION IS THE BEST AVAILABLE COPY.



A study of high speed flows in an aircraft transition duct

by

Bruce A. Reichert

A Dissertation Submitted to the Graduate Faculty in
Partial Fulfillment of the Requirements for the Degree
DOCTOR OF PHILOSOPHY

Major: Mechanical Engineering

Approved:

Signature was redacted for privacy.

In Charge of Major Work

Signature was redacted for privacy.

For the Major Department

Signature was redacted for privacy.

For the Graduate College

Iowa State University

Ames, Iowa

1991

The Transition Duct With Inlet Swirl	110
CHAPTER VI. ANALYSIS	123
Trace Gas Results	123
Aerodynamic Results	137
CHAPTER VII. CONCLUSIONS	154
CHAPTER VIII. RECOMMENDATIONS FOR FUTURE RESEARCH . . .	156
APPENDIX A. A PROCEDURE FOR FIVE-HOLE PROBE CALIBRATION AND DATA REDUCTION	157
The Five-Hole Probe	157
Calibration	158
Data Reduction	168
A Fortran Program For Five-Hole Probe Calibration	172
A Fortran Program For Five-Hole Probe Data Reduction	176
APPENDIX B. A NUMERICAL PROCEDURE FOR INTERPOLATION OF IRREGULARLY DISTRIBUTED DATA	185
Triangulation	186
Linear Interpolation	188
A Fortran Program For Triangulation	189
A Fortran Program for Linear Interpolation	203
APPENDIX C. A NUMERICAL PROCEDURE FOR CALCULATING MOMENTS OF A BIVARIATE DISTRIBUTION	214
The Calculation of Moments	214
A Fortran Program For Two-Dimensional Moments Calculation	219
BIBLIOGRAPHY	226

LIST OF FIGURES

Figure III.1.	The calibration tunnel used to test the trace gas equipment and measurement technique	14
Figure III.2.	The NASA Lewis Research Center Internal Fluid Mechanics Facility	18
Figure III.3.	The Mach number – Reynolds number relationship for the Internal Fluid Mechanics Facility	19
Figure III.4.	Circular-to-rectangular transition duct	20
Figure III.5.	Solid body rotation superimposed on uniform flow	24
Figure III.6.	Swirl generator schematic	26
Figure III.7.	Stationary blade design nomenclature	28
Figure III.8.	Blade fabrication from circular tubing	29
Figure III.9.	Geometric interpretation of blade design	30
Figure III.10.	Comparison of blade exit angles	33
Figure IV.1.	The location of surface static pressure measurements	36
Figure IV.2.	A typical five-hole probe	37
Figure IV.3.	The location of the four cross stream aerodynamic measurement planes	38
Figure IV.4.	The location of the transition duct probe opening axis	39
Figure IV.5.	Cantilever and catenary injection probe designs	44
Figure IV.6.	Trace gas injection locations and measurement planes	45
Figure IV.7.	Trace gas injection probe positioning equipment	46
Figure IV.8.	Trace gas sampling probe positioning equipment	50
Figure IV.9.	Parameters used for the trace gas sampling system coordinate transformation	51
Figure IV.10.	Schematic of the Pressure Systems Incorporated Model 780B electronically scanned pressure measurement system	56
Figure IV.11.	Schematic of hot wire anemometry equipment	58

Figure IV.12.	Hot wire calibration results	59
Figure V.1.	Concentration coefficient C^* distribution for preliminary tests to ascertain the spatial resolution of the trace gas technique	63
Figure V.2.	Concentration coefficient C^* distributions for preliminary trace gas tests to ascertain the sensitivity of concentration measurements to the ethylene injection flow rate	64
Figure V.3.	Concentration coefficient C^* distributions for preliminary trace gas tests to ascertain the sensitivity of concentration measurements to the sampling flow rate	65
Figure V.4.	The radial distributions of the axial component of the velocity coefficient M^* at $x/D = -0.5$ without swirl	66
Figure V.5.	The axial velocity distribution in law of the wall coordinates at $x/D = -0.5$ without swirl	68
Figure V.6.	The relationships between centerline total and static pressures at $x/D = -0.5$ and the settling chamber and wall static pressures with swirl	72
Figure V.7.	The relationship of swirl generator angular velocity to centerline Mach number	73
Figure V.8.	The radial distributions of the axial, radial and tangential components of the velocity coefficient M^* at $x/D = -0.5$ with swirl	75
Figure V.9.	The axial velocity distribution in law of the wall coordinates at $x/D = -0.5$ with swirl	76
Figure V.10.	The radial distributions of the total pressure coefficient p_0^* and static pressure coefficient p^* at $x/D = -0.5$ with swirl	77
Figure V.11.	Surface oil film visualization without inlet swirl	79
Figure V.12.	Surface oil film visualization without inlet swirl	80
Figure V.13.	Ethylene concentration coefficient C^* distributions in plane 1T	81
Figure V.14.	Ethylene concentration coefficient C^* distributions in plane 2T	82
Figure V.15.	Ethylene concentration coefficient C^* distributions in plane 3T	83

Figure V.16.	Ethylene concentration coefficient C^* distributions in plane 4T . . .	84
Figure V.17.	Surface static pressure coefficient p^* for flow without inlet swirl . . .	85
Figure V.18.	Axial (upper) and transverse (lower) components of the velocity coefficient M^* in plane 1A for $M_{\text{centerline}} = 0.20$ without inlet swirl	86
Figure V.19.	Axial (upper) and transverse (lower) components of the velocity coefficient M^* in plane 2A for $M_{\text{centerline}} = 0.20$ without inlet swirl	87
Figure V.20.	Axial (upper) and transverse (lower) components of the velocity coefficient M^* in plane 3A for $M_{\text{centerline}} = 0.20$ without inlet swirl	88
Figure V.21.	Axial (upper) and transverse (lower) components of the velocity coefficient M^* in plane 4A for $M_{\text{centerline}} = 0.20$ without inlet swirl	89
Figure V.22.	Static pressure coefficient p^* (upper) and total pressure coefficient p_0^* (lower) distributions in plane 1A for $M_{\text{centerline}} = 0.20$ without inlet swirl	90
Figure V.23.	Static pressure coefficient p^* (upper) and total pressure coefficient p_0^* (lower) distributions in plane 2A for $M_{\text{centerline}} = 0.20$ without inlet swirl	91
Figure V.24.	Static pressure coefficient p^* (upper) and total pressure coefficient p_0^* (lower) distributions in plane 3A for $M_{\text{centerline}} = 0.20$ without inlet swirl	92
Figure V.25.	Static pressure coefficient p^* (upper) and total pressure coefficient p_0^* (lower) distributions in plane 4A for $M_{\text{centerline}} = 0.20$ without inlet swirl	93
Figure V.26.	Axial (upper) and transverse (lower) components of the velocity coefficient M^* in plane 1A for $M_{\text{centerline}} = 0.35$ without inlet swirl	94

Figure V.27. Axial (upper) and transverse (lower) components of the velocity coefficient M^* in plane 2A for $M_{\text{centerline}} = 0.35$ without inlet swirl	95
Figure V.28. Axial (upper) and transverse (lower) components of the velocity coefficient M^* in plane 3A for $M_{\text{centerline}} = 0.35$ without inlet swirl	96
Figure V.29. Axial (upper) and transverse (lower) components of the velocity coefficient M^* in plane 4A for $M_{\text{centerline}} = 0.35$ without inlet swirl	97
Figure V.30. Static pressure coefficient p^* (upper) and total pressure coefficient p_0^* (lower) distributions in plane 1A for $M_{\text{centerline}} = 0.35$ without inlet swirl	98
Figure V.31. Static pressure coefficient p^* (upper) and total pressure coefficient p_0^* (lower) distributions in plane 2A for $M_{\text{centerline}} = 0.35$ without inlet swirl	99
Figure V.32. Static pressure coefficient p^* (upper) and total pressure coefficient p_0^* (lower) distributions in plane 3A for $M_{\text{centerline}} = 0.35$ without inlet swirl	100
Figure V.33. Static pressure coefficient p^* (upper) and total pressure coefficient p_0^* (lower) distributions in plane 4A for $M_{\text{centerline}} = 0.35$ without inlet swirl	101
Figure V.34. Axial (upper) and transverse (lower) components of the velocity coefficient M^* in plane 1A for $M_{\text{centerline}} = 0.50$ without inlet swirl	102
Figure V.35. Axial (upper) and transverse (lower) components of the velocity coefficient M^* in plane 2A for $M_{\text{centerline}} = 0.50$ without inlet swirl	103

Figure V.36.	Axial (upper) and transverse (lower) components of the velocity coefficient M^* in plane 3A for $M_{\text{centerline}} = 0.50$ without inlet swirl	104
Figure V.37.	Axial (upper) and transverse (lower) components of the velocity coefficient M^* in plane 4A for $M_{\text{centerline}} = 0.50$ without inlet swirl	105
Figure V.38.	Static pressure coefficient p^* (upper) and total pressure coefficient p_0^* (lower) distributions in plane 1A for $M_{\text{centerline}} = 0.50$ without inlet swirl	106
Figure V.39.	Static pressure coefficient p^* (upper) and total pressure coefficient p_0^* (lower) distributions in plane 2A for $M_{\text{centerline}} = 0.50$ without inlet swirl	107
Figure V.40.	Static pressure coefficient p^* (upper) and total pressure coefficient p_0^* (lower) distributions in plane 3A for $M_{\text{centerline}} = 0.50$ without inlet swirl	108
Figure V.41.	Static pressure coefficient p^* (upper) and total pressure coefficient p_0^* (lower) distributions in plane 4A for $M_{\text{centerline}} = 0.50$ without inlet swirl	109
Figure V.42.	Surface static pressure coefficient p^* for flow with and without inlet swirl	112
Figure V.43.	Surface oil film visualization with inlet swirl	113
Figure V.44.	Surface oil film visualization with inlet swirl	114
Figure V.45.	Axial (upper) and transverse (lower) components of the velocity coefficient M^* in plane 1A for $M_{\text{centerline}} = 0.35$ with inlet swirl	115
Figure V.46.	Axial (upper) and transverse (lower) components of the velocity coefficient M^* in plane 2A for $M_{\text{centerline}} = 0.35$ with inlet swirl	116

Figure V.47.	Axial (upper) and transverse (lower) components of the velocity coefficient M^* in plane 3A for $M_{\text{centerline}} = 0.35$ with inlet swirl	117
Figure V.48.	Axial (upper) and transverse (lower) components of the velocity coefficient M^* in plane 4A for $M_{\text{centerline}} = 0.35$ with inlet swirl	118
Figure V.49.	Static pressure coefficient p^* (upper) and total pressure coefficient p_0^* (lower) distributions in plane 1A for $M_{\text{centerline}} = 0.35$ with inlet swirl	119
Figure V.50.	Static pressure coefficient p^* (upper) and total pressure coefficient p_0^* (lower) distributions in plane 2A for $M_{\text{centerline}} = 0.35$ with inlet swirl	120
Figure V.51.	Static pressure coefficient p^* (upper) and total pressure coefficient p_0^* (lower) distributions in plane 3A for $M_{\text{centerline}} = 0.35$ with inlet swirl	121
Figure V.52.	Static pressure coefficient p^* (upper) and total pressure coefficient p_0^* (lower) distributions in plane 4A for $M_{\text{centerline}} = 0.35$ with inlet swirl	122
Figure VI.1.	Ethylene concentration distributions with transverse velocity components at plane 2T.	133
Figure VI.2.	Ethylene concentration distributions with transverse velocity components at plane 3T.	134
Figure VI.3.	Ethylene concentration distributions with transverse velocity components at plane 4T.	135
Figure VI.4.	Axial vorticity at plane 1A for $M_{\text{centerline}} = 0.35$ without inlet swirl	141
Figure VI.5.	Axial vorticity at plane 2A for $M_{\text{centerline}} = 0.35$ without inlet swirl	142

Figure VI.6.	Axial vorticity at plane 3A for $M_{\text{centerline}} = 0.35$ without inlet swirl	143
Figure VI.7.	Axial vorticity at plane 4A for $M_{\text{centerline}} = 0.35$ without inlet swirl	144
Figure VI.8.	Sketch of secondary flow patterns inferred from surface oil film visualization for transition duct flow without inlet swirl	146
Figure VI.9.	Sketch of swirl driven and duct geometry driven velocities for transition duct flow with inlet swirl	147
Figure VI.10.	Axial vorticity at plane 1A for $M_{\text{centerline}} = 0.35$ with inlet swirl	149
Figure VI.11.	Axial vorticity at plane 2A for $M_{\text{centerline}} = 0.35$ with inlet swirl	150
Figure VI.12.	Axial vorticity at plane 3A for $M_{\text{centerline}} = 0.35$ with inlet swirl	151
Figure VI.13.	Axial vorticity at plane 4A for $M_{\text{centerline}} = 0.35$ with inlet swirl	152
Figure A.1.	A typical five-hole probe	157
Figure A.2.	Different five-hole probe pitch angles	160
Figure A.3.	Nondimensional pressure functions for a typical five-hole probe	161
Figure A.4.	Flow direction relative to the probe coordinate system	170
Figure A.5.	The relation between the probe coordinate system and the experiment coordinate system	171
Figure C.1.	The change of variables from Δ_i to D	216

LIST OF TABLES

Table III.1.	Transition duct parameters for Equation III.3	22
Table III.2.	Blade corner and edge construction from geometric surfaces	31
Table III.3.	Cartesian coordinates of stationary blade	33
Table V.1.	Boundary layer thickness $\delta_{0.95}$, displacement thickness δ^* , momentum thickness θ and shape factor H at $x/D = -0.5$ without swirl.	68
Table V.2.	Boundary layer thickness $\delta_{0.95}$, displacement thickness δ^* , momentum thickness θ and shape factor H at $x/D = -0.5$ with swirl.	75
Table V.3.	Summary of test conditions and experimental methods for transition duct studies without inlet swirl	78
Table VI.1.	Plane 1T trace gas concentration distribution statistics	128
Table VI.2.	Plane 2T trace gas concentration distribution statistics	129
Table VI.3.	Plane 3T trace gas concentration distribution statistics	130
Table VI.4.	Plane 4T trace gas concentration distribution statistics	131
Table VI.5.	Location of trace gas and aerodynamic measurement planes	132
Table A.1.	The ten pressure combinations and the corresponding value of the determinant given in Equation A.27	165
Table C.1.	The values of the coefficients a_j , $b_{j,k}$ and $c_{j,k,l}$	219

NOMENCLATURE

A	Coefficient in hot wire calibration equation
A_i	Area of element of domain partition
a_j	Constants in moment integral calculations
$a_{i,j}$	Taylor's series coefficients for five-hole probe pressure coefficient functions
B	Coefficient in hot wire calibration equation, constant in law of the wall equation
$b_{j,k}$	Constants in moment integral calculations
C_{ethylene}	Ethylene concentration expressed as a mole fraction
$C_{\text{ethylene,peak}}$	Maximum ethylene concentration for a given cross stream concentration distribution
C^*	Ethylene concentration coefficient
\bar{C}	Mean concentration
c'	Fluctuating concentration
c	Sonic velocity
c_0	Sonic velocity at isentropic stagnation conditions
$c_{j,k,l}$	Constants in moment integral calculations
D	Diameter
D_{ij}	Turbulent diffusion coefficient tensor components with respect to Cartesian coordinates
D_m	Molecular diffusion coefficient
D_t	Scaler turbulent diffusion coefficient
E	Hot wire anemometer bridge voltage
\bar{E}	Mean hot wire anemometer bridge voltage
e'	Fluctuating hot wire anemometer bridge voltage
f_1, \dots, f_5	Five-hole probe pressure coefficient functions
H	Boundary layer shape factor

k	Constant in law of the wall equation
L	Length
l'_j	Fluctuating turbulent mixing length with respect to Cartesian coordinates
l_t	Representative turbulent mixing length
M	Mach number
$M_{\text{centerline}}$	Mach number of the axial velocity component at the centerline at $x/D = -0.5$
M^*	Velocity coefficient
n	Exponent in hot wire calibration equation, molar quantity of matter
n_{ethylene}	Molar quantity of ethylene
n_y, n_z	Exponent parameters in transition duct equation
p	Static pressure
p_{wall}	Surface static pressure at $x/D = -0.5$
$p_{\text{settling chamber}}$	Pressure measured in settling chamber
p_1, \dots, p_5	Pressures measured with five-hole probe
p^*	Static pressure coefficient
p_0	Total pressure
$p_{0,\text{centerline}}$	Centerline total pressure at $x/D = -0.5$
p_0^*	Total pressure coefficient
R	Swirl generator radius, straight pipe radius, transition duct inlet radius, autocorrelation function
r_y, r_z	Radius parameters in transition duct equation
Re	Reynolds number
Re_{crit}	Critical Reynolds number
Re_D	Transition duct Reynolds number based on transition duct inlet diameter
S	Trace gas source strength
Tu	Turbulence intensity

U, V, W, U_i	Velocity components with respect to Cartesian coordinates
$\bar{U}, \bar{V}, \bar{W}, \bar{U}_i$	Mean velocity components with respect to Cartesian coordinates
u', v', w', u'_i	Fluctuating velocity components with respect to Cartesian coordinates
u^*	Friction velocity
u^+	Axial velocity in law of the wall coordinates
\mathbf{V}	Velocity vector
V_x, V_θ, V_r	Velocity components with respect to cylindrical coordinates
$V_{\text{centerline}}$	Velocity measured at the centerline
v_t	Representative turbulent velocity fluctuation
x, y, z	Cartesian coordinates
x, θ, r	Cylindrical coordinates
y_0, z_0	Centerline parameters in transition duct equation
y^+	Distance normal to the surface in law of the wall coordinates
α	Five-hole probe pitch angle relative to probe shaft
$\alpha_1, \alpha_2, \beta_1, \beta_2, \gamma_1, \gamma_2$	Parameters in swirl generator blade design equations
γ	Specific heat ratio
Δ_i	Element of partition of domain
$\delta_{0.95}$	Boundary layer thickness
δ^*	Boundary layer displacement thickness
θ	Inclination angle of swirl generator blades, boundary layer momentum thickness, five-hole probe pitch angle relative to probe opening
θ_0	Five-hole probe pitch difference angle
Λ	Turbulence integral length scale
λ	Molecular mean free path length
μ	Viscosity

μ_0	Viscosity at isentropic stagnation conditions
μ_x, μ_y, μ_z	Mean values with respect to Cartesian coordinates
P	Radius of swirl generator blade curvature
ρ	Density, radius of swirl generator centerbody
ρ_0	Density at isentropic stagnation conditions
σ	Screen solidity
$\sigma_x^2, \sigma_y^2, \sigma_z^2$	Variances with respect to Cartesian coordinates
$\sigma_{xy}, \sigma_{xz}, \sigma_{yz}$	Covariances with respect to Cartesian coordinates
T	Turbulence integral time scale
τ	Time like variable in autocorrelation equation
τ_w	Surface shear stress
ϕ	Swirl angle
ϕ_{\max}	Maximum ideal swirl angle
ϕ_1, ϕ_2, ϕ_3	Transformation angles between five-hole probe coordinate system and experiment coordinate system
ψ	Five-hole probe yaw angle
ψ_0	Five-hole probe yaw reference angle
ψ_1	Swirl generator blade inlet angle
ψ_2	Swirl generator blade exit angle
$\psi_{2,\max}$	Swirl generator blade exit angle at $r = R$
Ω	Angular velocity, domain of integration
$\omega_x, \omega_y, \omega_z$	Vorticity components with respect to Cartesian coordinates

ABSTRACT

Circular-to-rectangular transition ducts are used on aircraft with rectangular exhaust nozzles to connect the engine and nozzle. Often, the incoming flow of these transition ducts includes a swirling velocity component remaining from the gas turbine engine. Previous transition duct studies have either not included inlet swirl or when inlet swirl was considered, only overall performance parameters were evaluated. This dissertation reports the study of circular-to-rectangular transition duct flows with and without inlet swirl. This study was completed in order to understand the effect of inlet swirl on the transition duct flow field and to provide detailed duct flow data for comparison with numerical code predictions.

A method was devised to create a swirling, solid body rotational flow with minimal associated disturbances. Details of the swirl generator design and construction are discussed. Coefficients based on velocities and total and static pressures measured in cross stream planes at four axial locations within the transition duct along with surface static pressures and surface oil film visualization are presented for both nonswirling and swirling incoming flows. For nonswirling flow, measurements were recorded for three inlet centerline Mach numbers; 0.20, 0.35, and 0.50. The centerline Mach number for the swirling flow measurements was 0.35. The maximum ideal swirl angle was 15.6° .

A method was developed to acquire trace gas measurements within the transition duct at high flow velocities. Trace gas results are presented for the case of nonswirling incoming flow with an inlet centerline Mach number of 0.50. Statistical methods are used to help interpret the trace gas results.

Inlet swirl significantly changes the transition duct flow field. For nonswirling flow, the distribution of static pressure is attributed to the response of the flow field outside the boundary layer to the changing duct geometry. With swirl, the static pressure distribution is additionally affected by the streamline curvature of the swirl. For nonswirling incoming flow the static pressure distribution produced skew-induced

secondary flows within the boundary layer that evolved into two pair of counter-rotating side wall vortices. These vortices were absent in the swirling incoming flow case. The results show the effects of inlet swirl should be included in the design and numerical analysis of circular-to-rectangular transition ducts for aircraft exhaust systems.

ACKNOWLEDGMENT

The research reported in this dissertation was funded by NASA Headquarters as part of their Graduate Student Researchers program and was conducted at NASA Lewis Research Center. Without the financial support of NASA this research would not have been possible. The dedication and skill of two technicians at NASA Lewis Research Center, Bob Davis and Bill Darby, deserve special mention. This research was aided by their skilled workmanship and seasoned advice.

I was fortunate in my graduate studies and research to be guided by a concerned and capable committee. The committee members were John Tannehill, Bill Cook, Mike Pate, Howard Levine, Warren Hingst and Ted Okiishi. Each committee member has made a valuable contribution to my development as an engineer and as a citizen of the research and academic community.

I was introduced to computational fluid dynamics through Professor Tannehill's thoughtful and well-prepared lessons. From Professor Cook I learned that creativity is a vital component of original experimental research. My association with Professor Pate spans both my master and doctoral studies and research. Without his assistance my graduate studies at Iowa State University would not have been possible. Professor Levine instructed more of the graduate courses I attended than any other professor. His uncompromising instruction challenged me to expand the limits of my abilities. Dr. Warren Hingst, a researcher at NASA Lewis Research Center, provided the day-to-day supervision of this research. His knowledge of experimental aerodynamics and his mentoring in all aspects of the experimental aerodynamics profession were invaluable. Professor Okiishi was my major professor, who guided both my doctoral studies and dissertation research. Beside his eminent technical skills, his lessons of personal character and leadership will always be remembered.

Finally, the support and encouragement of my friends, family and particularly my wife, Eileen, have made my graduate studies a favorable experience. This dissertation is dedicated to you, Eileen.

CHAPTER I. INTRODUCTION

Ducts are used in aircraft propulsion systems to conjoin different components. For example, S-shaped ducts are used to connect the inlet and engine of Boeing 727 and Lockheed L-1011 aircraft. Recently, nonaxisymmetric exhaust nozzles have been proposed for aircraft applications which offer improved maneuverability by means of thrust vectoring and reduced thermal emission in comparison to axisymmetric nozzles. Rectangular exhaust nozzles are visible on the F-117A fighter and the B-2 bomber prototype. Aircraft with rectangular exhaust nozzles require a circular-to-rectangular transition duct to connect the engine and nozzle.

Detailed aerodynamic measurements of the flow field of a circular-to-rectangular transition duct are important for at least two reasons; to identify the important fluid dynamic phenomena which determine the transition duct flow field, and to provide data to compare with CFD predictions of the transition duct flow field. Knowledge of the relevant fluid dynamics can guide the engineer in improving the design of circular-to-rectangular transition ducts. Comparison with experimental data can provide a benchmark to measure the accuracy of CFD flow field predictions which lead to improvements in CFD methods.

To the designer, the value of experimental model data is enhanced when experimental test conditions accurately reproduce the conditions encountered in applications. For circular-to-rectangular transition ducts the incoming flow often includes a significant rotational velocity component, which remains from the engine turbine. Inlet swirl can significantly alter the flow field throughout the transition duct.

This dissertation reports the study of circular-to-rectangular transition duct flows with and without inlet swirl. The objective of this research was to ascertain the effect of inlet swirl on the transition duct flow field and to provide detailed duct flow data for comparison with CFD flow field predictions. Previous transition duct studies have either not included inlet swirl, or when swirl was considered only overall performance parameters were evaluated.

An improved understanding of circular-to-rectangular transition duct fluid dynamics was gained through detailed measurements of the transition duct flow field. Coefficients based on extensive measurements of velocity, total pressure and static pressure, acquired near the inlet and in four cross stream measurement planes within a circular-to-rectangular transition duct, are presented for flows with and without inlet swirl. Surface static pressure coefficients and surface oil film visualization results are also displayed. Additionally, a trace gas technique was used to obtain a Lagrangian description of the transition flow field without inlet swirl and those results are reported.

The simulation of circular-to-rectangular transition duct flows was improved through the use of a new swirl generator conceived, designed and constructed for this study. This swirl generator provides a solid body rotational flow with minimal disturbances, suitable for detailed experimental measurements and comparison with CFD predictions. A novel and original method was invented to produce solid body rotational flows which employs blades fabricated from cylindrical tubing with diminishing chord length, followed by rotating honeycomb and screen. The design, testing and operation of this swirl generator are reported herein.

A refinement of the five-hole probe aerodynamic measurement calibration and data reduction technique was used extensively for transition duct flow field measurements. This measurement technique is based on an analysis that provides a mathematical foundation for the calibration and use of five-hole probes. The results of the mathematical analysis used to develop the calibration and data reduction procedures and the numerical algorithms used to implement these procedures are included in an appendix.

The ethylene trace gas technique was adapted to higher speed (e.g., compressible, subsonic) flows and used to obtain Lagrangian data in the circular-to-rectangular transition duct. Trace gas results are presented for the flow field without inlet swirl. Statistical methods are used to quantitatively interpret the trace gas results. Numerical algorithms that implement the procedures used to calculate trace gas statistics are included in an appendix. Novel methods are described that were employed to inject

ethylene trace gas in the transition duct flow field with minimal disturbances and to sample the flow with effectively unlimited spatial resolution of the measurement locations within a cross stream plane.

The experimental measurements and analysis of the circular-to-rectangular transition duct flow field reported in this dissertation will be valuable to an engineer designing circular-to-rectangular transition ducts or using CFD methods to calculate similar internal flows. The methods described and used for swirl generation, five-hole probe calibration and data reduction, and ethylene trace gas measurements will be useful to an engineer employed in similar experimental studies.

CHAPTER II. REVIEW OF PRIOR RESEARCH

Past work is briefly reviewed in this chapter to offer a perspective on how the present research project was conceived and why it was conducted as reported. This project is an extension of progress made in past development of transition ducts. Transition duct research is discussed first and the case for new data is established. The need for an effective swirl generator is ascertained next. Finally, the usefulness of the trace gas technique as a vital measurement tool in this project is proposed and the adaptation of this technique to compressible flow is described.

Transition Duct Research

Nonaxisymmetric exhaust nozzles are employed on high performance aircraft to improve performance. The Pratt and Whitney two-dimensional/convergent-divergent nozzle described by Stevens *et al.* [1] is a rectangular nozzle designed to allow thrust vectoring, thrust reversal, jet area variation, and expansion area variation. Reduced thermal emission is another benefit attributed to rectangular exhaust nozzles. Rectangular exhaust nozzles require a circular-to-rectangular transition duct to connect the engine and nozzle. To allow proper exhaust nozzle performance, the transition duct should minimize transverse velocity components at the duct exit and total pressure losses throughout the duct.

The experimental study of circular-to-rectangular transition duct flows is one component of several in an effort at the NASA Lewis Research Center to accumulate experimental measurements of subsonic flows through various duct geometries. These data are used to identify and understand primary fluid phenomena governing the flow fields involved and to compare with relevant CFD predictions. These experimental efforts support the extensive enterprise of developing CFD methods to aid the design and analysis of aircraft propulsion components and systems. A review of the related numerical methods development is given by Anderson [2].

Under grants awarded by the NASA Lewis Research Center, Taylor *et al.* acquired laser Doppler velocimetry measurements in a square cross section duct with 90° bend [3], a square-to-round transition duct [4], an S-shaped square cross section duct [5] and an S-shaped circular cross section duct [6]. Enayet *et al.* [7] made comparable measurements in a circular cross section duct with a 90° bend. A common feature of these five studies is that measurements were made for both laminar and turbulent incompressible flow with thin inlet boundary layers. Also funded as part of the NASA Lewis Research Center effort were studies by Vakili *et al.* of compressible flow through an S-shaped circular cross section duct with constant cross-sectional area [8–10] and compressible flow through an S-shaped circular cross section duct with increasing cross-sectional area [11–13]. The research of Vakili *et al.* was also characterized by thin inlet boundary layers.

Researchers have also experimentally explored the aerodynamics of circular-to-rectangular transition ducts. Patrick and McCormick [14, 15] acquired experimental measurements at the inlet and exit planes of two circular-to-rectangular transition ducts, the first with an aspect ratio of 3 and a length-to-diameter ratio of 1 and the second with an aspect ratio of 6 and a length-to-diameter ratio of 3. The first duct maintained a constant cross-sectional area throughout the transition region. In the second duct the cross-sectional area at the inlet and exit of the transition region were equal but the cross-sectional area increased up to 10% in the transition region. Total pressures were measured with pressure probes and the three mean velocity and three normal Reynolds stress components were measured with a laser Doppler velocimeter. For this research the inlet Mach number was nominally 0.10, the Reynolds number, based on the inlet velocity and the duct inlet diameter, was 460,000 and 320,000 for the first and second ducts, respectively. The difference in Reynolds number resulted from the ducts having different inlet diameters. The ratio of the inlet boundary layer thickness to the duct inlet diameter was approximately 0.10 for both ducts.

Miau *et al.* [16, 17] acquired measurements in three circular-to-rectangular transition ducts for three different inlet flow conditions. The aspect ratio of each

duct was 2.0, the length-to-diameter ratios of the transition region were 1.08, 0.92, and 0.54. The inlet Mach numbers ranged between approximately 0.018 for the lowest inlet velocity condition to 0.106 for the highest inlet velocity. The Reynolds numbers, based on the free stream velocity and the duct inlet diameter, ranged between 195,000 and 1,140,000. The ratios of the inlet boundary layer thickness to the duct inlet diameter ranged between 0.0205 and 0.0175. Mean velocities at the transition duct exits and within the boundary layer along the diverging walls and turbulence intensity at the transition duct exits were measured with a hot wire anemometer. Surface static pressures were measured along 12 cross stream planes and water tunnel dye visualization results were also presented.

In a benchmark study, Davis and Gessner [18] measured static pressures, mean velocities, and all six Reynolds stress components in three cross stream planes within a circular-to-rectangular transition duct. Mean velocity and turbulence measurements were made with a hot wire anemometer, static pressures were measured with a pressure probe. The ratio of the boundary layer thickness to the inlet duct diameter was approximately 0.14. The Reynolds number, based on the bulk velocity and duct inlet diameter, was 390,000. The free stream Mach number was nominally 0.10. The transition duct of Davis and Gessner was identical to the one used in this study, and is described in detail in Chapter III.

In exhaust component applications the incoming flow to the circular-to-rectangular transition duct is turbulent and subsonic. Often, the incoming flow retains a significant rotational velocity component. The term swirl refers to this rotational velocity component, which remains from the engine turbine. Representative studies of turbine exit flow angles [19–21] have shown that swirl often exists at turbine design operating conditions, and may be as great as 30° or more at off-design operating conditions. Inlet swirl can significantly alter the flow field throughout the transition duct.

Each of the above mentioned circular-to-rectangular transition duct studies involved incompressible flow without inlet swirl. Burley *et al.* [22, 23] tested five circular-to-rectangular transition ducts including one with swirl vanes installed up-

stream of the duct inlet. Four of these transition ducts maintained a constant cross-sectional area throughout the transition region. For one transition duct the cross-sectional area decreased in the downstream direction. The aspect ratio of all five transition ducts was 6.33. The measurements were, however, limited to surface static pressures, a thrust ratio performance parameter and a discharge coefficient. No information was provided regarding the inlet Mach number, inlet boundary layer thickness or Reynolds number for these experiments. Test conditions were described by a nozzle pressure ratio.

The objective of the transition duct research reported in this dissertation was two-fold; to ascertain the effect of inlet swirl on the transition duct flow field and to provide a set of detailed data for comparison with CFD predictions of transition duct flows with and without inlet swirl. A swirl generator was designed and constructed to add a swirling component to the flow immediately upstream of the transition duct. The intent of the swirl generator was to create a solid body rotational flow, free of wakes and other disturbances.

Swirling Flow Generation

Ahmed *et al.* [24] studied the generation and management of swirling flows. The focus of their effort was to study how flow manipulators (e.g., honeycomb, screen, etc.) affect swirling flows. Three different swirl generator designs were investigated. The first, called the airfoil swirl generator, consisted of two NACA 0012 airfoils mounted in a circular cross section duct. Each airfoil was approximately one pipe radius long, allowing the two airfoils to join at a common hinge point at the centerline and span the duct. Swirl was induced by inclining the airfoils to the centerline. This swirl generator produced a strong rotational core. Plots of the radial distribution of axial vorticity, measured with a vane vorticity indicator, showed the maximum axial vorticity occurred at the flow center and reached zero near the wall. A tangential-jet swirl generator was the second configuration tested. This apparatus produced swirl by injecting air through eight equally spaced tangential jets into the primary stream

of a circular cross section duct. This configuration produced strong rotation near the walls. Measurements showed the radial distribution of axial vorticity reached a maximum very near the wall and rapidly approached zero a short distance away from the wall. The final swirl generator was named the swirling-jet ejector. Swirl was generated by flow through a section of annular vanes followed by a radial flow section. The swirling flow was used as the primary flow of an ejector. Like the airfoil swirl generator, this device produced a strong rotational core within a nearly irrotational outer region.

The swirl generator used by Burley *et al.* [22, 23] in their transition duct studies employed 12 flat plate vanes attached to a central hub and inclined to the flow axis. This swirl generator is similar in principal to the airfoil swirl generator of Ahmed *et al* [24], although no measurements of the flow field exiting the swirl generator were presented. The swirling flow cases studied were characterized by the angle the vanes were inclined to the centerline.

Hallett [25] described a swirl generator designed for the investigation of jet mixing and vortex breakdown. Air was injected tangentially from four slots along the periphery of the principal stream. This swirl generator is similar in principal to the tangential-jet swirl generator of Ahmed *et al.*

A rotating pipe was used to generate swirling flows by Weske and Sturov [26]. The purpose of their research was to study the turbulence of confined swirling flows. Their measurements show this swirl generator produced a flow with solid body rotation. The power required to rotate the pipe was provided externally. The facility size and mass flow rates of air through the facility were low compared to the requirements for aircraft transition duct studies.

The review of swirl generation literature revealed a new swirl generator design was necessary for the transition duct study. The swirl generator designs studied by Ahmed *et al.*, and their variations used by Burley *et al.* and Hallett do not produce the desired solid body rotation in the flow. The swirl generator of Weske and Sturov is

promising, it produces a flow with solid body rotation but requires an external motor to supply the power to rotate the pipe. A new design which employs the passive features of the airfoil type swirl generator with a rotating pipe was developed. The design of the new swirl generator is described in Chapter III, and measurements of the swirling flow field are presented in Chapter V.

The Trace Gas Technique

The trace gas technique involves injecting and tracking a nonreacting discernible foreign gas in the host flow field being investigated. Information about the host flow field is acquired by measuring the concentration of the trace gas in the host gas at many locations downstream of the point of injection. The trace gas technique is a valuable tool for several reasons; it is relatively inexpensive, easy to use, and is a source of Lagrangian flow field data. Previous trace gas experiments can be characterized by several important features, such as:

1. The objectives the trace gas technique were used to achieve
2. The types of trace gas used and their methods of detection
3. The class of flow fields investigated
4. The methods of trace gas injection used
5. The trace gas sampling methods employed
6. Important information about the trace gas technique that were revealed by the experiments

The relevant trace gas literature will be discussed in the context of these features.

Previous experiments can be divided into two broad categories distinguished by the objectives the trace gas technique were used to achieve. The two classifications are inferential experiments and direct experiments. Inferential experiments refer to studies where the information about the flow field was deduced from the trace gas concentration measurements. Inferential trace gas experiments often require *a priori* assumptions about the host flow field being investigated or additional flow

field data acquired by other measurement techniques. The information deduced from the concentration measurements may be the mean streamline of a fluid particle or the relative importance of convection and diffusion in the mixing of trace gas with the host flow.

Some important inferential trace gas experiments include the research of Kerrebrock and Mikolajczak [27], who tracked fluid flow from the pressure side of a rotor blade through the downstream stator row. Denton and Usui [28] studied the transport of fluid from the end wall boundary layers of a single-stage low speed air turbine. Smith [29], Moore [30], and Moore and Smith [31] used the trace gas technique in a linear turbine cascade to help locate the source of high and low total pressure loss fluid. Gallimore [32] and Gallimore and Cumpsty [33] used the trace gas technique in two low speed, four-stage air compressors. Their investigation was performed to ascertain the relative importance of convection and turbulent diffusion in spanwise (radial) mixing within multistage compressors. Bauer [34] and Wisler *et al.* [35] also used the trace gas technique to investigate spanwise convection and mixing in the third stage stator row of a low speed, four-stage, axial flow research compressor.

Direct experiments refer to studies where the extent of mixing of the trace gas into the flow field was of interest. In this case the final result was made by direct observation. Often, the trace gas was used to represent another gas, or the trace gas concentration represented another fluid property such as temperature. Direct experiments include the work reported by Hallett and Guenther [36], who used the trace gas technique to quantify the degree of mixing within a combustor. McGreehan *et al.* [37] employed the trace gas technique to measure the rate at which airflow leaked through a labyrinth seal in a gas turbine engine. Joslyn and Dring [38] performed an experiment in a large scale low speed turbine where trace gas concentration was used as an analogy to temperature to study the radial redistribution of temperature in the turbine. Folayan and Whitelaw [39] and Humphrey and Whitelaw [40] used the trace gas and temperature analogy to better understand film cooling methods on convex and concave surfaces.

Ethylene was used for the trace gas in References 28–35. Other gases that have been used as a trace gas are helium [27, 37, 39, 40], carbon dioxide [37, 38], and natural gas [36]. The instruments used for trace gas detection were largely determined by the choice of trace gas. A flame ionization detector provides a very accurate measurement of ethylene concentration and was used in References 28–35. Researchers that use helium have frequently used a thermal conductivity cell for trace gas detection [27, 37, 39, 40]. Carbon dioxide concentration was commonly measured with a nondispersive infrared detector [37, 38].

The class of flows investigated by the trace gas technique may be categorized by the geometry or application of the experiment such as turbomachines or mixing nozzles, or more importantly by features of the flow, particularly the flow velocity. All of the uses of ethylene trace gas that have been cited above have been at relatively low velocities, in nearly all cases the Mach number of the host flow was less than 0.10. One objective of the research reported in this dissertation was to adapt the ethylene trace gas technique to higher speed, compressible, subsonic flows. Building on this success, Davis *et al.* [41] recently used the ethylene trace gas technique at NASA Lewis Research Center to measure the mixing of two supersonic streams in a study of mixing nozzles for scramjet applications.

The methods used to inject the trace gas into the host flow field can be classified as either surface injection methods or probe injection methods. The choice of trace gas injection method largely depends on the objectives of the trace gas experiment. Static pressure taps were used for surface trace gas injection in References 27, 28, 34, 35. Slot shaped openings have also been used for surface trace gas injection [39, 40]. The most common trace gas probe injection method used was an L-shaped probe, like a downstream facing total pressure probe. This type of probe, or variations of it, have been used in References 28–35. The diameters of the injection probes reported in these references range from 3.2 mm to 0.56 mm. The results of experiments designed to measure and minimize disturbances from L-shaped type probes are reported in References 29, 30, 32, 33 and by Moore *et al.* [42]. These results are discussed

in Chapter IV. A different approach to trace gas injection was employed by Joslyn and Dring [38]. In their experiment trace gas was injected simultaneously at many point locations distributed throughout the injection plane to simulate the temperature distribution in an air turbine.

The most common trace gas sampling probe design used in the past employed features similar to a single-hole Pitot type pressure probe [27–31, 34, 35]. The flow field sample was drawn through the single probe opening. Another trace gas sampling probe design reported was similar to a three-hole “cobra” type pressure probe [32, 33]. When using this kind of probe, the two side holes were used to align the yaw axis of the probe with the flow field direction while the center hole was used to draw the sample. Other sampling methods involved the use of a trace gas sampling probe rake [29–31, 38] and sampling through surface static pressure tap openings [39, 40, 38].

Several ethylene trace gas experiments have revealed important information about the ethylene trace gas technique. The paper of Wisler *et al.* [35] generated considerable discussion. Some controversy centered around their conclusions regarding the relative importance of convection and turbulent diffusion in the radial transport of fluid in multistage axial flow compressors. Differences in the interpretation of the trace gas results, that is, deciding the roles of convection and turbulent diffusion in producing the measured ethylene concentration distributions were proposed by discussants. For example, Gallimore and Cumpsty proposed different interpretations of the Wisler *et al.* data. Lylek and Wisler [43] continued the study reported by Wisler *et al.* Additional ethylene trace gas data and Navier-Stokes code computational results were used to aid trace gas data interpretation. The difficulties of interpreting trace gas concentration measurements are discussed in Chapter VI.

CHAPTER III. FACILITIES

This chapter describes the experimental facilities used during the course of this research. The calibration tunnel and the swirl generator are described in detail in the first and fourth sections of this chapter, titled Calibration Tunnel and Swirl Generator, respectively. These facilities were designed and constructed specifically for this research. The Internal Fluid Mechanics Facility, described in the second section of this chapter, and the transition duct, described in the third section, already existed prior to the beginning this research.

Calibration Tunnel

A small air flow tunnel was designed and constructed at the NASA Lewis Research Center to test the trace gas equipment and measurement technique before trace gas measurements were attempted in the transition duct. This tunnel was designed to operate at flow velocities comparable to those used in the transition duct. The tunnel involved an air jet stream that expands into a quiescent chamber. The jet was designed to have a large core of uniform, mean, axially directed velocity with low turbulence intensity. The use of this tunnel and the results of the trace gas experiments conducted in this tunnel are described in Chapter V.

Components

The tunnel, pictured in Figure III.1 consists of three principal components. They are:

1. The settling chamber
2. The contraction
3. The test section

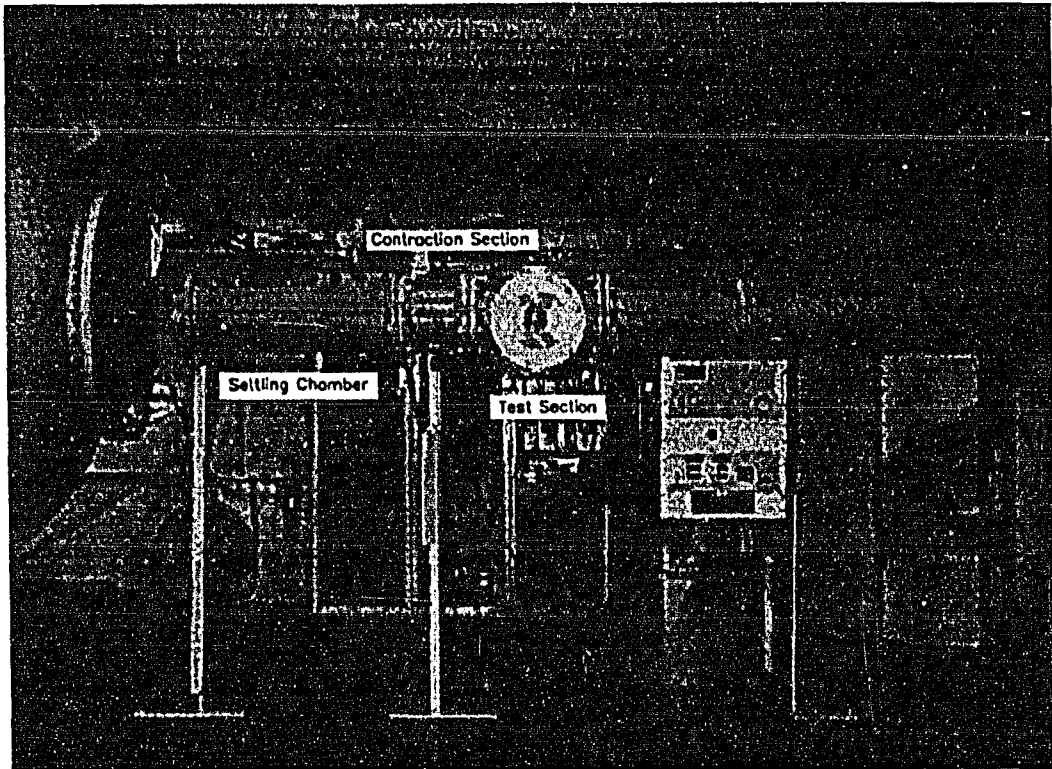


Figure III.1 The calibration tunnel used to test the trace gas equipment and measurement technique

Settling chamber The settling chamber consisted of a 91.4 cm length of 25.4 cm diameter schedule 40 pipe. The settling chamber employed a honeycomb and screen combination to reduce the free stream turbulence. Scheiman [44] observed that a honeycomb alone is more effective at reducing lateral turbulence while a screen alone is more effective at reducing axial turbulence. Scheiman concluded that the combination of screens downstream of honeycomb is a productive way to utilize the turbulence reduction characteristics of each device.

Loehrke and Nagib [45] attribute the effectiveness of a honeycomb at reducing lateral turbulence to the constraint of the lateral velocity components by the honeycomb side walls. Accordingly, they recommended that the Reynolds number, based on the honeycomb cell diameter, be less than the value for transition to turbulent flow. The honeycomb used in the settling chamber was constructed of stainless steel

and had a 0.95 cm cell diameter. When the jet is operating at a choked condition (its maximum velocity), the air velocity within the settling chamber is approximately 4.45 m/s, resulting in a Reynolds number of approximately 2,500. At all operating conditions but the highest velocities this Reynolds number is less than the value of Reynolds number generally accepted as indicating transition to turbulent flow, 2300.

The experiments of Loehrke and Nagib also indicate the ratio of the honeycomb cell length to the cell diameter has a significant effect on the ability of the honeycomb to reduce turbulence. Of the three different lengths they tested, the shortest, with a cell length to diameter ratio of eight, was most effective at reducing turbulence. The honeycomb used in the calibration tunnel has a cell length of 5.08 cm, providing a length-to-diameter ratio of 5.3 which conforms with Loehrke and Nagib's recommendation of using a relatively short length honeycomb.

Schubauer *et al.* [46] showed that a wire screen is most effective in reducing turbulence when the Reynolds number, based on the screen wire diameter, is below a critical value. Reynolds numbers above this value produce vortex shedding downstream of the screen, resulting in higher, rather than lower, turbulence intensities. This critical Reynolds number depends upon the screen solidity σ , which is the ratio of the closed area of the screen to the total area. An approximate relation, based on data in Reference 46 is $Re_{crit} = 77.5 - 62.5\sigma$ for solidity values in the range $0.2 \leq \sigma \leq 0.5$.

The screen used in the calibration tunnel was a 24 mesh stainless steel wire screen with a solidity of $\sigma = 0.327$ and a wire diameter of 0.1905 mm. Based on this solidity and wire diameter, the critical Reynolds number should be approximately 57. When the jet is operating at a choked condition, the resulting Reynolds number is approximately 52. Therefore, in all operating conditions the Reynolds number is less than the critical value.

Contraction An axisymmetric contraction with a 52:1 area ratio was located immediately downstream of the settling chamber. Contractions are used downstream of settling chambers to increase the mean velocity, lower turbulence intensities, and

insure uniform mean flow. This contraction was machined from a solid aluminum round bar. The shape of the inside radius of the contraction was machined to match the curve of the two smoothly joined cubics given by Equation III.1. This curve is smooth in the sense it is continuous and has a continuous first derivative. In a study of axisymmetric wind tunnel contractions, Morel [47] compared six different families of curves and concluded that two smoothly joined cubics was the curve best suited to use as the wall shape for an axisymmetric wind tunnel contraction. In Equation III.1 R_1 is the upstream radius of the contraction, R_2 is the downstream radius, and L is the length of the contraction. The values used for the construction of the contraction were $R_1 = 12.541$ cm, $R_2 = 1.7145$ cm and $L = 25.083$ cm.

$$\frac{r}{R_1} = \begin{cases} 1 - 4\left(1 - \frac{R_2}{R_1}\right)\left(\frac{x}{L}\right)^3 & 0 \leq \frac{x}{L} \leq \frac{1}{2} \\ \frac{R_2}{R_1} - 4\left(1 - \frac{R_2}{R_1}\right)\left(\frac{x}{L} - 1\right)^3 & \frac{1}{2} \leq \frac{x}{L} \leq 1 \end{cases} \quad (\text{III.1})$$

The outside diameter of the contraction was a constant 25.4 cm, to allow the contraction to be installed inside a 30.5 cm length of 25.4 cm diameter schedule 40 pipe. This section of pipe was drilled and tapped to accept set screws to secure the contraction section. The outlet of the contraction was connected to a short section of 3.81 cm diameter stainless steel tube which exhausted as a jet into the test section.

Test section The test section was constructed from a 25.4 cm diameter schedule 40 pipe cross on which two additional legs of 25.4 cm diameter schedule 40 pipe were added, providing six legs. The contraction section was attached to one leg, while the opposite leg was connected to an exhaust line. Windows, constructed of aluminum frames and 15.2 cm diameter quartz lenses, were installed in opposite legs to provide optical access of the test section. The optical access allowed visual inspection of the trace gas injection and sampling probes under operational conditions. The remaining pair of opposite legs were blanked off with aluminum plates and were used to allow instrument access.

Internal Fluid Mechanics Facility

All transition duct experiments were conducted at the NASA Lewis Research Center using the Internal Fluid Mechanics Facility. This facility, shown in Figure III.2, was designed to support the research of a variety of internal flow configurations. Air may be supplied from either the test cell or from a continuous source of pressurized air. After passing through a large settling chamber containing a honeycomb and two screens the flow proceeds through an axisymmetric contraction having an area ratio of 57:1. The flow passes from the contraction through either a straight pipe to provide a nonswirling uniform incoming flow to the transition duct or the swirl generator to provide a swirling incoming flow to the transition duct. After passing through the transition duct the flow is exhausted into a discharge plenum which is continuously evacuated by central compressor facilities. In Figure III.2 the Internal Fluid Mechanics Facility is shown with the transition duct installed, the straight pipe in place instead of the swirl generator, and with air drawn from the test cell through the open end of the settling chamber.

Throughout this dissertation, discussion of the swirl generator or the straight pipe, which are upstream of the transition duct, are with respect to a cylindrical coordinate system, x, θ, r . The x -axis of the coordinate system is coincident with the swirl generator or straight pipe centerline. Distances have been nondimensionalized with respect to the swirl generator or straight pipe radius, 10.21 cm. The radius, rather than the diameter, was used to conform with standard convention for axisymmetric flows.

For all transition duct experiments the air was supplied from the test cell. This configuration does not allow the Mach number and Reynolds number to be varied independently, their relationship is given in Equation III.2.

$$Re = \frac{\rho_0 c_0 D}{\mu_0} M \left(1 + \frac{\gamma - 1}{2} M^2 \right)^{\frac{\gamma - 1}{2(\gamma - 1)}} \quad (\text{III.2})$$

The total pressure and temperature of the airflow is dependent on the ambient pressure and temperature within the test cell. Figure III.3 is a plot of Equation III.2 for

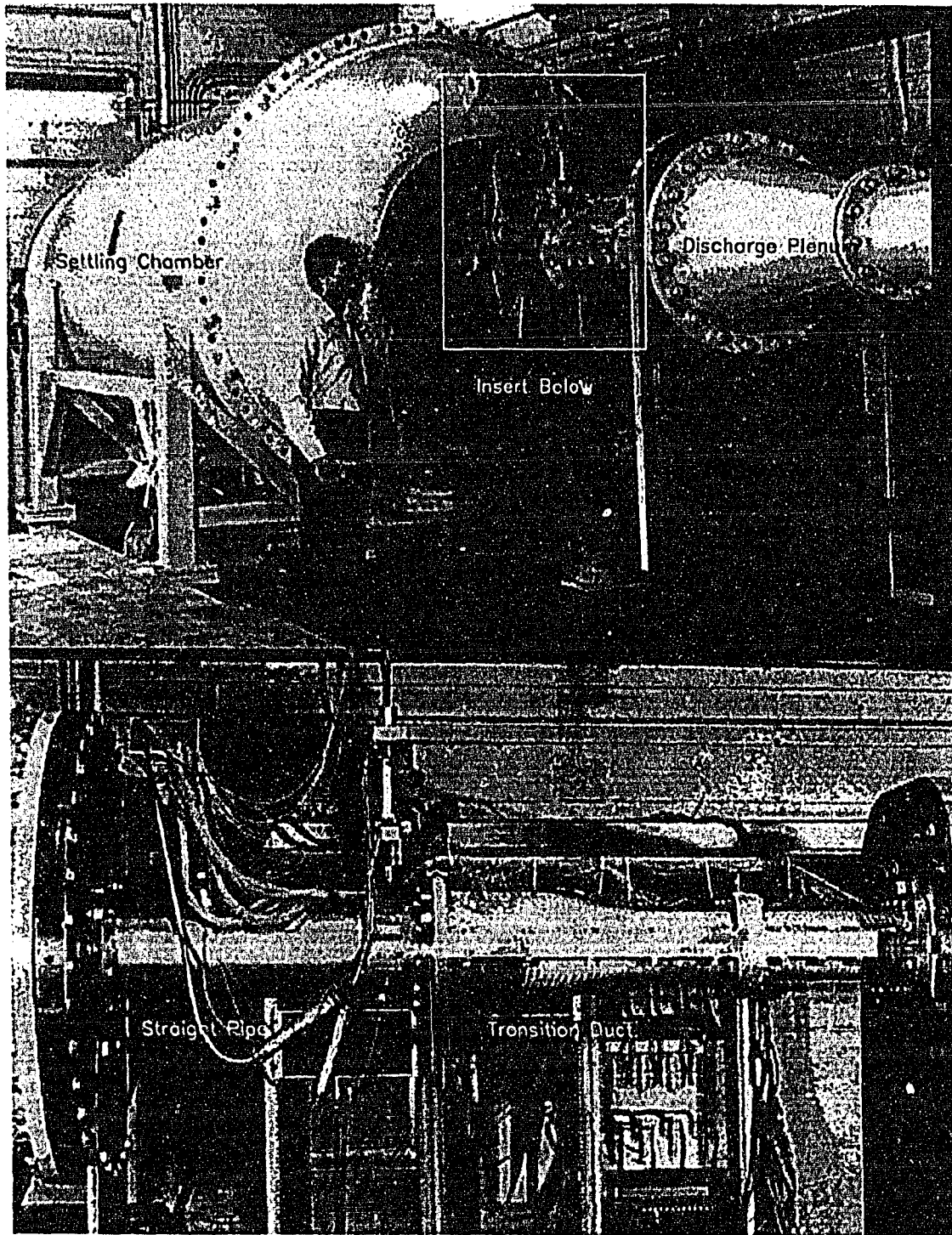


Figure III.2 The NASA Lewis Research Center Internal Fluid Mechanics Facility

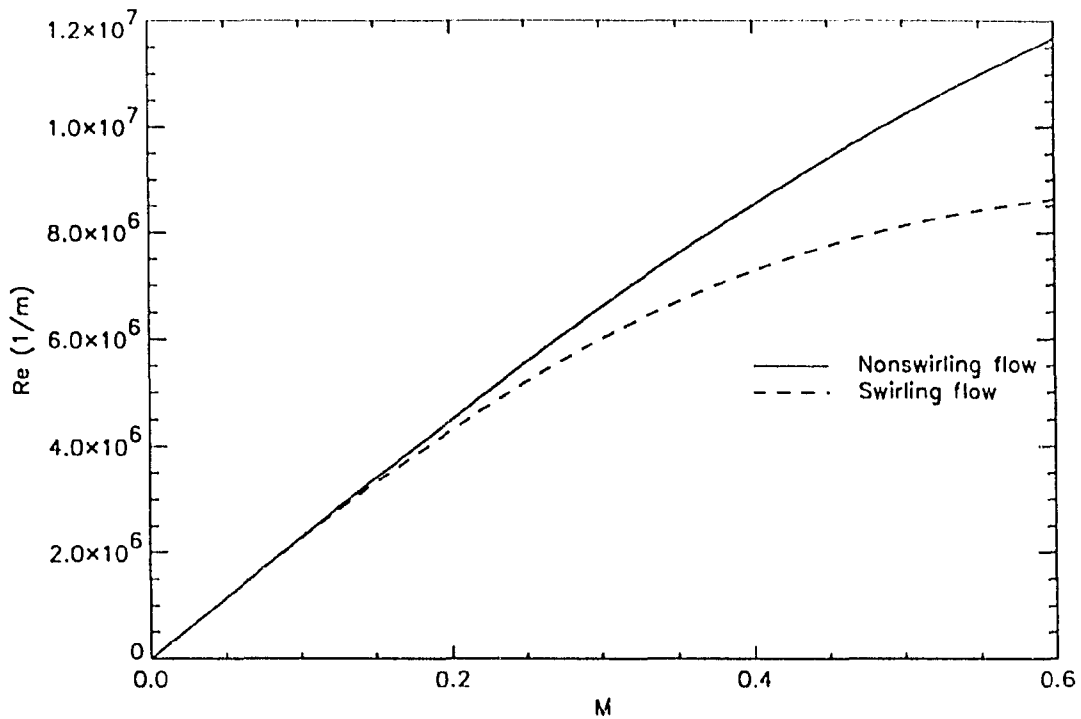


Figure III.3 The Mach number – Reynolds number relationship for the Internal Fluid Mechanics Facility

conditions evaluated at the inlet of the transition duct. The example test cell air pressure and temperature for generating Figure III.3 are 101.3 KPa and 294 °K. The Reynolds number, shown on the ordinate of Figure III.3 is per meter of characteristic length. The solid line represents nonswirling flow, the broken line represents swirling flow. The difference between these two curves results from total pressure losses produced by the swirl generator. These total pressure losses are discussed in the Swirl Generator Validation section of Chapter V.

Transition Duct

Figure III.4 shows a wireframe drawing of the circular-to-rectangular transition duct that was tested. All discussion of the transition duct throughout the dissertation is with respect to the Cartesian coordinate system shown in Figure III.4. The origin

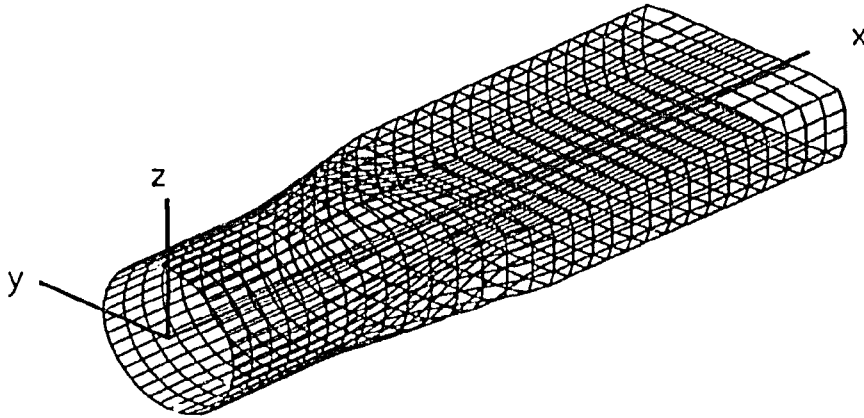


Figure III.4 Circular-to-rectangular transition duct

of the coordinate system is located one diameter upstream of the beginning of the transition region. This origin coincides with the physical beginning of the transition duct (or the exit of the straight pipe or swirl generator). The x -axis is coincident to the duct centerline. Distances have been nondimensionalized with respect to the inlet diameter of the transition duct, 20.42 cm.

This transition duct is a member of a family of ducts designed at the NASA Lewis Research Center. In the yz -plane through each cross section, the surface of the family of ducts satisfies Equation III.3.

$$\left(\frac{y - y_0}{r_y}\right)^{n_y} + \left(\frac{z - z_0}{r_z}\right)^{n_z} = 1 \quad (\text{III.3})$$

The parameters y_0 , r_y , n_y , z_0 , r_z , n_z , which specify the exact geometry of the members of this family, are all functions of the axial distance x .

$$F : x \rightarrow y_0, r_y, n_y, z_0, r_z, n_z \quad (\text{III.4})$$

The functional relation represented by Equation III.4 is summarized in Table III.1.

The transition duct geometry possesses two planes of symmetry, the xy -plane and xz -plane. If the point (x, y, z) satisfies Equation III.4, then so do the points $(x, -y, z)$, $(x, y, -z)$, and $(x, -y, -z)$.

The transition region of the duct is the region where the cross section in the yz -plane varies with axial distance. The transition region lies within $1.0 \leq x/D \leq 2.5$. The ratio of the length of the transition region to the inlet diameter is $L/D = 1.5$. The ratio of major to minor axis dimensions at the duct exit, referred to as the aspect ratio, is $r_y/r_z = 3.0$. The cross-sectional areas at the inlet and exit are equal. In the transition region the cross-sectional area increases to 1.15 times the inlet area. The distribution of cross-sectional area in the transition region is equal to the cross-sectional area that would result if a duct with the same aspect ratio and transition region length to inlet diameter ratio were constructed of circular and flat sections of metal only. This type of construction was believed to more accurately represent fabrication methods used in the aviation industry. The cross-sectional shape of these transition ducts becomes more rectangular as the value of the exponents increase, but they are never truly rectangular. This was done to provide the smooth boundary required by some CFD methods. The circular-to-rectangular ducts studied in References 14, 15, 18, 22, 23 are all members of this family of transition ducts.

The transition duct was constructed in two halves joined at the xy -plane. Each half was machined from a single piece of aluminum using a numerically controlled mill. This transition duct was also used as a mold to produce an identical fiberglass duct used by Davis and Gessner for measurements made at the University of Washington [18].

Table III.1 Transition duct parameters for Equation III.3

x/D	y_0/D	r_y/D	n_y	z_0/D	r_z/D	n_z
0.00	0.00000	0.500000	2.00000	0.00000	0.5000000	2.00000
1.00	0.00000	0.500000	2.00000	0.00000	0.5000000	2.00000
1.06	0.00000	0.500165	2.10467	0.00000	0.499854	2.10467
1.12	0.00000	0.501236	2.21536	0.00000	0.498904	2.21536
1.18	0.00000	0.503911	2.33308	0.00000	0.496531	2.33308
1.24	0.00000	0.508676	2.45877	0.00000	0.492306	2.45877
1.30	0.00000	0.515822	2.59342	0.00000	0.485967	2.59342
1.36	0.00000	0.525474	2.73825	0.00000	0.477408	2.73825
1.42	0.00000	0.537602	2.89471	0.00000	0.466651	2.89471
1.48	0.00000	0.552048	3.06449	0.00000	0.453840	3.06449
1.54	0.00000	0.568540	3.24972	0.00000	0.439214	3.24972
1.60	0.00000	0.586718	3.45288	0.00000	0.423092	3.45288
1.66	0.00000	0.606151	3.67704	0.00000	0.405858	3.67704
1.72	0.00000	0.626356	3.92613	0.00000	0.387938	3.92613
1.78	0.00000	0.646823	4.20500	0.00000	0.369787	4.20500
1.84	0.00000	0.667028	4.51993	0.00000	0.351867	4.51993
1.90	0.00000	0.686461	4.87910	0.00000	0.334633	4.87910
1.96	0.00000	0.704640	5.29319	0.00000	0.318511	5.29319
2.02	0.00000	0.721131	5.77751	0.00000	0.303885	5.77751
2.08	0.00000	0.735577	6.35245	0.00000	0.291074	6.35245
2.14	0.00000	0.747705	7.04838	0.00000	0.280317	7.04838
2.20	0.00000	0.757357	7.91061	0.00000	0.271758	7.91061
2.26	0.00000	0.764503	9.01307	0.00000	0.265419	9.01307
2.32	0.00000	0.769268	10.00000	0.00000	0.261194	10.00000
2.38	0.00000	0.771943	10.00000	0.00000	0.258821	10.00000
2.44	0.00000	0.773015	10.00000	0.00000	0.257871	10.00000
2.50	0.00000	0.773180	10.00000	0.00000	0.257725	10.00000
5.47	0.00000	0.773180	10.00000	0.00000	0.257725	10.00000

Swirl Generator

Rotating flow

The function of the swirl generator was to create a solid body rotational flow superimposed on a uniform, one-dimensional flow. In cylindrical coordinates this velocity field is described by Equation III.5, where $V_{\text{centerline}}$ is the velocity at the swirl generator centerline and Ω is the angular velocity of the solid body rotation.

$$V_x = V_{\text{centerline}}, V_\theta = \Omega r, V_r = 0 \quad (\text{III.5})$$

An example of this flow is represented in Figure III.5. The swirl angle, ϕ , is given by Equation III.6. This is the angle of the flow relative to the x -axis measured by a stationary observer. This angle increases as the radius increases but it is V_θ , not ϕ , that increases linearly with the radius.

$$\phi = \arctan\left(\frac{V_\theta}{V_x}\right) \quad (\text{III.6})$$

Ideally, this rotating flow would be free of wakes or other disturbances caused by the mechanism which creates the rotation. In principle this can be achieved by flow through a sufficiently long pipe rotating about its axis at a constant angular velocity. For the desired case of no radial velocity, the radial momentum equation requires that the radial pressure gradient balance the centrifugal forces acting on the fluid, as shown in Equation III.7.

$$\frac{\partial p}{\partial r} = \rho \frac{V_\theta^2}{r} \quad (\text{III.7})$$

This condition is referred to as simple radial equilibrium [48]. For solid body rotation, where $V_\theta = \Omega r$, the radial pressure gradient is given by Equation III.8. Equation III.8 requires the static pressure distribution to increase parabolically in the radial direction from the centerline. For the rotating pipe, the Coriolis force is negligible since the axis of rotation corresponds to the principal direction of fluid motion.

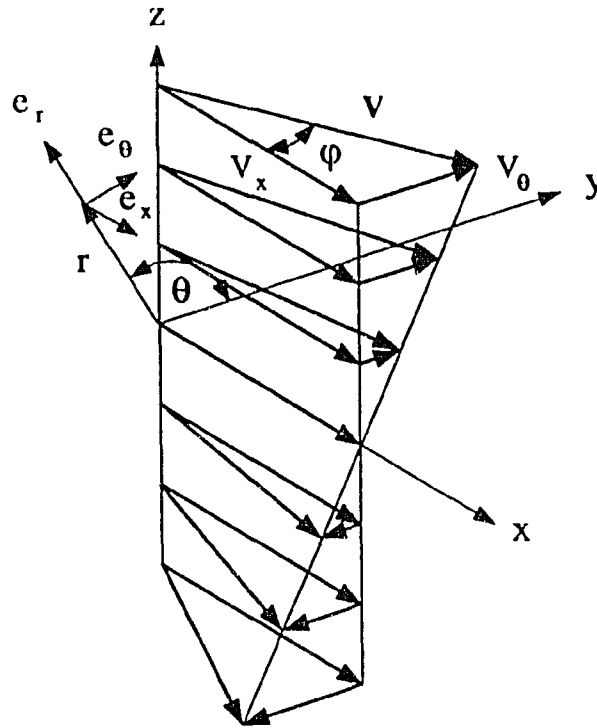


Figure III.5 Solid body rotation superimposed on uniform flow

$$\frac{\partial p}{\partial r} = \rho \Omega^2 r \quad (\text{III.8})$$

Solid body rotation and the resulting static pressure distribution is centrifugally stable in the sense that a fluid particle whose position is perturbed radially will tend to return to its original position by the influence of the radial static pressure distribution. This stability is unlike the case of flow between concentric cylinders when the inner pipe is rotating and outer pipe is stationary [49].

$$\phi = \arctan \left(\frac{\Omega r}{V_x} \right) \quad (\text{III.9})$$

The amount of swirl for this flow is given by Equation III.9. The amount of swirl is determined by the incoming velocity and the angular velocity, which may be varied independently. This flow field will have a constant axial component of vorticity

of magnitude 2Ω everywhere, and negligible radial and tangential components of vorticity everywhere except within the boundary layer.

In important consideration in the analysis of a rotating pipe is whether work is added or extracted from the flow. Ignoring the boundary layer for the moment, consider an initially irrotational, incompressible, inviscid, uniform flow entering a rotating pipe. The flow entering the pipe will have constant radial total and static pressure distributions. The radial static pressure distribution of the exiting flow will increase parabolically from the centerline at a rate determined by the angular velocity of the rotating flow in order to maintain radial equilibrium. If no work is added or extracted from the flow the radial total pressure distribution of the exiting flow will remain constant and at the same level as the entering flow. This will require the total velocity magnitude and hence the axial component of velocity to decrease radially for the exiting flow. If work is added to the flow, like in a compressor, the exiting flow will have a radial total pressure distribution that will also increase parabolically from the centerline. The radial decrease of the axial component of velocity of the flow exiting the pipe will be less than the case when no work is added or extracted from the flow. If work is extracted from the flow, like a turbine, the radial total pressure distribution of the exiting flow will decrease parabolically from the centerline. The radial decrease of the axial component of velocity of the exiting flow will be greater than the case when no work is added or extracted from the flow.

Swirl generator design

A rotating pipe alone as a swirl generator was not satisfactory for this research for several reasons. A developing internal flow was desired. When shear stress has transferred momentum from the rotating pipe wall into the initially irrotational flow and solid body rotation is achieved the flow would be fully developed as well. If honeycomb were used at the entrance of the rotating pipe, like the swirl generator of Weske and Sturov [26], solid body rotation can be achieved before the flow is fully developed. However, the power requirements necessary to achieve solid body rotation

become excessive for large angular velocities and particularly for large through flow velocities. It was doubtful whether this energy could be transferred to the flow by the honeycomb without destroying the honeycomb.

Another possible design was a set of stationary blades designed to create solid body rotation. This design would also create a rotating flow field immediately, but it was not satisfactory because of the presence of unwanted wakes created by the stationary blades and the difficulty in designing blades that exactly produce solid body rotation.

Figure III.6 shows a schematic of the swirl generator that was conceived, designed and constructed for this study. This generator employs both stationary blades and a rotating pipe. The flow entering the stationary blades is nominally uniform and one-dimensional. The stationary blades create a near solid body rotation at an angular velocity that depends on both the axial flow velocity and the stationary blade design, which may be varied independently. Ideally, the angular velocity of the rotating pipe is given by Equation III.10.

$$\Omega = \frac{V_x \tan \phi}{r} \quad (\text{III.10})$$

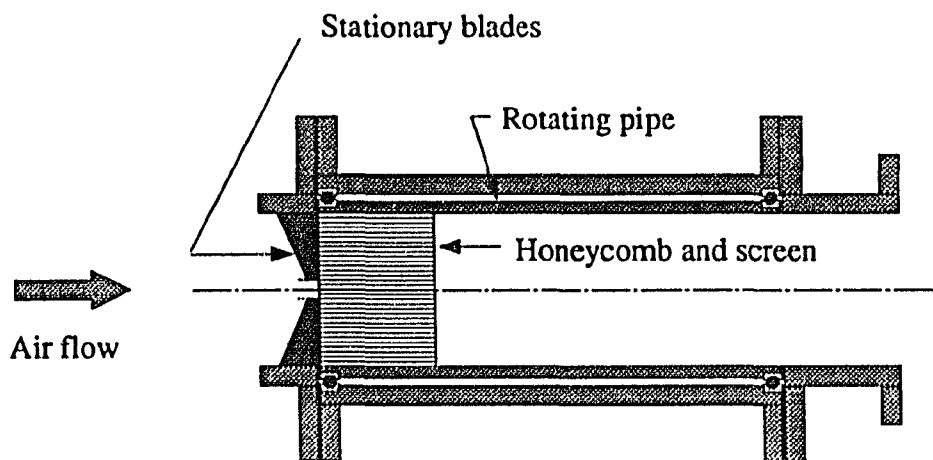


Figure III.6 Swirl generator schematic

Immediately downstream of the stationary blades is the rotating pipe. The honeycomb and screen are fixed to the rotating pipe and these components rotate as one assembly. The honeycomb serves three functions:

1. To serve as a rotor to impart motion to the rotating pipe. Ideally, the rotating pipe will achieve an angular velocity that matches the solid body rotation of the flow exiting the stationary blades.
2. To reinforce the solid body rotation initiated by the stationary blades. The honeycomb is performing its customary roll by straightening the flow, this time within the rotating frame of reference.
3. To dissipate the wakes created by the stationary blades.

A screen is located downwind of the honeycomb to dissipate the wakes created by the honeycomb. The final section of the swirl generator is the stationary exit section. This section functions as a stationary component to which the transition duct may be attached.

Stationary blade design

The terminology used to discuss blade design, shown in Figure III.7, has been adopted from Glassman [50]. Several assumptions were made to simplify the design of the stationary blades. It was presumed that the incoming flow is uniform and that along blade surfaces the flow satisfies the tangency condition.

To accommodate the assumed incoming flow conditions the blade inlet angle, ψ_1 , must be zero everywhere along the blade leading edge. The assumptions require the flow exiting the stationary blades be parallel to the camber line at the trailing edge. Therefore, the exiting flow is at an angle ψ_2 relative to the x -axis and the amount of swirl will be equal to the blade exit angle, $\phi = \psi_2$. To achieve solid body rotation, the blade exit angle must satisfy Equation III.11.

$$\psi_2 = \arctan \left(\frac{r}{R} \tan \psi_{2,\max} \right) \quad (\text{III.11})$$

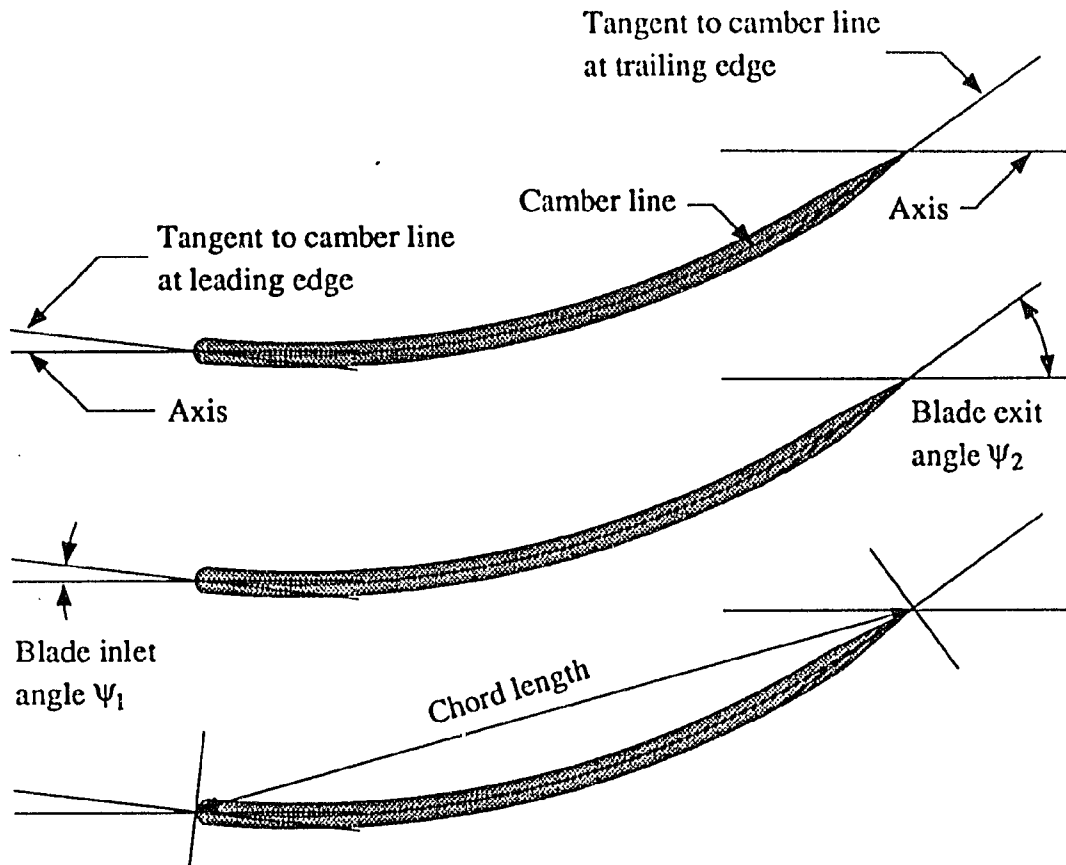


Figure III.7 Stationary blade design nomenclature

In Equation III.11 R is maximum radius and $\psi_{2,\max}$ is the blade exit angle at $r = R$. The angular velocity of the flow is given by Equation III.12.

$$\Omega = \frac{V_x \tan \psi_{2,\max}}{R} \quad (\text{III.12})$$

This simple analysis cannot be used to determine the shape of the blade from leading to trailing edge or the total number of blades required.

A novel approach to blade design and construction was used to produce blades that exactly satisfy the blade inlet angle requirement and closely approximate the blade exit angle requirement, Equation III.11. These blades were fabricated by cutting the triangular shape a-b-e from a thin circular tube, as shown in Figure III.8. The portion of the triangle used to construct the blade is the shaded shape a-b-c-d, the lower

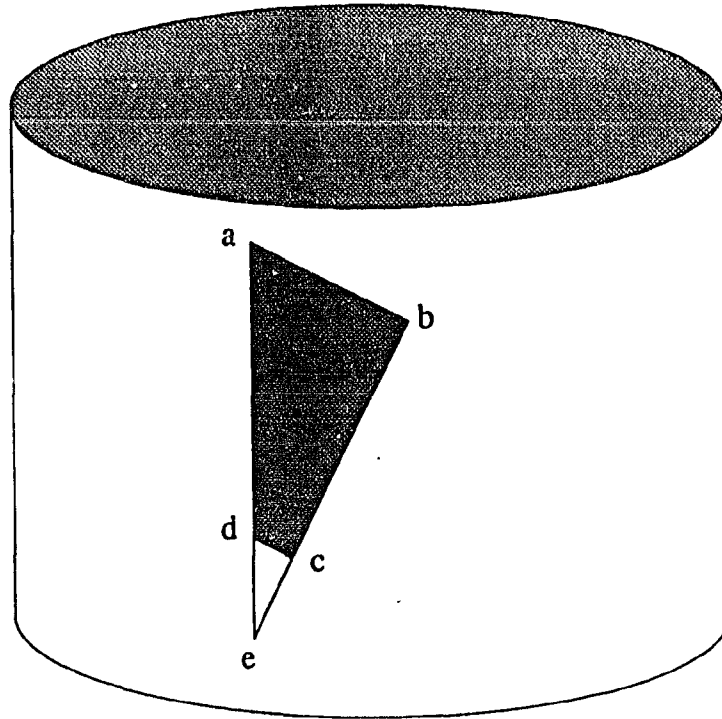


Figure III.8 Blade fabrication from circular tubing

part of the triangle, c-d-e, is truncated to allow attachment of the blade to a small annular center body. The blade leading edges were made blunt, the trailing edges were sharpened.

Figure III.9 shows the blade design interpreted geometrically as the intersection of three circular cylinders and two planes. Cylinders 2 and 3 are concentric, with their centerlines along the x -axis. Cylinder 2 represents the inside of the inlet pipe, cylinder 3 represents the annular center body. Plane 2 is equivalent to the yz -plane, plane 1 is equivalent to an inclination of the yz -plane about the y -axis by the angle θ . The centerline of cylinder 1 lies in plane 1 and is normal to the y -axis. Cylinder 1 contains the blade surface which is shaded, the dark shaded surface is visible, the light shaded surface is hidden. Each blade edge is the intersection of two surfaces, each blade corner the intersection of three surfaces. The blade edges, corners, and their corresponding surfaces are listed in Table III.2.

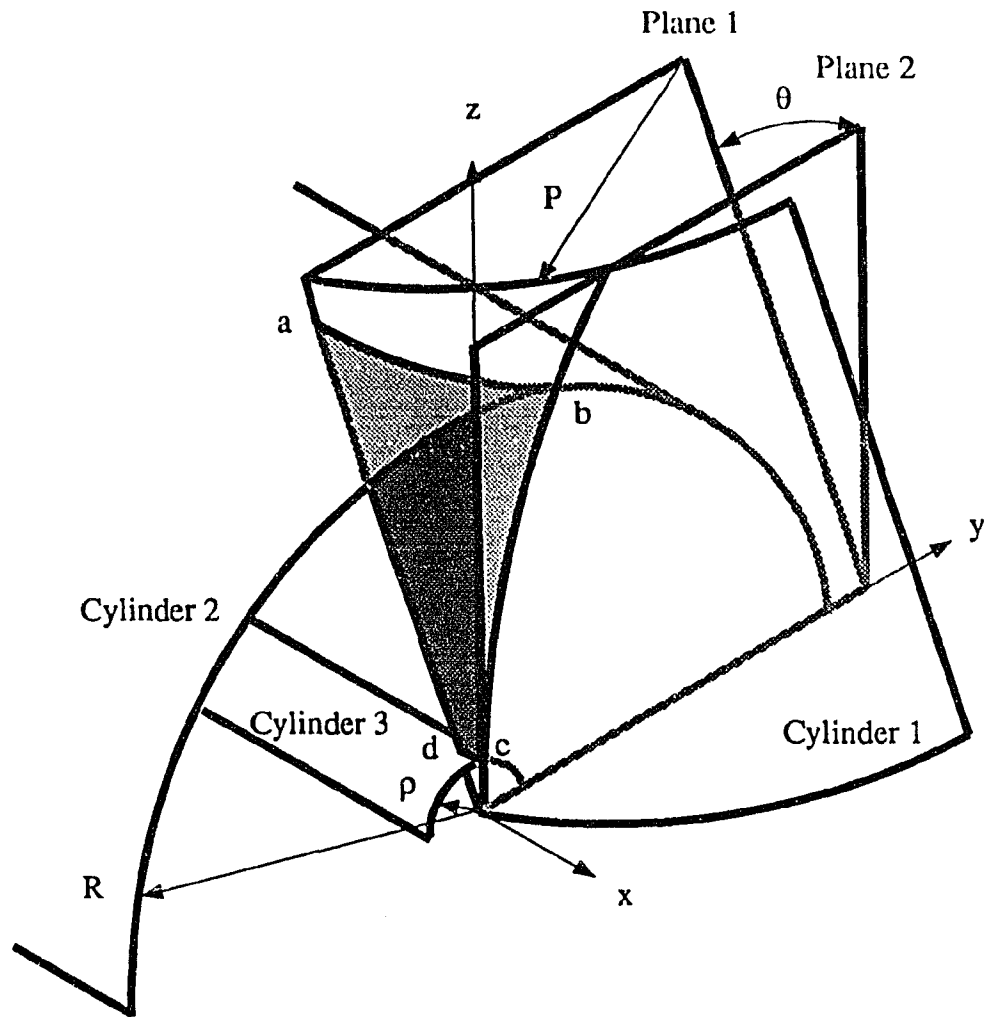


Figure III.9 Geometric interpretation of blade design

Parametric equations which describe the surface of the three cylinders are:

Cylinder 1:

$$\begin{aligned}
 C_1 : \alpha_1, \alpha_2 \rightarrow x, y, z \quad \alpha_1 \geq 0, -\pi \leq \alpha_2 \leq \pi \\
 x = P \sin \alpha_2 \cos \theta - \alpha_1 \sin \theta, \quad y = P - P \cos \alpha_2 \\
 z = P \sin \alpha_2 \sin \theta + \alpha_1 \cos \theta
 \end{aligned} \tag{III.13}$$

Cylinder 2:

$$\begin{aligned}
 C_2 : \beta_1, \beta_2 \rightarrow x, y, z \quad \beta_1 \geq 0, -\pi \leq \beta_2 \leq \pi \\
 x = -\beta_1, \quad y = R \sin \beta_2, \quad z = R \cos \beta_2
 \end{aligned} \tag{III.14}$$

Table III.2 Blade corner and edge construction from geometric surfaces

Corner	Surfaces	Edge	Surfaces
a	Cylinder 1 Cylinder 2 Plane 1	a-b	Cylinder 1 Cylinder 2
b	Cylinder 1 Cylinder 2 Plane 2	b-c (trailing edge)	Cylinder 1 Plane 2
c	Cylinder 1 Cylinder 3 Plane 2	c-d	Cylinder 1 Cylinder 3
d	Cylinder 1 Cylinder 3 Plane 1	d-a (leading edge)	Cylinder 1 Plane 1

Cylinder 3:

$$C_3 : \gamma_1, \gamma_2 \rightarrow x, y, z \quad \gamma_1 \geq 0, -\pi \leq \gamma_2 \leq \pi \quad (\text{III.15})$$

$$x = -\gamma_1, \quad y = \rho \sin \gamma_2, \quad z = \rho \cos \gamma_2$$

To design and construct the blades required calculating the location of the blade corners. Each corner was determined by finding the intersection of the three corresponding surfaces. The Cartesian coordinates of point a is $x = -R \tan \theta$, $y = 0$, $z = R$. To find the location of point b, Equation III.16, a quadratic form in $\cos \alpha_2$, was solved to find α_2 . This result was used in Equation III.17 to find α_1 and the two are substituted into Equation III.13 to determine the Cartesian coordinates.

$$\cos^2 \alpha_2 + 2 \tan^2 \theta \cos \theta + \tan^2 \theta \left[\left(\frac{R}{P} \right)^2 - 1 \right] - \sec^2 \theta = 0 \quad (\text{III.16})$$

$$\alpha_1 = P \sin \alpha_2 \cot \theta \quad (\text{III.17})$$

Alternatively, Equation III.18, a quadratic form in $\sin \beta_2$, was solved to find β_2 . This result and $\beta_1 = 0$ were substituted into Equation III.14 to verify the Cartesian coordinates of point b.

$$\sin^2 \beta_2 - 2 \left(\frac{P}{R} \right) \sec^2 \theta + \tan^2 \theta = 0 \quad (\text{III.18})$$

The Cartesian coordinates of point d are $x = -\rho \tan \theta$, $y = 0$, $z = \rho$. The location of point c was found by both the procedures used to find point b, by either substituting ρ for R in Equation III.16 or substituting ρ for R in Equation III.18 and γ_2 for β_2 in III.18 and using III.15 rather than III.14 to find the Cartesian coordinates of point b.

With the Cartesian coordinates of a point on the blade surface known, the blade camber angle was determined from Equation III.19.

$$\psi_2 = \arctan \left(\frac{\sqrt{y^2 + z^2}(x \cos \theta + z \sin \theta)}{zP \sec \theta + xy \sin \theta - yz \cos \theta} \right) \quad (\text{III.19})$$

Only two parameters determine the design of this type of stationary blade, P and θ . The location of the four corners and blade exit angle were calculated for different parameter values and compared with two criteria in mind:

1. The maximum blade exit angle, $\psi_{2,\text{max}}$, equal 20° . This value was consistent with swirl angles reported in studies of isolated single and multiple stage turbine flow exit angles [19–21].
2. The chord length of the blade be reasonably long. This is an attempt to minimize adverse pressure gradients along the blade surface.

The values used for construction are $P = 10.16$ cm and $\theta = 21.5^\circ$. The total number of blades used was 24. The consequence of too many blades (excessive wakes and total pressure loss) or too few blades (single airfoil behavior rather than cascade behavior) were considered, but the determination of the number of blades used was

very subjective. Table III.3 lists the Cartesian and cylindrical coordinates of the blade constructed. Figure III.10 shows how the blade exit angle of the designed blade, given by Equation III.19, deviated from the ideal blade exit angle, given by Equation III.11.

Table III.3 Cartesian coordinates of stationary blade

Point	Cartesian			Cylindrical		
	x/R	y/R	z/R	x/R	r/R	θ
a	-0.3940	0.0000	1.0000	-0.3940	1.0000	90.00
b	0.0000	0.0697	0.9975	0.0000	1.0000	86.01
c	0.0000	0.0010	0.1241	0.0000	0.1244	89.52
d	-0.0490	0.0000	0.1244	-0.0490	0.1244	90.00

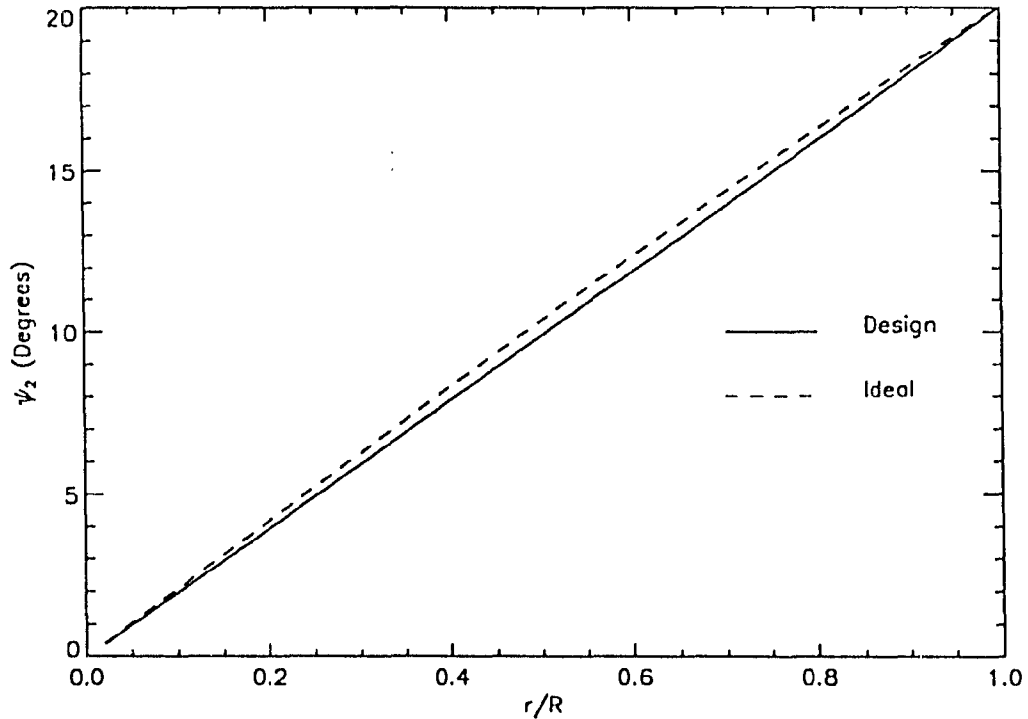


Figure III.10 Comparison of blade exit angles

CHAPTER IV. EXPERIMENTAL MEASUREMENTS AND INSTRUMENTS

This chapter describes the experimental measurements made, the measurement techniques used, and the instruments employed during the course of this research. The Trace Gas Measurements section describes the trace gas technique in considerable detail. The instruments and technique used for trace gas measurements were developed specifically for this project and represent one of the major components of this dissertation. In addition, an improved procedure for five-hole probe calibration and data reduction was developed. This procedure is referred to in the Pressure Measurements section, but the complete description has been deferred to Appendix A because of its length.

Surface Oil Film Visualization

A surface oil film visualization technique was used to obtain preliminary information about the flow field near the surface of the transition duct. Surface oil film visualization involves applying a mixture of oil and pigment to the duct surface. The air flowing over the surface induces motion within the oil film, depositing a streak of pigment indicating the direction of the flow field near the surface. This initial "quick look" was performed before other investigations and the results were used to guide the detailed aerodynamic and trace gas measurements.

Validity of surface oil film visualization

Surface oil film visualization is best for observing steady flows due to the slow response of the oil film. Transient phenomena such as those associated with flow start up are not followed by the oil. Two important questions regarding the validity of surface oil film visualization, even for steady flows, are:

1. Does the presence of the oil film alter the boundary conditions of the flow to such a degree that it results in a different flow field?
2. Does the pattern produced by the oil film accurately represent the flow field near the surface?

An analysis by Squire *et al.* [51] showed the most significant parameter affecting the performance of surface oil film visualization is the ratio of the absolute viscosity of the boundary layer fluid to the viscosity of oil. For small viscosity ratios and thin oil films the boundary conditions are not materially changed by the presence of the oil film. Furthermore, for small viscosity ratios and large local shear stresses the direction indicated by the oil flow will accurately represent the flow field direction near the surface. Where the shear stress is small (e.g., near separation) the oil film motion becomes influenced by near surface pressure gradients and may not accurately reflect the near surface flow field direction. Squires analysis did not include gravitational forces acting on the oil film. In practice this can significantly alter the oil film pattern on other than horizontal surfaces in a manner similar to “runs” that appear in wet paint. Fortunately, these gravitational affects are relatively easy to identify.

Surface oil film visualization technique

The surface oil film visualization technique used is similar to methods described by Gessner and Chan [52] and Jurkovich *et al.* [53]. The resulting air to oil viscosity ratio was 10^{-6} . A commercial dye which fluoresces when illuminated with ultraviolet light was mixed with the oil. Using fluorescent dye with ultraviolet illumination produces brighter images and reduces glare from the duct surface.

At the beginning of a visualization test, the upper half of the transition duct was removed and the oil and dye mixture was applied to the lower duct surface. Care was taken in applying the oil and dye mixture to avoid a visible pattern. The upper half of the duct was replaced and the test facility was started, operated at test conditions for several minutes, then shut down. The upper half of the transition duct was subsequently removed and the lower half was illuminated with ultraviolet light

to excite the fluorescent dye. The resulting oil flow pattern was photographed with a 35mm camera with sufficient exposure time to use ultraviolet light for illumination.

Pressure Measurements

Surface static pressure measurements

Surface static pressure measurements were made through small (0.51 mm) tap holes in the transition duct surface. The tap hole axes were oriented normal to the duct surface. There were 50 surface static pressure taps equally spaced along the duct surface in the xz -plane. The location of the surface static pressure openings is shown in Figure IV.1 as a solid line along the lower surface of the duct. The equipment used for measuring and recording pressure is described in the Manometry and Data Acquisition section of this chapter.

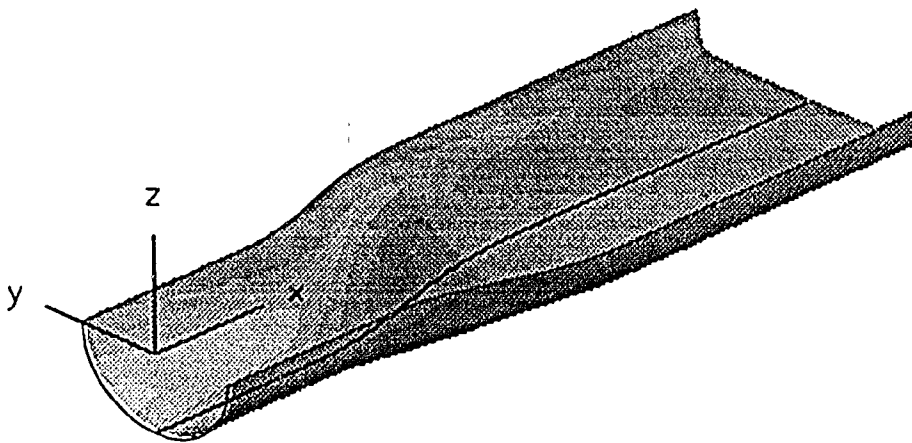


Figure IV.1 The location of surface static pressure measurements

Five-hole probe measurements

A calibrated five-hole probe was used to measure flow field velocity direction, total pressure and static pressure at numerous points. From the total and static pressures the corresponding Mach number was calculated. This value of Mach number and the flow direction defined the Mach vector. The procedure used for five-hole probe calibration and data reduction is described in Appendix A.

The five-hole probe Figure IV.2 shows a typical five-hole probe. Each of the five tubes are connected to a pressure transducer. All five-hole probe measurements were made using the yaw nulling technique. In this technique the five-hole probe is rotated around the axis of the probe shaft until the pressure measured at tubes two and four are equal. The angle through which the probe was rotated, the yaw nulling angle, was recorded along with the five pressure measurements. The equipment used for measuring and recording these pressures is described in the Manometry and Data Acquisition section of this chapter.

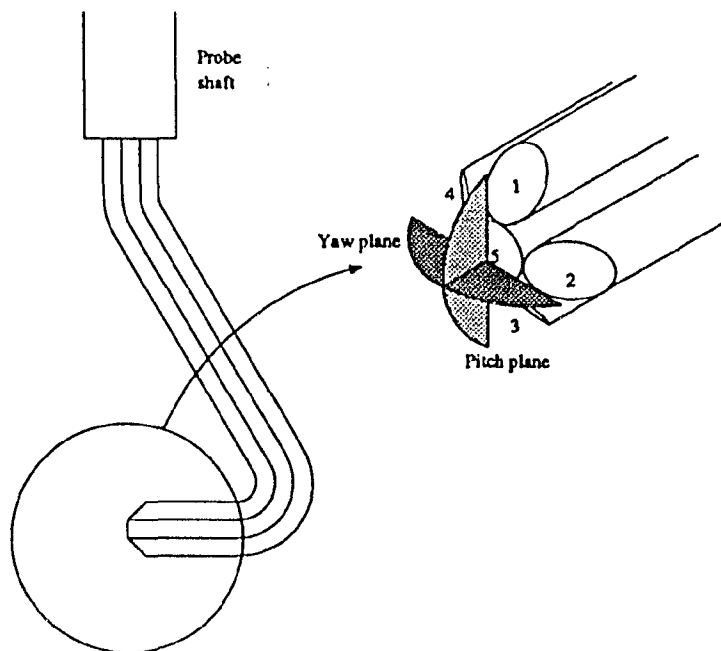


Figure IV.2 A typical five-hole probe

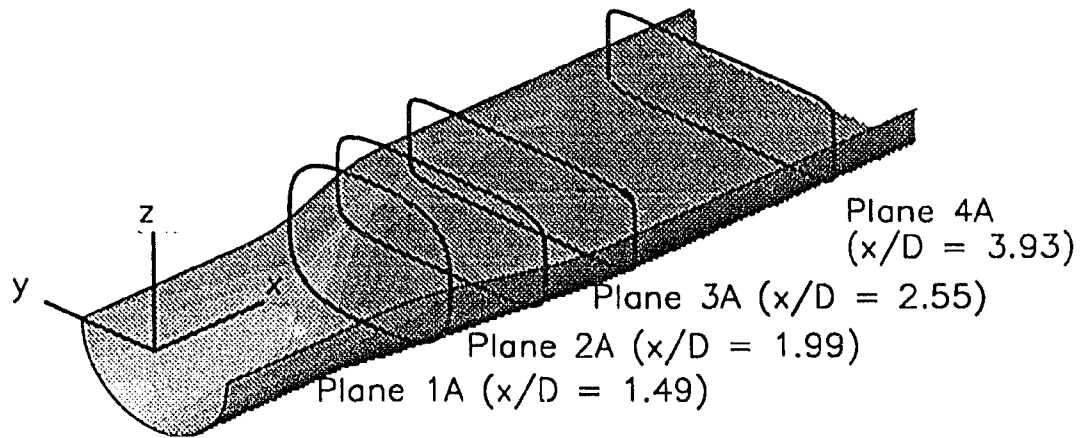


Figure IV.3 The location of the four cross stream aerodynamic measurement planes

Five-hole probe measurement locations Five-hole probe access to the flow was provided by machined openings in the transition duct. The axis of each opening was located to lie within one of the four cross stream aerodynamic measurement planes shown in Figure IV.3. For the designation of the measurement planes the letter suffix A in Figure IV.3 refers to aerodynamic and is used to differentiate the aerodynamic measurement planes from the trace gas measurement planes. The trace gas measurement planes, which are described in the next section, carry the letter suffix T and have axial locations that are different than for the aerodynamic measurement planes.

For each aerodynamic measurement plane, the number of probe openings, their location, and the orientation of their axes varied. Figure IV.4 shows each probe opening axis in each measurement plane as a broken line. The first plane had nine probe openings located symmetrically about z-axis. The axis of each probe opening passed through the duct centerline. There were thirteen probe openings in the second

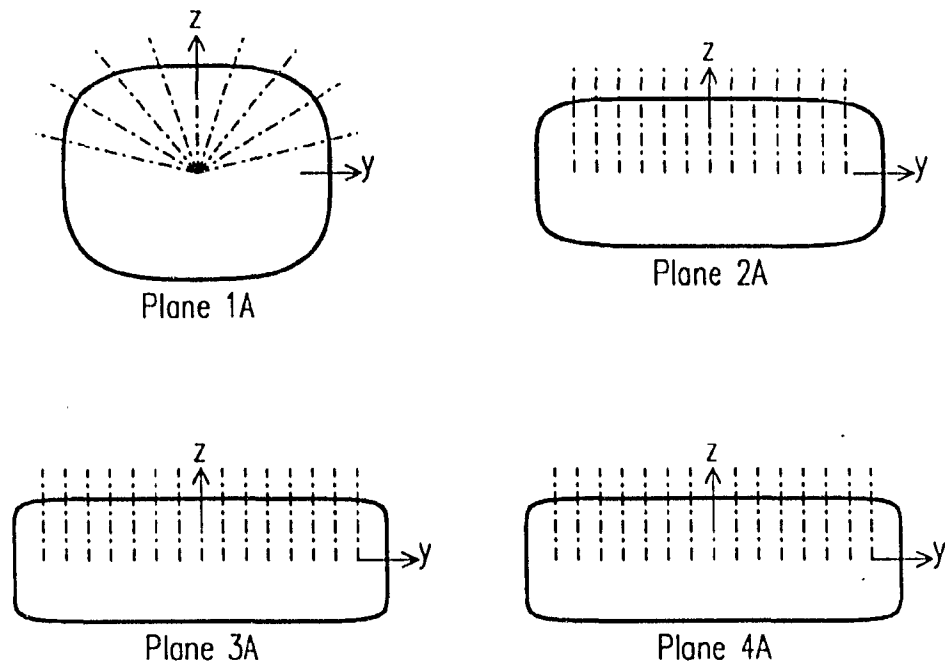


Figure IV.4 The location of the transition duct probe opening axis plane and fifteen probe openings each in the third and fourth planes. In these planes the probe openings were located symmetrically about the z -axis, and their axes were parallel to the z -axis. The middle probe opening of each plane passed through the duct centerline.

Because the transition duct is symmetric with respect to the xy - and xz -planes it would have been sufficient to make measurements in only one quadrant of each measurement plane for flow without inlet swirl. Measurements were made in two quadrants, however, on both sides of the xz -plane for flow with and without inlet swirl. These additional measurements were made to confirm that the flow field does reproduce the symmetry of the transition duct for the case without inlet swirl, and to provide a comparison for the inlet swirl case, where flow field measurements in two adjacent quadrants are necessary. Approximately 480 five-hole probe measurements were recorded at each measurement plane for each test condition.

Five-hole probe positioning equipment The five-hole probe was positioned by a mechanism with five degrees of freedom. Three degrees of freedom were involved in positioning the probe at the probe opening and placing the probe shaft axis in alignment with the probe opening axis. This positioning was controlled manually and remained fixed while measurements were made at that probe opening. The remaining two degrees of freedom were controlled by an electromechanical actuator and included translation along the probe shaft axis to position the probe for the measurement, and rotation of the probe about the probe shaft axis to null the probe.

Pitch and yaw angle reference measurements The procedure of making a set of measurements at one probe opening is referred to as a survey. The data reduction procedure used requires a reference measurement to establish pitch and yaw reference angles to which all angles measured during a survey are referred. One method of obtaining this reference is to make the reference measurement in a different facility with known flow field properties, usually a free jet. This procedure requires physically moving the actuator and probe from one facility to the other. In practice it is difficult or impossible to exactly reproduce the orientation of the actuator and probe between different facilities.

Early trace gas tests in the transition duct suggested no deviation in the air flow along the duct centerline from the centerline. This result established the air flow along the duct centerline as a direction reference. The five-hole probe positioning equipment was designed to move the actuator and probe to any survey location without having to remove the actuator and disturb its orientation with respect to the positioning system or the transition duct. Before each survey a reference direction was established at the duct centerline. This procedure avoided the potential source of errors that exist when the reference direction measurements are made in a different facility.

Survey procedures For each survey the actuator and probe were first moved to the survey probe opening. The actuator was translated to its fully extended position with the probe free of the actuator and held stationary to avoid contact with the

transition duct. Then, the probe was slid through the opening until it rested on the lower surface of the transition duct. The probe was then secured to the actuator, establishing the orientation between the probe and the actuator. This procedure established the reference for actuator position measurements and guaranteed that the probe could not be damaged by the actuator translating the probe into the duct surface. Once this orientation was established it was not disturbed until the survey was complete. The probe was then moved to the center probe opening of the plane to make the direction reference measurement. Then, the probe and actuator were moved back to the survey probe opening where the survey measurements were made.

Preliminary measurements indicated the surface boundary layer was nominally 7.62 mm thick. Each survey began at the surface of the lower half of the duct and proceeded upwards toward the horizontal plane of symmetry. Thirteen measurements, equally spaced at 0.63 mm intervals, were made in the first 7.62 mm of each survey. Measurements were continued at 2.54 mm intervals until the probe had crossed the xy -plane. All measurements were made in the duct half opposite the probe opening to avoid aerodynamic disturbances near the duct surface created by the probe opening.

Trace Gas Measurements

The objectives of the trace gas technique were described earlier, in Chapter II. This section focuses on the equipment and procedures used to make the trace gas measurements. The equipment necessary to make aerodynamic trace gas measurements can be divided into three major components:

1. The trace gas injection system.
2. The trace gas sampling system.
3. The trace gas concentration measuring system.

Because there are no commercially available trace gas equipment items specifically intended for aerodynamic tests like those presently described, the equipment must be assembled from components designed for other applications.

Trace gas injection system

The trace gas injection system was designed to introduce the trace gas into the flow field at a point and with a specific flow rate as unobtrusively as possible. The injection system included an injection probe, a probe positioning system, a trace gas flow rate control system, and a trace gas supply system.

Trace gas injection probe Three outcomes considered important in the design of the injection probe are:

1. Minimal downstream flow disturbance from the probe.
2. An injection probe rugged enough to operate in the free stream at Mach numbers as great as 0.5.
3. An injection probe capable of injecting trace gas at a sufficient rate to allow detection throughout the downstream flow field using the flame ionization detector.

Some disturbance of the flow downstream of the injection probe is unavoidable. One obvious disturbance minimization step is to make the injection probe as thin as possible. However, this may lead to some pitfalls. The flow field downstream of the injection probe may be reasonably approximated by considering a circular cylinder in cross flow. Roshko's [54] investigation of the wake of a circular cylinder in cross flow suggested that a stable, periodic, Karman vortex street occurs for a range of Reynolds number, based on cylinder diameter, from 40 to 150. This wake street decays very slowly and maintains its periodic structure for a long distance downstream. For a Reynolds number in the range from 300 to 10,000 the vortex street is quickly dissipated and by 50 diameters downstream the wake is completely turbulent. Therefore, the desire to make the probe as thin as possible was tempered by the requirement to keep the Reynolds number greater than 300, as well as less than 10,000. For the velocity levels anticipated in the transition duct tests, for $M = 0.50$, this required the probe diameter to be greater than 0.03 mm and less than 1.04 mm.

The review of trace gas literature in Chapter II briefly described trace gas injection methods. Several of the studies cited in Chapter II included the results of experiments

designed to measure and minimize disturbances from L-shaped type probes. Smith [29] and Moore [30] compared ethylene concentration distributions produced from trace gas injected through 3.2 mm and 1.1 mm outside diameter L-shaped probes into the boundary layer within a linear turbine cascade. They concluded the trace gas was probably affected very little by probe diameter. The 3.2 mm probe was used for their turbine cascade measurements.

Gallimore [32] and Gallimore and Cumpsty [33] compared three different injection probe designs in a uniform free stream and within a turbulent boundary layer over a flat plate. The first probe was constructed from a straight length of 1.0 mm outside diameter tube, closed at one end with a 0.2 mm opening drilled through the tube wall near the closed end. The other two injection probes had an outside diameter of 0.56 mm but differed in design, one was L-shaped and the other a “crooked” L-shape with an offset opening. The difference in concentration distributions resulting from trace gas injection by the different probes was most apparent in the free stream experiments. The smaller probes produced noticeably less trace gas spreading. The concentration distributions produced by the two smaller probes were nearly identical. The straight probe and the crooked L-shaped probes were used for the compressor measurements.

Moore *et al.* [42] tested the performance of several different probes in a uniform free stream, a turbulent boundary layer, and a linear turbine cascade. Their free stream results showed the smaller probe, 1.07 mm, produced concentration distributions with less spreading, indicating the probe itself was contributing to turbulent mixing of the trace gas. In the boundary layer and linear turbine cascade, however, the effect of the probe size was much less apparent. Taken together, these two results indicate that in regions of low turbulence intensity some minor probe disturbance is unavoidable, while in regions of higher turbulence intensity, the disturbance created by the probe is not of significant magnitude compared to the existing turbulence to materially effect the mixing of the trace gas.

All the trace gas injection probes described in the cited literature were operated in comparatively low speed flows and utilized a cantilever design. For the injection

probe to be as small as possible and yet withstand the aerodynamic loading imposed when it is extended to the center of the free stream at Mach numbers as great as 0.50 required abandoning the cantilever design of previously used probes. Instead, a catenary design was used as shown in Figure IV.5. The injection tube is supported along its full length by a second tube which is held in tension across the rigid frame. The cross section of the rigid frame and the wall bounding the flow are shown in Figure IV.5. The catenary probe design requires an additional probe opening in the wall bounding the air flow.

The trace gas injection probe was constructed from stainless steel hypodermic needle tubing with an outside diameter of 0.56 mm. The catenary design allowed the trace gas injection probe to be as slender as the smallest reported in the literature,

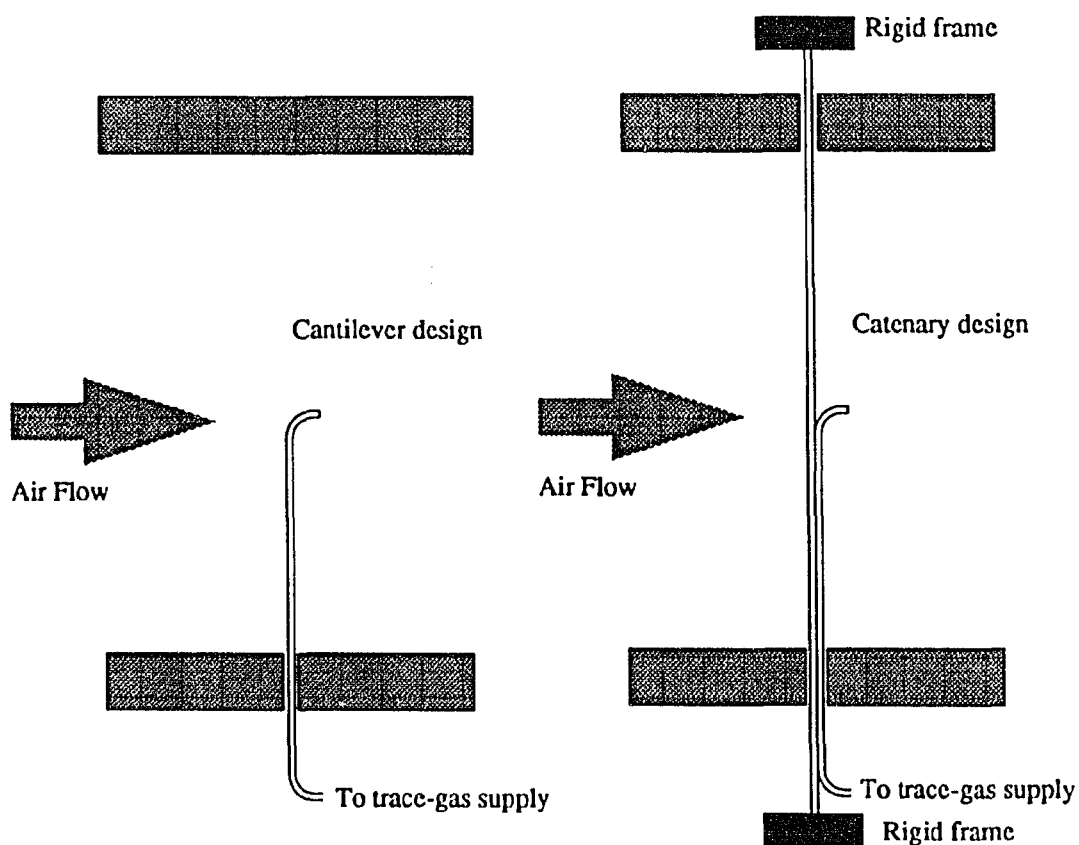


Figure IV.5 Cantilever and catenary injection probe designs

yet be operated at significantly higher flow field velocities than is capable with a cantilever configuration.

The flow rate of trace gas was chosen so that the bulk velocity of trace gas at the injection probe exit would approximately match the free stream velocity. The area of the trace gas injection probe exit was 0.067 mm^2 . For the transition duct experiments, with the free stream Mach number nominally equal to 0.50, this required a trace gas volumetric flow rate of approximately 600 ml/min.

Trace gas injection probe positioning system Trace gas was injected from the seven different locations shown in Figure IV.6. All trace gas injection locations were within an axial plane situated one radius upstream of the beginning of the transition duct. One injection location was coincident with the centerline. The remaining six injection locations were placed radially at $r/R = 0.498$ and $r/R = 0.995$ along the z -axis and along lines through the centerline 60° on either side of the z -axis.

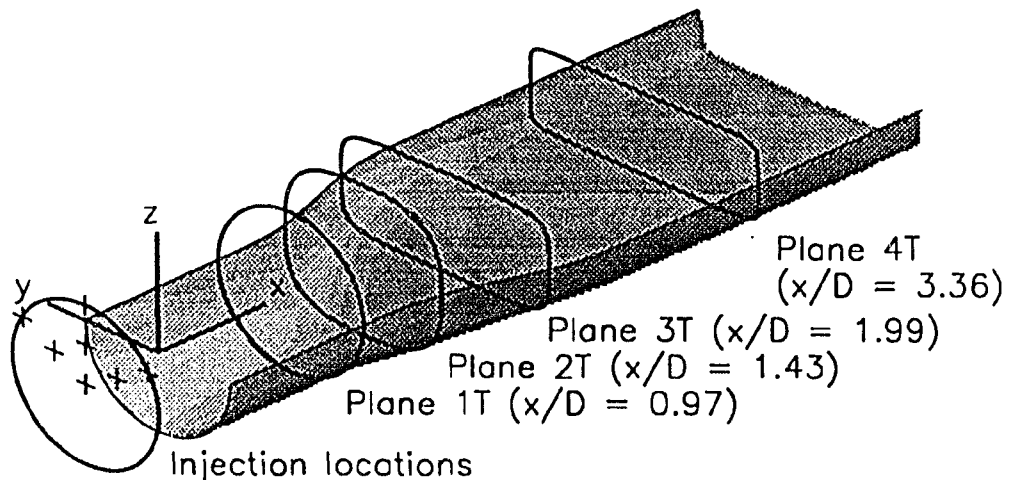


Figure IV.6 Trace gas injection locations and measurement planes

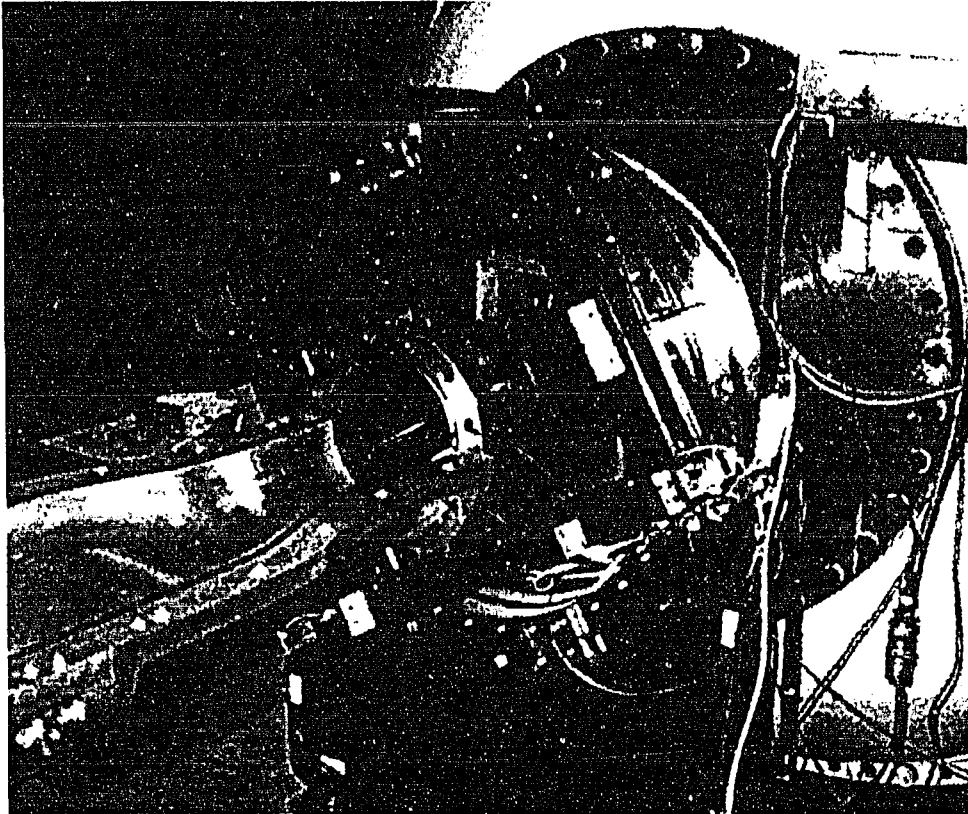


Figure IV.7 Trace gas injection probe positioning equipment

The equipment used to position the trace gas injection probe is shown in Figure IV.7. The trace gas injection probe was positioned by controlling two degrees of freedom, the radial movement and the circumferential movement. The radial position was controlled by moving radially the rigid frame which holds the trace gas injection probe in tension. A stepper motor and potentiometer were used to control and measure this radial motion. The rigid frame was attached to a large bearing whose center of rotation was coincident with the transition duct centerline. The circumferential motion was manually controlled by rotating the rigid frame around its rotation axis and accessing the flow through different pairs of probe access holes.

Trace gas flow rate control system To achieve consistent trace gas results required carefully controlling the rate at which trace gas was injected. This was

accomplished in the transition duct test by using a Datametries type 825 mass flow controller. This equipment allowed the desired mass flow rate of trace gas to be specified in engineering units at the controller panel, and it maintained the desired flow rate to within 1% of the specified flow rate. The controller measured the flow rate by heating a fraction of the gas and sensing the resulting temperature increase. Details of the principles and operation of the equipment are contained in Reference 55.

The mass flow controller was calibrated by timing the displacement of water in an inverted graduated cylinder by gas passing through the controller. Since the pressure and temperature of the gas were known, the mass of the gas was calculated from the volume of displaced water. This procedure was repeated several times for several different mass flow rates, and this information was used to adjust the controller. Because of the heat transfer principle used by the controller to determine the flow rate, the calibration results were, in general, only valid for a specific trace gas.

Trace gas supply system. In this study, ethylene was used as the trace gas. Ethylene possesses several properties which make it desirable for trace gas studies:

1. The molecular weight of ethylene, 28.1, is nearly the same as air, 29.0. This eliminates the effect of buoyancy forces on the motion of the trace gas.
2. Under normal circumstances, ethylene and other hydrocarbon gases are only found in very minute quantities in air. Thus, the problem of having to adjust the trace gas concentration measurements to compensate for the background level of trace gas in air is avoided.
3. The mean concentration of ethylene, or any hydrocarbon gas, can be measured very accurately with a flame ionization detector. This instrument is described later in this section.

A potential hazard of ethylene is its flammability. The lower and upper flammability limits of ethylene in air are 31,000 ppm and 320,000 ppm, respectively, and the autoignition temperature is 763 °K [56]. For the transition duct experiments, the injection rate of ethylene was such that far downstream, where the ethylene is well

mixed with air, the resulting concentration was approximately 2 ppm, well below the lower flammability limit. Undoubtedly, there are locations within the flow field where the concentration levels are within the flammability limits, but the flow field total temperature was nominally 294 °K, well below the autoignition temperature.

The supply system included a supply cylinder of ethylene, a two-stage pressure regulator at the cylinder, and the associated tubing. Because of the flammable nature of ethylene, a small supply cylinder was used and the cylinder was stored outdoors when not in use. All ethylene supply connections were leak checked each day before the experiment.

Trace gas sampling system

The purpose of the trace gas sampling system was to provide the trace gas concentration measurement instrument with a steady and continuous supply of flow field sample from a specified location. The components of the trace gas sampling system included the sampling probe or tube, the probe positioning system, and the sample pump and tubing necessary to maintain the flow of sample from the sampling probe to the trace gas concentration measurement instrument.

Trace gas sampling probe Trace gas sampling probes that have been used in previous studies were reviewed in Chapter II. For the references cited in Chapter II the measurements were performed at relatively low velocities, in nearly all cases the Mach number was less than 0.10. One difficulty in applying the trace gas technique to higher speed flows has been the assumed need of isokinetic sampling of the trace gas [29], sampling at a velocity through the probe opening that matches the local host flow velocity. Isokinetic sampling is actually not necessary to accurately measure the local concentration of trace gas in a host gas flow. Injecting trace gas into the flow field creates an Eulerian concentration field. The local value of the concentration in the flow field does not depend on the rate at which the sample is acquired. The only possible pitfall resulting from the sampling rate is if the velocity through the

probe opening greatly exceeds the local host flow velocity, in which case the spatial resolution ability of the probe deteriorates.

Another sampling issue is the importance of aligning the sampling probe precisely in the direction of the host flow. This concern is also largely unnecessary if the proper precaution is taken. Because of the measurement technique, the concentration of the sample will not depend on the orientation of the probe when the sample is acquired, provided the presence of the probe doesn't materially alter the flow field. The sampling probe is usually the same size as a pressure probe, where the disturbance caused by the probe is usually acceptable. These principals of sampling rate and sampling probe alignment were confirmed during the initial tests of the trace gas instruments and technique described in Chapter V.

If a conventional trace gas sampling probe design had been employed in the present study, probe access would have been through the same openings used for five-hole probe access that were described in the Pressure Measurements section of this chapter. However, the distance between these openings, 1.91 cm, was too large to satisfactorily resolve the concentration gradients expected in the yz -plane.

A novel method for sampling was designed to allow finer spatial resolution in the yz -plane while still using the existing five-hole probe access openings. The design employed as the sampling probe a flexible tube that extended upstream to the sampling plane while firmly base mounted at a fixed location at the exit of the transition duct. The tube was constructed from stainless steel hypodermic needle tubing with outside and inside diameters of 1.83 mm and 1.37 mm, respectively. The position of the tube opening was controlled by the trace gas sampling probe positioning equipment, and the flow field sample was drawn through the tube opening.

Trace gas sampling probe positioning equipment The trace gas sampling probe and positioning mechanism are shown in Figure IV.8. The location where the probe is mounted at the duct exit lies downstream beyond the right border of this photograph. The position of the probe opening can be visualized as lying on

the surface of an imaginary scribed sphere whose radius is equal to the probe length. Because the probe length was sufficiently large, the deviation of the surface of the scribed sphere from the measurement plane was negligible.

The position of the sampling probe arm was controlled by the same electro-mechanical actuator used to position five-hole probes. Both the translation, or axial, and rotation, or radial, modes of the actuator were used to position the trace gas sampling probe opening to the desired position in the measurement plane. The location of the trace gas measurement planes were shown in Figure IV.6. Different length sampling tubes were used for each measurement plane.

A computer program was written to relate the actuator radial and axial coordinates to transition duct coordinates. Figure IV.9 shows an idealization of the trace gas sampling probe and positioning system. The transformation is given by Equations

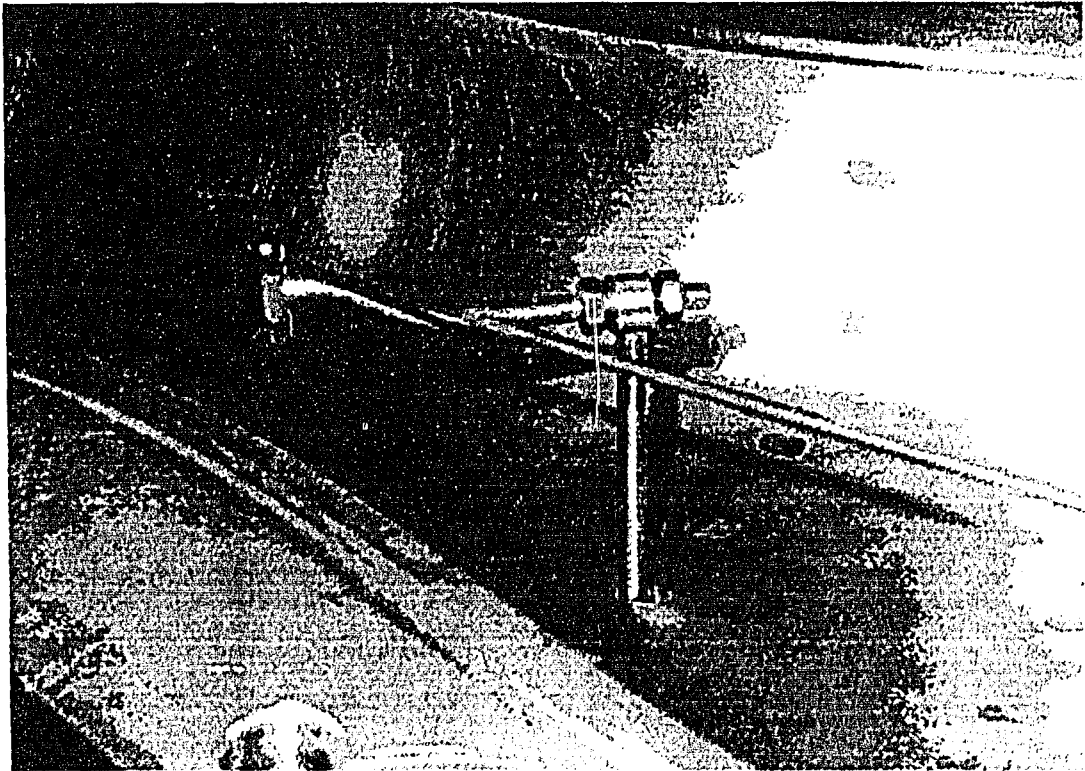


Figure IV.8 Trace gas sampling probe positioning equipment

IV.1. These coordinate transformations are an idealization, they represent a close approximation but fail to account for deviations such as deflections of the sampling probe tube.

$$y = b_2 + \frac{R(a_2 + r \sin \theta - b_2)}{\sqrt{(a_1 - r \cos \theta - b_1)^2 + (a_2 + r \sin \theta - b_2)^2 + h^2}} \quad (IV.1)$$

$$z = \frac{Rh}{\sqrt{(a_1 - r \cos \theta - b_1)^2 + (a_2 + r \sin \theta - b_2)^2 + h^2}}$$

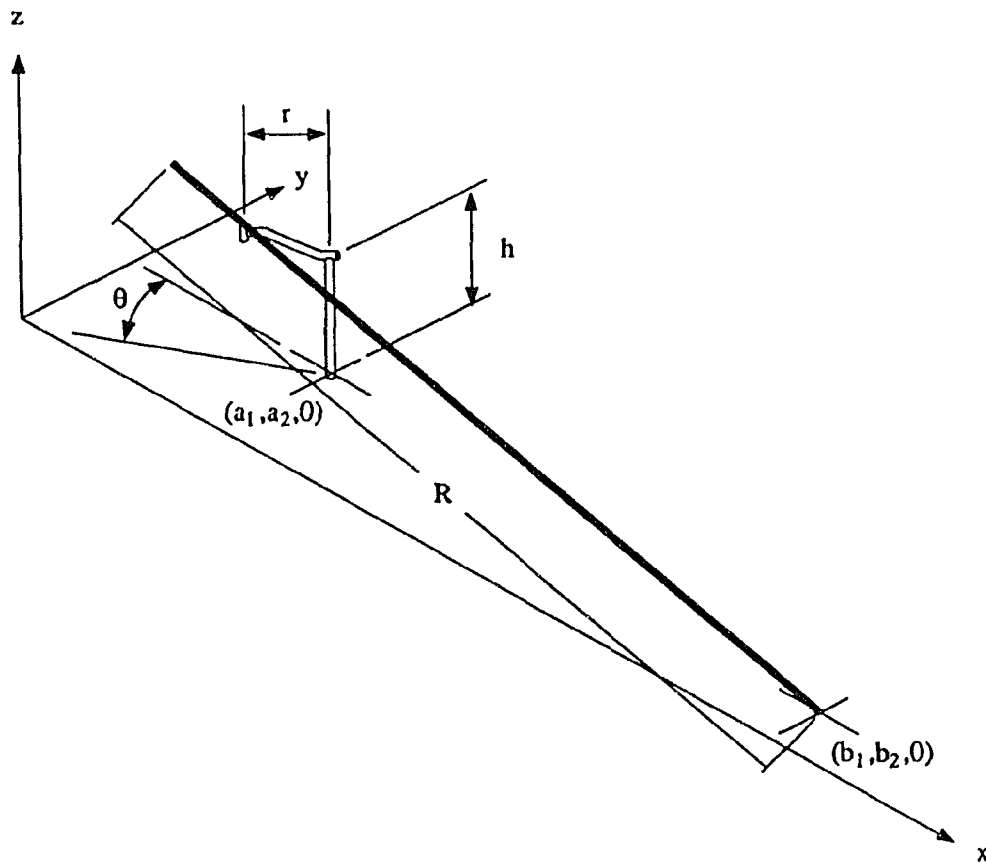


Figure IV.9 Parameters used for the trace gas sampling system coordinate transformation

To produce a closer approximation, a_1, a_2, b_1, b_2, R and r were considered variables rather than constants and the set of functions given by Equations IV.1 were calculated while varying these six parameters. The error of Equations IV.1 was defined to be the sum of the magnitude of the difference of the measured and calculated sampling tube opening positions. A numerical scheme known as the steepest decent method was used to search the parameter space to minimize this error. In using this method a beginning point was entered and the gradient of the error is approximated using finite differences. The negative of the gradient is a vector in the parameter space which points in the direction of values which result in the most rapid decrease of error. The search proceeded along this direction until the error no longer decreased at which time the gradient was again calculated. The search was then repeated in the new direction and this process was continued until the search in a new direction no longer produced any further decrease in the error.

The typical procedure involved measuring the position of the sampling probe tube in transition duct coordinates for many different actuator axial and radial positions. The six physical quantities which correspond to the parameters were also measured and used as the starting condition of the search. The numerical method was then used to calculate the parameters which were used in the coordinate transformation program. There is no guarantee that this method resulted in parameter values that produced a global minimum in error, or even a local minimum. However, in all cases it did significantly reduce the error, the average error usually being only about 0.25 mm. This procedure was repeated for each actuator location for each of the four measurement planes.

Trace gas sampling pump and tubing A sampling pump was required to supply the trace gas concentration measurement instrument with a continuous supply of sample. This pump was necessary to overcome the pressure loss in the tubing between the sampling probe opening and the concentration measurement instrument and because the total pressure of the flow field was less than atmospheric pressure.

An important consideration was whether the sampling pump should be located upstream or downstream of the gas concentration measurement instrument. Smith [29] and Gallimore [32] used a sampling pump upstream of the trace gas concentration measurement instrument, the sampling pump of Bauer [34] was located downstream. The advantage of a downstream location is the pump cannot contaminate the sample with hydrocarbons, which are present in the pump lubricating oil. The disadvantage of a downstream location is that much of the tubing from the trace gas sampling probe to the pump, including the trace gas concentration measurement instrument, will operate below atmospheric pressure. This allows the possibility of atmospheric air leaking into the sampling system and diluting the sample. When the sampling pump is placed upstream of the trace gas concentration measurement instrument the pressure downstream of the pump will be greater than atmospheric. Any leaks of the sample fluid out will not change the concentration of the sample. For this study, the sample pump was located upstream of the trace gas concentration measurement instrument. A K.N.F. Neuberger, Inc., Model N05ANI pump was used. This is an oil free pump designed specifically for contamination free pumping of gasses.

Stainless steel tubing was used throughout the trace gas sampling system. A special cleaning procedure was used to remove any hydrocarbons from the tubing before installation. First, the tubing was continuously flushed with acetone for several minutes. This was accomplished with a pump and large reservoir of acetone. The pump forced the acetone through the tubing which discharged back into the reservoir. Then, this procedure was repeated with methyl alcohol to remove any acetone residue. Finally, the tubing was dried with a continuous flow of nitrogen for several minutes.

Trace gas concentration measurement system

The instrument used for is largely determined by the choice of trace gas. Researchers that use helium frequently use a thermal conductivity cell [27, 39, 40, 37]. Carbon dioxide concentration is commonly measured with a nondispersive infrared detector [57, 38, 37]. A flame ionization detector provides a very accurate measure-

ment of ethylene concentration and has been used extensively for trace gas studies [28–35, 43, 58, 42], and was used for this investigation.

Trace gas concentration detection equipment used in previous studies was briefly reviewed in Chapter II. A GOW-MAC Instrument Company Model 23–500 Total Hydrocarbon Analyzer was used for this research project. This instrument utilizes a flame ionization detector for measuring hydrocarbon concentration. The flame ionization detector may be thought of as a carbon atom counter. It consists of a small burner within which fuel and oxidizer are mixed and burned. Hydrogen and zero-gas air (air containing less than 0.5 ppm total hydrocarbons), were used as fuel and oxidizer, respectively, so there are no hydrocarbons present in this flame. When the sample is mixed with the flame, any hydrocarbons are burned and the carbon atoms become ionized. The carbon ions and electrons pass between two electrodes, decreasing the resistance between the electrodes and thus permitting an electric current to pass. This current is directly proportional to the amount of carbon ions present. Additional details about the principles and operation of this instrument are provided in Reference 59. The electronic output of the total hydrocarbon analyzer was routed to the data acquisition system, described in the next section.

The flame ionization detector responds to both the amount of carbon atoms present in the sample, and the rate at which the sample passes through the detector. This makes it very important to maintain a constant flow rate of sample through the flame ionization detector. This was accomplished within the total hydrocarbon analyzer with a “tee” connector in the sample supply line with a capillary tube restrictor on the leg of the tee to the flame ionization detector and a back pressure regulator on the other leg. This arrangement provides a constant flow rate of sample to the flame ionization detector regardless of the sample flow rate into the tee, provided, of course, the flow rate into the tee exceeded the desired flow rate to the detector. The fraction of sample fluid not directed to the flame ionization detector was discharged to the atmosphere. Therefore, fluctuations in the flow rate of the trace gas sampling pump did not affect the flow rate into the flame ionization detector. The suggested flow

rate of sample fluid into the flame ionization detector specified by the manufacturer, 25 ml/min, was used.

It is also important to maintain a constant flow rate of fuel and oxidizer to the flame ionization detector. Pressure regulators followed by capillary tube restrictors upstream of the flame ionization detector were used to maintain constant flow rates. The suggested flow rates of fuel and oxidizer specified by the manufacturer, 25 ml/min and 245 ml/min, respectively, were used. Because of the extreme flammability of hydrogen, a small hydrogen supply cylinder was used. This cylinder was stored outdoors when not in use, and all connections were leak checked daily during tests.

The flame ionization detector was calibrated by preparing a mixture of ethylene and zero-gas air of known concentration and supplying this as a sample to the total hydrocarbon analyzer. This calibration was performed periodically throughout the period of trace gas testing. After the initial calibration, it was seldom necessary to make any further adjustments.

Manometry and Data Acquisition

Pressure measurements

Five-hole probe pressures and surface static pressures were measured with a Pressure Systems Incorporated Model 780B electronically scanned pressure measurement system. The system is described in Reference 60.

The system consists of four major components; the systems controller, the data acquisition and control unit, the pressure calibration unit, and the sensor modules. A schematic diagram of these components is shown in Figure IV.10. Each experimental pressure was measured with an individual electronic pressure transducer contained in a sensor module. For these experiments, four sensor modules, each containing 32 individual differential pressure transducers, were used. Each individual pressure transducer had a full scale range of 34.5 KPa, and was referenced to atmospheric

pressure so the difference between experimental pressures and atmospheric pressure was measured.

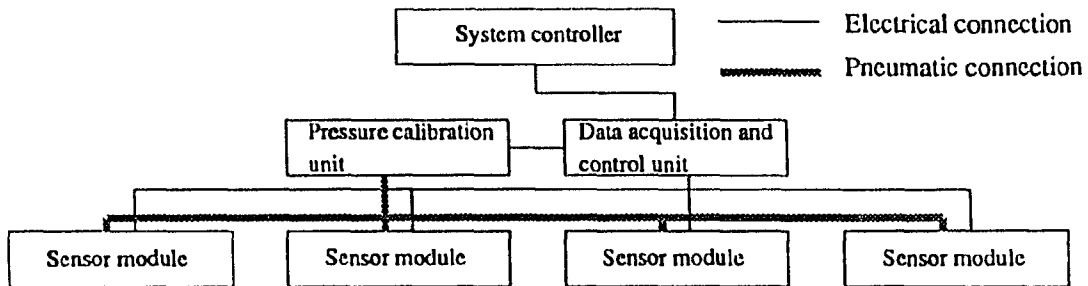


Figure IV.10 Schematic of the Pressure Systems Incorporated Model 780B electronically scanned pressure measurement system

The pressure calibration unit included pneumatic valves to switch the input of the individual pressure transducers from the experiment pressure to a calibration pressure. The calibration pressure was also measured with a single, high-accuracy, pressure transducer contained in the pressure calibration unit. For these experiments a Digiquartz absolute pressure transducer with a full scale range of 103.4 KPa and an accuracy of 0.02% of full scale, or 21 Pa, was used.

The measurement of the calibration pressure by the Digiquartz transducer was used to calibrate each individual pressure transducer. The calibration procedure was controlled by the data acquisition and control unit. Three different calibration pressures, spanning the range of pressure anticipated in the experiment, were used to calculate separate calibration curves for each individual pressure transducer. These calculations were performed by the data acquisition and control unit. By calibrating the differential transducers in the sensor modules with an absolute transducer the resulting calibration allowed the differential transducers to measure absolute pressure. This calibration procedure was performed at the beginning of each test day and was repeated at approximately 30 minute intervals during tests.

Measurement of the individual pressure transducers and the frequency of their calibration were controlled by the data acquisition and control unit which received its commands from the systems controller, a personal computer. While acquiring data, the data acquisition and control unit measured each experimental pressure sequentially at a rate of 0.00001 seconds per measurement. This was repeated until eight measurements were recorded for each transducer. The arithmetic mean of these measurements was calculated and converted to an absolute pressure using the calibration. This pressure was then passed to the systems controller.

Data acquisition

The purpose of the data acquisition was to display and record all of the experimental data as well as ancillary data which describe the facility operating condition. This task was performed by an existing data acquisition hardware and software package called Escort 2, which was developed at NASA Lewis Research Center. The data acquisition system accepted both digital input, such as the pressures measured by the electronically scanned pressure measurement system, and analog input, such as the voltage output of the total hydrocarbon analyzer or the potentiometers used to measure probe position.

The data were continuously updated, converted to engineering units, and displayed on a CRT monitor in the control room of the test facility. When requested, the data were recorded by a centrally located minicomputer. Archival files of all recorded data were maintained. The data files were transferred from the minicomputer to a computer engineering workstation for data reduction, display and analysis.

Hot Wire Measurements

Thermal anemometry

A schematic of the hot wire measurement equipment is shown in Figure IV.11. All measurements were made with a single normal wire probe. A standard TSI model 1260A-T1.5 hot wire probe with a 4 μm diameter tungsten sensing element was used.

A TSI model IFA100 constant temperature anemometer was used to acquire hot wire measurements. The details of this anemometer are described in Reference 61. The anemometer bridge voltage was output to a Hewlett Packard model 7603 oscilloscope, a Fluke model 8920 RMS voltmeter and a Masscomp model MC 5450 computer and high speed digital data acquisition system. All hot wire measurements were recorded with the digital data acquisition system. The oscilloscope and RMS voltmeter were used only to detect problems at run time. The analysis of the digitized hot wire data were performed with Sun computer workstations.

Attempts to make hot wire measurements using a standard TSI hot wire probe holder were unsuccessful for Mach numbers greater than 0.10 because of aerodynamic buffeting of the probe holder. This buffeting was detected by the oscilloscope representation of the signal which became less random and more periodic as the Mach number increased. A much stiffer probe holder with approximately the same

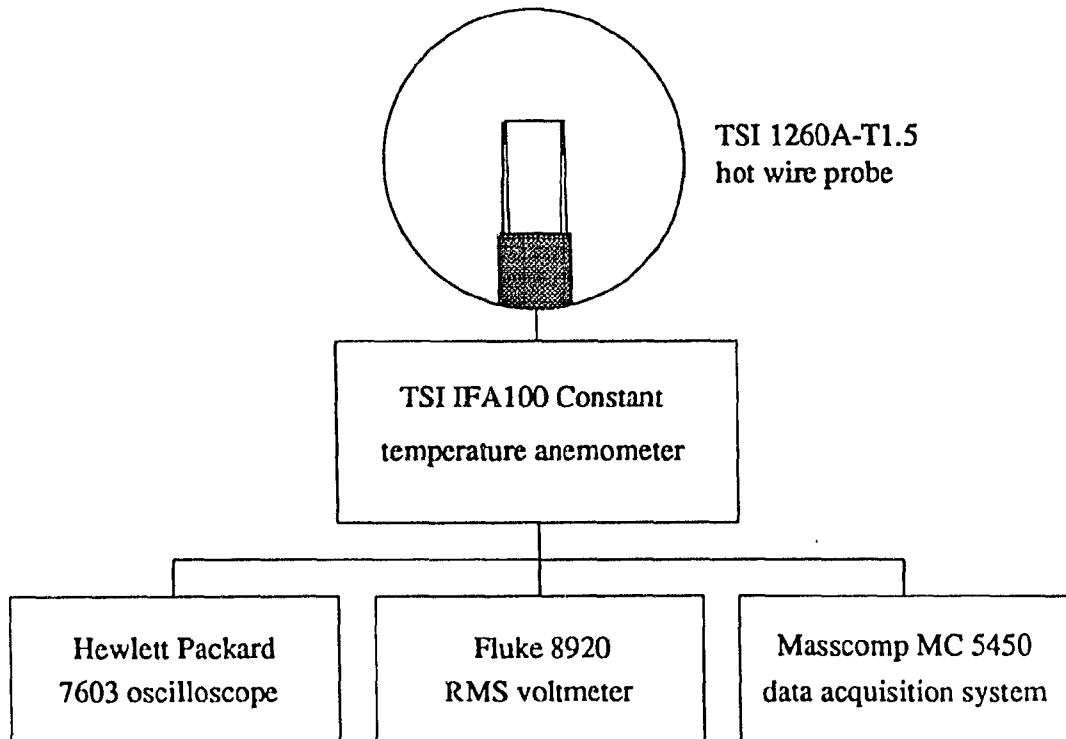


Figure IV.11 Schematic of hot wire anemometry equipment

cross stream projected area as the TSI probe holder but having a highly elliptical cross section was fabricated in order to make hot wire measurements at the higher velocities. Both the oscilloscope and frequency analysis of the digitized signal showed this new probe holder worked satisfactorily at velocities up to the highest Mach number recorded, 0.50.

Hot wire calibration

To calibrate the hot wire probe, the probe was placed at the centerline of the straight pipe in the Internal Fluid Mechanics Facility with the wire oriented normal to the mean flow direction. The mean flow velocity was varied and determined with total and static pressure measurements. The mean anemometer bridge voltage and the mean velocity were recorded and used for calibration. Data were recorded at

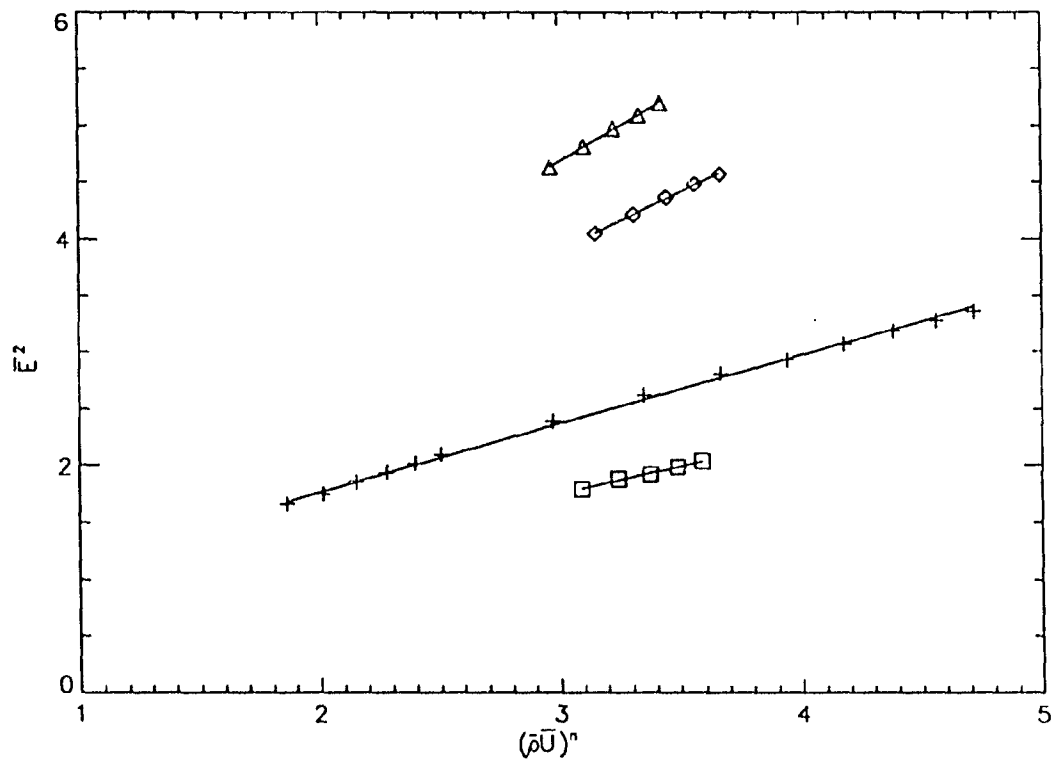


Figure IV.12 Hot wire calibration results

five overheat ratios, 1.2, 1.4, 1.6, 1.8, 2.0. The calibration data were approximated with a King's law [62] relation, Equation IV.2. A least squares procedure was used to determine the value of the constants B and n for each overheat ratio. The value of A was determined from zero velocity measurements. Figure IV.12 shows the hot wire calibration results. The data recorded at the lowest overheat ratio, 1.2, were unsatisfactory and is not presented.

$$\overline{E}^2 = A + B(\overline{\rho U})^n \quad (\text{IV.2})$$

CHAPTER V. RESULTS

The data presented in this chapter can be divided into two categories; data gathered to validate an experimental facility or experimental technique, and data acquired to examine the aerodynamics of the transition duct flows. The first three sections present validation data for the trace gas technique, the Internal Fluid Mechanics Facility and the swirl generator. The last two sections present the results of the transition duct measurements for flow without and with inlet swirl. Analysis of the transition duct results is contained in Chapter VI.

All of the results presented in this chapter are nondimensional. Total and static pressures are presented as pressure coefficients p_0^* and p^* , having been nondimensionalized as indicated in Equations V.1 and V.2. Measured velocity vectors were divided by the local sonic velocity c to yield a Mach vector. This result was then normalized by the centerline Mach number, as shown in Equation V.3, resulting in a velocity coefficient M^* . Bold type in Equation V.3 indicates vector quantities. In Equations V.1 through V.3 the reference variables, subscripted centerline ($r = 0$) or wall ($r = R$), were evaluated at a location one radius upstream of the transition duct inlet ($x/D = -0.5$). This location represents conditions near the exit of the straight pipe or swirl generator or the inlet of the transition duct.

$$p_0^* = \frac{p_0 - p_{\text{wall}}}{p_{0,\text{centerline}} - p_{\text{wall}}} \quad (\text{V.1})$$

$$p^* = \frac{p - p_{\text{wall}}}{p_{0,\text{centerline}} - p_{\text{wall}}} \quad (\text{V.2})$$

$$M^* = \frac{\mathbf{V}/c}{M_{\text{centerline}}} \quad (\text{V.3})$$

The concentration measured in trace gas surveys was the ethylene mole fraction, given by Equation V.4. In Equation V.4 n_{ethylene} refers to the molar amount of

ethylene present in a sample and n refers to the total molar amount of the quantity of matter in the sample. The results are presented as an ethylene concentration coefficient C^* , where the local ethylene concentration has been normalized by the peak value of ethylene concentration measured for that particular distribution, as shown in Equation V.5.

$$C_{\text{ethylene}} = \frac{n_{\text{ethylene}}}{n} \quad (\text{V.4})$$

$$C^* = \frac{C_{\text{ethylene}}}{C_{\text{ethylene,peak}}} \quad (\text{V.5})$$

Plotting contours of the trace gas and aerodynamic data presented a challenge because the locations of the data points were not on a regular grid. The irregular grids occurred when there was an unequal number of data points in the surveys in a measurement plane or when additional data were taken in a region to resolve a flow feature. Similar problems resulting from irregularly distributed data occurred in the statistical analysis of the trace gas results. No available software could satisfactorily resolve both these problems so a numerical computer program was written to interpolate the irregularly distributed data onto a regular grid. A portion of this program was also used for statistical analysis of trace gas data. The details of the interpolation procedure are presented in Appendix B.

Trace Gas Method Validation

Prior to conducting the transition duct experiments, preliminary trace gas measurements were made in the calibration tunnel described in Chapter III to insure all the trace gas equipment was operating properly. These measurements were also performed to reveal information about the trace gas technique itself. To test the spatial resolution of the sampling probe, ethylene was injected at the centerline of the calibration tunnel jet and the flow was extensively sampled in a cross stream

plane approximately 60 mm downstream of the injection point. Figure V.1 shows a contour plot of the measured distribution of the concentration coefficient, C^* . This figure shows that the trace gas system is capable of resolving flow features as small as approximately 1.0 mm.

A test was performed to determine the sensitivity of the ethylene concentration measurements to the ethylene injection rate. Ethylene was injected at the center-line of the calibration tunnel jet. Two separate cross stream sample surveys were conducted approximately 110 mm downstream of the injection point. The rate of ethylene injection varied between the two surveys while all other test conditions were unchanged. A comparison of the measured concentration distributions, shown in Figure V.2, when presented as concentration coefficients, show very little difference.

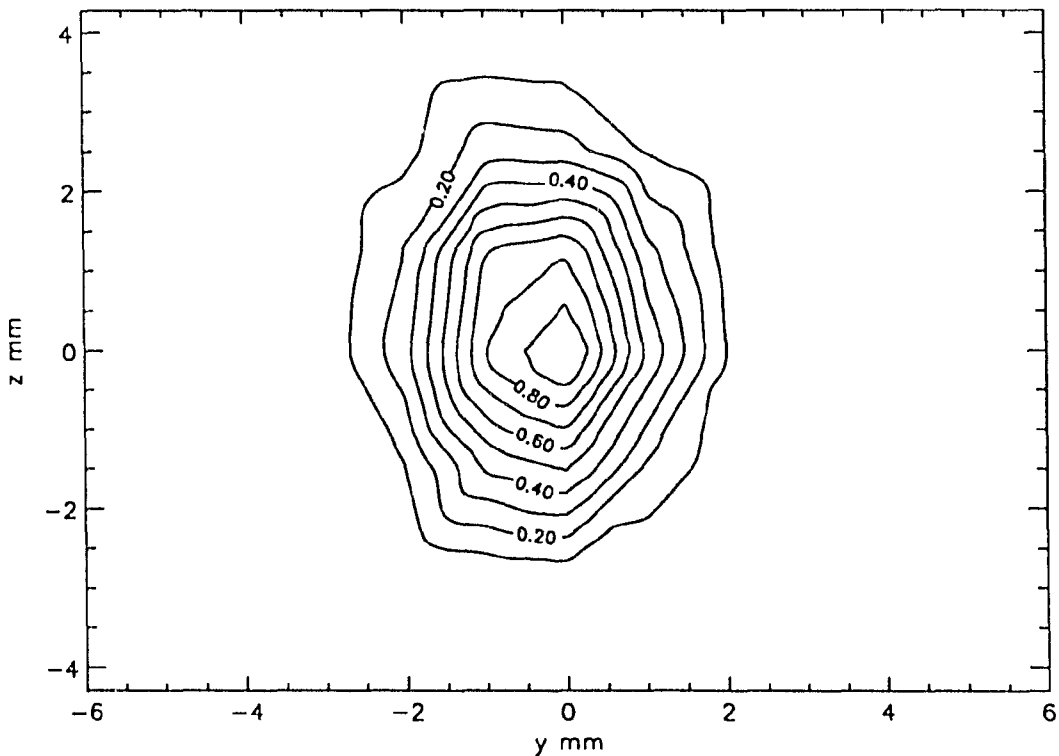


Figure V.1 Concentration coefficient C^* distribution for preliminary tests to ascertain the spatial resolution of the trace gas technique

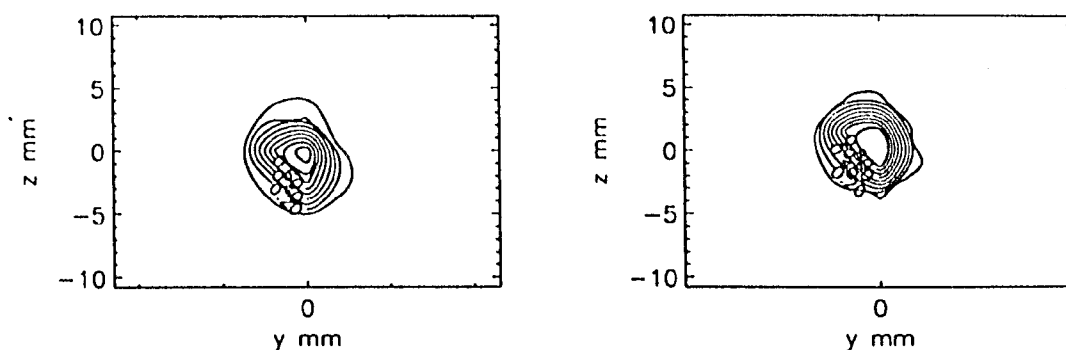


Figure V.2 Concentration coefficient C^* distributions for preliminary trace gas tests to ascertain the sensitivity of concentration measurements to the ethylene injection flow rate

The rate of ethylene injection for the result shown on the right hand side of Figure V.2 was 1.5 times greater than that used for the left hand side result. Within some reasonable limitations, the concentration coefficient appears to be insensitive to the rate at which ethylene is injected into the host flow.

To test the sensitivity of the ethylene concentration measurements to a mismatch between the sample velocity at the probe opening and the host flow velocity, two cross stream sample surveys were compared. For both surveys ethylene was injected at the centerline of the calibration tunnel jet and the flow was sampled in cross stream planes approximately 110 mm downstream of the point of injection. For the results shown on the left hand side of Figure V.3 the jet Mach number was approximately 0.10. The jet Mach number was approximately 0.60 for the results shown on the right hand side Figure V.3. The rate at which the sample was drawn was held constant, insuring a significant velocity mismatch between these two cases. The results presented in Figure V.3, however, show little difference in the concentration coefficient. These results demonstrate that isokinetic sampling is not necessary.

To test the sensitivity of the ethylene concentration measurements to the sampling probe alignment, an L-shaped type sampling probe was employed. This probe was

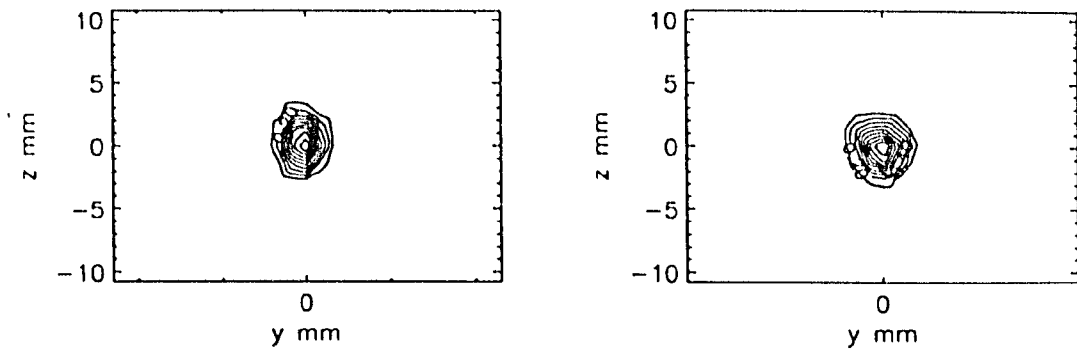


Figure V.3 Concentration coefficient C^* distributions for preliminary trace gas tests to ascertain the sensitivity of concentration measurements to the sampling flow rate constructed so the probe opening was in line with the probe shaft axis so that the probe could be rotated, changing the probe orientation, without changing the location of the probe opening. This allowed the probe to be intentionally misaligned with the host flow direction without changing the probe opening location. Ethylene was injected at the jet centerline and measurements were made downstream at a single location. The probe alignment was displaced approximately 30° either side of the host flow direction without any discernible change in the measured sample concentration. This evidence suggests that at least within this range of angles, the concentration measurements are insensitive to misalignment of the probe with the host flow.

Internal Fluid Mechanics Facility Validation

Measurements were made of the velocity distribution and free stream turbulence near the straight pipe exit at a location one radius upstream of the transition duct inlet ($x/D = -0.5$). The purposes of these measurements were to assess the flow quality of the Internal Fluid Mechanics Facility and to provide inlet conditions for CFD calculations of the transition duct flow field.

Velocity measurements

The velocity measurements were made within the straight pipe along a radial line from the wall to the centerline using a three-hole pressure probe. Data were recorded at approximately 0.64 mm intervals within the boundary layer and at 2.54 mm intervals from the boundary layer edge to the centerline. Measurements were made at three different centerline Mach numbers, 0.20, 0.35, and 0.50, corresponding to the three nonswirling inlet conditions at which transition duct measurements were recorded.

Figure V.4 shows the measured distribution of the axial component of the velocity coefficient M^* at $x/D = -0.5$. Distances were measured from the centerline and normalized with the pipe radius. Outside the boundary layer the axial component

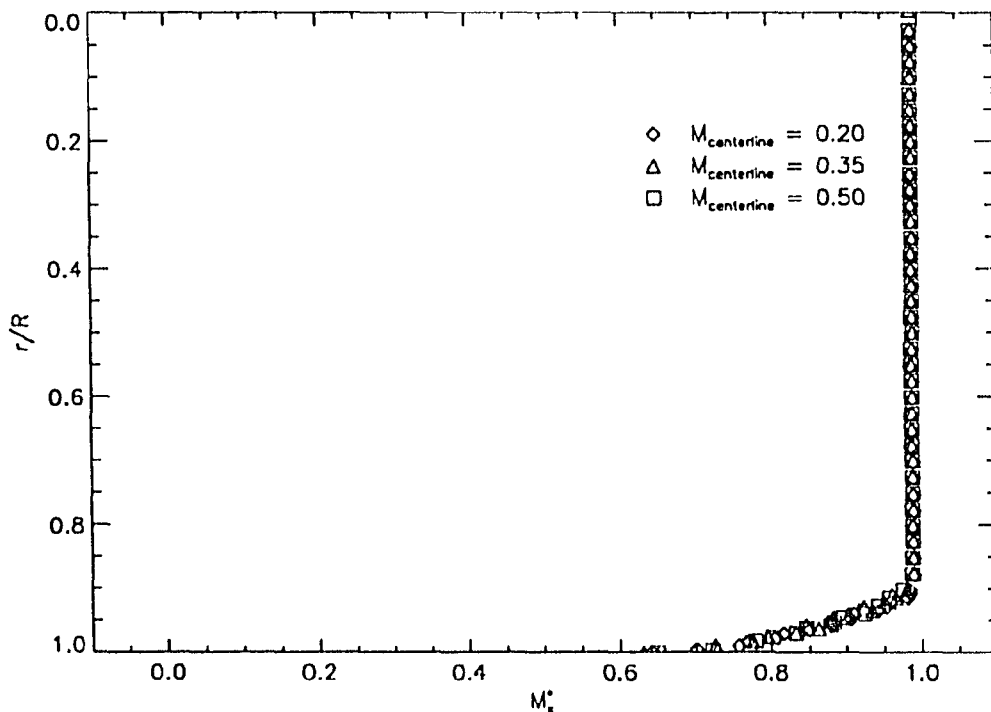


Figure V.4 The radial distributions of the axial component of the velocity coefficient M^* at $x/D = -0.5$ without swirl

of velocity was notably uniform. There were no measurable tangential velocity components. Radial velocity components were assumed to be negligibly small.

For each of the three centerline Mach numbers the boundary layer thickness $\delta_{0.95}$ (Equation V.6), displacement thickness δ^* (Equation V.7), momentum thickness θ (Equation V.8), and shape factor H (Equation V.9) were determined by numerical integration of the experimental data. These results are summarized in Table V.1. Equations V.7 and V.8 have been modified from their conventional formulations by a factor of r/R within the integrand because of the axisymmetric geometry of the pipe. Table V.1 shows that the boundary layers are quite thin; in all cases the boundary layer thickness is less than 10% of the pipe radius and the displacement thickness is less than 2% of the pipe radius. The shape factors measured indicate the boundary layers are turbulent and there is little streamwise pressure gradient.

$$\frac{\delta_{0.95}}{R} = \sup \left\{ 1 - \frac{r}{R} \mid U(r) < 0.95U_{\text{centerline}} \right\} \quad (\text{V.6})$$

$$\frac{\delta^*}{R} = \int_{\frac{r}{R}=0}^{\frac{r}{R}=1} \left(1 - \frac{U}{U_{\text{centerline}}} \right) \left(\frac{r}{R} \right) d\left(\frac{r}{R} \right) \quad (\text{V.7})$$

$$\frac{\theta}{R} = \int_{\frac{r}{R}=0}^{\frac{r}{R}=1} \frac{U}{U_{\text{centerline}}} \left(1 - \frac{U}{U_{\text{centerline}}} \right) \left(\frac{r}{R} \right) d\left(\frac{r}{R} \right) \quad (\text{V.8})$$

$$H = \frac{\delta^*}{\theta} \quad (\text{V.9})$$

Figure V.5 shows the velocity data within the boundary layer plotted in law of the wall coordinates. The conventional formulations of the law of the wall coordinate variables (Equation V.10) were used. The distance y refers to the distance from the wall, $y = R - r$. The friction velocity, u^* , defined by Equation V.11 was determined by calculating the value of u^* that provides the best approximation of the experimental

Table V.1 Boundary layer thickness $\delta_{0.95}$, displacement thickness δ^* , momentum thickness θ and shape factor H at $x/D = -0.5$ without swirl.

$M_{\text{centerline}}$	$\delta_{0.95}/R (\times 100)$	$\delta^*/R (\times 100)$	$\theta/R (\times 100)$	H
0.20	6.85	1.37	0.95	1.42
0.35	8.01	1.49	1.03	1.44
0.50	7.52	1.41	0.99	1.42

data by Equation V.12, where $k = 0.41$ and $B = 5.5$. These results also indicate no noticeable anomalies in the boundary layer entering the transition duct.

$$u^+ = \frac{u}{u^*}, \quad y^+ = \frac{yu^*}{\nu} \quad (\text{V.10})$$

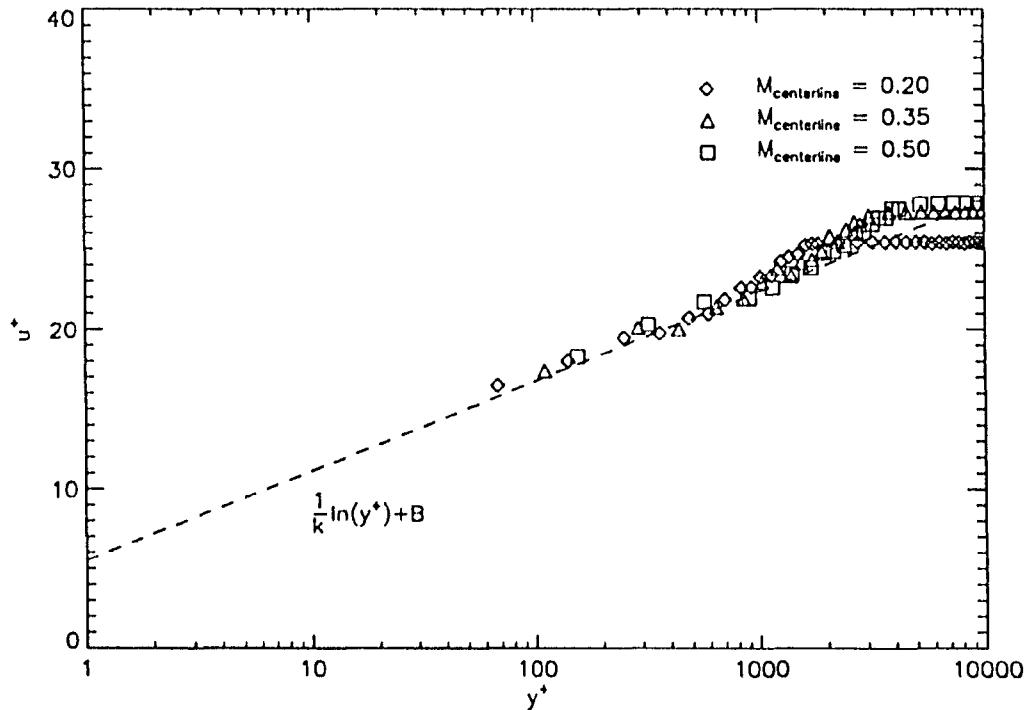


Figure V.5 The axial velocity distribution in law of the wall coordinates at $x/D = -0.5$ without swirl

$$u^* = \sqrt{\frac{\tau_w}{\rho}} \quad (\text{V.11})$$

$$u^+ = \frac{1}{k} \ln y^+ + B \quad (\text{V.12})$$

Turbulence measurements

Hot wire measurements were made at the centerline of the straight pipe section of the Internal Fluid Mechanics Facility for flow without swirl. Measurements were made for Mach numbers ranging from 0.05 to 0.50 and at five different overheat ratios. These data were gathered to ascertain the turbulence intensity Tu and turbulence integral length scale Λ in the free stream flow. The intention of these measurements was not to study the turbulence in detail but rather to determine velocity and length scale values which in general terms characterize the turbulence.

The calibration of the hot wire probe, described in Chapter IV, and the acquisition of the turbulence data were conducted simultaneously. The known mean flow information was used to determine the calibration parameters while the digitized signal was analyzed to discover the turbulence information. A 50 KHz data acquisition sampling rate was used and the anemometer output was recorded for 2 seconds, acquiring at total of 100,000 recorded anemometer bridge voltage values for each Mach number and overheat ratio. The mean and RMS values of the bridge voltage were calculated numerically. The turbulence intensity was calculated using Equation V.13 for each Mach number and overheat ratio. These results indicate turbulence the intensity is nominally 0.65%.

$$Tu = \frac{\sqrt{u'^2}}{\bar{U}} = \frac{2\bar{E}\sqrt{e'^2}}{(\bar{E}^2 - A)n} \quad (\text{V.13})$$

$$R(\tau) = \frac{\overline{u'(t)u'(t+\tau)}}{\overline{u'^2}} \quad (\text{V.14})$$

The definitions of the turbulence integral scales and their significance are described by Bradshaw [63]. To determine the integral length scale required first calculating the autocorrelation $R(\tau)$ of the velocity fluctuations given by Equation V.14. Rough estimates indicated the value of the integral time scale was no larger than approximately 0.015 seconds. Since data were recorded for 2 seconds the whole data signal was partitioned and 20 independent values of the autocorrelation were calculated. An ensemble average of all 20 autocorrelations was then calculated. This average autocorrelation was then integrated to determine the integral time scale T as shown in Equation V.15. Taylor's hypothesis was then invoked to use the mean velocity to calculate the integral length scale by Equation V.16. This process was repeated for each Mach number and overheat ratio. The results showed some variation, but the nominal value of the integral length scale was approximately 3 mm.

$$T = \int_0^{\infty} R(\tau) d\tau \quad (\text{V.15})$$

$$\Lambda = \bar{U}T \quad (\text{V.16})$$

Swirl Generator Validation

Measurements were made of the operating conditions (e.g., centerline Mach number and maximum ideal swirl angle), velocity and pressure distributions near the exit of the swirl generator at a location one radius upstream of the transition duct inlet ($x/D = -0.5$). This data provided information about the operating characteristics of the swirl generator as well as inlet conditions for CFD calculations of the transition duct flow field.

Swirl generator operating condition

To determine the swirl generator operating conditions and for nondimensionalizing experimental results, knowing the centerline total and static pressures near the

swirl generator exit and the angular velocity of this flow was essential. A series of experiments was therefore conducted to explore how these operating conditions could be determined.

Centerline conditions During transition duct experiments a way to determine the centerline total and static pressure at $x/D = -0.5$ without using an intrusive probe was sought in order to avoid flow field disturbances in the transition duct. Without the swirl generator the centerline total pressure was assumed to be equal to the upstream settling chamber pressure ($p_{0,\text{centerline}} = p_{\text{settling chamber}}$) and the centerline static pressure was taken to be equal to the static pressure measured at the pipe wall ($p_{\text{centerline}} = p_{\text{wall}}$). The wall static pressure was measured with two surface static pressure taps located at $x/D = -0.5$. The centerline Mach number was calculated using Equation V.17.

$$M_{\text{centerline}} = \sqrt{\left[\left(\frac{p_{0,\text{centerline}}}{p_{\text{centerline}}} \right)^{\frac{\gamma-1}{\gamma}} - 1 \right] \frac{2}{\gamma-1}} \quad (\text{V.17})$$

Two critical assumptions in this procedure are no total pressure loss between the settling chamber and inlet centerline and no radial static pressure gradient at the inlet. These are reasonable assumptions for flow without the swirl generator. However, neither assumption is valid with the swirl generator installed. There are significant total pressure losses associated with the blades, honeycomb, and screen of the swirl generator and a radial pressure gradient exists downstream of the swirl generator to balance centrifugal forces established in the fluid by the swirling flow.

A series of experiments were conducted with the swirl generator installed to determine the relationship between the centerline total and static pressures at $x/D = -0.5$ and the settling chamber and wall static pressures. A calibrated five-hole pressure probe was used to measure the centerline total and static pressures while the swirl generator operating conditions were varied. The relationships between centerline total and static pressures at $x/D = -0.5$ and the settling chamber and

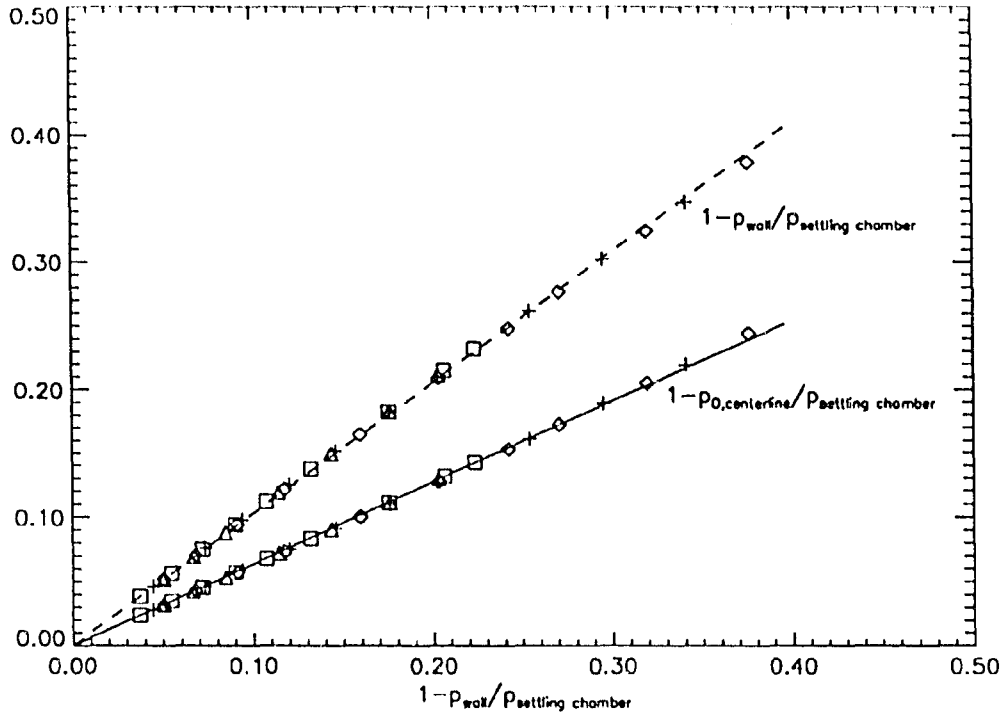


Figure V.6 The relationships between centerline total and static pressures at $x/D = -0.5$ and the settling chamber and wall static pressures with swirl wall static pressures are shown in Figure V.6. Different symbols mark experimental measurements recorded on different days. The solid line is a plot Equation V.18, the broken line is a plot of Equation V.19.

$$1 - \frac{P_0}{P_{\text{settling chamber}}} = c_1 \left(1 - \frac{P_{\text{wall}}}{P_{\text{settling chamber}}} \right) \quad (\text{V.18})$$

$$1 - \frac{P}{P_{\text{settling chamber}}} = c_2 \left(1 - \frac{P_{\text{wall}}}{P_{\text{settling chamber}}} \right) \quad (\text{V.19})$$

Both constants of Equations V.18 and V.19 were determined by a least squares linear approximation. Equations V.18 and V.19 allowed the centerline total and static pressures at $x/D = -0.5$ to be determined from the settling chamber and wall static

pressures, which were measured without an intrusive probe. The ratio of total to static pressure at the centerline was used in Equation V.17 to determine the centerline Mach number.

Angular velocity A nonintrusive proximity sensor was used to measure the angular velocity of the swirl generator. This proximity sensor, which detects ferrous metal, was attached to the stationary outer casing. A steel screw was attached to the aluminum rotating pipe of the swirl generator. A voltage spike was produced in the output signal of the proximity sensor with each revolution of the aluminum pipe. A frequency counter was used to measure the time between consecutive voltage spikes. Figure V.7 shows the relationship between the swirl generator angular velocity and centerline Mach number. Different symbols denote experimental

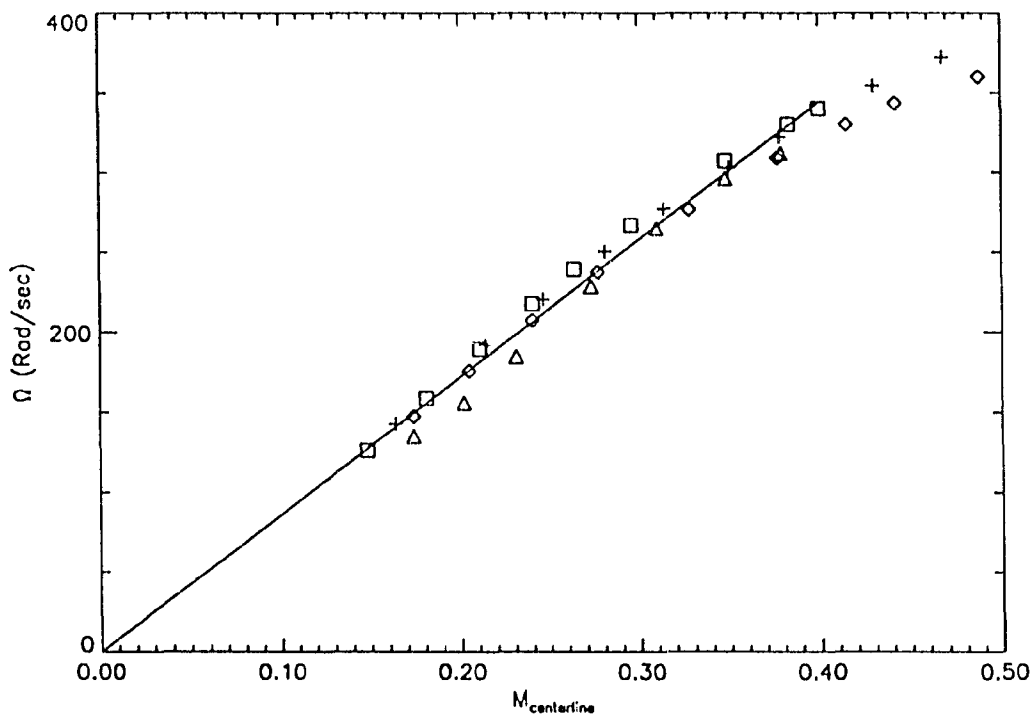


Figure V.7 The relationship of swirl generator angular velocity to centerline Mach number

measurements recorded on different days. The solid line shows a linear approximation of the data for $0 \leq M_{\text{centerline}} \leq 0.4$. For $M_{\text{centerline}} \geq 0.4$ the data deviates significantly from the linear approximation. The standard deviation of the data for $0 \leq M_{\text{centerline}} \leq 0.4$ is 8.6 rad/s. At $M_{\text{centerline}} = 0.35$, the operating condition used for the transition duct measurements with swirl, this equates to an angular velocity uncertainty of 2.8%. The maximum ideal swirl angle calculated using Equation III.9 is $\phi_{\text{max}} = 15.6^\circ$.

Swirl generator aerodynamic survey

Measurements were made with a calibrated five-hole probe of the velocity, total pressure, and static pressure distribution near the exit of the swirl generator at $x/D = -0.5$. These data were used to assess the flow field produced by the swirl generator and provide inlet conditions for CFD calculations of the transition duct flow field.

Velocity measurements Figure V.8 shows the distributions of the axial, radial and tangential components of the velocity coefficient M^* at $x/D = -0.5$. The results are for three different centerline Mach numbers.

The radial component of the velocity coefficient confirms that there is no measurable radial velocity component at the swirl generator exit. The tangential velocity coefficient component data show that tangential velocity increases nearly linearly with radial distance from the centerline, achieving the desired objective of solid body rotation. The axial component of the velocity coefficient has a small aberration near the centerline. This is a result of the total pressure losses produced by the small annular center body used to hold the stationary swirl generator blades.

The boundary layer thickness $\delta_{0.95}$, displacement thickness δ^* , momentum thickness θ and shape factor H were calculated from this data. The results are contained in Table V.2. The boundary layer entering the transition duct is thicker for the inlet swirl case compared to the nonswirling case. The additional boundary layer thickness results primarily from work extracted from the flow to rotate the swirl generator

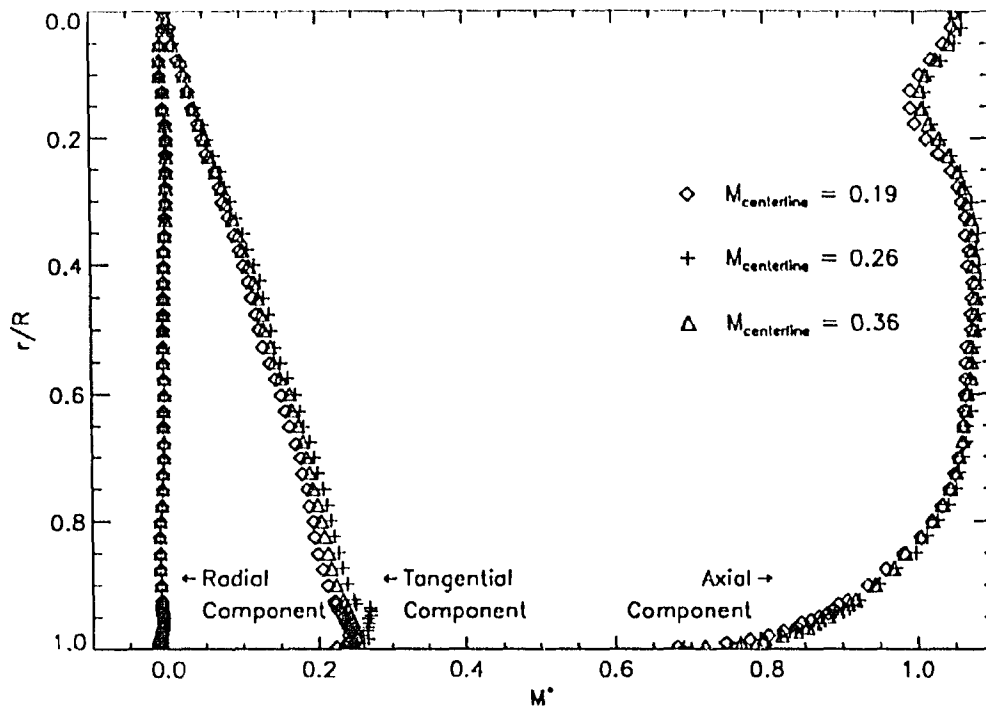


Figure V.8 The radial distributions of the axial, radial and tangential components of the velocity coefficient M^* at $x/D = -0.5$ with swirl

pipe against the bearing friction. The shape factors in table V.2 are higher than the nonswirling case. This is also probably a feature of the axial velocity deficit resulting from work extraction rather than an indication of an axial pressure gradient.

Figure V.9 shows the velocity data plotted in law of the wall coordinates. Because the boundary layer is thicker than the nonswirling case the values of y^+ for the data

Table V.2 Boundary layer thickness $\delta_{0.95}$, displacement thickness δ^* , momentum thickness θ and shape factor H at $x/D = -0.5$ with swirl.

$M_{\text{centerline}}$	$\delta_{0.95}/R (\times 100)$	$\delta^*/R (\times 100)$	$\theta/R (\times 100)$	H
0.19	19.99	4.02	2.41	1.67
0.26	20.18	4.03	2.40	1.68
0.36	20.48	4.05	2.37	1.71

in Figure V.9 are lower than in Figure V.5. There is some deviation from the law of the wall behavior at the lowest values of y^+ measured but, in general, the agreement appears quite good.

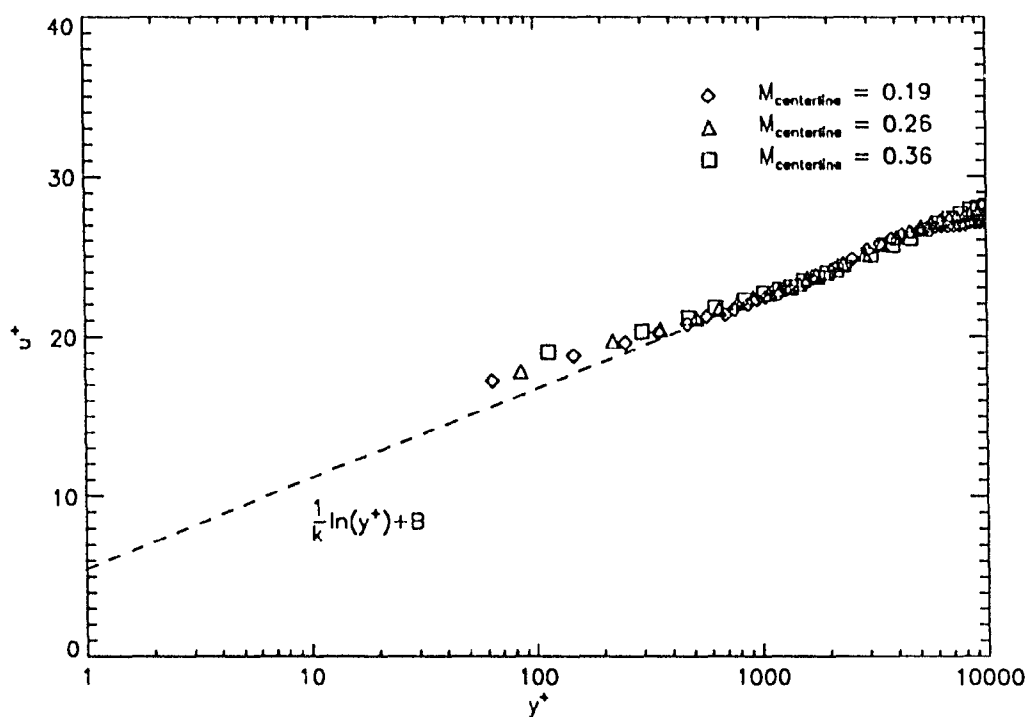


Figure V.9 The axial velocity distribution in law of the wall coordinates at $x/D = -0.5$ with swirl

Pressure measurements Figure V.10 shows the radial distributions of the total and static pressure coefficients measured at $x/D = -0.5$. The parabolic static pressure profile predicted by Equation III.8 is apparent in Figure V.10. The losses in total pressure associated with the swirl generator annular center body near $r/R = 0.15$ and from work extracted to rotate the swirl generator pipe against the bearing friction at $r/R > 0.75$ is conspicuous.

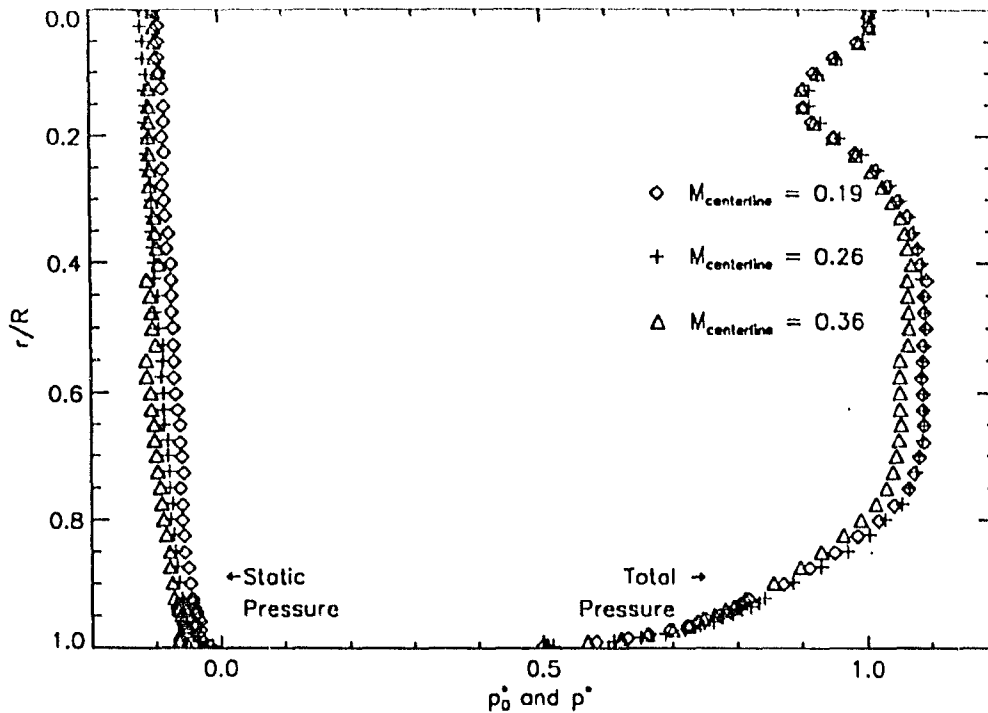


Figure V.10 The radial distributions of the total pressure coefficient p_0^* and static pressure coefficient p^* at $x/D = -0.5$ with swirl

The Transition Duct Without Inlet Swirl

Table V.3 is a summary of the test conditions and measurement methods employed for the transition duct experiments without inlet swirl. The aerodynamic measurements include surface static pressure measurements and detailed surveys with a five-hole probe in four cross stream measurement planes. For trace gas measurements, ethylene was injected at seven different locations in the injection plane and the trace gas concentration levels were measured in four cross stream measurement planes. The nondimensionalized aerodynamic measurement data vary little between test conditions, showing independence of inlet centerline Mach number or Reynolds number within the range of each considered.

Table V.3 Summary of test conditions and experimental methods for transition duct studies without inlet swirl

$M_{\text{centerline}}$	Re_D	Measurements recorded
0.20	918,000	Aerodynamic
0.35	1,547,000	Aerodynamic
0.50	2,086,000	Aerodynamic, trace gas and surface oil film visualization

Surface oil film visualization

The first experiments conducted were surface oil film visualization in the transition duct without inlet swirl. Figures V.11 and V.12 show the flow visualization results from two different views. In both figures the flow is from the left to the right. A local coordinate system is shown in each figure to help establish the orientation of the photographs. These photographs were digitized with an image scanner and then numerically enhanced to improve their contrast.

Trace gas measurements

In Figures V.13 through V.16 the cross section of the duct is drawn to the same scale. Each figure shows contours of the ethylene concentration coefficient C^* measured in that plane for all seven injection locations. The contour levels shown in Figures V.13 through V.16 are at 20, 40, 60, and 80 percent of the peak value.

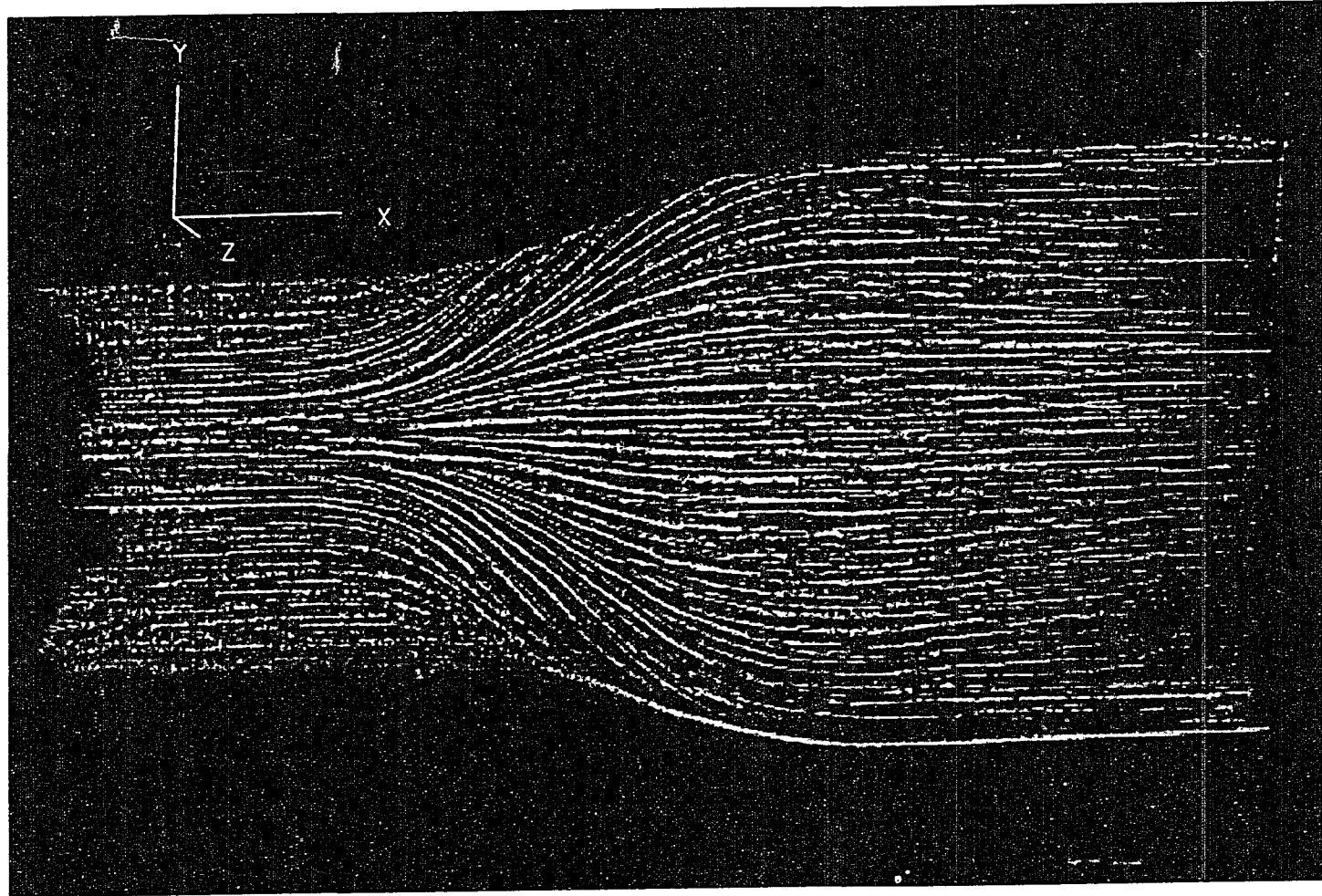


Figure V.11 Surface oil film visualization without inlet swirl

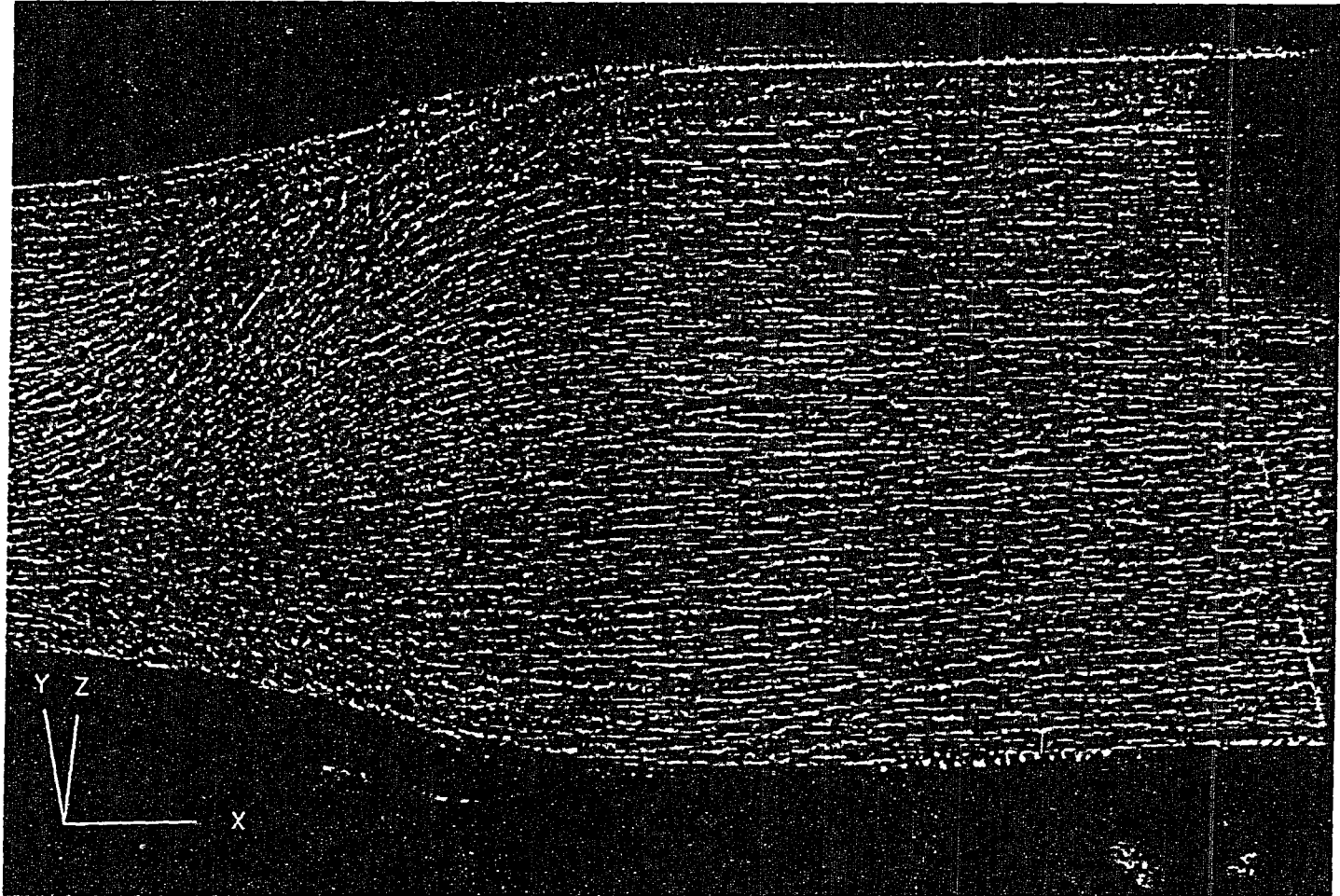


Figure V.12 Surface oil film visualization without inlet swirl

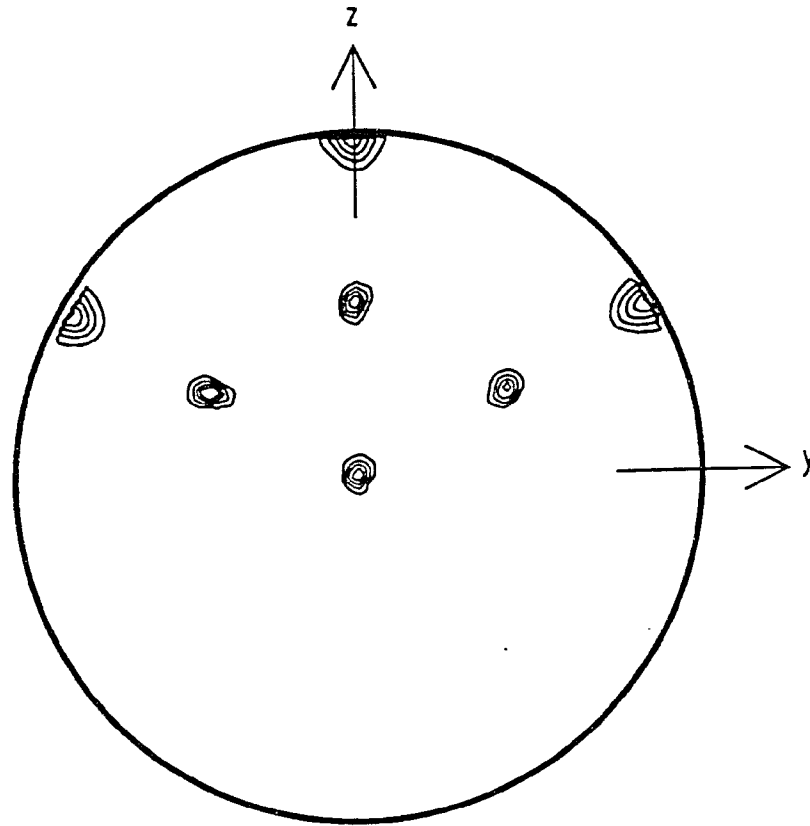


Figure V.13 Ethylene concentration coefficient C^* distributions in plane 1T

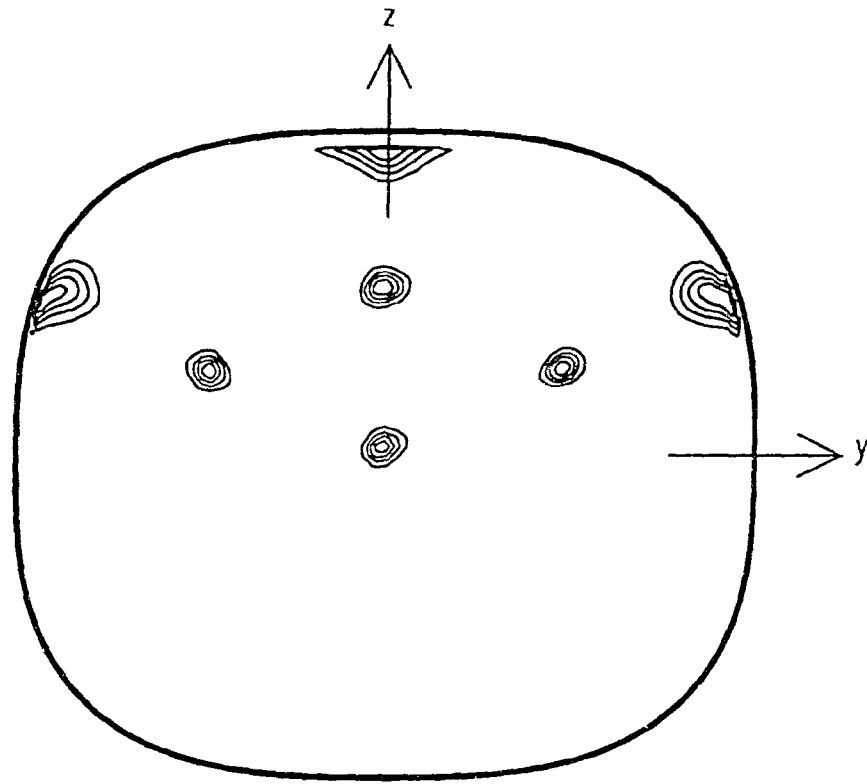


Figure V.14 Ethylene concentration coefficient C^* distributions in plane 2T

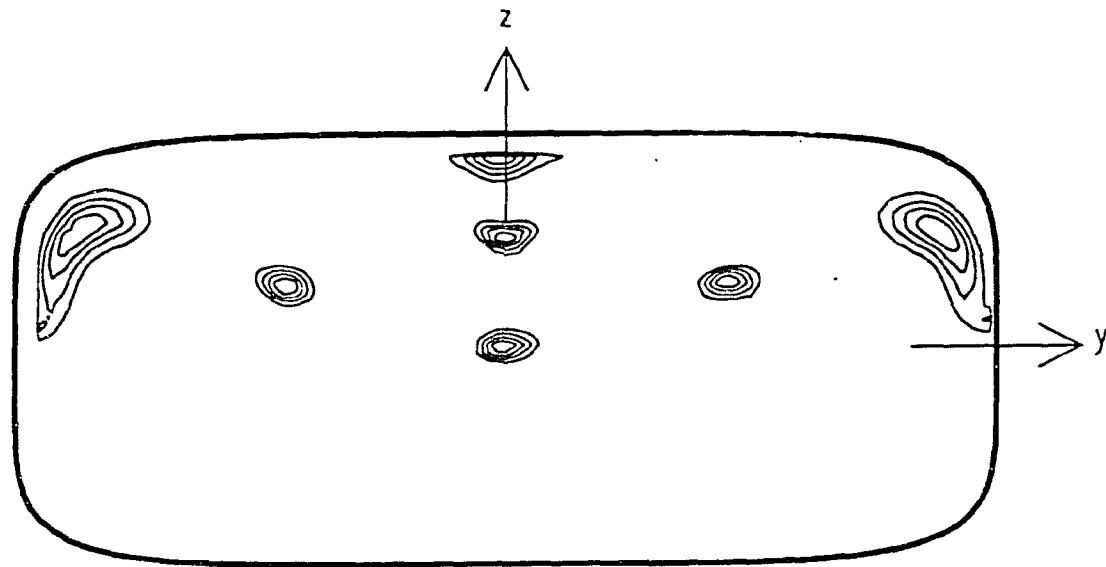


Figure V.15 Ethylene concentration coefficient C^* distributions in plane 3T

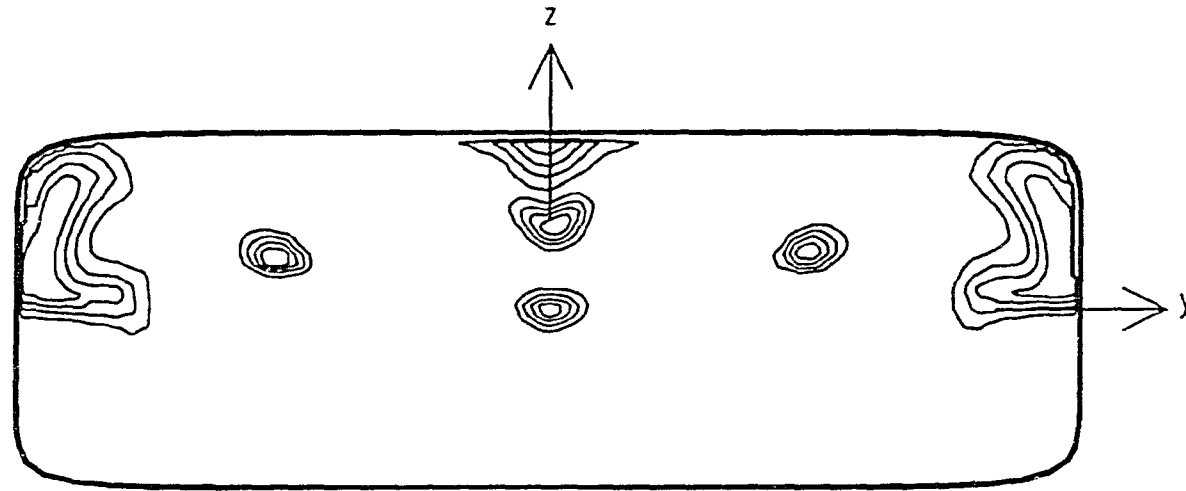


Figure V.16 Ethylene concentration coefficient C^* distributions in plane 4T

Aerodynamic measurements

Surface static pressure measurements Open symbols in Figure V.17 represent values of the static pressure coefficient p^* distributed along the lower surface of the duct for all three test conditions. Shown as vertical broken lines are the locations of the four aerodynamic measurement planes. The solid symbols on these lines represent the static pressure coefficient measured at the duct centerline with a five-hole probe.

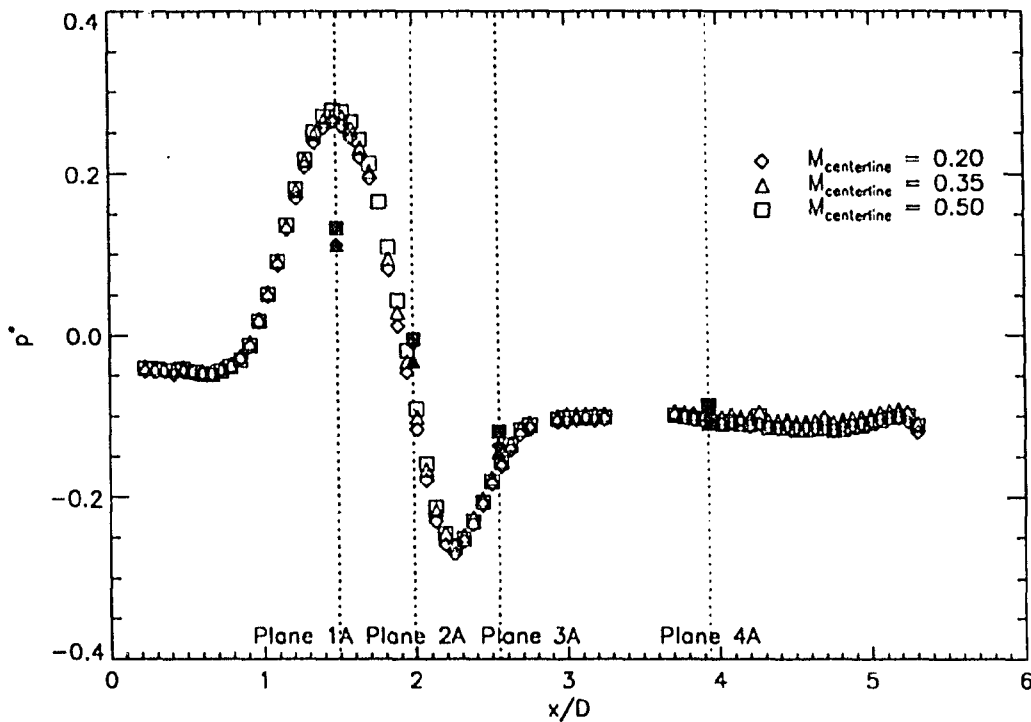


Figure V.17 Surface static pressure coefficient p^* for flow without inlet swirl

Five-hole probe measurements The results of the detailed five-hole probe surveys in four cross stream measurement planes within the transition duct are shown in Figures V.18 through V.41. The cross section of the duct is drawn to the same scale in each figure. Figures V.18 through V.25 show results at $M_{\text{centerline}} = 0.20$,

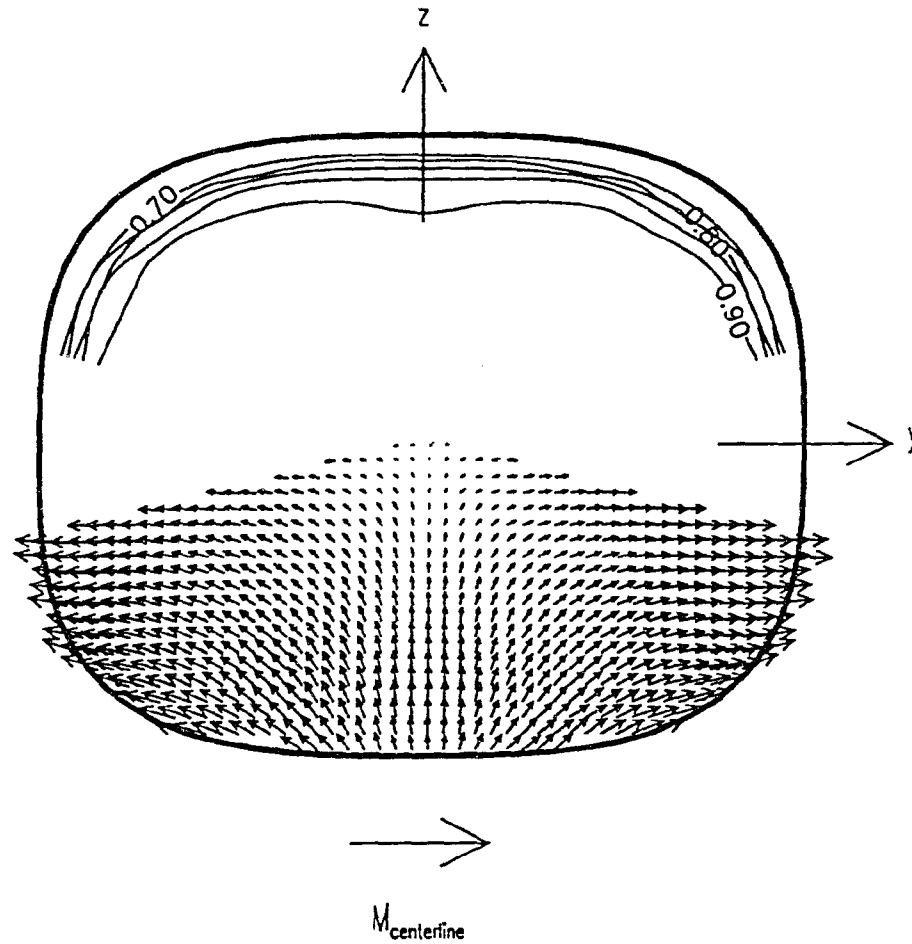


Figure V.18 Axial (upper) and transverse (lower) components of the velocity coefficient M^* in plane 1A for $M_{\text{centerline}} = 0.20$ without inlet swirl

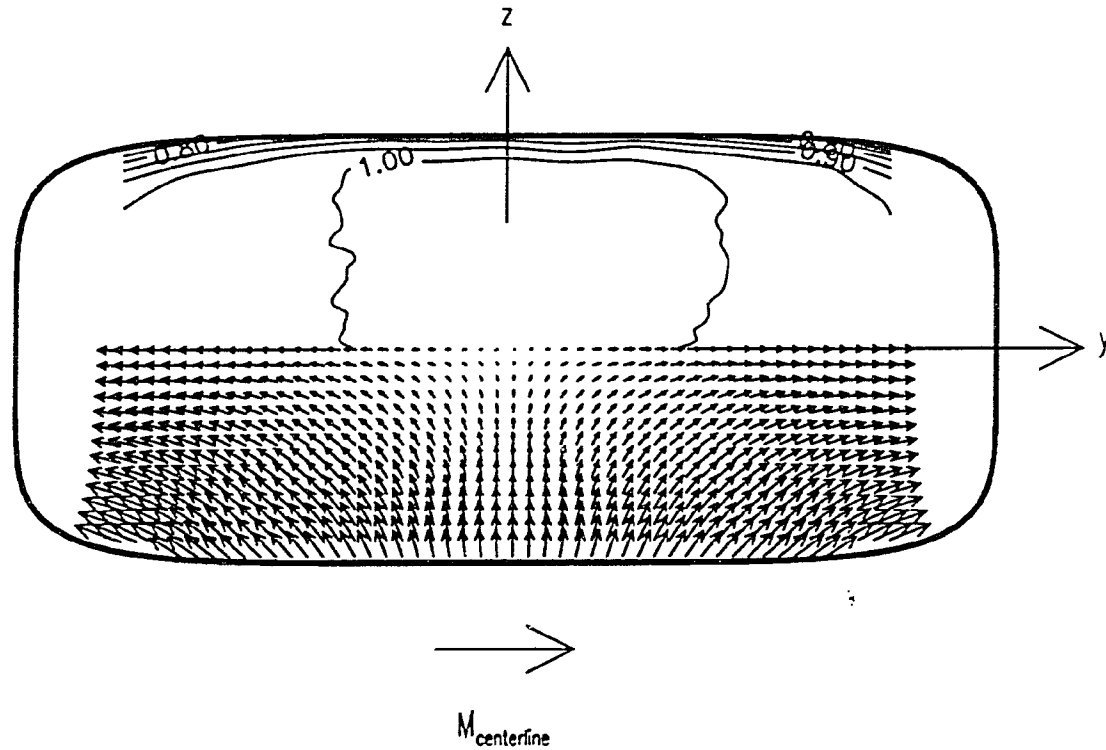


Figure V.19 Axial (upper) and transverse (lower) components of the velocity coefficient M^* in plane 2A for $M_{\text{centerline}} = 0.20$ without inlet swirl

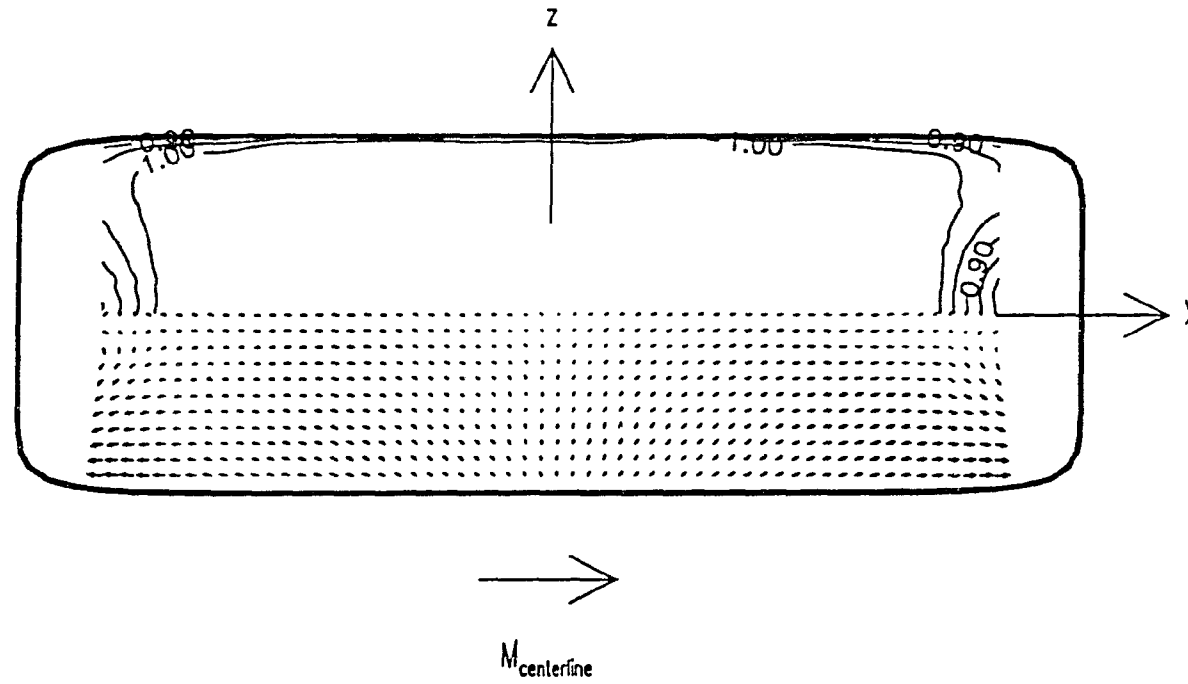


Figure V.20 Axial (upper) and transverse (lower) components of the velocity coefficient M^* in plane 3A for $M_{\text{centerline}} = 0.20$ without inlet swirl

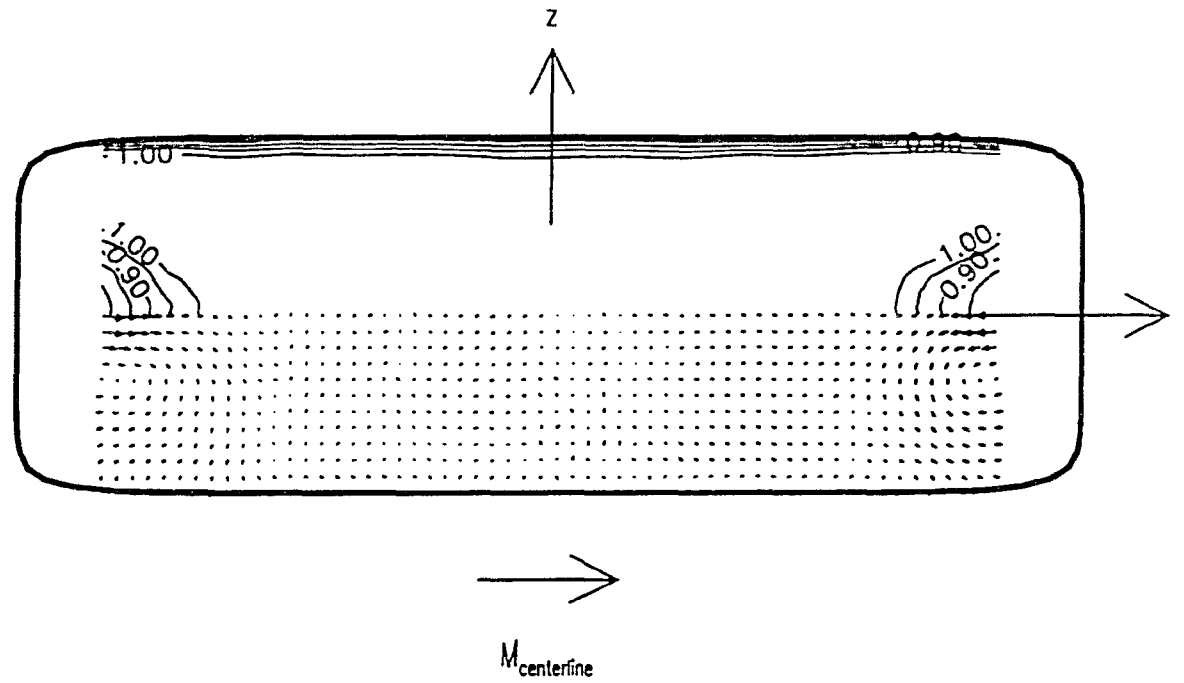


Figure V.21 Axial (upper) and transverse (lower) components of the velocity coefficient M^* in plane 4A for $M_{\text{centerline}} = 0.20$ without inlet swirl

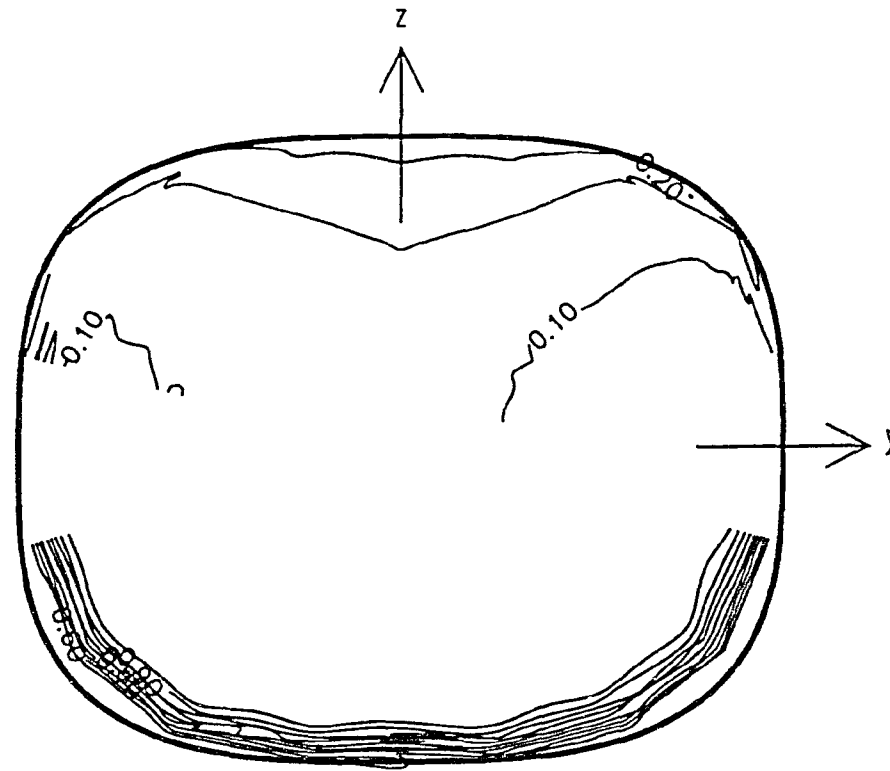


Figure V.22 Static pressure coefficient p^* (upper) and total pressure coefficient p_0^* (lower) distributions in plane 1A for $M_{\text{centerline}} = 0.20$ without inlet swirl

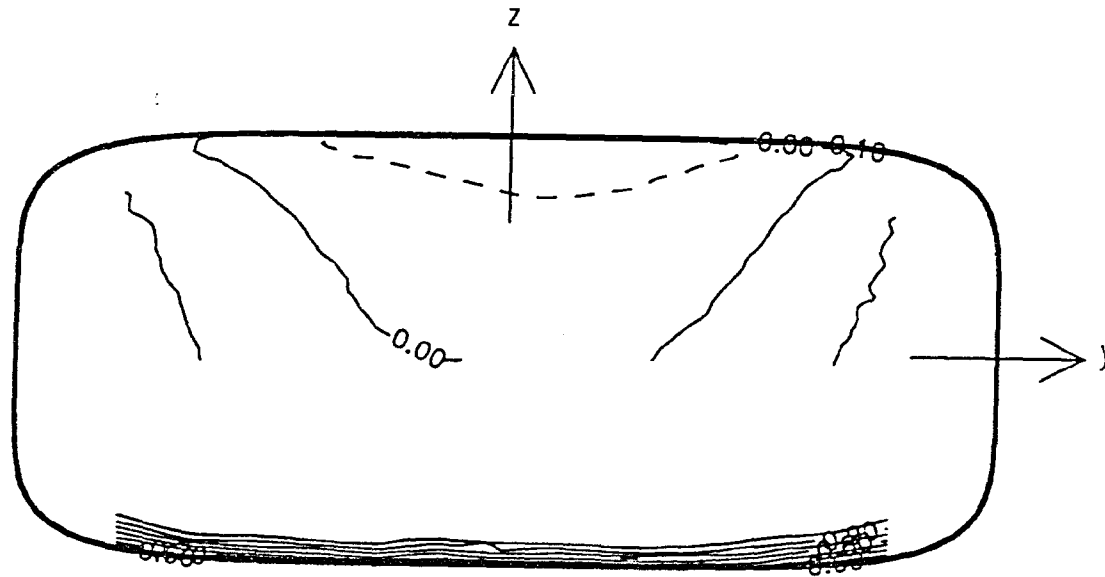


Figure V.23 Static pressure coefficient p^* (upper) and total pressure coefficient p_0^* (lower) distributions in plane 2A for $M_{\text{centerline}} = 0.20$ without inlet swirl

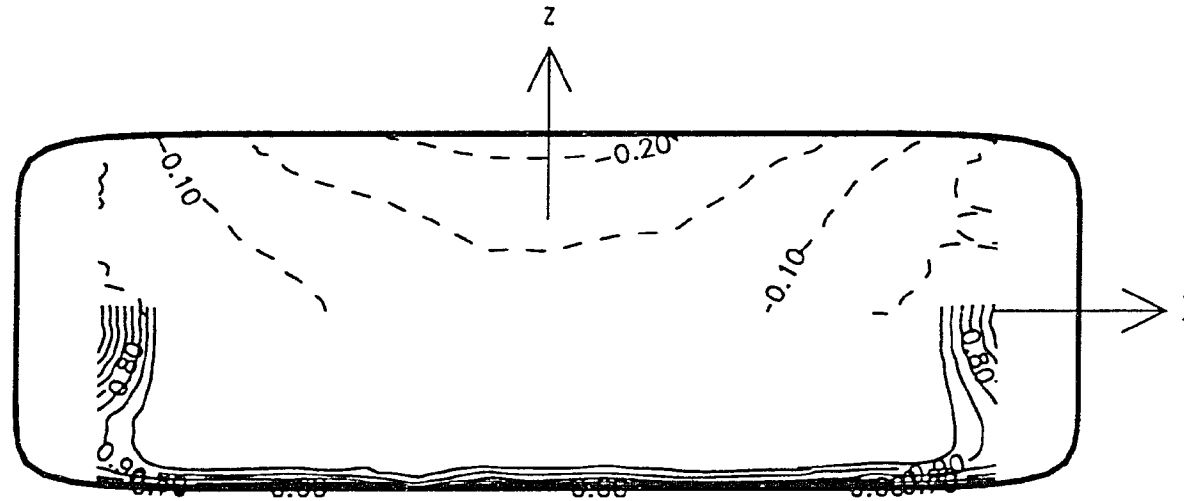


Figure V.24 Static pressure coefficient p^* (upper) and total pressure coefficient p_0^* (lower) distributions in plane 3A for $M_{\text{centerline}} = 0.20$ without inlet swirl

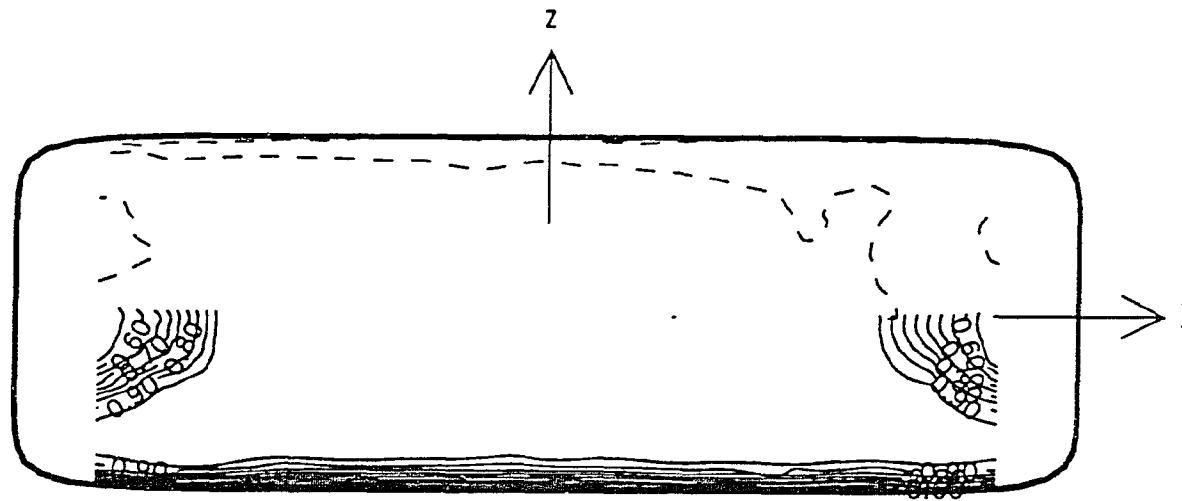


Figure V.25 Static pressure coefficient p^* (upper) and total pressure coefficient p_0^* (lower) distributions in plane 4A for $M_{\text{centerline}} = 0.20$ without inlet swirl

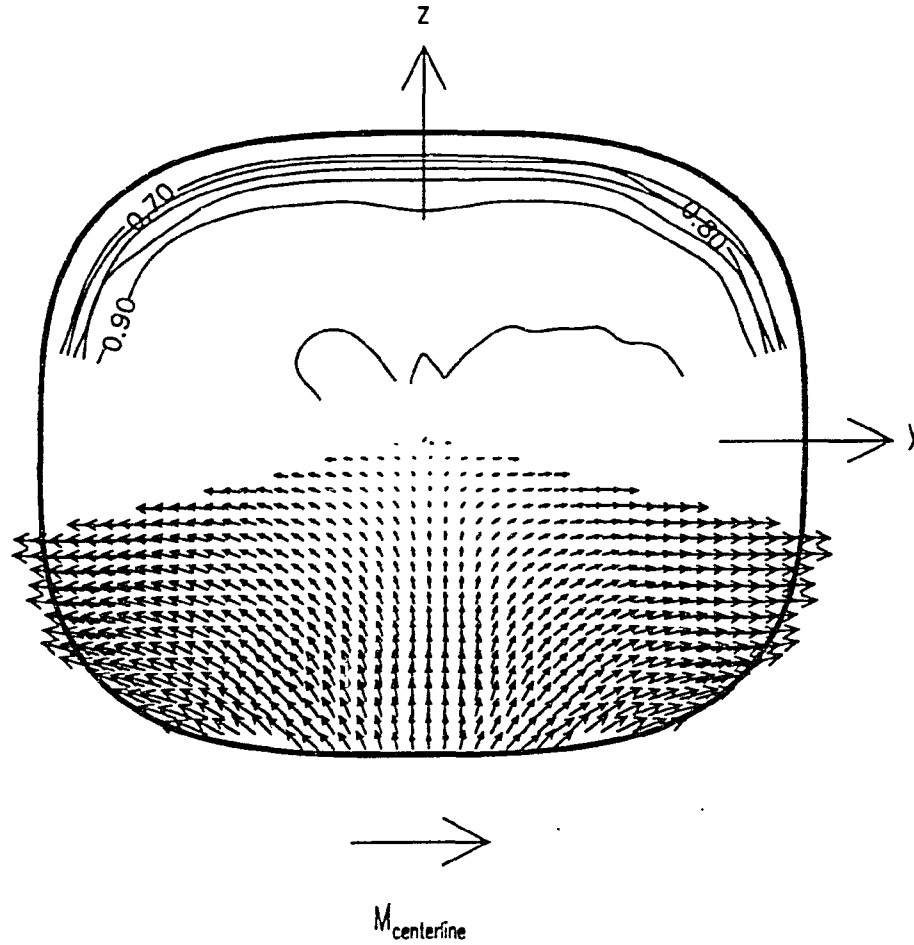


Figure V.26 Axial (upper) and transverse (lower) components of the velocity coefficient M^* in plane 1A for $M_{\text{centerline}} = 0.35$ without inlet swirl

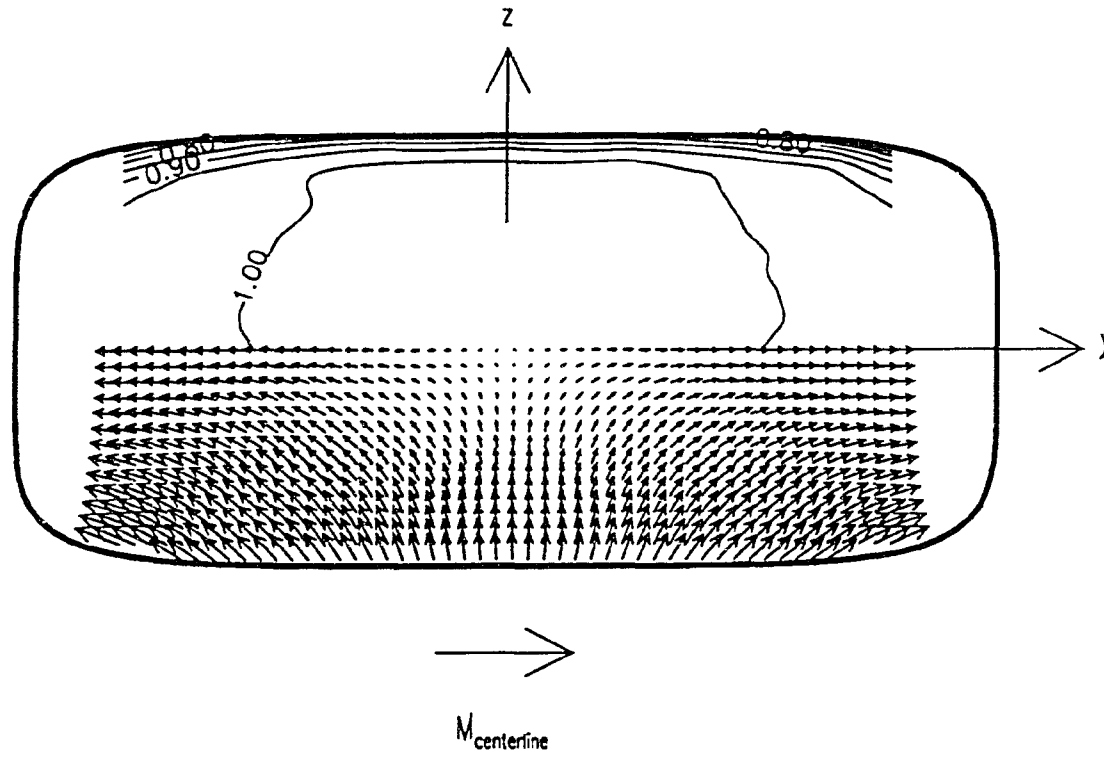


Figure V.27 Axial (upper) and transverse (lower) components of the velocity coefficient M^* in plane 2A for $M_{\text{centerline}} = 0.35$ without inlet swirl

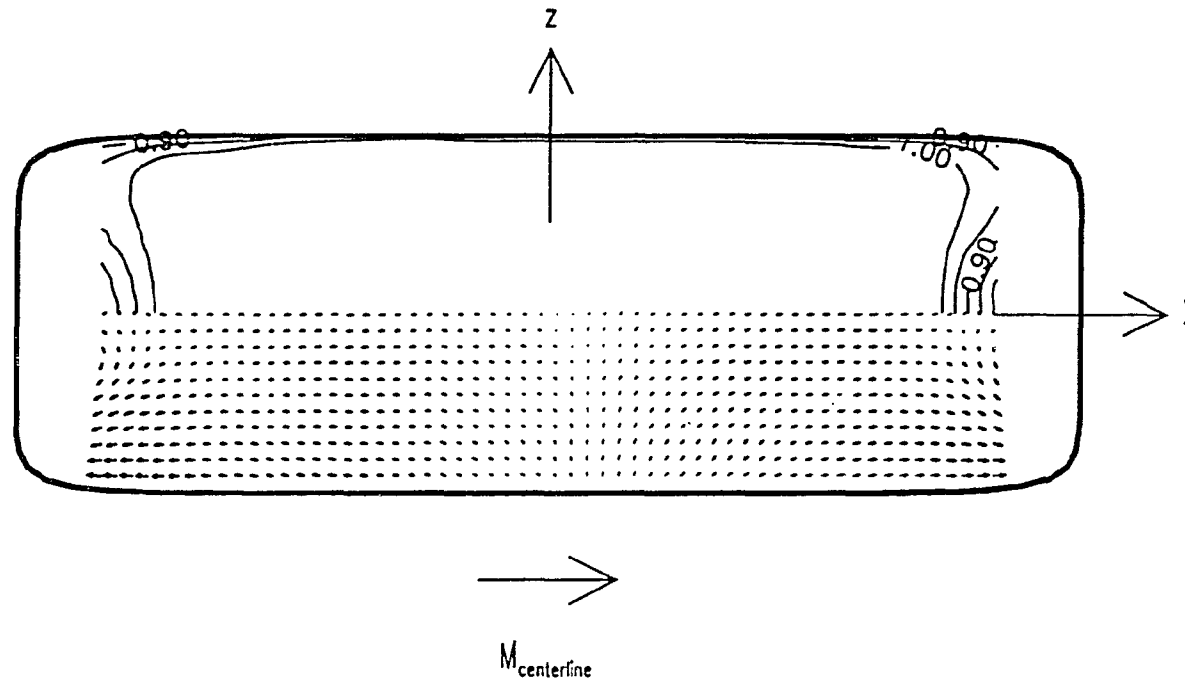


Figure V.28 Axial (upper) and transverse (lower) components of the velocity coefficient M^* in plane 3A for $M_{\text{centerline}} = 0.35$ without inlet swirl

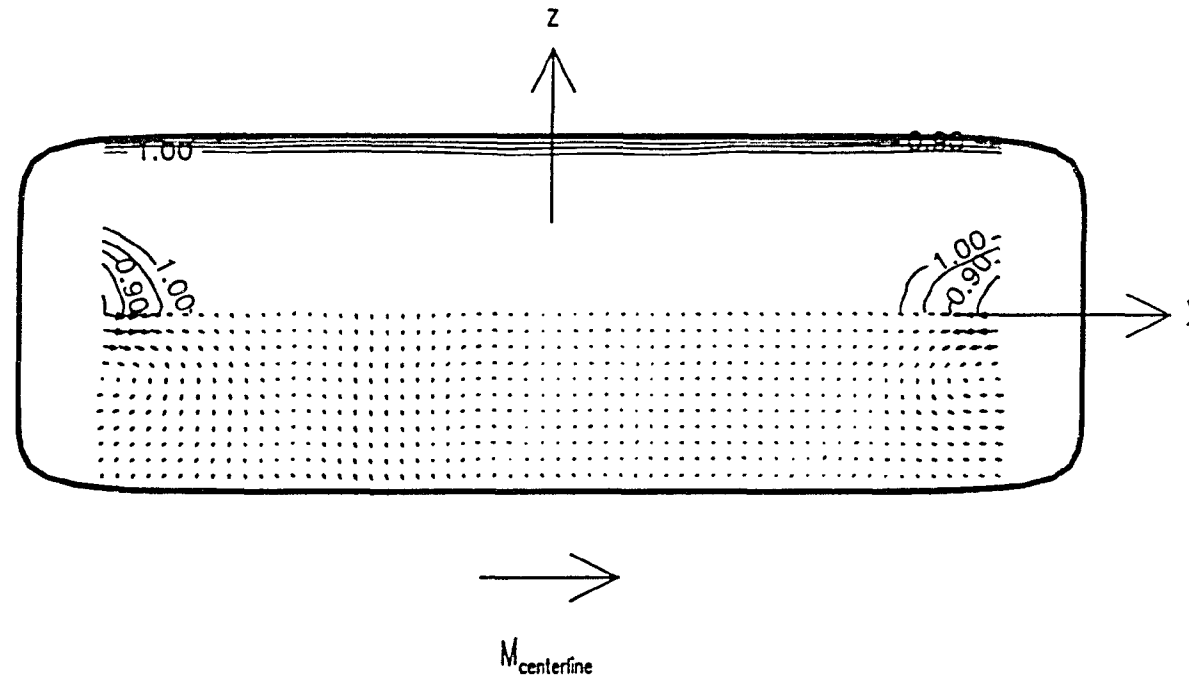


Figure V.29 Axial (upper) and transverse (lower) components of the velocity coefficient M^* in plane 4A for $M_{\text{centerline}} = 0.35$ without inlet swirl

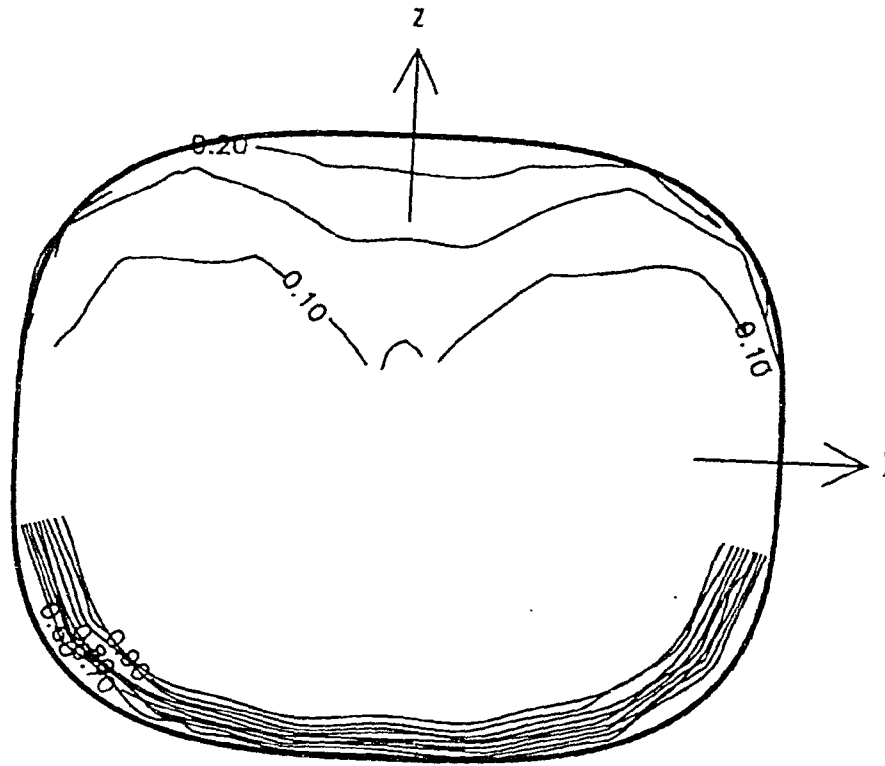


Figure V.30 Static pressure coefficient p^* (upper) and total pressure coefficient p_0^* (lower) distributions in plane 1A for $M_{\text{centerline}} = 0.35$ without inlet swirl

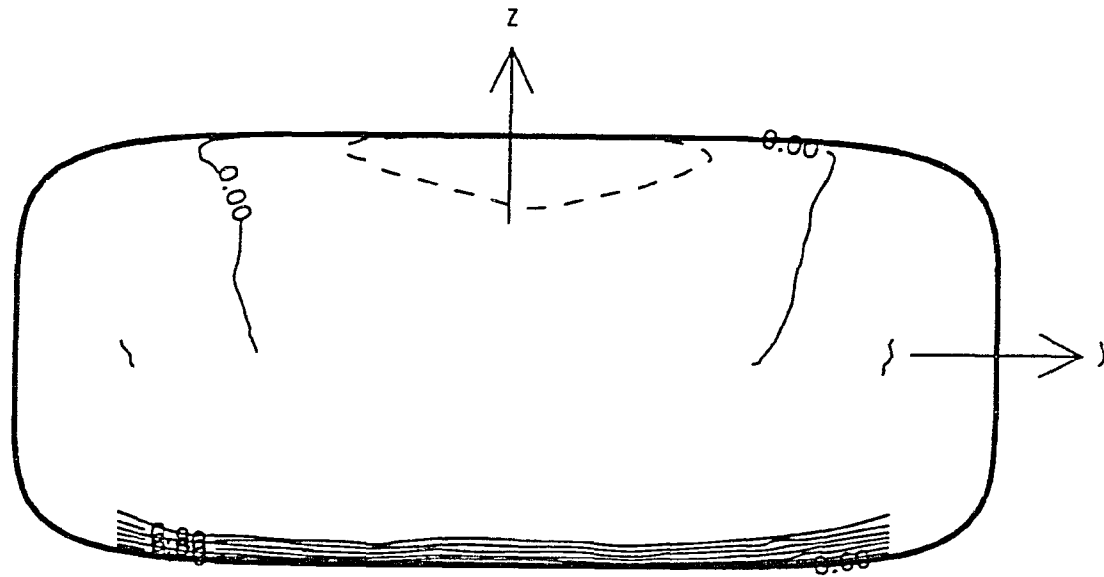


Figure V.31 Static pressure coefficient p^* (upper) and total pressure coefficient p_0^* (lower) distributions in plane 2A for $M_{\text{centerline}} = 0.35$ without inlet swirl

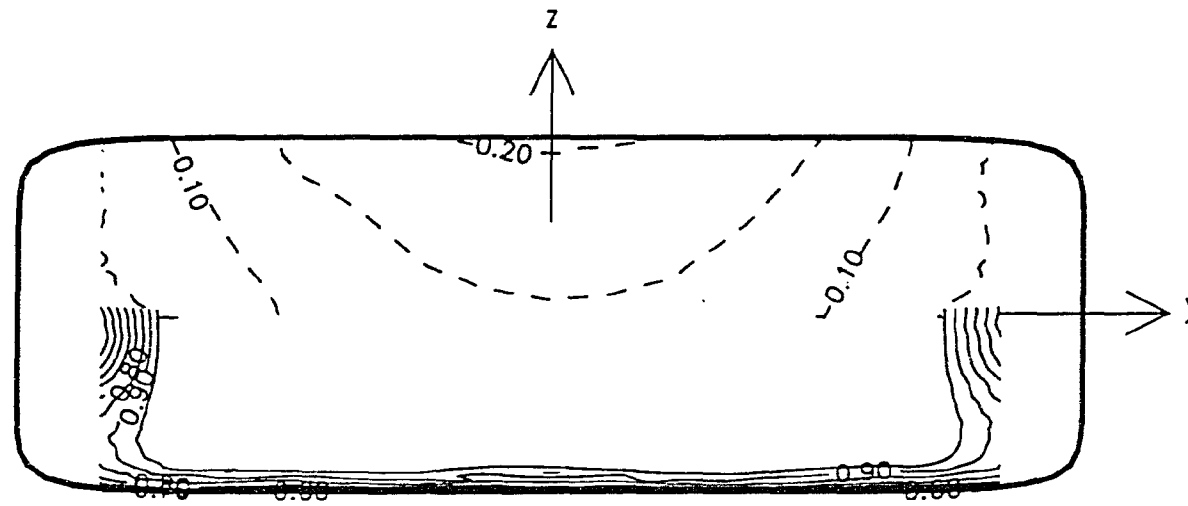


Figure V.32 Static pressure coefficient p^* (upper) and total pressure coefficient p_0^* (lower) distributions in plane 3A for $M_{\text{centerline}} = 0.35$ without inlet swirl

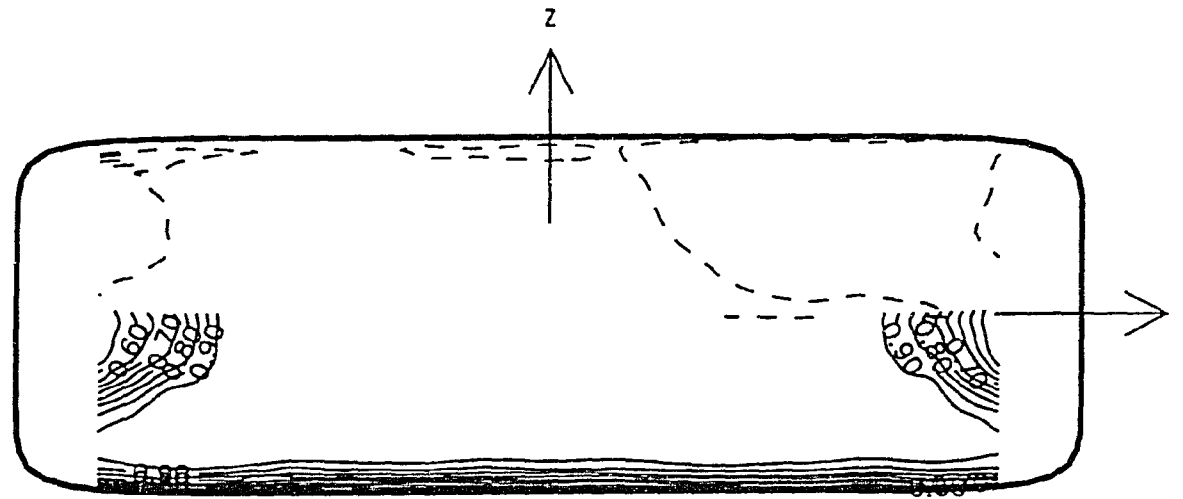


Figure V.33 Static pressure coefficient p^* (upper) and total pressure coefficient p_0^* (lower) distributions in plane 4A for $M_{\text{centerline}} = 0.35$ without inlet swirl

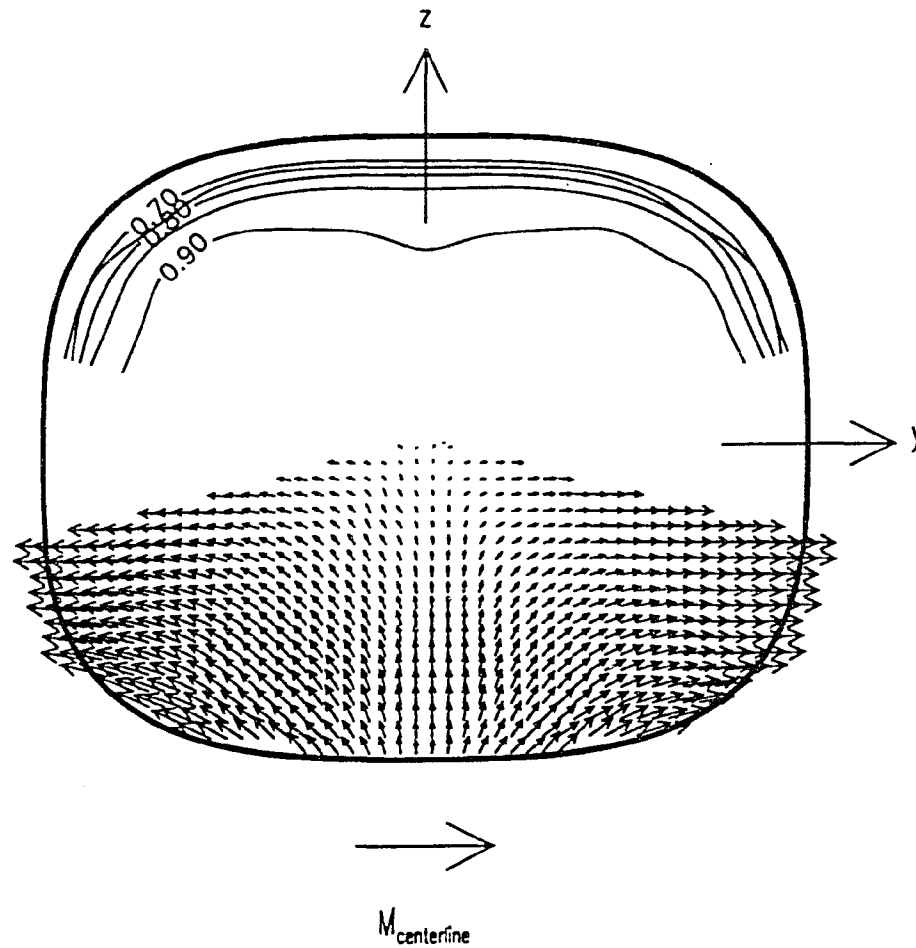


Figure V.34 Axial (upper) and transverse (lower) components of the velocity coefficient M^* in plane 1A for $M_{\text{centerline}} = 0.50$ without inlet swirl

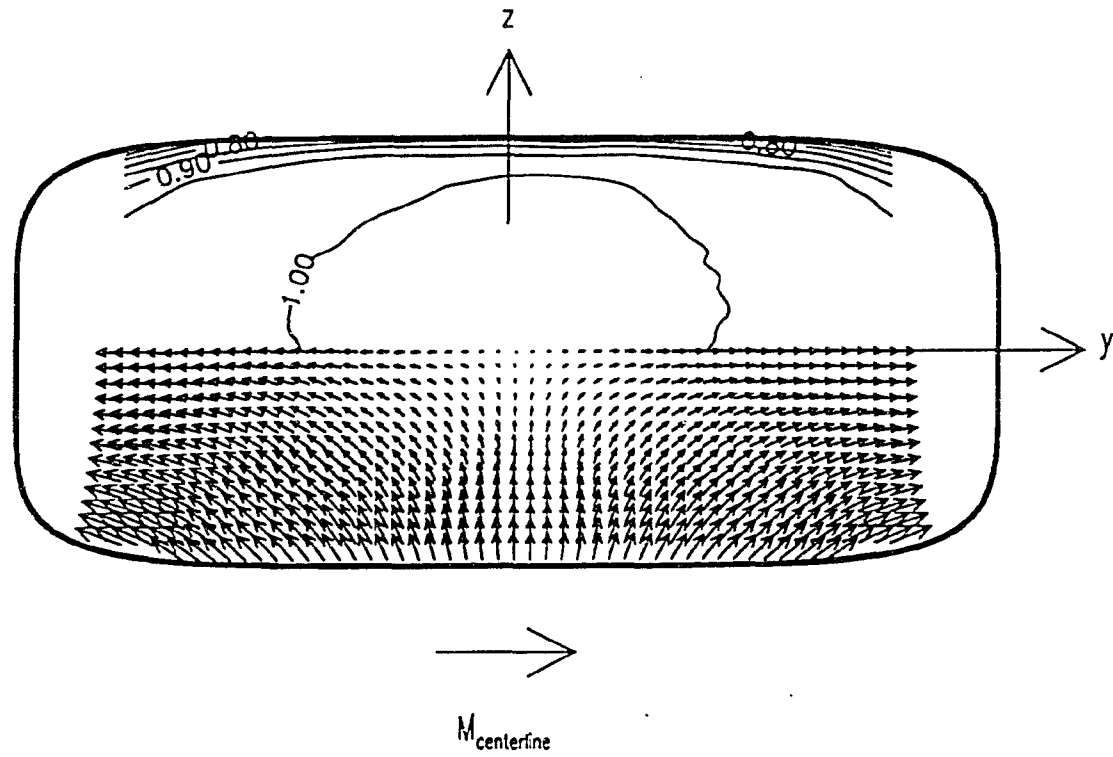


Figure V.35 Axial (upper) and transverse (lower) components of the velocity coefficient M^* in plane 2A for $M_{\text{centerline}} = 0.50$ without inlet swirl

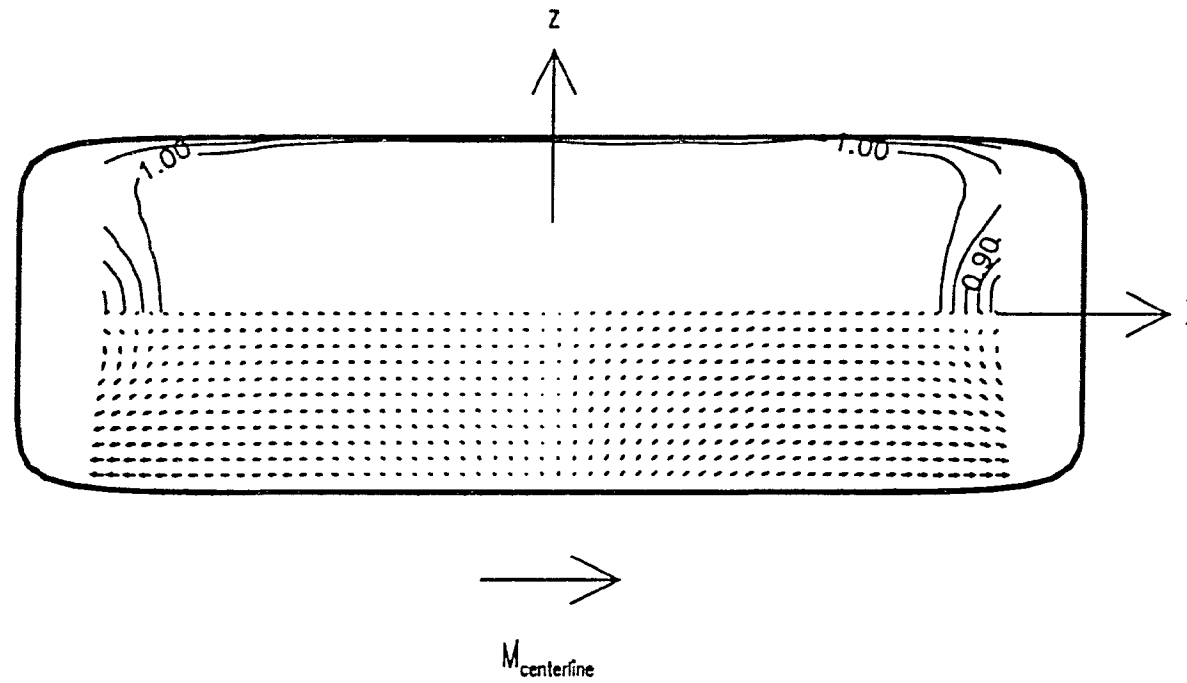


Figure V.36 Axial (upper) and transverse (lower) components of the velocity coefficient M^* in plane 3A for $M_{\text{centerline}} = 0.50$ without inlet swirl

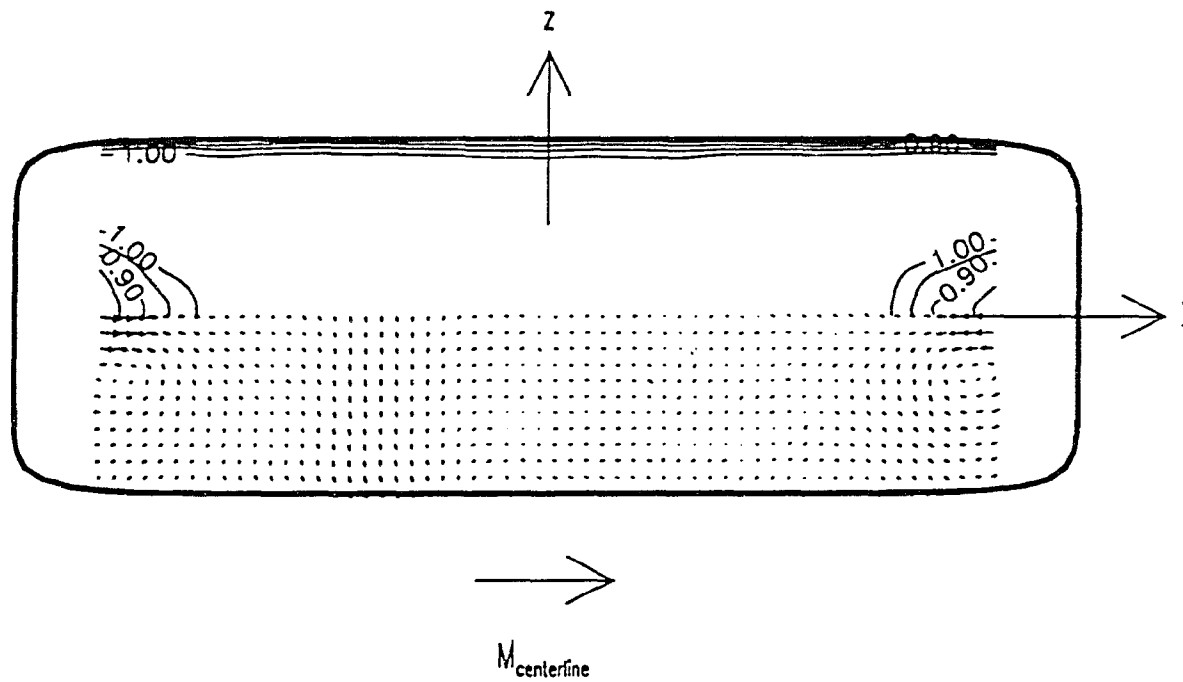


Figure V.37 Axial (upper) and transverse (lower) components of the velocity coefficient M^* in plane 4A for $M_{\text{centerline}} = 0.50$ without inlet swirl

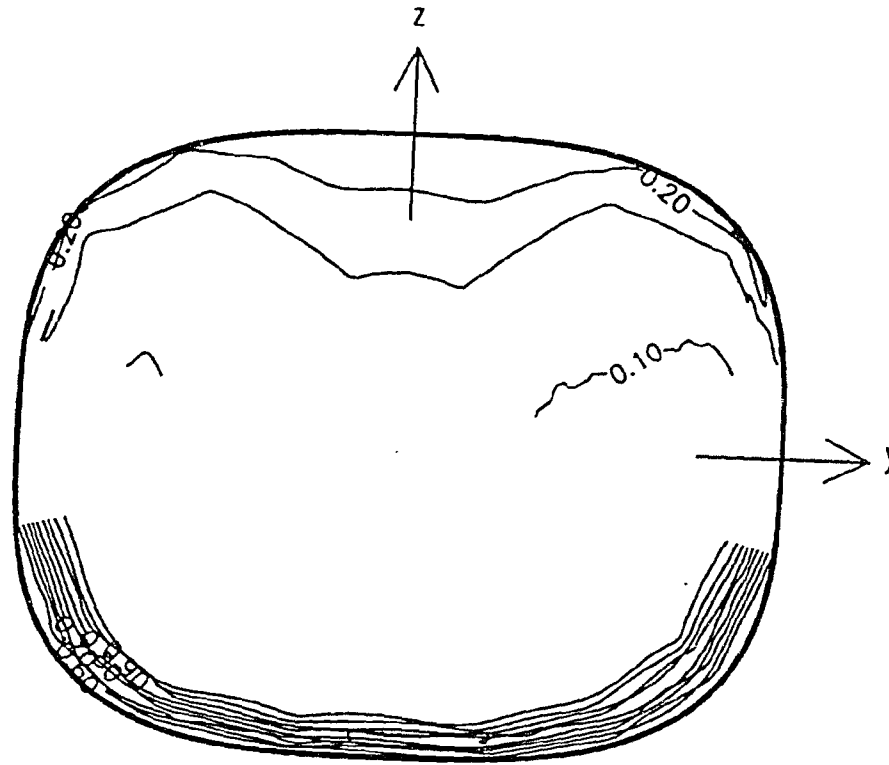


Figure V.38 Static pressure coefficient p^* (upper) and total pressure coefficient p_0^* (lower) distributions in plane 1A for $M_{\text{centerline}} = 0.50$ without inlet swirl

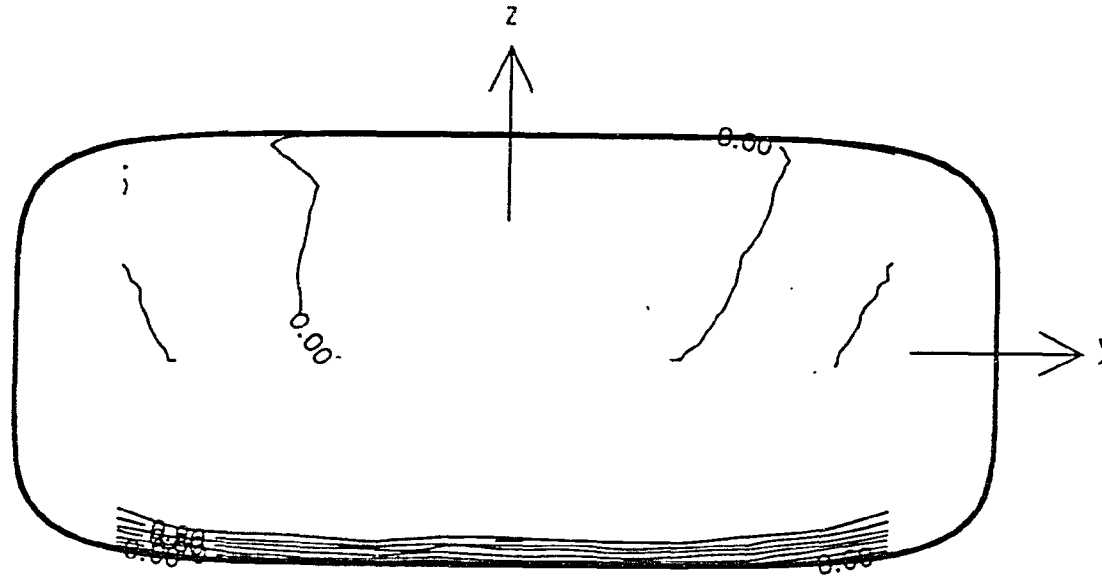


Figure V.39 Static pressure coefficient p^* (upper) and total pressure coefficient p_0^* (lower) distributions in plane 2A for $M_{\text{centerline}} = 0.50$ without inlet swirl

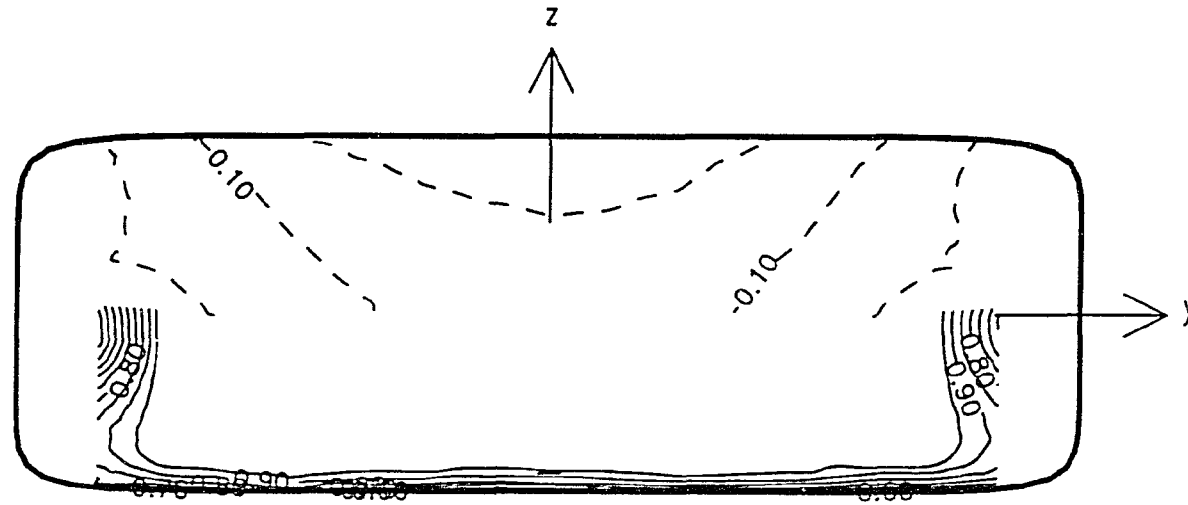


Figure V.40 Static pressure coefficient p^* (upper) and total pressure coefficient p_0^* (lower) distributions in plane 3A for $M_{\text{centerline}} = 0.50$ without inlet swirl

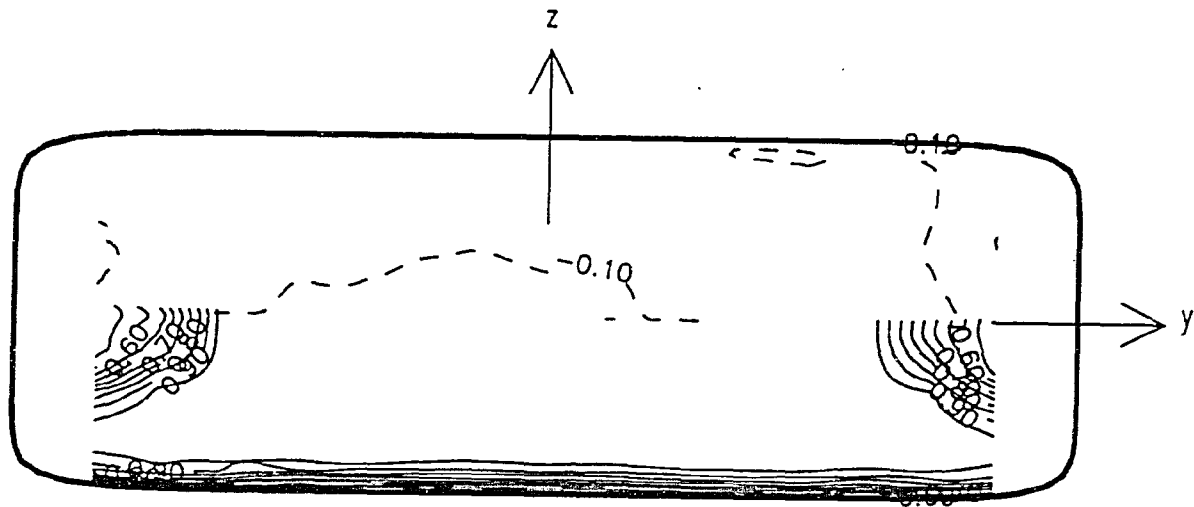


Figure V.41 Static pressure coefficient p^* (upper) and total pressure coefficient p_0^* (lower) distributions in plane 4A for $M_{\text{centerline}} = 0.50$ without inlet swirl

Figures V.26 through V.33 show results at $M_{\text{centerline}} = 0.35$, and Figures V.34 through V.41 show results at $M_{\text{centerline}} = 0.50$.

Figures V.18 through V.21, V.26 through V.29, and V.34 through V.37 show all three components of the velocity coefficient M^* . Vector plots of the transverse velocity coefficient components are shown in the lower half of the duct. In the upper half of the duct are contour plots of the magnitude of the axial velocity coefficient component. Beneath the duct in each figure is a vector labeled $M_{\text{centerline}}$. This is the reference length scale used for the vector plots of the transverse velocity coefficient components. The same reference length was used in all figures. This allows direct comparisons of the velocity coefficient components to be made between measurement planes.

Distributions of the total pressure coefficient p_0^* and the static pressure coefficient p^* are shown in Figures V.22 through V.25, V.30 through V.33, and V.38 through V.41. Drawn in the lower half of the duct are contour plots of total pressure coefficient. Contour plots of the static pressure coefficient are drawn in the upper half of the duct. The same contour levels are used in all cases. The dashed lines that appear in some static pressure coefficient contours indicate negative values.

In all cases the actual measurements were made in the lower half of the duct only, the data shown in the duct upper half are a rotation from the duct lower half.

The Transition Duct With Inlet Swirl

Surface oil film visualization and aerodynamic measurements were acquired for flow in the transition duct with inlet swirl. The aerodynamic measurements consist of surface static pressures and detailed aerodynamic surveys in four cross stream measurement planes. All transition duct measurements for the inlet swirl case were made at one condition, $M_{\text{centerline}} = 0.35$. The nonswirling flow aerodynamic data showed insignificant sensitivity to Mach number level within the range $0.20 \leq M_{\text{centerline}} \leq 0.50$ and Reynolds number within the range $918,000 \leq$

$Re \leq 2,086,000$. The locations of the surface static pressure measurements and the aerodynamic measurement planes are identical to those for the nonswirling aerodynamic measurements. Trace gas measurements were not repeated for the swirling flow case.

Surface oil film visualization

Figures V.43 and V.44 show the results of the surface oil film visualization tests for the transition duct flow with inlet swirl. The same procedures used to digitize and enhance the nonswirling surface oil film visualization photographs were applied to these results. A local coordinate system is shown to help establish the orientation of these photographs.

Aerodynamic measurements

Surface static pressure measurements In Figure V.42 the transition duct surface static pressure coefficients p^* distributed along the lower surface of the duct with inlet swirl are plotted with open symbols. The surface static pressure coefficients for flow without inlet swirl at the same centerline Mach number are also plotted for comparison. Shown as vertical broken lines are the locations of the four aerodynamic measurement planes. The solid symbols represent the centerline static pressure coefficients measured during the aerodynamic surveys.

Five-hole probe measurements The results of the aerodynamic surveys of the transition duct flow with inlet swirl are shown in Figures V.45 through V.52. The same conventions used in plotting the nonswirling results have been used in the figures for swirling flow. The velocity plots are shown in Figures V.45 through V.48, the total and static pressure plots are shown in Figures V.49 through V.52.

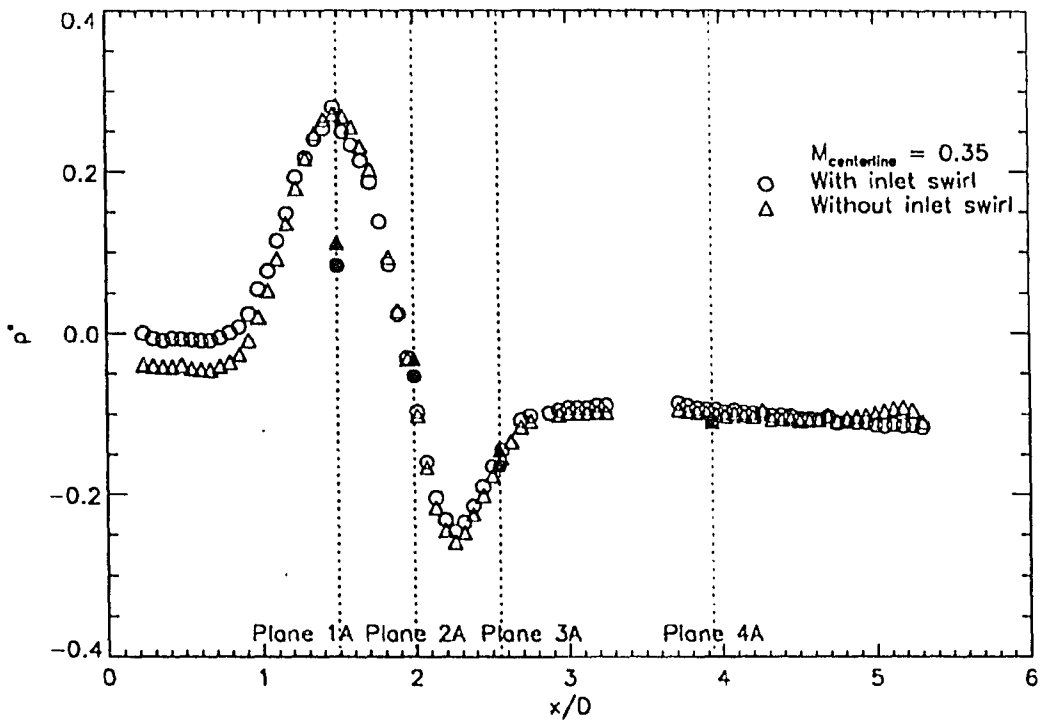


Figure V.42 Surface static pressure coefficient p^* for flow with and without inlet swirl

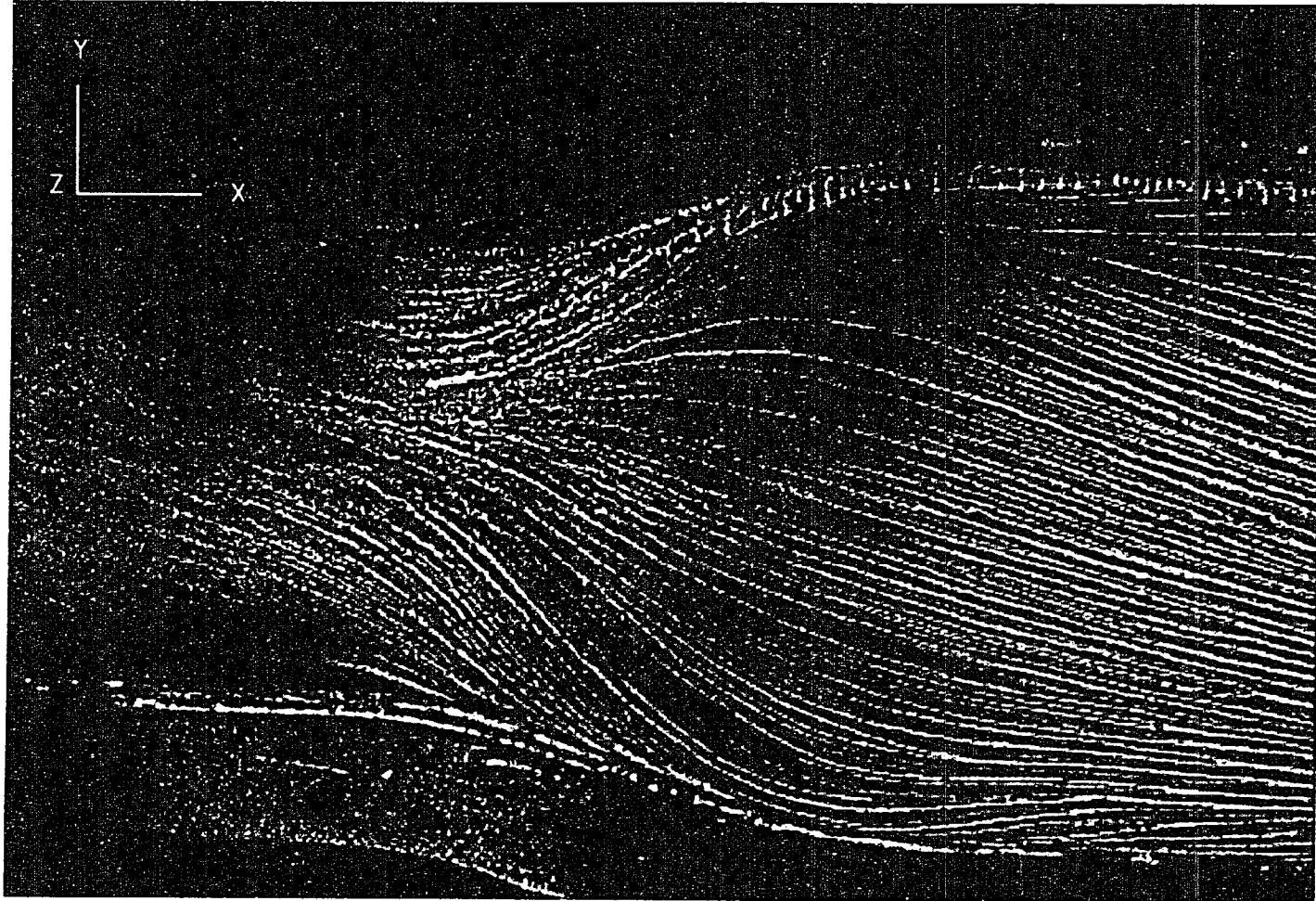


Figure V.43 Surface oil film visualization with inlet swirl

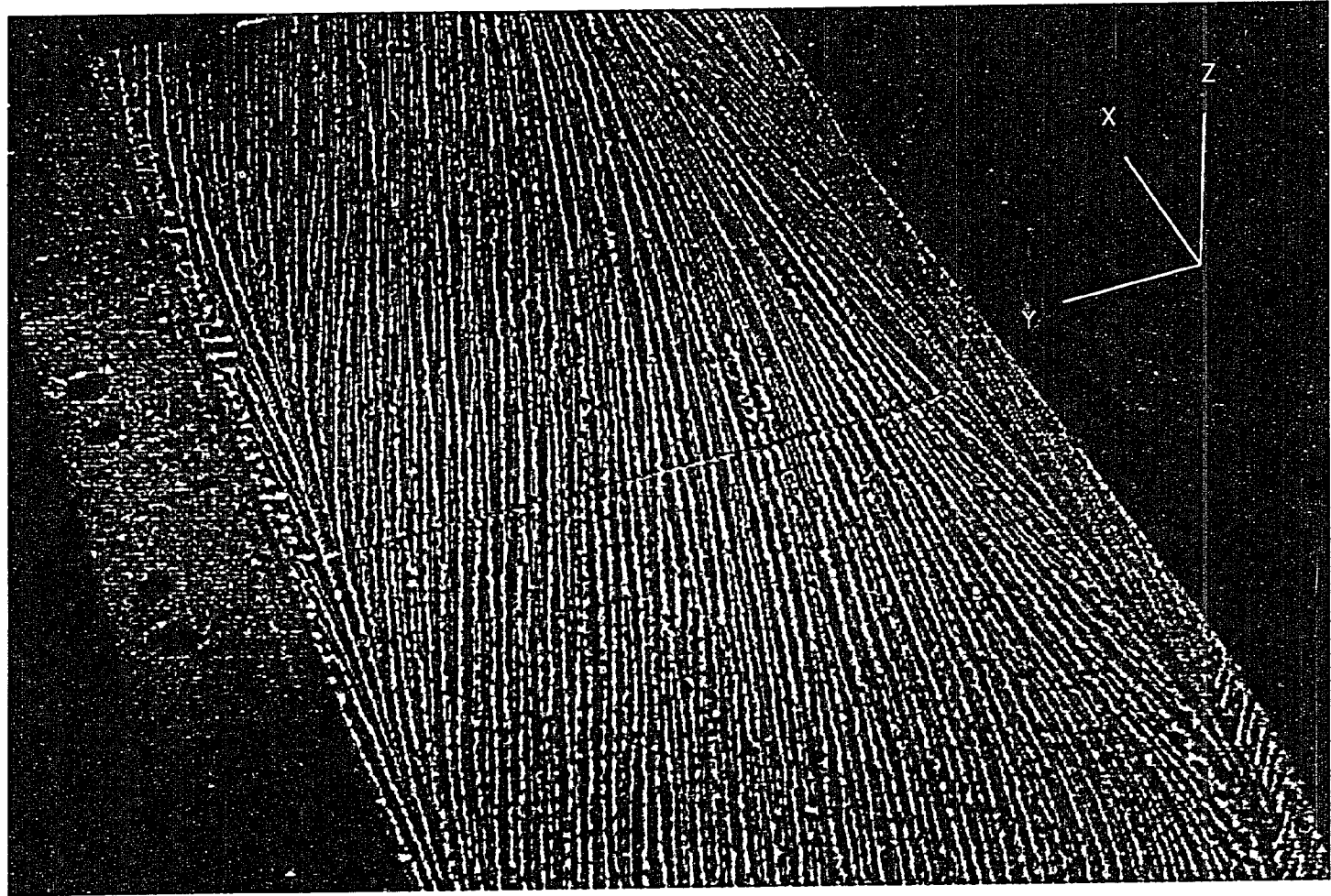


Figure V.44 Surface oil film visualization with inlet swirl

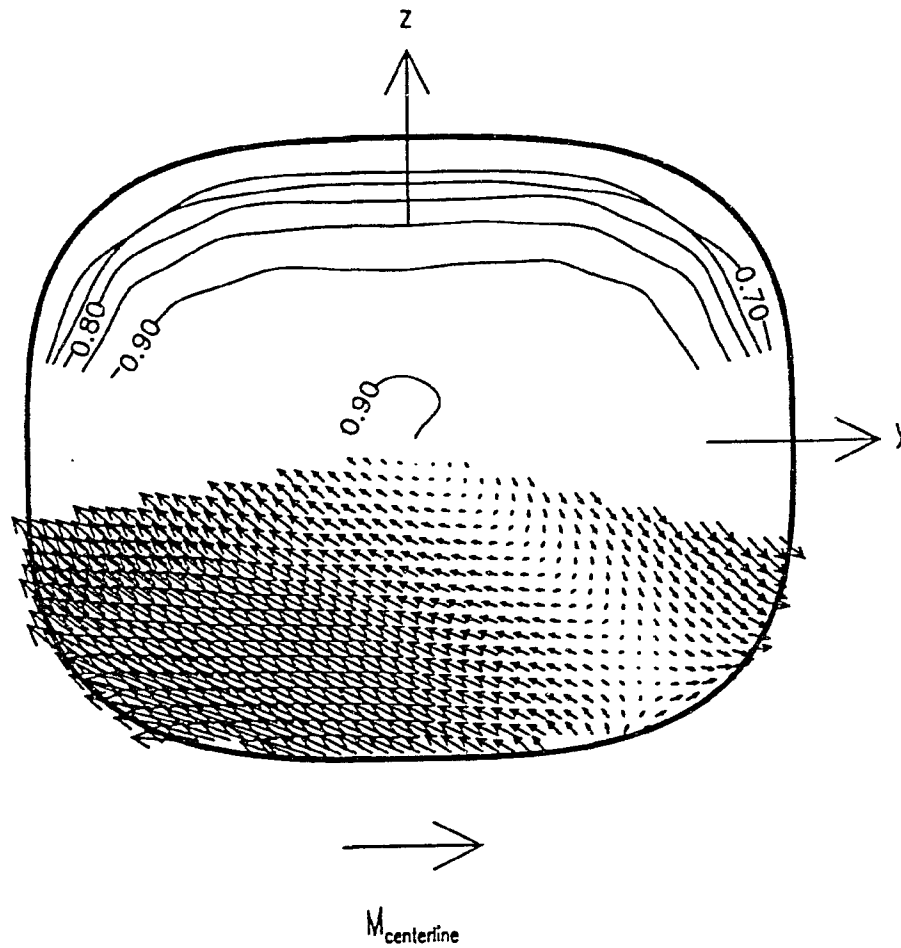


Figure V.45 Axial (upper) and transverse (lower) components of the velocity coefficient M^* in plane 1A for $M_{\text{centerline}} = 0.35$ with inlet swirl

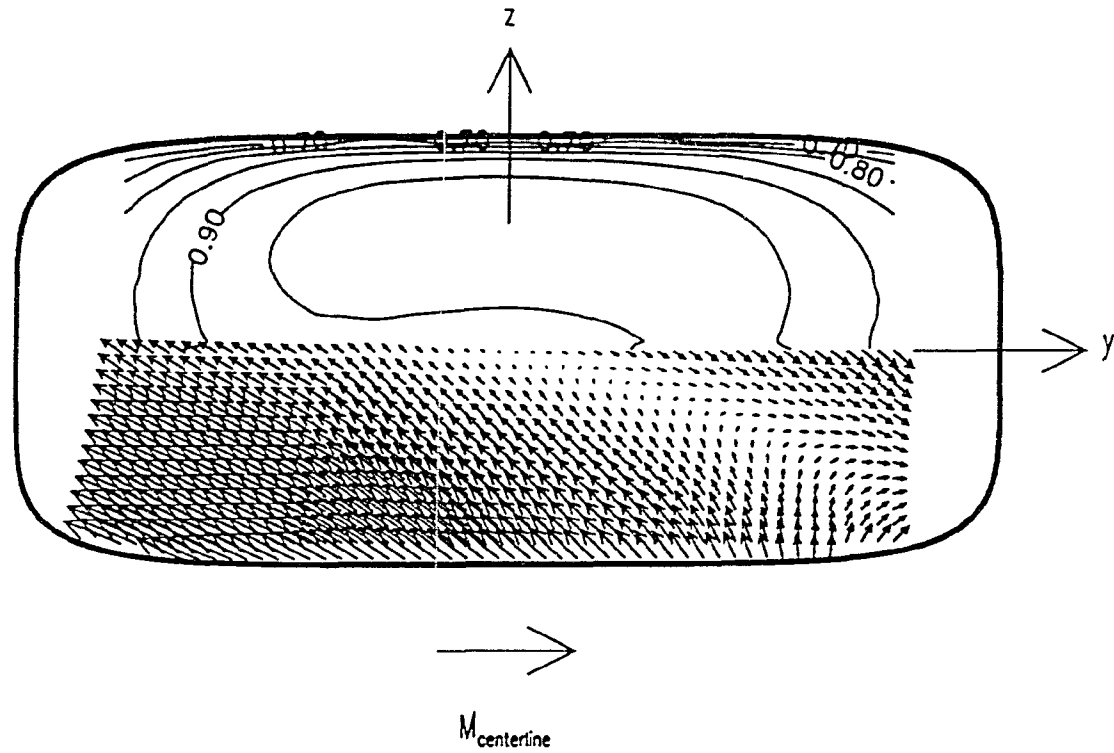


Figure V.46 Axial (upper) and transverse (lower) components of the velocity coefficient M^* in plane 2A for $M_{\text{centerline}} = 0.35$ with inlet swirl

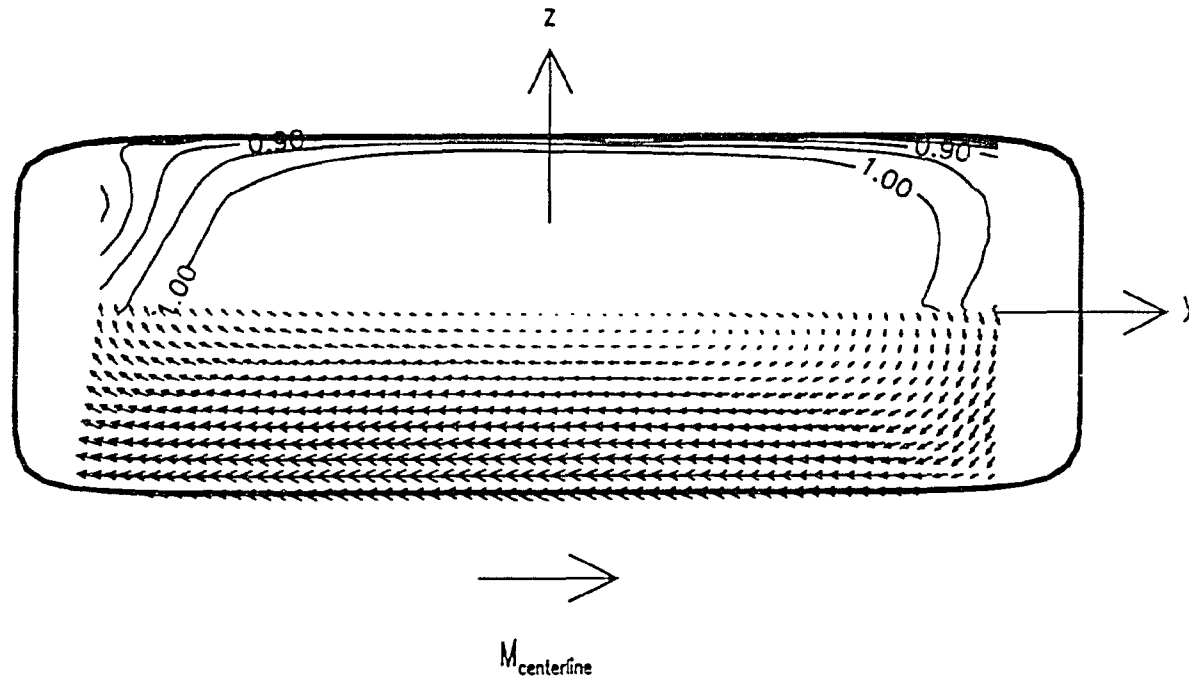


Figure V.47 Axial (upper) and transverse (lower) components of the velocity coefficient M^* in plane 3A for $M_{\text{centerline}} = 0.35$ with inlet swirl

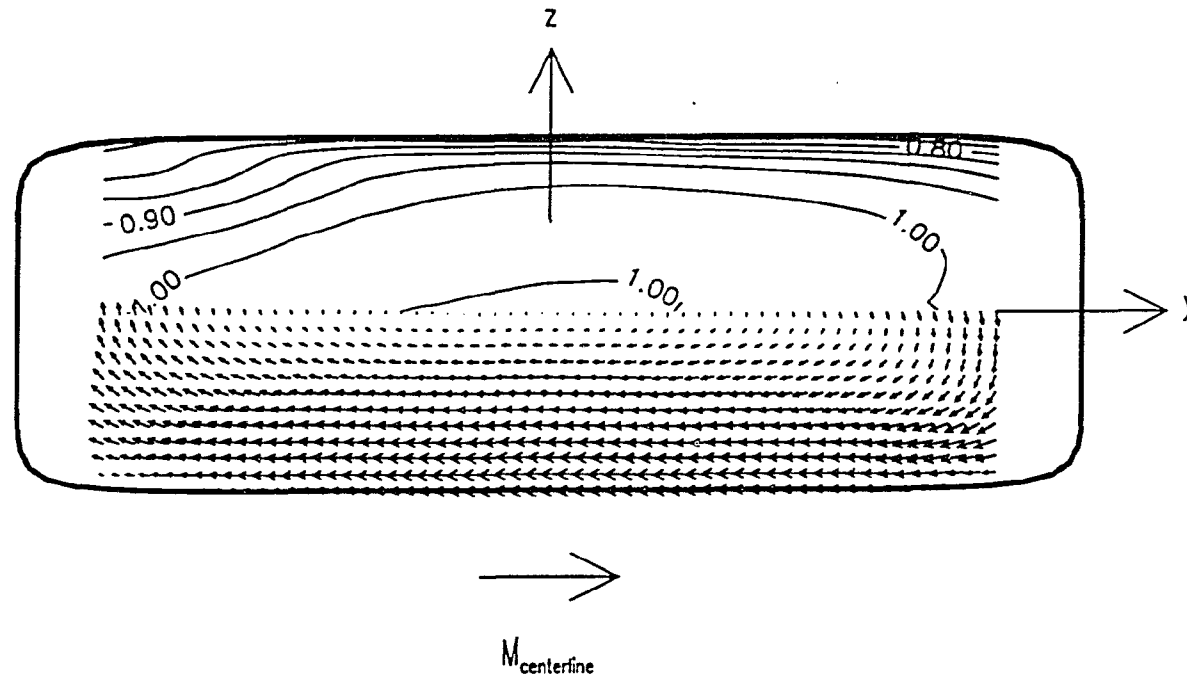


Figure V.48 Axial (upper) and transverse (lower) components of the velocity coefficient M^* in plane 4A for $M_{\text{centerline}} = 0.35$ with inlet swirl

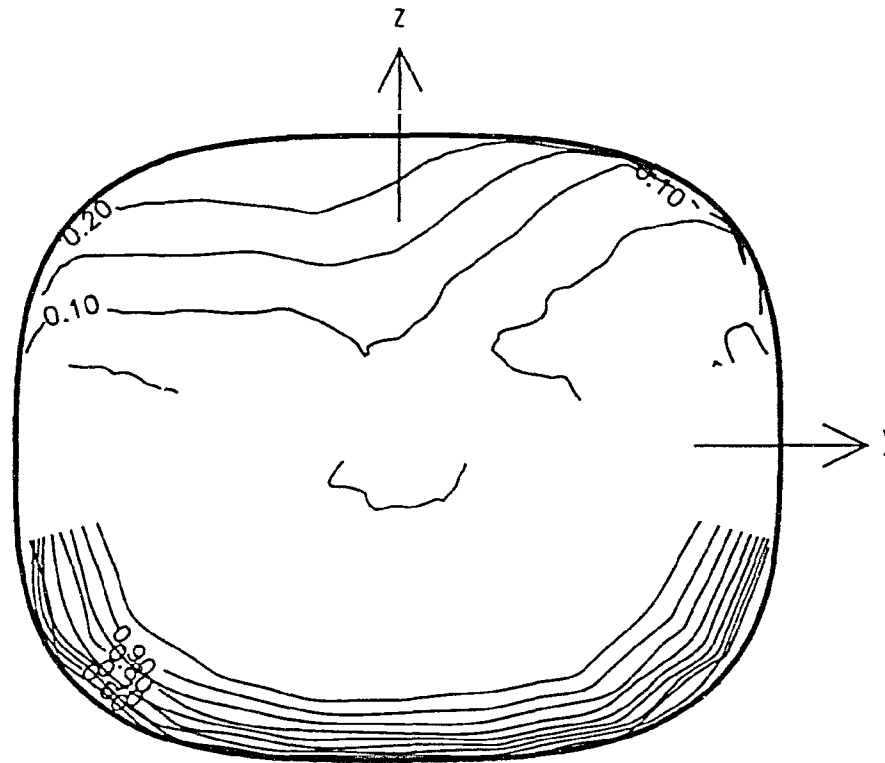


Figure V.49 Static pressure coefficient p^* (upper) and total pressure coefficient p_0^* (lower) distributions in plane 1A for $M_{\text{centerline}} = 0.35$ with inlet swirl

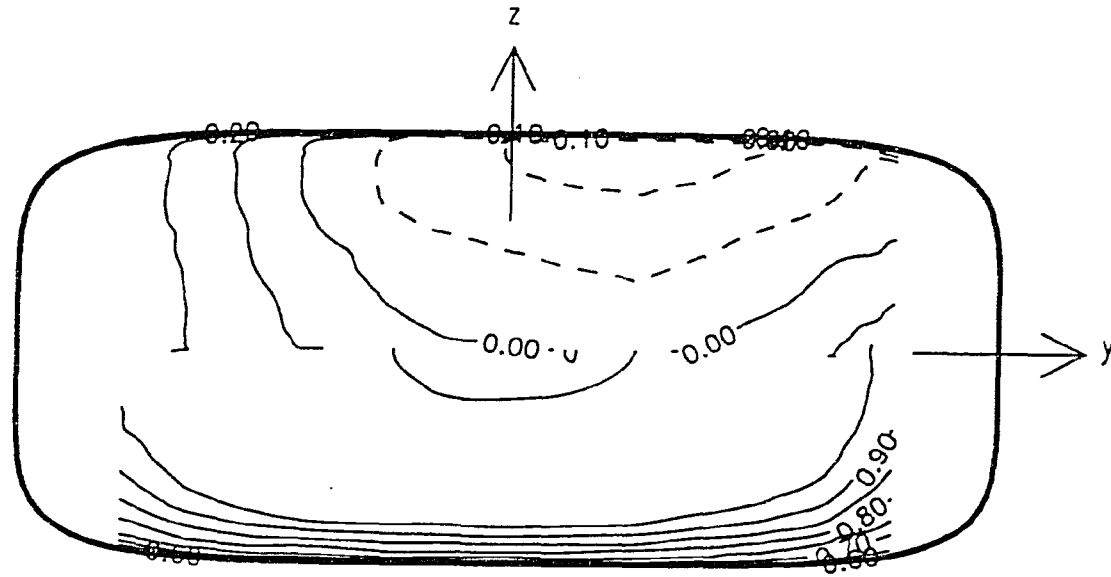


Figure V.50 Static pressure coefficient p^* (upper) and total pressure coefficient p_0^* (lower) distributions in plane 2A for $M_{\text{centerline}} = 0.35$ with inlet swirl

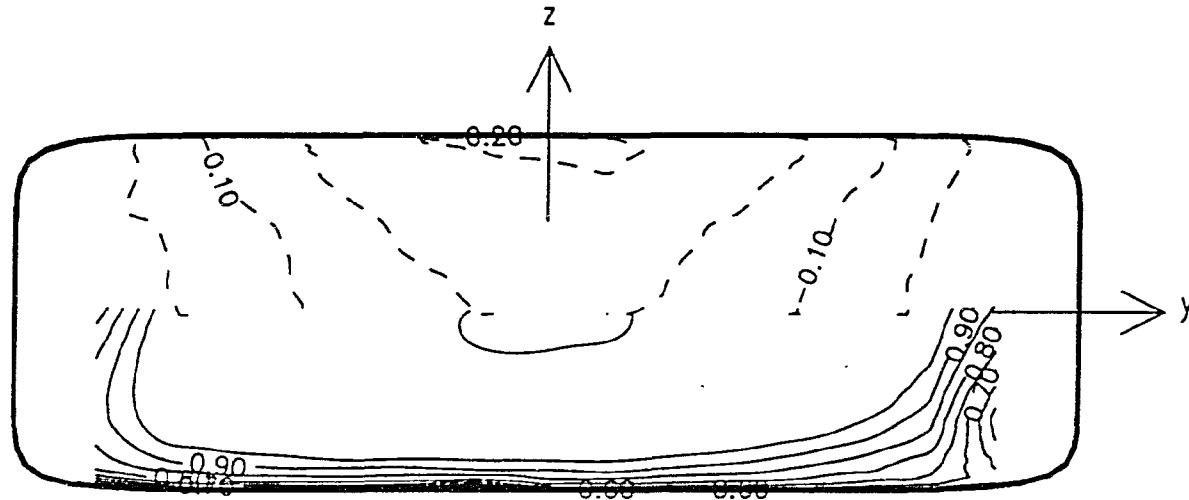


Figure V.51 Static pressure coefficient p^* (upper) and total pressure coefficient p_0^* (lower) distributions in plane 3A for $M_{\text{centerline}} = 0.35$ with inlet swirl

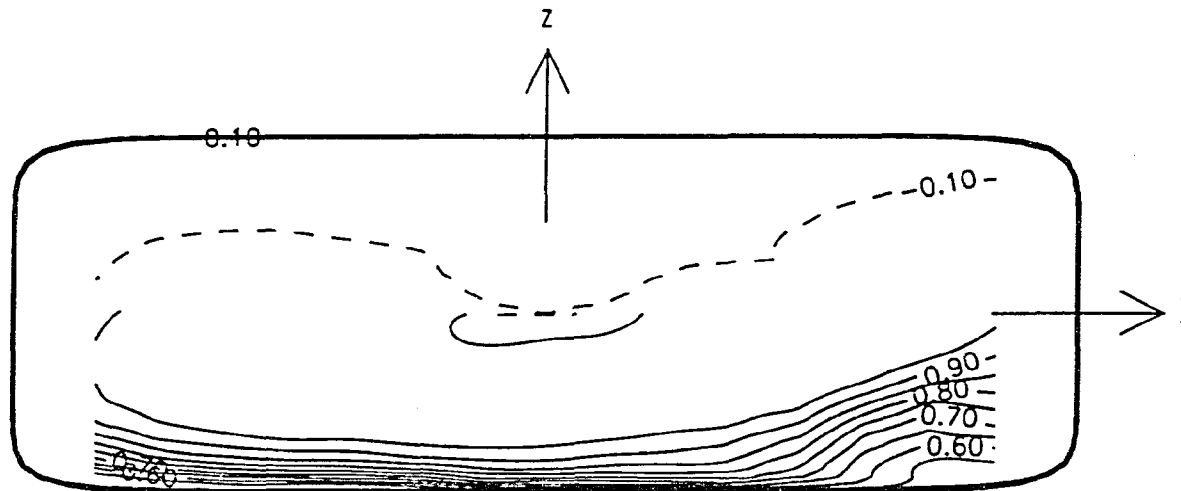


Figure V.52 Static pressure coefficient p^* (upper) and total pressure coefficient p_0^* (lower) distributions in plane 4A for $M_{\text{centerline}} = 0.35$ with inlet swirl

CHAPTER VI. ANALYSIS

This chapter discusses the results of the measurements of the transition duct flow field. The focus of the first section is an analysis of the trace gas results. The statistics of the trace gas concentration distributions are presented and discussed. The procedure used to calculate the trace gas statistics is described in Appendix C. Aerodynamic measurements of the transition duct flow without inlet swirl are used to help interpret the trace gas results. The second section concentrates on the aerodynamic measurements of the flow through the transition duct and a comparison of the flow field with and without inlet swirl. In this chapter the nondimensional quantities p_0^* , p^* , M^* and C^* are referred to simply as total pressure, static pressure, velocity and concentration.

Trace Gas Results

In a turbulent flow that is steady in the mean, the injection of trace gas will create a concentration field which itself is steady in the mean. Equation VI.1 governs the transport of trace gas in a turbulent incompressible flow. The left hand side of Equation VI.1 represents the convection of the mean concentration of trace gas by the mean flow, the first term on the right hand represents the molecular diffusion of the mean trace gas concentration, the second term represents the turbulent diffusion of the trace gas concentration.

$$\bar{U} \frac{\partial \bar{C}}{\partial x} + \bar{V} \frac{\partial \bar{C}}{\partial y} + \bar{W} \frac{\partial \bar{C}}{\partial z} = D_m \nabla^2 \bar{C} - \left(\frac{\partial(\overline{u'c'})}{\partial x} + \frac{\partial(\overline{v'c'})}{\partial y} + \frac{\partial(\overline{w'c'})}{\partial z} \right) \quad (\text{VI.1})$$

For engineering calculations, mixing length theory is commonly used to relate the turbulent diffusion of any quantity (e.g., mass, momentum, energy) to the gradient of the mean value of the quantity, as shown in Equation VI.2. This creates a turbulent diffusion term in Equation VI.1 that is similar to the molecular diffusion term. The

turbulent diffusivity coefficients are the product of a turbulent velocity and a turbulent mixing length, as shown in Equation VI.3. Often, the turbulent velocities are related to correlations of velocity fluctuations, which persist in the free stream, rather than gradients of the mean velocities, which vanish in the free stream. The mixing length is a measure of the distance a fluid particle travels before it interacts with the mean flow. In Equation VI.2, D_{ij} is a turbulence velocity and length scale correlation coefficient defined by Equation VI.3. This creates a second order tensor in the transport equation for the rate of turbulent diffusion, shown in Equation VI.4, written in index summation notation [64].

$$\overline{u'c'} = - \left(D_{xx} \frac{\partial \overline{C}}{\partial x} + D_{xy} \frac{\partial \overline{C}}{\partial y} + D_{xz} \frac{\partial \overline{C}}{\partial z} \right) \quad (\text{VI.2})$$

$$D_{ij} = \overline{u'_i l'_j} \quad (\text{VI.3})$$

$$\overline{U}_i \frac{\partial \overline{C}}{\partial x_i} = D_m \frac{\partial}{\partial x_i} \left(\frac{\partial \overline{C}}{\partial x_i} \right) + \frac{\partial}{\partial x_i} \left(D_{ij} \frac{\partial \overline{C}}{\partial x_j} \right) \quad (\text{VI.4})$$

When the trace gas technique is used to infer information about the flow field there is an ambiguity problem, referred to earlier in the literature review in Chapter II in the discussion of the paper by Wisler *et al.* [35]. The ambiguity problem arises when experimental measurements, which represent a solution to Equation VI.4 with a known boundary condition, are used to determine the coefficients of Equation VI.4, \overline{U}_i and D_{ij} , which are unknown. Although the solutions to Equation VI.4, with some restrictions on the coefficients and boundary conditions, are unique, Equation VI.4 with different coefficients and identical boundary conditions can give rise to identical solutions. The ambiguity problem is exacerbated by the fact that the experimental data are not known everywhere, but only at a finite number of locations where measurements are made. This makes it difficult to interpret trace gas results without either making some assumptions which simplify Equation VI.4, or supplementing the

trace gas data with additional information, or both. The supplemental information may be experimental data or numerical results.

For homogeneous turbulence, the turbulent diffusion tensor can be written in terms of a symmetric tensor. With the additional simplification of assuming the turbulence to be isotropic, the turbulent diffusion tensor reduces to a single turbulent diffusion coefficient D_t . Even when the turbulence is not homogenous and not isotropic, it is common in engineering calculations to use a single turbulent diffusion coefficient.

The mixing length theory of turbulence is analogous to the kinetic theory of gases where the molecular diffusivity coefficient is the product of velocity and length scales that govern molecular transport, the sonic velocity c , and the molecular mean free path λ . For molecular diffusion, the diffusivity coefficient is essentially constant throughout the flow field, however, for turbulent diffusion, the coefficient changes with location.

$$\frac{D_t}{D_m} \approx \frac{v_t l_t}{c \lambda} \quad (\text{VI.5})$$

The relative importance of turbulent and molecular diffusion is expressed as the ratio of the two diffusivity coefficients, which varies with location. An estimate of the magnitude of this ratio is given by Equation VI.5. In the free stream, the turbulent velocity and integral length scale were determined experimentally, and the ratio is approximately 180. By analogy with the turbulent viscosity coefficient, in the boundary layer this ratio increases across the wake region and then decreases across the overlap region, approaching zero at the wall [65]. This is adequate justification to neglect the molecular diffusion of trace gas in further analysis. Neglecting molecular diffusion and using a single turbulent diffusion parameter reduces Equation VI.4 to Equation VI.6.

$$\bar{U} \frac{\partial \bar{C}}{\partial x} + \bar{V} \frac{\partial \bar{C}}{\partial y} + \bar{W} \frac{\partial \bar{C}}{\partial z} = D_t \nabla^2 \bar{C} \quad (\text{VI.6})$$

Another assumption commonly used is to neglect diffusion in the streamwise direction. For the simple case of a uniform flow in the x direction, this changes Equation VI.6 from an elliptic to a parabolic partial differential equation, like the heat equation, where the x dimension corresponds to time in the heat equation.

The following analysis will consider one special case of the turbulent transport equation, when the molecular diffusion is negligible, the turbulent diffusion is homogeneous but not necessarily isotropic, the turbulent diffusion in the axial direction is negligible, and the mean flow is uniform and in the x direction. Under these restrictions, Equation VI.4 reduces to Equation VI.7. Without any loss in generality, it is assumed the y - and z -axis are coincident with the principal axis of the tensor D_{ij} , so that $D_{yz} = 0$.

$$\bar{U} \frac{\partial \bar{C}}{\partial x} = D_{yy} \frac{\partial^2 \bar{C}}{\partial y^2} + 2D_{yz} \frac{\partial}{\partial y} \left(\frac{\partial \bar{C}}{\partial z} \right) + D_{zz} \frac{\partial^2 \bar{C}}{\partial z^2} \quad (\text{VI.7})$$

$$\bar{C} = \frac{S\bar{U}}{4\pi x \sqrt{D_{yy}D_{zz}}} \exp -\frac{\bar{U}}{4x} \left(\frac{y^2}{D_{yy}} + \frac{z^2}{D_{zz}} \right) \quad (\text{VI.8})$$

$$\sigma_y^2 = \frac{D_{yy}2x}{\bar{U}} \quad \sigma_z^2 = \frac{D_{zz}2x}{\bar{U}} \quad (\text{VI.9})$$

For the case of a point source of trace gas located at the origin, the solution to Equation VI.7 is given by Equation VI.8. The variances of the solution are given by Equation VI.9, the covariance is zero because of the choice of axes. Although equation VI.7 appears simplified beyond the point of relevance, its solution provides some useful insight into interpreting the trace gas results. For this particular case:

1. The contours of the solution will always be concentric ellipses
2. The variances of the solution will always increase with axial distance
3. The area of the trace gas spreading can be estimated by Equation VI.10 which is the area of the ellipse defined by Equation VI.11

$$\pi \sqrt{\sigma_y^2 \sigma_z^2 - \sigma_{yz}^2} \quad (\text{VI.10})$$

$$\frac{y^2 \sigma_z^2}{\sigma_y^2 \sigma_z^2 - \sigma_{yz}^2} - \frac{2yz \sigma_{yz}}{\sigma_y^2 \sigma_z^2 - \sigma_{yz}^2} + \frac{z^2 \sigma_y^2}{\sigma_y^2 \sigma_z^2 - \sigma_{yz}^2} = 1 \quad (\text{VI.11})$$

For each of the 28 concentration distributions measured, the mean values, variances, and covariances of the concentration distributions were calculated. These values are presented in Tables VI.1 through VI.4. Also presented in these tables are the covariance correlation coefficient and an estimate of the spreading area. The statistics are useful to help quantify characteristics of the trace gas measurements, like the amount of trace gas spreading or the shape and orientation of the contours. The definition of these statistics and the numerical method used to calculate their values are described in Appendix C. All values in the tables are nondimensional.

The locations of the four cross stream measurements planes differed between the trace gas and aerodynamic measurements, as was described in Chapter IV. This was a result of the difference in hardware required for each method. The locations of the measurement planes for each method are summarized in Table VI.5.

It is useful to use the aerodynamic results to assist in interpreting the trace gas data when possible. The location of trace gas plane 3T and aerodynamic plane 2A are identical. Figure VI.2 shows the transverse velocity components from aerodynamic plane 2A superimposed over the results from trace gas plane 3T. Trace gas plane 2T and aerodynamic plane 1A are near enough that it is reasonable to superimpose the transverse velocity components from aerodynamic plane 1A and contours from trace gas plane 2T. This is shown in Figure VI.1. Trace gas plane 4T lies between aerodynamic planes 3A and 4A. These planes are located in the constant cross section region of the duct. Gradients in the axial direction are small enough that it is reasonable to interpolate aerodynamic measurements between planes 3A and 4A to compare with the trace gas measurements at plane 4T. This result is shown in Figure

Table VI.1 Plane 1T trace gas concentration distribution statistics

Injection location		Peak value location		Mean value location		Variance			Correlation	Area estimate
$\frac{y}{D}$	$\frac{z}{D}$	$\frac{y}{D}$	$\frac{y}{D}$	$\frac{\mu_y}{D}$	$\frac{\mu_z}{D}$	$\frac{\sigma_y^2}{D^2}$	$\frac{\sigma_{yz}}{D^2}$	$\frac{\sigma_z^2}{D^2}$	$\frac{\sigma_{yz}}{\sigma_y\sigma_z}$	$\frac{\pi}{D^2} \sqrt{\sigma_y^2\sigma_z^2 - \sigma_{yz}^2}$
(×100)	(×100)	(×100)	(×100)	(×100)	(×100)	(×10 ⁴)	(×10 ⁴)	(×10 ⁴)	(×100)	(×10 ⁴)
0.0	0.0	0.0	0.1	-0.1	0.4	2.2	0.0	3.2	1.7	8.3
0.0	24.9	-0.1	25.7	-0.2	25.3	2.1	0.2	3.5	8.9	8.4
0.0	49.8	-0.1	49.4	-0.1	47.3	6.2	-0.1	2.5	-3.7	12.3
-21.5	12.4	-21.7	12.1	-21.4	12.6	3.9	-0.6	1.8	-21.4	8.2
-43.0	24.9	-42.1	24.1	-39.6	23.4	4.1	1.0	5.5	20.1	14.7
21.5	12.4	21.8	12.5	21.4	12.4	3.0	0.9	3.0	29.7	8.9
43.0	24.9	42.2	24.7	40.3	23.2	3.9	-0.8	4.8	-18.5	13.4

Table VI.2 Plane 2T trace gas concentration distribution statistics

Injection location		Peak value location		Mean value location		Variance			Correlation	Area estimate
$\frac{y}{D}$	$\frac{z}{D}$	$\frac{y}{D}$	$\frac{z}{D}$	$\frac{\mu_y}{D}$	$\frac{\mu_z}{D}$	$\frac{\sigma_y^2}{D^2}$	$\frac{\sigma_{yz}}{D^2}$	$\frac{\sigma_z^2}{D^2}$	$\frac{\sigma_{yz}}{\sigma_y\sigma_z}$	$\frac{\pi}{D^2} \sqrt{\sigma_y^2\sigma_z^2 - \sigma_{yz}^2}$
(×100)	(×100)	(×100)	(×100)	(×100)	(×100)	(×10 ⁴)	(×10 ⁴)	(×10 ⁴)	(×100)	(×10 ⁴)
0.0	0.0	0.0	1.2	-0.2	1.2	2.8	0.4	2.5	16.1	8.3
0.0	24.9	0.0	23.9	-0.4	24.3	3.3	0.2	2.5	8.0	9.0
0.0	49.8	0.0	44.1	-0.2	42.4	23.3	-0.3	2.3	-4.6	22.8
-21.5	12.4	-25.8	11.6	-25.7	12.1	3.2	-0.6	2.6	-21.3	8.8
-43.0	24.9	-46.6	21.9	-46.6	23.0	6.9	2.6	7.1	36.5	20.5
21.5	12.4	25.6	12.7	25.6	12.7	3.0	0.8	2.4	31.5	8.0
43.0	24.9	49.9	21.6	46.3	22.9	6.9	-2.4	6.9	-35.5	20.3

Table VI.3 Plane 3T trace gas concentration distribution statistics

Injection location		Peak value location		Mean value location		Variance			Correlation	Area estimate
$\frac{y}{D}$	$\frac{z}{D}$	$\frac{y}{D}$	$\frac{z}{D}$	$\frac{\mu_y}{D}$	$\frac{\mu_z}{D}$	$\frac{\sigma_y^2}{D^2}$	$\frac{\sigma_{yz}}{D^2}$	$\frac{\sigma_z^2}{D^2}$	$\frac{\sigma_{yz}}{\sigma_y\sigma_z}$	$\frac{\pi}{D^2} \sqrt{\sigma_y^2\sigma_z^2 - \sigma_{yz}^2}$
($\times 100$)	($\times 100$)	($\times 100$)	($\times 100$)	($\times 100$)	($\times 100$)	($\times 10^4$)	($\times 10^4$)	($\times 10^4$)	($\times 100$)	($\times 10^4$)
0.0	0.0	0.0	0.7	0.0	0.4	5.3	0.3	1.8	8.5	9.6
0.0	24.9	0.0	15.9	0.0	16.5	5.6	-0.1	2.0	-1.8	10.4
0.0	49.8	0.0	28.4	-0.4	26.9	40.3	0.1	1.5	1.0	24.6
-21.5	12.4	-32.2	9.7	-32.0	9.5	5.3	-1.0	2.2	-29.6	10.3
-43.0	24.9	-62.4	17.1	-61.2	15.9	17.8	12.4	25.9	57.9	55.0
21.5	12.4	32.2	9.4	32.5	9.4	5.9	0.6	1.8	19.3	10.2
43.0	24.9	62.5	17.2	62.9	14.5	17.3	-13.3	25.1	-63.9	50.4

Table VI.4 Plane 4T trace gas concentration distribution statistics

Injection location		Peak value location		Mean value location		Variance			Correlation	Area estimate
$\frac{y}{D}$	$\frac{z}{D}$	$\frac{y}{D}$	$\frac{z}{D}$	$\frac{\mu_y}{D}$	$\frac{\mu_z}{D}$	$\frac{\sigma_y^2}{D^2}$	$\frac{\sigma_{yz}}{D^2}$	$\frac{\sigma_z^2}{D^2}$	$\frac{\sigma_{yz}}{\sigma_y\sigma_z}$	$\frac{\pi}{D^2}\sqrt{\sigma_y^2\sigma_z^2 - \sigma_{yz}^2}$
($\times 100$)	($\times 100$)	($\times 100$)	($\times 100$)	($\times 100$)	($\times 100$)	($\times 10^4$)	($\times 10^4$)	($\times 10^4$)	($\times 100$)	($\times 10^4$)
0.0	0.0	0.1	-0.1	0.4	0.2	7.4	0.0	3.0	0.9	14.8
0.0	24.9	1.5	11.8	0.5	13.0	9.9	-0.1	4.9	-1.2	21.8
0.0	49.8	0.0	25.0	-0.3	22.4	50.7	0.0	4.7	-0.1	48.7
-21.5	12.4	-40.8	8.2	-39.9	8.2	8.4	-1.4	3.3	-27.7	15.8
-43.0	24.9	-72.7	12.8	-69.0	9.7	24.1	-5.4	55.1	-14.9	113.2
21.5	12.4	38.3	8.1	38.2	8.7	8.2	1.7	3.5	31.0	16.0
43.0	24.9	72.6	14.9	69.1	9.9	25.0	5.1	53.8	13.8	114.2

Table VI.5 Location of trace gas and aerodynamic measurement planes

Trace gas measurements		Aerodynamic measurements	
Plane	$\frac{x}{D}$	Plane	$\frac{x}{D}$
1T	0.97	1A	1.49
2T	1.43	2A	1.99
3T	1.99	3A	2.55
4T	3.36	4A	3.93

VI.3. No comparison of trace gas measurements with aerodynamic measurements is possible at trace gas plane 1T.

For trace gas injected at the transition duct centerline, $y/D = 0.0$ $z/D = 0.0$, the covariance remained relatively small along the length of the duct. This indicates that the turbulence field is symmetric along the duct centerline. These trace gas contours became increasingly elongated in the y direction at downstream locations. This can be seen in the ratio of σ_y^2 to σ_z^2 . Two possible explanations for this are either the turbulence is anisotropic, that is $\sqrt{v'^2} > \sqrt{w'^2}$ or the concentration distribution is being affected by the transverse components of velocity. Two experimental facts suggest that the elongation is produced by the transverse velocity components. First, the value of σ_z^2 is decreasing from plane 1T to plane 3T and then increases from plane 3T to plane 4T. It would be impossible for σ_z^2 to decrease by turbulent diffusion alone in a uniform flow field. Second, velocity measurements show flow converging in the xz -plane and diverging in the xy -plane. The region of decreasing σ_z^2 corresponds to the region where transverse velocity components are greatest. This can be seen in Figures VI.1 and VI.2. At plane 4T, Figure VI.3, the transverse velocity components near the centerline are negligible and σ_z^2 has increased between planes 3T and 4T.

For trace gas injected at $y/D = 0.000$ $z/D = 0.249$ (12 o'clock, halfway between the duct centerline and the wall) the results are statistically similar to the results for trace gas injected at $y/D = 0.000$ $z/D = 0.000$. However, at planes 3T and 4T the

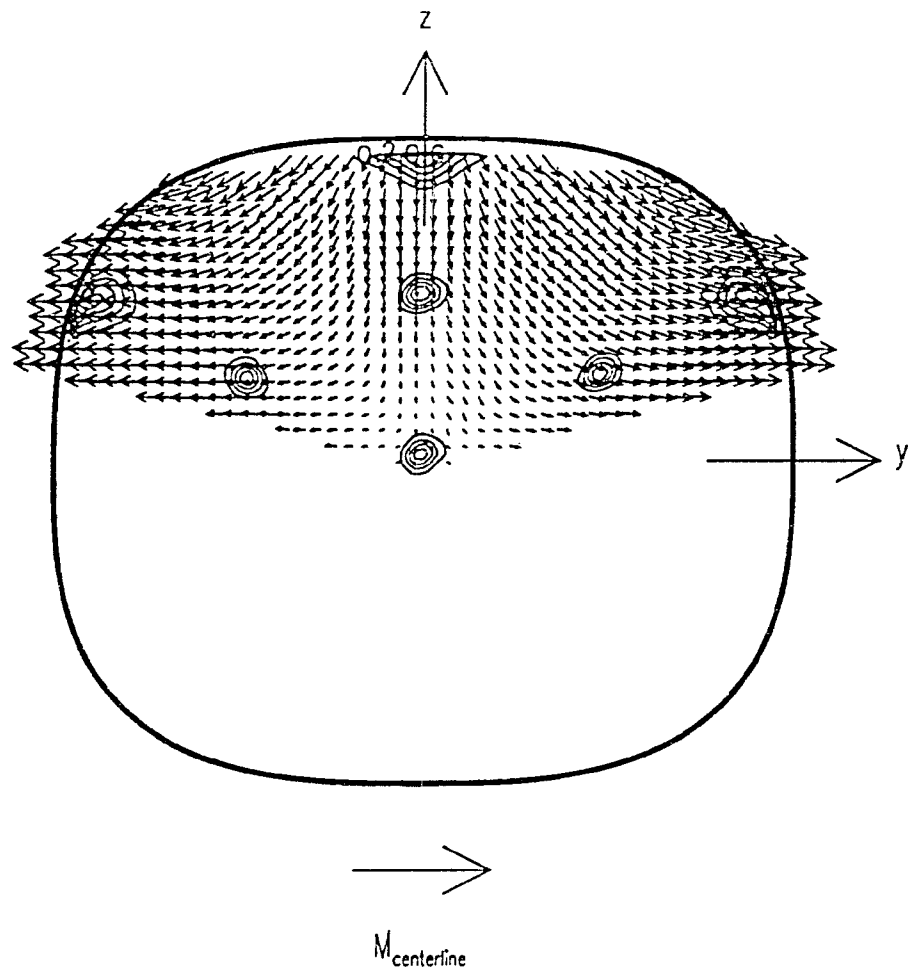


Figure VI.1 Ethylene concentration distributions with transverse velocity components at plane 2T.

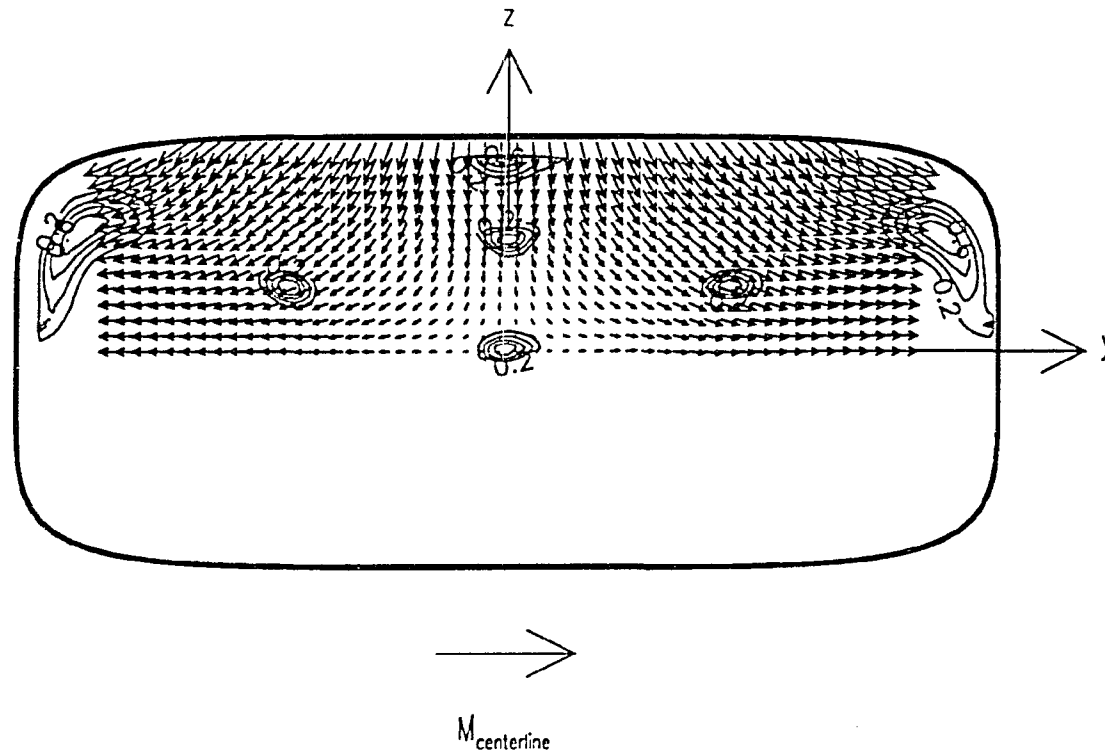


Figure VI.2 Ethylene concentration distributions with transverse velocity components at plane 3T.

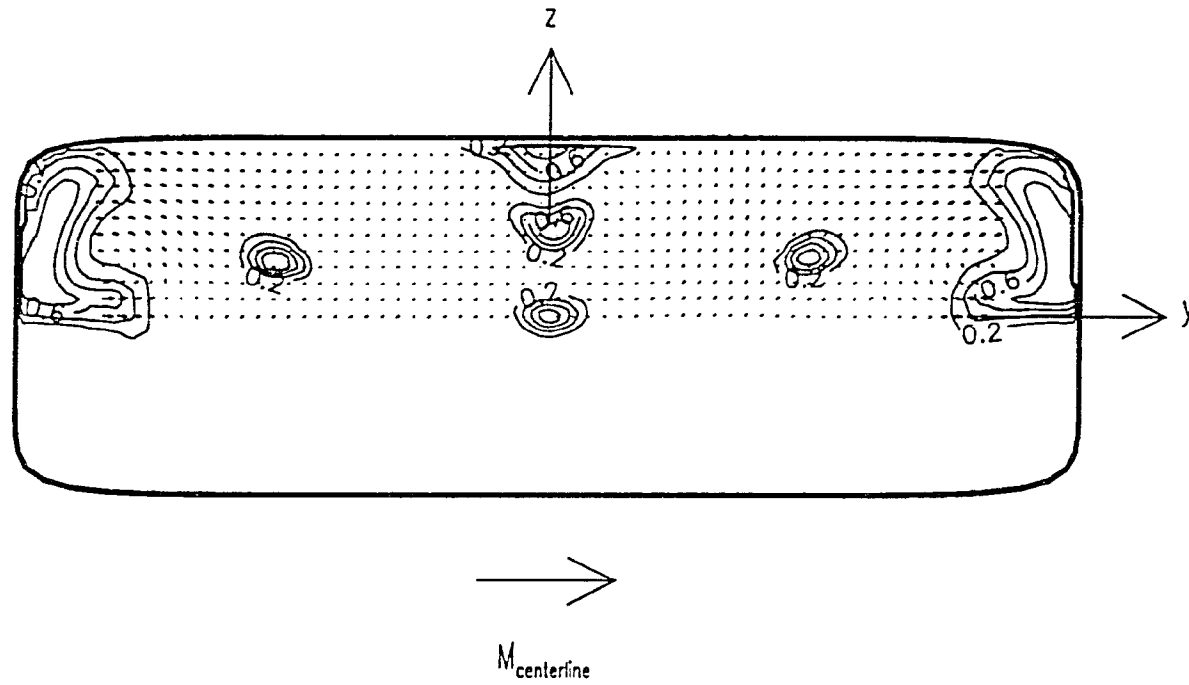


Figure VI.3 Ethylene concentration distributions with transverse velocity components at plane 4T.

contour shapes appear to be noticeably different. The contour shapes are no longer elliptic, rather they are bean shaped, having only one plane of symmetry. The simple model of homogeneous turbulence in a uniform mean flow allows only elliptic shaped contours, which would indicate the contours result from turbulence inhomogeneity, or from nonuniformity in the mean flow. The mean flow certainly is nonuniform. However, there is nothing to indicate the turbulence is not homogeneous. Thus, the bean shape of the contours probably results from transverse velocity components. Also, the amount of spreading is approximately the same as for trace gas injected at $y/D = 0.000$ $z/D = 0.000$ which indicates roughly the same turbulence conditions.

For trace gas injected at $y/D = 0.000$ $z/D = 0.498$ (12 o'clock, near the duct wall) the statistics of the measurements indicate a very large elongation in the y direction. The results of Klebanoff [65] show that the magnitude of the transverse turbulent velocity fluctuations, and turbulent viscosity coefficient, increase greatly in a turbulent boundary layer. In a turbulent boundary layer the turbulence is very inhomogeneous. The turbulence decreases rapidly away from the duct surface, in this case the z direction, while retaining its magnitude in directions parallel to the wall, specifically the y direction. This should lead to preferential diffusion in the y direction. However, turbulent diffusion alone is not exclusively responsible for the observed contours because σ_z^2 again decreases from plane 1T to plane 3T. The total amount of spreading is roughly twice that observed of trace gas injected at $y/D = 0.000$ $z/D = 0.000$ and $y/D = 0.000$ $z/D = 0.249$. It appears that both turbulent diffusion and transverse velocities are responsible for the large transport of trace gas in the y direction displayed by the contours.

For trace gas injected at $y/D = -0.215$ $z/D = 0.124$ and $y/D = 0.215$ $z/D = 0.124$ (about 10 and 2 o'clock, between the duct centerline and wall) the amount of spreading at each of the four planes is comparable to the spreading of trace gas injected at $y/D = 0.000$ $z/D = 0.000$ and $y/D = 0.000$ $z/D = 0.249$. This indicates that in the free stream the turbulence is nominally homogeneous. Each contour becomes

more elongated as it travels downstream. Unlike the results for trace gas injected at $y/D = 0.000$ $z/D = 0.000$ and $y/D = 0.000$ $z/D = 0.249$, the contours change their orientation. This can be observed in the covariance values or the correlation coefficient. The major axis of the contours are no longer parallel to the y -axis, but are inclined to the y -axis. This probably results from the transverse velocities.

Trace gas injected at $y/D = -0.430$ $z/D = 0.249$ and $y/D = 0.430$ $z/D = 0.249$ (about 10 o'clock and 2 o'clock, near the duct wall) produced the most interesting results. At planes 1T and 2T the statistics are nearly identical to the statistics for trace gas injected at $y/D = 0.000$ $z/D = 0.498$, except for the orientation. At plane 2T, however, the contours appear visibly different, assuming a cusped teardrop shape. At plane 3T the statistics differ significantly from the statistics of trace gas injected at $y/D = 0.000$ $z/D = 0.498$. The spreading was approximately twice as great. This probably resulted from the transfer of boundary layer fluid, with its greater turbulence intensity and diffusivity, over a large area near the side walls by the axial vortices. At plane 4T the much greater spreading is obvious. The unusual shape results from vortices near the transition duct side wall, which are discussed in the following section.

Aerodynamic Results

Flow without inlet swirl

The distribution of static pressures in the transition duct flow was generally attributed to the response of the flow field outside the boundary layer to the changing duct geometry. The change in cross section of the duct requires the flow to converge in the xz -plane and diverge in the xy -plane. The duct wall deflected the incoming flow, initially parallel to the x -axis, away from the x -axis in the xy -plane and towards the x -axis in the xz -plane. For the duct flow without inlet swirl, the curved streamlines initially generate a saddle-shaped static pressure distribution in the yz -plane, with minimum static pressures near either end of the y -axis and maximum static pressures

near either end of the z -axis. This static pressure distribution can be seen at plane 1A, shown in Figures V.19, V.27, and V.35. The maximum pressures are also observable as the maximum value that appear in the surface static pressure plot shown in Figure V.14.

Another saddle-shaped static pressure distribution in the yz -plane was developed further downstream by curved streamlines when the flow was forced by the duct wall back to a direction that is nominally parallel to the x -axis in the constant cross section region following the transition region. This static pressure distribution involved maximum static pressures near either end of the y -axis and minimum static pressures near either end of the z -axis. Evidence of this distribution can be seen in the static pressure distributions at plane 3A, shown in Figures V.21, V.29, and V.37 and as the minimum value of the surface static pressure plot shown in Figure V.14. Miao *et al.* [16, 17] and Davis and Gessner [18] also observed this reversal of the static pressure distribution in their surface static pressure measurements.

The location of the maximum and minimum static pressures were reversed between planes 1A and 3A by the change in streamline curvature between these planes. In order to affect this reversal of static pressure, there must be an intermediate location where the static pressure distribution in the yz -plane is nominally flat. The results show the intermediate location must be between planes 1A, at $x/D = 1.49$, and 2A, at $x/D = 1.99$. The static pressure distribution at plane 2A, shown in Figures V.20, V.28 and V.36, already shows the reversal of the location of the maximum and minimum static pressures, although the gradients are less than those observed at plane 3A. The surface static pressure measurements made along axial cross sections in an identical duct by Davis and Gessner [18] show that the reversal occurs between $x/D = 1.60$ and $x/D = 1.90$. The overall level of static pressure was higher at planes 1A and 2A because of the increase in cross-sectional area at these measurement planes.

The static pressure distribution at plane 4A, shown in Figures V.22, V.30 and V.38, is nominally flat. The slight gradients observed in the static pressure distribution

probably resulted from the upstream influence of the discharge plenum at the transition duct exit, which was an abrupt enlargement.

Because the static pressure distribution was established by the flow field outside the boundary layer where the momentum is greatest, the resulting static pressure distribution can produce significant turning of the flow within the boundary layer where the momentum is less. This is the source of skew-induced secondary flow referred to by Bradshaw [66]. This can be seen in Figures V.16, V.24 and V.32, where the greatest transverse velocity components appear near the duct surface towards the side walls.

The explanation of skew-induced secondary flows in the preceding paragraph has its foundation in the vorticity transport equation. The x component of the vorticity transport equation, neglecting viscous and Reynolds stress terms, is given by Equation VI.12. The first term in the right hand side of Equation VI.12 is referred to as the vortex stretching term, the next two terms are referred to as the vortex tilting terms.

$$\frac{D\omega_x}{Dt} = \omega_x \frac{\partial U}{\partial x} + \omega_y \frac{\partial U}{\partial y} + \omega_z \frac{\partial U}{\partial z} \quad (\text{VI.12})$$

Consider aside from the transition duct flow the idealized case of a simple boundary layer in the xz -plane, $U(y)$, $V = 0$, $W = 0$, with a cross stream pressure gradient, $\frac{\partial p}{\partial x} = \frac{\partial p}{\partial y} = 0$, $\frac{\partial p}{\partial z} \neq 0$, Equation VI.12 reduces to VI.13. The right hand side of Equation VI.13 arises from the second term of the right hand side of Equation VI.12.

$$U \frac{\partial \omega_x}{\partial x} = \frac{1}{\rho U} \frac{\partial p}{\partial z} \frac{\partial U}{\partial y} \quad (\text{VI.13})$$

The outward directed flow in the boundary layer near the side walls seen in the transverse velocity plots at planes 1A and 2A was the genesis of the two pair of counter-rotating side wall vortices that were clearly present at planes 3A and 4A. Although the static pressure distribution reversed orientation between planes 1A and 2A, the second static pressure distribution failed to completely reverse the secondary fluid motion initiated by the first static pressure distribution. This is so because the

outward directed flow in the boundary layer near the side walls followed the duct surface around the corner and was redirected inwards along the side walls before the static pressure distribution had reversed its orientation. This can be seen in the surface oil film visualization results, Figure V.9. Along the side wall the flow is now approaching the xy -plane from top and bottom. Continuity forces the converging flow outward away from the side walls and the vortex pattern was established. The reversal in the orientation of the static pressure distribution only drove the vortices further away from the side walls. This can be seen by comparing the plots of transverse velocity components at planes 3A and 4A.

Davis and Gessner [18] observed nearly identical behavior in the transverse velocity in their measurement planes downstream of the transition region in an identical transition duct. Patrick and McCormick [14, 15] observed similar side wall vortices at the exit plane of their aspect ratio six duct. The side wall vortices were not apparent at the exit plane of their aspect ratio three duct, although outward directed flow in the boundary layer near the side walls, which gives rise to axial vorticity, was observed at the exit plane. Miao *et al.* [16, 17] observed axial vorticity near the exit plane of their aspect ratio two transition duct which is opposite in sign to the dominant side wall vortices seen in Figures V.18, V.26 and V.34.

Figures VI.4 through VI.7 show contours of axial vorticity in the upper half of the transition duct cross section for flow without inlet swirl. The axial vorticity was calculated from a finite difference approximation using the transverse velocity components which are shown in the lower half of the cross section. Positive vorticity (counter clockwise) is represented by solid lines, negative vorticity (clockwise) is represented by broken lines.

In Figure VI.4, at plane 1A, the initiation of the side wall vortices can be seen in the generation of positive axial vorticity in the upper left quadrant and negative axial vorticity in the upper right quadrant. This axial vorticity resulted from pressure gradient driven, skew-induced secondary flow in the boundary layer, as explained earlier. The sign of the axial vorticity shown in Figure VI.4 is correctly predicted by

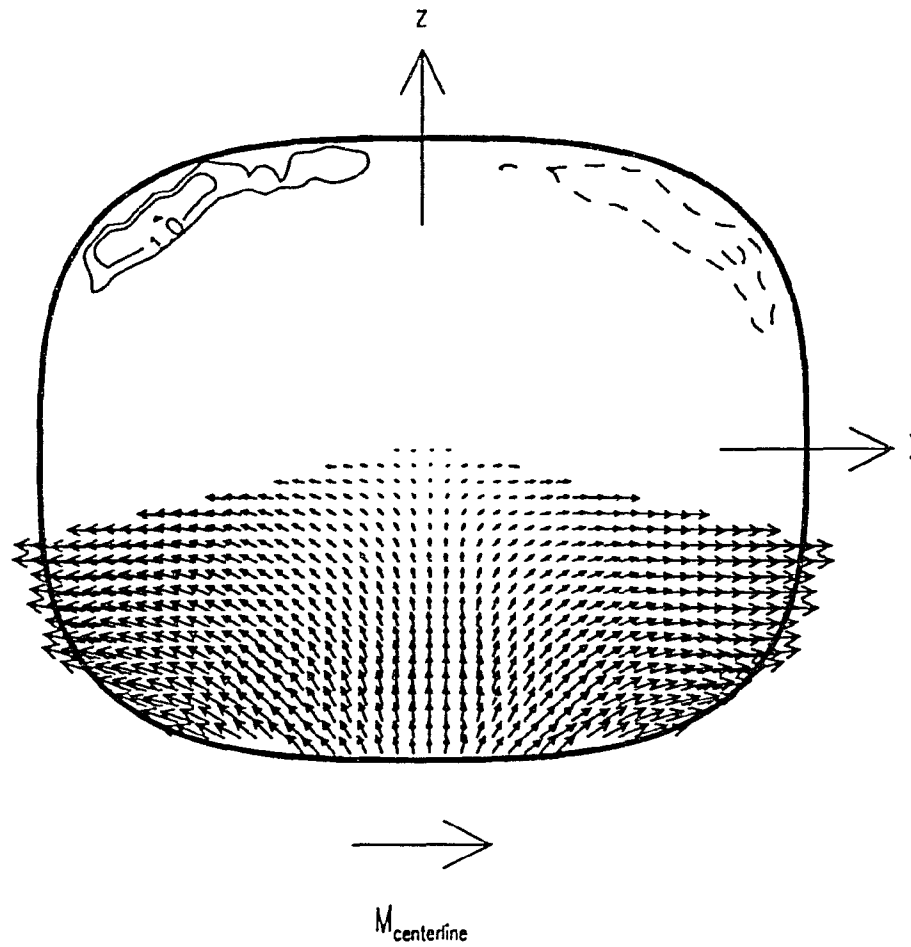


Figure VI.4 Axial vorticity at plane 1A for $M_{\text{centerline}} = 0.35$ without inlet swirl

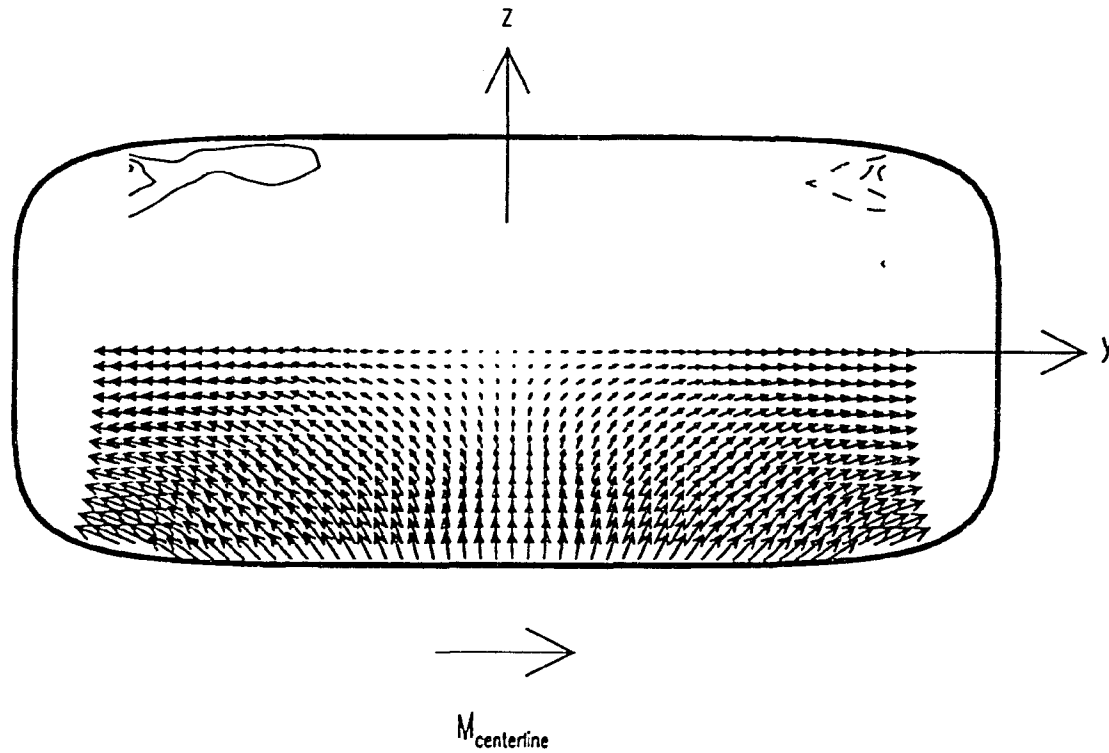


Figure VI.5 Axial vorticity at plane 2A for $M_{\text{centerline}} = 0.35$ without inlet swirl

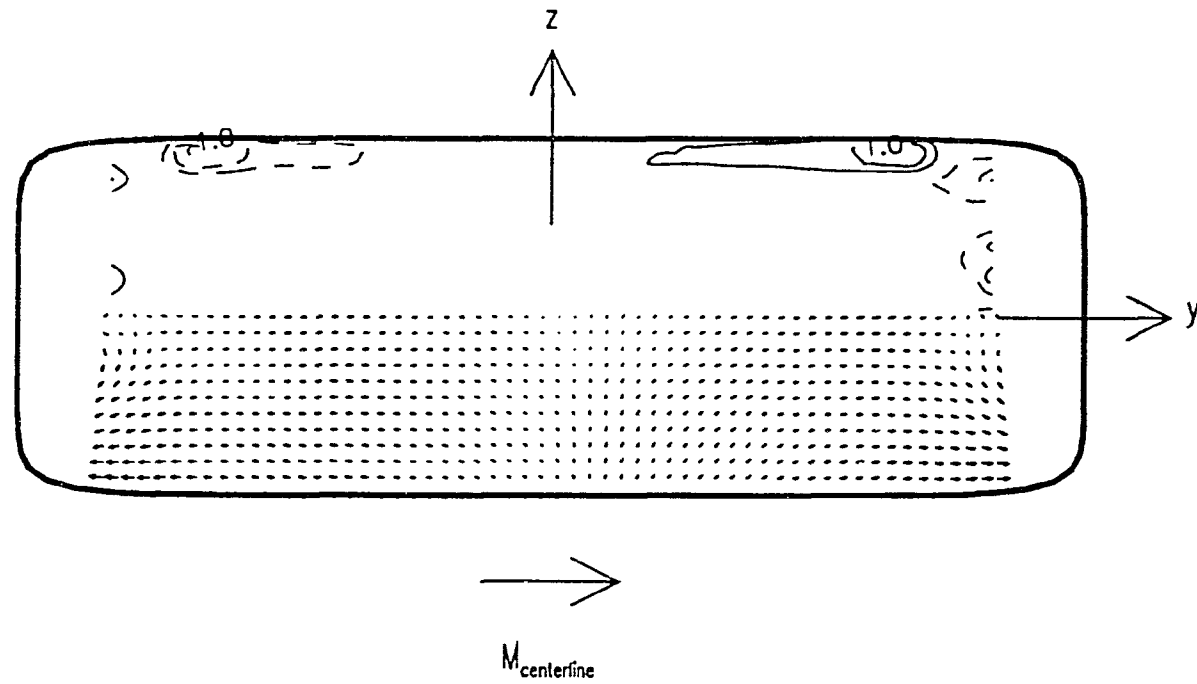


Figure VI.6 Axial vorticity at plane 3A for $M_{\text{centerline}} = 0.35$ without inlet swirl

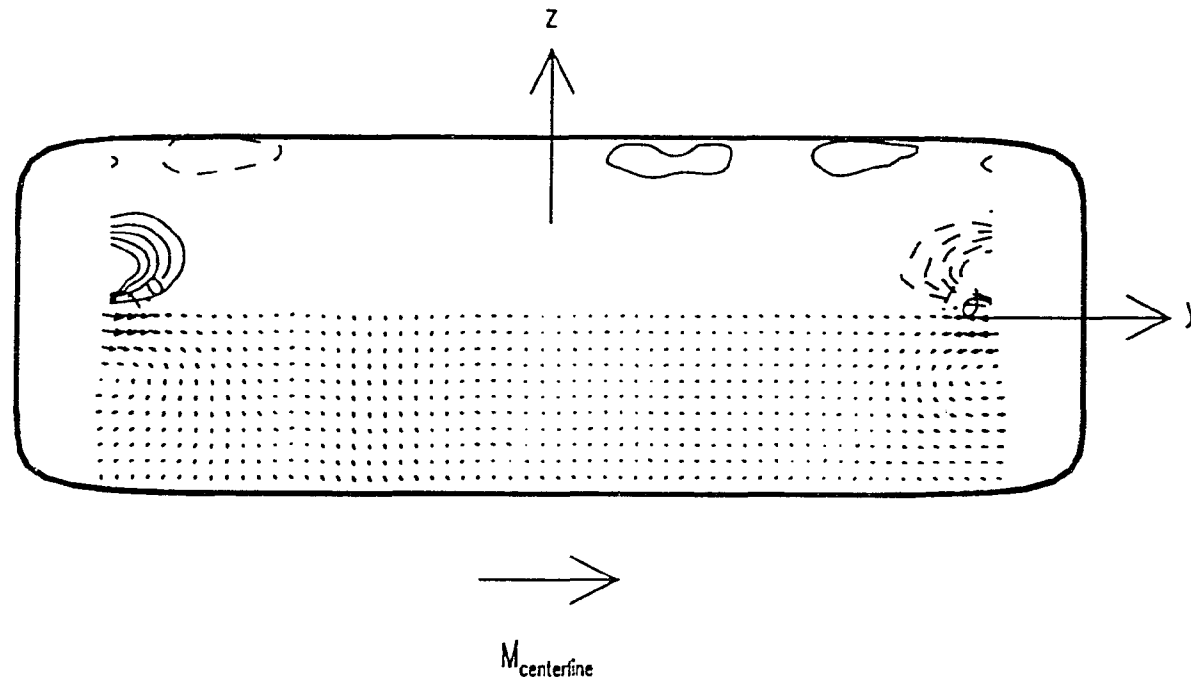


Figure VI.7 Axial vorticity at plane 4A for $M_{\text{centerline}} = 0.35$ without inlet swirl

Equation VI.13. In Figure VI.5, at plane 2A, convection had carried the axial vorticity outwards towards the side walls. At plane 3A, shown in Figure VI.6, convection had carried the axial vorticity observed at plane 1A to the side walls and out of the measurement region. The new static pressure distribution, however, had generated axial vorticity which is opposite in sign from the axial vorticity observed at plane 1A. This provides additional evidence that the second static pressure distribution doesn't simply eliminate the axial vorticity produced by the first static pressure distribution because convection had carried the vorticity observed at plane 1A away from the region where the opposite signed axial vorticity is produced. In Figure VI.7 the axial vorticity observed at plane 1A is now readily apparent near the side walls, while the much weaker opposite signed axial vorticity has remained in nearly the same location as observed at plane 3A.

Although there is no aerodynamic data very near the duct side wall, the surface oil film visualization provides evidence of a two additional pair of vortices in this region. This can be seen in surface oil film visualization results presented in Figure V.9. In the constant cross section region downstream of the transition region a bright line appears on the duct side wall approximately 0.15 radius from the xy -plane. Nearby lines exhibit asymptotic behavior, approaching the bright line from either side. Figure VI.8 is a sketch representing the pattern of secondary flow inferred from the surface oil film visualization. Numerical calculations at NASA Lewis Research Center using Navier-Stokes codes support this interpretation of the surface oil film visualization [67].

An effect of the vortices observed downstream of the transition region was the convection of fluid from the boundary layer into the free stream region. This produced distortion in the axial velocity and total pressure contours. This is particularly apparent at plane 4A, in Figures V.19, V.27 and V.35, where the high total pressure loss fluid, normally associated with the boundary layer, extends outwards from the side wall towards the duct centerline.

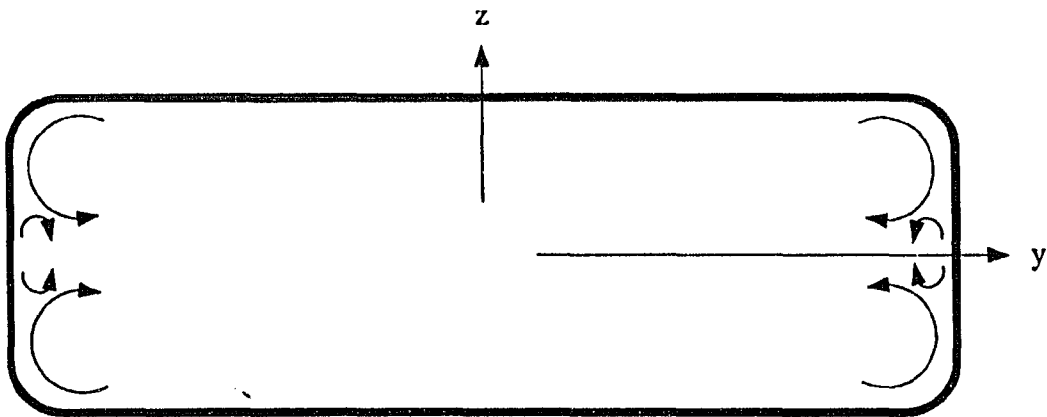


Figure VI.8 Sketch of secondary flow patterns inferred from surface oil film visualization for transition duct flow without inlet swirl

There are no results which indicate any region of separated flow in the transition duct. Davis and Gessner [18] made this same observation in their study of an identical transition duct. Miao *et al.* [16, 17] observed a region of separated flow along the diverging side wall in all three of the ducts they tested, at the lowest Reynolds number condition. No separation was observed at higher Reynolds numbers. Boundary layer measurements along the diverging side walls indicated the boundary layers were laminar at the lowest Reynolds number condition and turbulent at higher Reynolds numbers, explaining the existence of the separated flow region at the low Reynolds number.

Flow with inlet swirl

The effect of inlet swirl on the transition duct flow field is complex. On one hand, there appears to be little influence of inlet swirl on the duct surface static pressure distribution, shown in Figure V.39. However, the difference in detailed data, in particular the transverse components of velocity in all measurement planes for flow without and with inlet swirl is striking. For example, there is no evidence in plane 3A, Figure V.44, or plane 4A, Figure V.45 of the two pair of counter-rotating side wall vortices that were observed for flow without inlet swirl.

When viewed looking upstream, the incoming flow with swirl is rotating clockwise, resulting in a region outside the wall boundary layer of nearly constant negative axial vorticity. The overwhelming fluid flow effect was that the duct geometry driven convergence in the xz -plane and the divergence in the xy -plane was aided by the clockwise swirl in the upper right and lower left quadrants and opposed by the clockwise swirl in the upper left and lower right quadrants, as shown in the sketch in Figure VI.9. This flow pattern established the static pressure distribution for plane 1A seen in Figure V.46. The static pressure distribution again was saddle shaped, but the regions of highest static pressure were now located near the lower right and upper left corners and the regions of lowest pressure were located near the lower left and upper right corners. The static pressure gradient associated with the maximum and minimum static pressures drove the boundary layer flow near the lower right and upper left corners in two directions, some against the direction of rotation and some

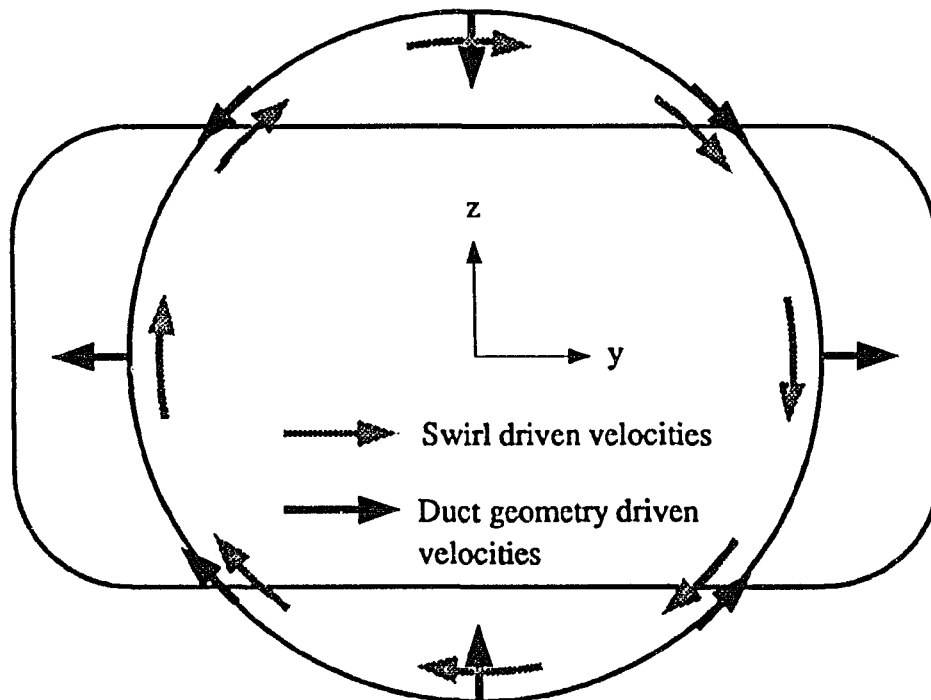


Figure VI.9 Sketch of swirl driven and duct geometry driven velocities for transition duct flow with inlet swirl

towards the direction of rotation. Near the lower left and upper right corners there was no radial static pressure gradient to balance the centrifugal forces and there the flow field was directed outward. Both of these effects can be seen in the plot of transverse velocity at plane 1A, Figure V.42.

The response to the pressure gradient was again greater in the boundary layer where the momentum is less, resulting in skew-induced secondary flows. Near the four corners this produces positive vorticity. This can be seen in Figure VI.10, which shows axial vorticity and transverse velocity components at plane 1A for flow with inlet swirl. The positive axial vorticity in the upper left quadrant resulted from the pressure gradient tangent to the surface. The positive axial vorticity in the upper left quadrant resulted from the lack of radial pressure gradient.

The saddle-shaped pressure distribution observed in plane 1A persisted to plane 2A, shown in Figure V.47, however, it was not as pronounced. The complete 90° change in the orientation of the static pressure distribution seen in the flow field without inlet swirl was not observed. Rather, the regions of highest pressure remained in the lower right and upper left quadrants, but they appeared to be displaced counter clockwise, the highest pressure being nearer the y -axes and the lowest static pressures nearer the z -axes.

Figure VI.11 shows the axial vorticity at plane 2A. The positive axial vorticity observed in the upper left quadrant of plane 1A convected counter clockwise, against the principal direction of rotation, outwards towards the diverging side wall and out of the measurement region. This can be discerned from the surface oil film visualization shown in Figure V.40. The positive axial vorticity seen in the upper right quadrant of plane 1A has also convected outwards towards the diverging side wall, but this motion is clockwise, with the principal direction of rotation.

At plane 3A the static pressure distribution, Figure V.48, does not differ significantly from the nonswirling static pressure at the same plane. The location of the regions of maximum static pressure were on the y -axes and the regions of mini-

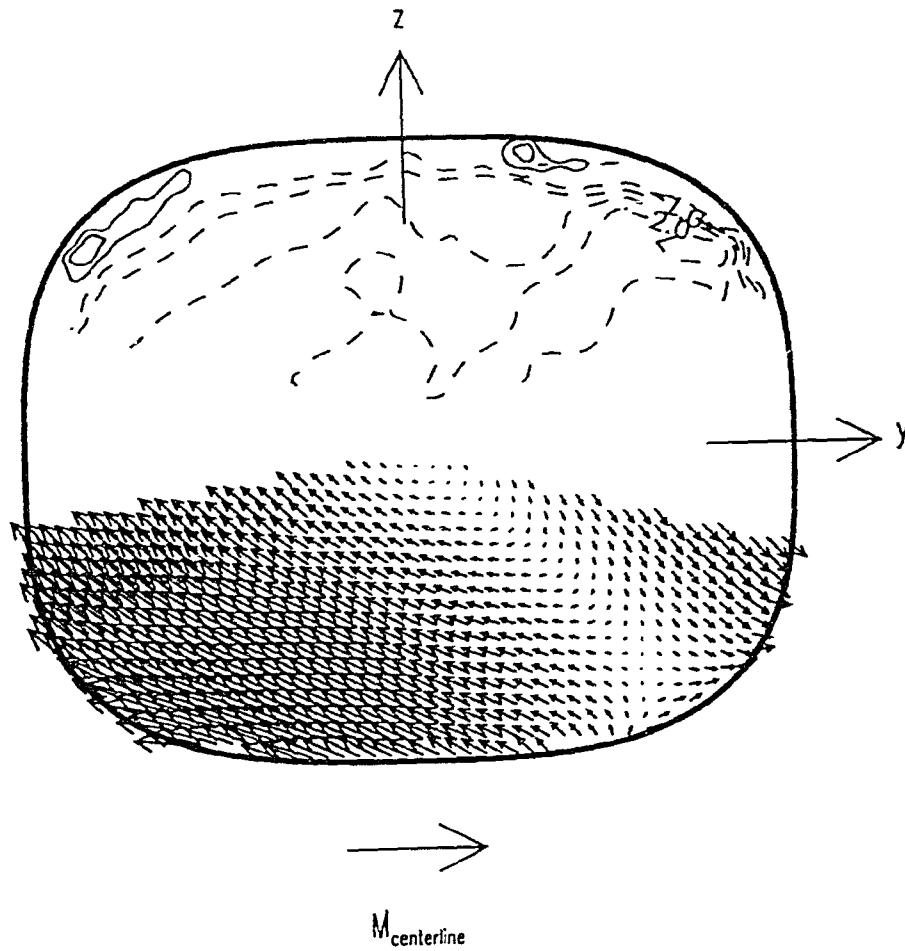


Figure VI.10 Axial vorticity at plane 1A for $M_{\text{centerline}} = 0.35$ with inlet swirl

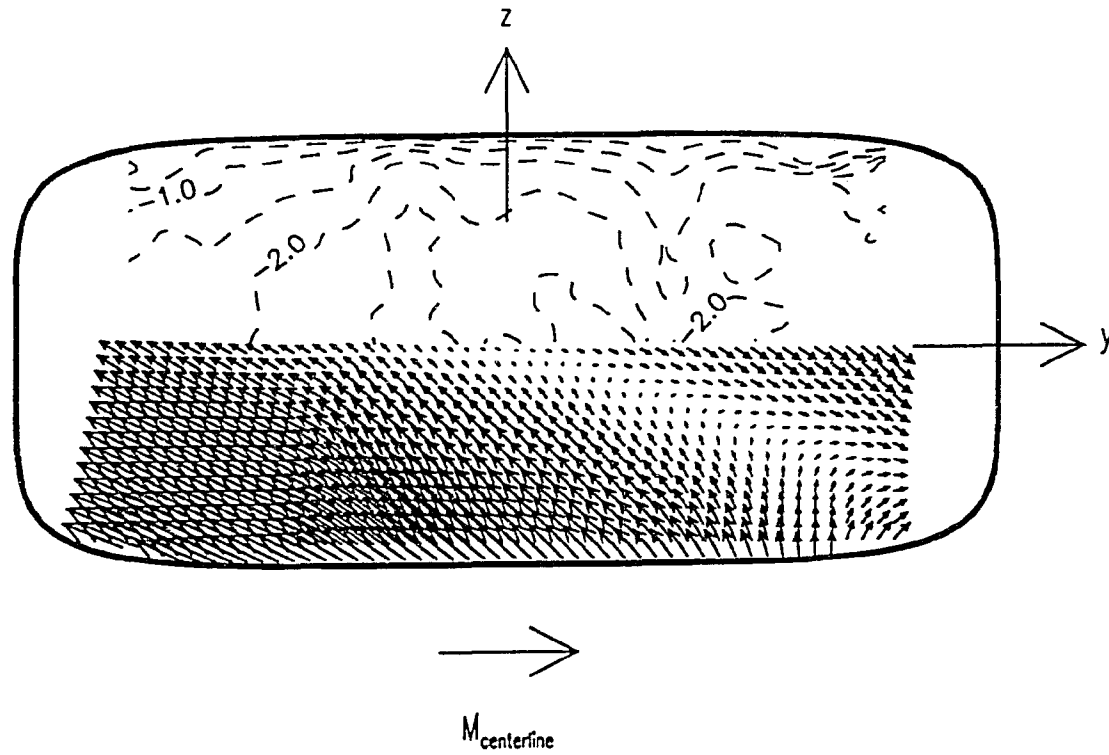


Figure VI.11 Axial vorticity at plane 2A for $M_{\text{centerline}} = 0.35$ with inlet swirl

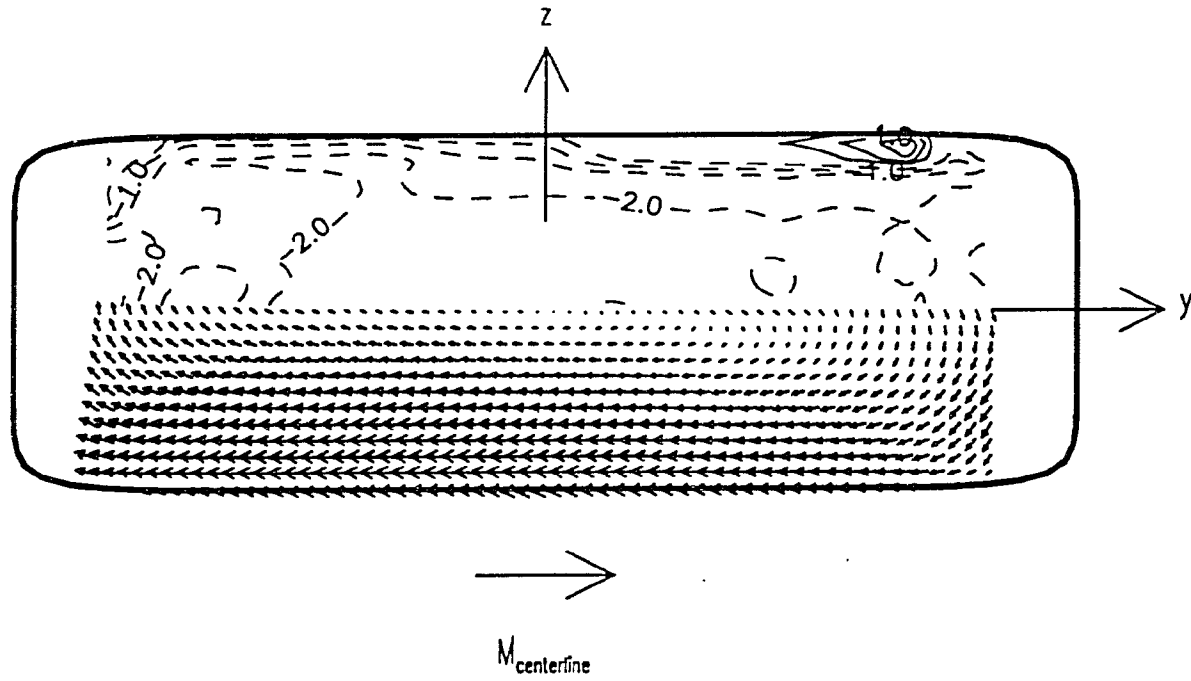


Figure VI.12 Axial vorticity at plane 3A for $M_{\text{centerline}} = 0.35$ with inlet swirl

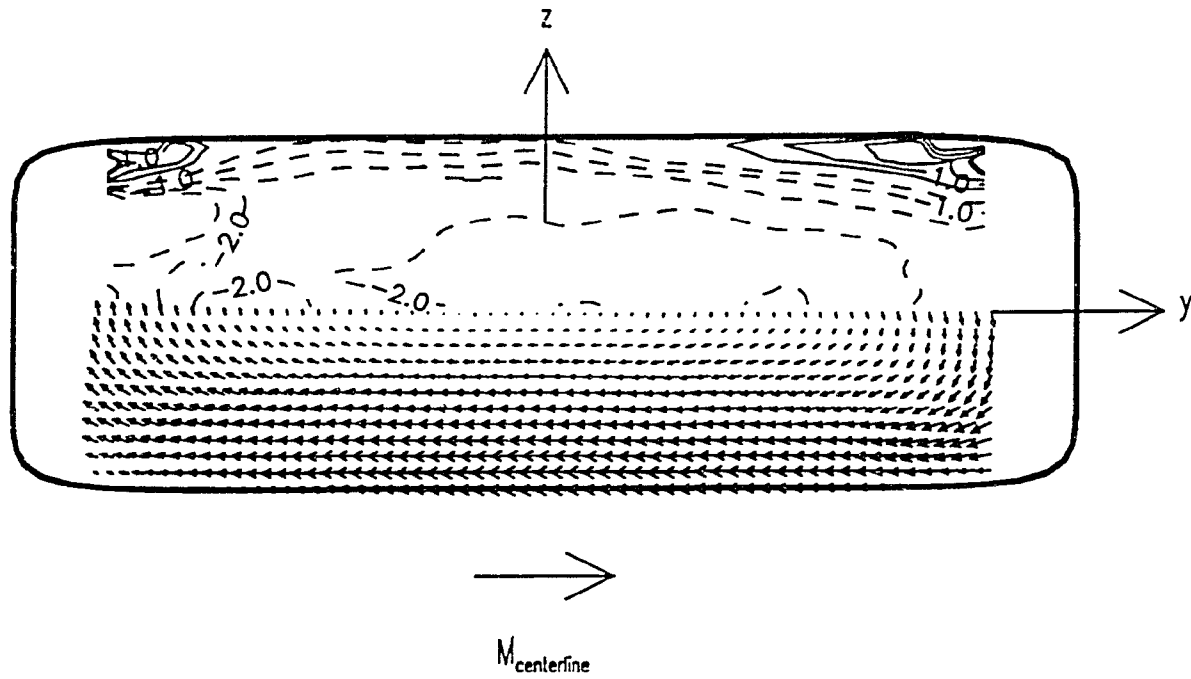


Figure VI.13 Axial vorticity at plane 4A for $M_{\text{centerline}} = 0.35$ with inlet swirl

imum static pressure were located on the z -axes. The static pressure distribution has changed its orientation nearly 90° from plane 1A. The reversal of the static pressure distribution orientation for flow without inlet swirl was described earlier. For the nonswirling case, the reversal was accomplished by passing through a nearly flat pressure distribution. For the swirling case, the reversal of the pressure distribution orientation was accomplished without passing through a flat pressure distribution, the orientation of the static pressure distribution appeared to experience in effect a counter clockwise rotation.

The axial vorticity at plane 3A is shown in Figure VI.12. The positive axial vorticity in upper right quadrant was aided by the gradient in the static pressure distribution. The positive axial vorticity in the upper left quadrant was still out of the measurement region. This axial vorticity was not affected by the gradient in the pressure distribution because of its location.

The static pressure distribution measured at plane 4A, Figure V.49, has the same shape as the distribution in plane 3A, however, the gradients were not as great. At this location and further downstream, the static pressure distribution had little effect on the boundary layer flow. Figure VI.13 shows positive axial vorticity present in each corner at plane 4A. This was the same positive axial vorticity generated in each respective quadrant at plane 1A. The vorticity in the upper right quadrant was observed at all four measurement planes. The vorticity in the upper left quadrant was seen at plane 1A, but had convected out of the measurement region at planes 2A and 3A, and reappears at plane 4A.

The distortion of total pressure is most apparent in the lower right quadrant in planes 3A and 4A, Figures V.48 and V.49. As in the nonswirling case, this distortion resulted from the convection of boundary layer fluid by secondary flows. The slight depression in total pressure near the centerline that appeared in all four planes is an artifact of the swirl generator which was described in Chapter V. All measurements indicate that the flow remains attached throughout the transition duct.

CHAPTER VII. CONCLUSIONS

The combination of stationary blades followed by a rotating pipe containing a honeycomb and screen proved to be an effective way of generating a solid body swirling flow. The flow produced by the swirl generator was suitable for detailed downstream flow field measurements. The procedure of fabricating the stationary blades from cylindrical tubing with diminishing chord length saved considerable cost when compared to alternative fabrication methods involving extensive machine work.

When utilized as exhaust system components of aircraft with rectangular nozzles, circular-to-rectangular transition ducts often involve an incoming flow that includes a swirling velocity component remaining from the gas turbine engine. Using the swirl generator improves the simulation of such transition duct flows. Detailed measurements of the transition duct flow field were obtained for flows with and without inlet swirl. A refinement of the five-hole probe aerodynamic measurement calibration and data reduction technique was used extensively for transition duct flow field measurements. These results provided greater insight into the fluid dynamics of circular-to-rectangular transition duct flows.

Experimental results have shown that inlet swirl significantly changes the transition duct flow field. Outside the boundary layer, the response of the flow field velocity to the changing duct geometry gives rise to the static pressure distribution. For nonswirling incoming flow the static pressure distribution produced skew-induced secondary flows within the boundary layer which evolved into two pair of counter-rotating side wall vortices. For the inlet swirl case the side wall vortices were not observed. The static pressure distribution was altered by the swirling velocity flow field to an extent that the side wall vortices were suppressed. The effects of inlet swirl should be included in the design of circular-to-rectangular transition ducts for aircraft exhaust systems.

The ethylene trace gas technique provided an accurate Lagrangian flow field representation at high flow velocities within the transition duct. The methods developed

to obtain the ethylene trace gas data can be used in other experimental configurations with very little modification. In fact, this technique is presently being used in supersonic flows to study mixing nozzles. The statistical methods used to help interpret the trace gas data provided a reliable way to quantify and compare contour characteristics such as shape, orientation or the amount of contour spreading.

CHAPTER VIII. RECOMMENDATIONS FOR FUTURE RESEARCH

A requirement exists for further measurements in circular-to-rectangular transition ducts. Heat transfer is a particular problem in transition ducts used as components of aircraft exhaust systems. The ability of current CFD methods to predict heat transfer in transition ducts has to some degree suffered because of a lack of experimental heat transfer type data in these configurations. Experiments that utilize surface hot film gauges or liquid crystal methods to acquire surface shear stresses or convective heat transfer coefficients would help fulfill this requirement. Inlet swirl should be included in this type of study.

Another concern in aircraft propulsion design is the integration of various subsystems. A requirement exists to accurately predict how the performance of a propulsion component is influenced by the incoming flow resulting from upstream components. Using a swirl generator in the present transition duct study was partly a response to this concern. A continuation of transition duct research involves making flow field and surface measurements in a converging/diverging nozzle immediately downstream of a circular-to-rectangular transition duct.

Another duct geometry that is interesting because of its application in aircraft propulsion systems is one with an S-shaped centerline. S-ducts are employed in both aircraft inlet and exhaust systems. A requirement exists for an S-duct experiment comparable to the present transition duct study. Swirl would again be a relevant inlet condition for an S-duct experiment.

Additional experiments and analysis should be directed towards the trace gas technique. There remains several unanswered questions regarding the interpretation of trace gas data when used to infer other flow field information. Using the trace gas technique to predict the effectiveness of transpiration and film cooling efforts in transition ducts and to provide a comparison with CFD predictions of these cooling methods should be explored.

APPENDIX A. A PROCEDURE FOR FIVE-HOLE PROBE CALIBRATION AND DATA REDUCTION

The Five-Hole Probe

Figure IV.2, reproduced below in Figure A.1, shows a typical five-hole probe and the nomenclature that will be used in this appendix. The openings of the four outer tubes were inclined, usually 45° , to their axis. The opening of the center tube was normal to its axis. This arrangement produced symmetry at the probe openings on the pitch and yaw planes. Away from the probe openings the five tubes were bundled inside the probe shaft. The tube openings were aligned with the probe shaft axis so the openings would not translate when the probe shaft is rotated. The pressure measured in the i th tube was denoted p_i .

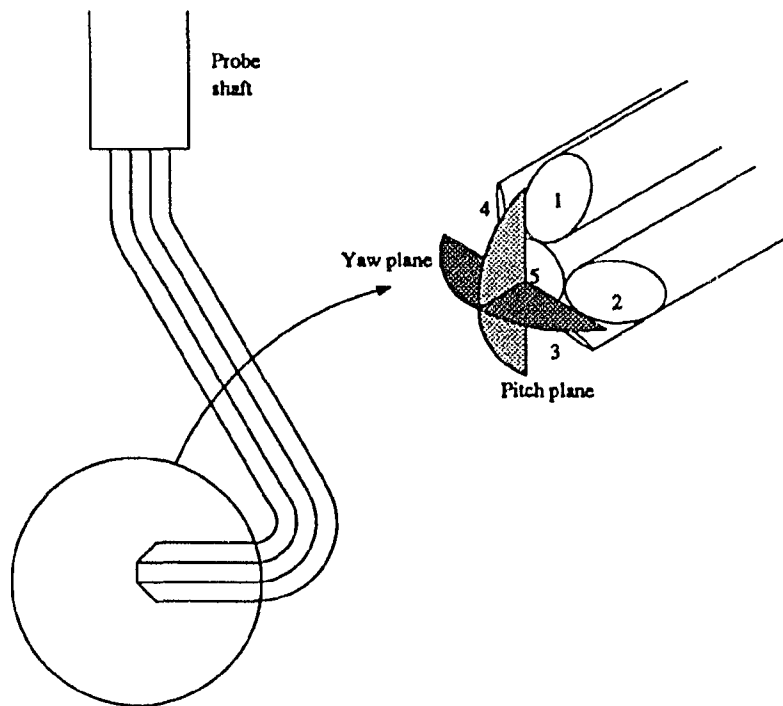


Figure A.1 A typical five-hole probe

There are two methods used to obtain aerodynamic data using the five-hole probe, the yaw-nulling method and the stationary probe method. In the yaw-nulling method the probe was rotated about the probe shaft until the pressures p_2 and p_4 are equal. The yaw angle was measured directly. This appendix describes the calibration and data reduction procedure for the yaw-nulling method.

The objective of five-hole probe calibration was to empirically determine the function, Equation A.1, relating the flow total pressure p_0 , the flow static pressure p , and pitch angle α , to the subspace (p_i, p_j, p_k) of the five measured pressures.

$$F : (p_0, p, \alpha) \rightarrow (p_i, p_j, p_k) \subset (p_1, \dots, p_5) \quad (\text{A.1})$$

The inverse of this function, A.2, used in data reduction, allowed the total and static pressure and pitch angle to be calculated from three of the five measured pressures.

$$F^{-1} : (p_i, p_j, p_k) \rightarrow (p_0, p, \alpha) \quad (\text{A.2})$$

The success of this procedure depended on the existence of this inverse function. The conditions necessary for the existence of the inverse function are described in the following section.

Calibration

Experimental procedure

The calibration was accomplished by placing the probe in a uniform flow and varying the probe pitch angle and Mach number while measuring the probe's five pressures. By varying the Mach number the ratio of static to total pressure was varied. This procedure was performed in the Internal Fluid Mechanics Facility. The probe and actuator were mounted on a gimbal with the probe placed so the probe openings were located at the gimbal's center of rotation. This allowed the pitch angle to change without a translation of the probe openings. While the k th Mach number remained constant the probe was positioned at the l th different pitch angle

and the five probe pressures, probe pitch angle, and the flow total pressure and static pressure were recorded. Measurements were recorded at a total of N_k different pitch angles for the k th Mach number. This procedure was repeated for a total of N_{Mach} different Mach numbers.

Dimensional considerations

The five pressures measured by the probe were nondimensionalized by Equation A.3. This is the same pressure coefficient given by Equations V.1 and V.2 that were used to nondimensionalize experimental static and total pressure data.

$$\frac{p_i - p}{p_0 - p} = f_i \left(Re, M, \gamma, \alpha, \frac{l}{d} \right), i = 1, \dots, 5 \quad (\text{A.3})$$

The pressure coefficients could depend on flow parameters such as the Mach number M , the Reynolds number Re , the specific heat ratio γ , and probe parameters such as the pitch angle α , and the probe length-to-diameter ratio l/d . Air was used for both the calibration and experiments so the specific heat ratio was removed from the list of independent variables. The Mach and Reynolds number could not be varied independently in the Internal Fluid Mechanics Facility so Mach number dependence was considered while the Reynolds number was removed from the list of independent variables.

When calibrating the five-hole probe it was the pitch angle relative to the probe shaft α , that was varied and recorded, but it was the pitch angle relative to the probe openings θ , to which the probe responded. These different angles are shown in Figure A.2. The difference between the two pitch angles was the total pitch difference angle θ_0 , where $\theta_0 = \theta - \alpha$. Figure A.3 shows typical calibration data results. The five pressure coefficients are plotted as functions of θ for three different Mach numbers. These results are essentially independent of Mach number for the range of Mach number tested. It was in the angle θ_0 that the Mach number and length-to-diameter ratio dependence appeared, as symbolized by Equation A.4.

$$f_i = f_i(\theta) = f_i(\alpha + \theta_0), i = 1, \dots, 5 \quad \theta_0 = \theta_0 \left(M, \frac{l}{d} \right) \quad (\text{A.4})$$

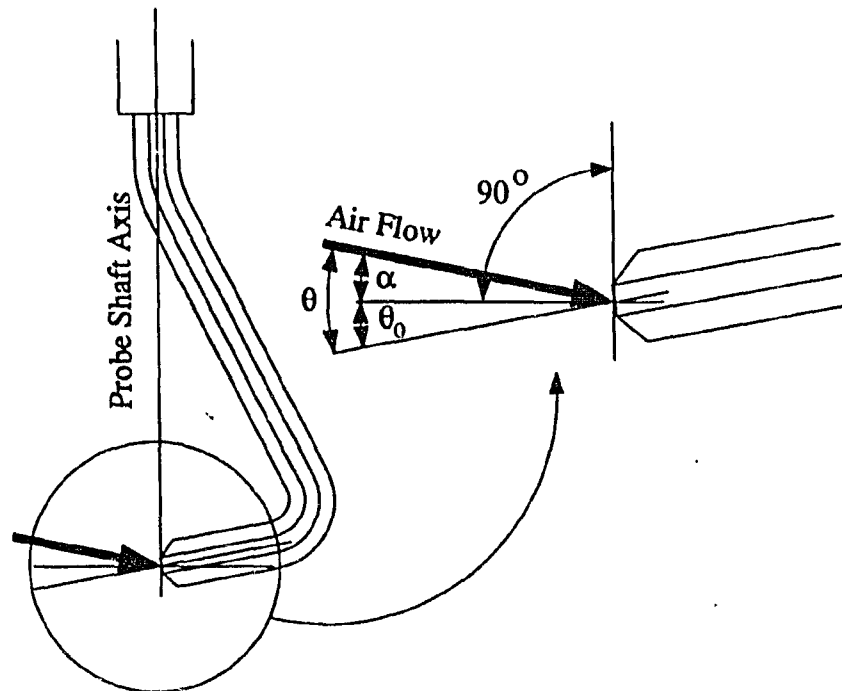


Figure A.2 Different five-hole probe pitch angles

Two principal causes contributed to the total pitch difference angle θ_0 . The first was any difference from perpendicular in the angle between the probe sensing area and the probe shaft caused by probe construction. This difference in angle could be an intentional design feature of the probe or could result unintentionally from imperfect construction. This was the static pitch difference angle. The static pitch difference angle was unaffected by flow Mach number and the probe length-to-diameter ratio. The second cause was the deflection of the probe produced by aerodynamic loading, which did depend on flow Mach number and the probe length-to-diameter ratio. This was the dynamic pitch difference angle. The sum of these two angles was the total pitch difference angle θ_0 .

The pitch angle θ , not α , was used for probe calibration and data reduction. Using the pitch angle θ had several important advantages.

1. The calibration results were independent of Mach number for a significant range of subsonic Mach numbers, as seen in Figure A.3.

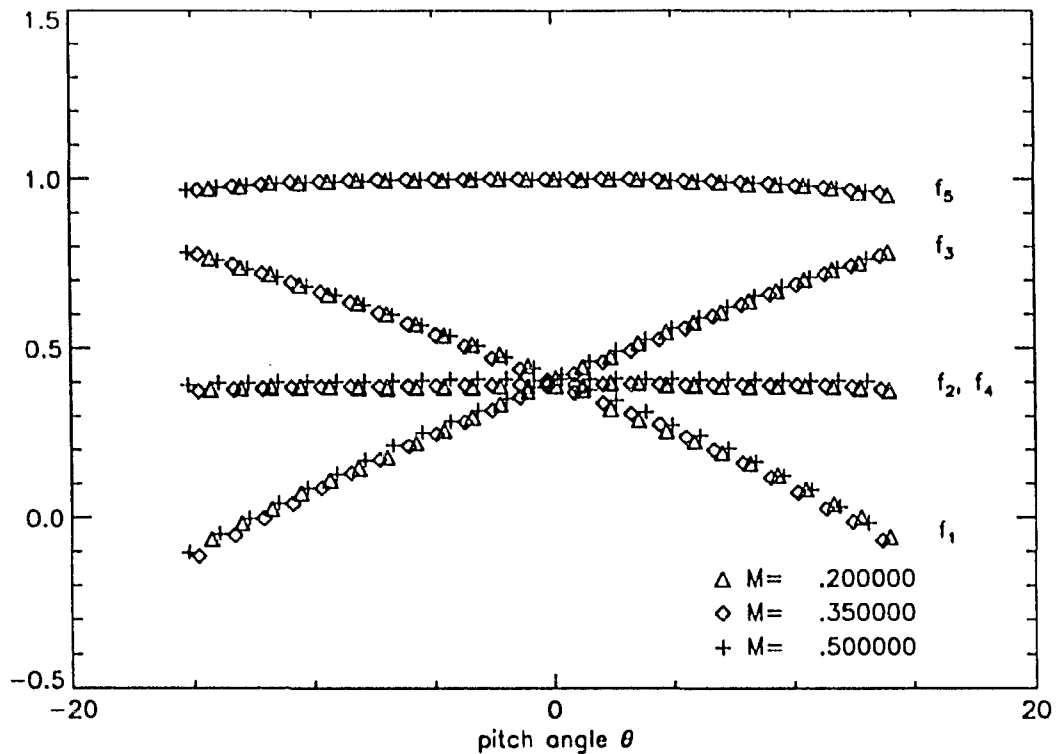


Figure A.3 Nondimensional pressure functions for a typical five-hole probe

2. The symmetry of the probe lead to several important simplifications in the analysis of the calibration data and the data reduction procedure. This is discussed in detail later.
3. During experimental tests probes are occasionally bent slightly by striking solid surfaces. When this occurs, experience has shown the functions A.3 are unaffected, only the total pitch difference angle, θ_0 , is changed. Recalibrating the probe was often unnecessary.

The objective of probe calibration, to relate p_0 , p , and α to three of the five measured pressures remained unchanged, however, the functional relation actually used in the calibration and data reduction procedure is more accurately represented by Equations A.5 and A.6. In order to satisfy the original objective the angle θ_0 must

be known to determine α . The procedures used to find θ_0 for calibration and data reduction are described later.

$$F : (p_0, p, \theta) \rightarrow (p_i, p_j, p_k) \subset (p_1, \dots, p_5) \quad (\text{A.5})$$

$$F^{-1} : (p_i, p_j, p_k) \rightarrow (p_0, p, \theta) \quad (\text{A.6})$$

Symmetry conditions and Taylor's series

The symmetry of the probe required the pressure coefficients satisfy the conditions given in Equations A.7 to A.11.

$$f_1(\theta) = f_3(-\theta) \quad (\text{A.7})$$

$$f_2(\theta) = f_2(-\theta) \quad (\text{A.8})$$

$$f_2(\theta) = f_4(\theta) \quad (\text{A.9})$$

$$f_5(\theta) = f_5(-\theta) \quad (\text{A.10})$$

$$f_1(0) = f_2(0) = f_3(0) = f_4(0) \quad (\text{A.11})$$

For subsonic flow, aerodynamic considerations required Equation A.12 be satisfied.

$$f_5(0) = 1 \quad (\text{A.12})$$

The Taylor's series for the pressure coefficients is shown in Equation A.13.

$$f_i = a_{i,0} + a_{i,1}\theta + a_{i,2}\theta^2 + \dots = \sum_{j=1}^{\infty} a_{i,j}\theta^j, \quad i = 1, \dots, 5 \quad (\text{A.13})$$

The symmetry conditions had important consequences for the Taylor's series of each pressure coefficient. Condition A.7 required Equations A.14 and A.15 be satisfied.

$$a_{1,j} = a_{3,j}, \quad j = 0, 2, \dots \quad (\text{A.14})$$

$$a_{1,j} = -a_{3,j}, \quad j = 1, 3, \dots \quad (\text{A.15})$$

Condition A.8 required Equation A.16 be satisfied.

$$a_{2,j} = 0, \quad j = 1, 3, \dots \quad (\text{A.16})$$

Condition A.9 required Equation A.17 be satisfied.

$$a_{2,j} = a_{4,j}, \quad j = 0, 1, \dots \quad (\text{A.17})$$

Condition A.10 required Equation A.18 be satisfied.

$$a_{5,j} = 0, \quad j = 1, 3, \dots \quad (\text{A.18})$$

Condition A.11 required Equation A.19 be satisfied.

$$a_{i,1} = a_{i,2} = a_{i,3} = a_{i,4} \quad (\text{A.19})$$

The aerodynamic condition, A.12, required Equation A.20 be satisfied.

$$a_{5,0} = 1 \quad (\text{A.20})$$

Using these results, the Taylor's series of the pressure coefficients are given in Equations A.21 through A.25.

$$f_1(\theta) = a_{1,0} + a_{1,1}\theta + a_{1,2}\theta^2 + \dots \quad (\text{A.21})$$

$$f_2(\theta) = a_{1,0} + a_{2,2}\theta^2 + \dots \quad (\text{A.22})$$

$$f_3(\theta) = a_{1,0} - a_{1,1}\theta + a_{1,2}\theta^2 + \dots \quad (\text{A.23})$$

$$f_4(\theta) = a_{1,0} + a_{2,2}\theta^2 + \dots \quad (\text{A.24})$$

$$f_5(\theta) = 1 + a_{5,2}\theta^2 + \dots \quad (\text{A.25})$$

Inverse function theorem

For the inverse function given by Equation A.6 to exist the inverse function theorem required three of the five measured pressure satisfy Equation A.26 for all values of p_0 , p , and θ of interest.

$$\det \begin{bmatrix} \frac{\partial p_i}{\partial p_0} & \frac{\partial p_i}{\partial p} & \frac{\partial p_i}{\partial \theta} \\ \frac{\partial p_j}{\partial p_0} & \frac{\partial p_j}{\partial p} & \frac{\partial p_j}{\partial \theta} \\ \frac{\partial p_k}{\partial p_0} & \frac{\partial p_k}{\partial p} & \frac{\partial p_k}{\partial \theta} \end{bmatrix} \neq 0 \quad (\text{A.26})$$

The magnitude of this determinant was an indication of the suitability of the inverse function for data reduction. A large magnitude was desirable. Substituting the pressure coefficients into Equation A.26 resulted in Equation A.27. The case when $p_0 = p$ corresponded to no fluid motion and was of no importance. By using the Taylor's series of the pressure coefficients in Equation A.27 it was possible to predict which three pressures are most suitable for use in calibration and data reduction.

$$\det \begin{bmatrix} \frac{\partial p_i}{\partial p_0} & \frac{\partial p_i}{\partial p} & \frac{\partial p_i}{\partial \theta} \\ \frac{\partial p_j}{\partial p_0} & \frac{\partial p_j}{\partial p} & \frac{\partial p_j}{\partial \theta} \\ \frac{\partial p_k}{\partial p_0} & \frac{\partial p_k}{\partial p} & \frac{\partial p_k}{\partial \theta} \end{bmatrix} = (p_0 - p) \left| \frac{df_i}{d\theta}(f_j - f_k) - \frac{df_k}{d\theta}(f_i - f_j) + \frac{df_j}{d\theta}(f_k - f_i) \right| \quad (\text{A.27})$$

The magnitude of the determinant in Equation A.27 for the ten combinations resulting from five pressures taken three at a time is summarized in Table A.1. Three

Table A.1 The ten pressure combinations and the corresponding value of the determinant given in Equation A.27

Pressure Combinations	$\det \begin{bmatrix} \frac{\partial p_i}{\partial p_0} & \frac{\partial p_i}{\partial p} & \frac{\partial p_i}{\partial \theta} \\ \frac{\partial p_j}{\partial p_0} & \frac{\partial p_j}{\partial p} & \frac{\partial p_j}{\partial \theta} \\ \frac{\partial p_k}{\partial p_0} & \frac{\partial p_k}{\partial p} & \frac{\partial p_k}{\partial \theta} \end{bmatrix}$
p_1, p_2, p_3	$(p_0 - p) 2a_{1,1}(a_{2,2} - a_{1,2})\theta^2 $
p_1, p_2, p_4	0
p_1, p_2, p_5	$(p_0 - p) -a_{1,0}a_{1,1} + 2a_{1,0}(a_{2,2} - a_{1,2})\theta + a_{1,1}(a_{2,2} - a_{5,2})\theta^2 $
p_1, p_3, p_4	$(p_0 - p) 2a_{1,1}(a_{2,2} - a_{1,2})\theta^2 $
p_1, p_3, p_5	$(p_0 - p) -2a_{1,0}a_{1,1} + 2a_{1,1}(a_{1,2} - a_{5,2})\theta^2 $
p_1, p_4, p_5	$(p_0 - p) -a_{1,0}a_{1,1} + 2a_{1,0}(a_{2,2} - a_{1,2})\theta + a_{1,1}(a_{2,2} - a_{5,2})\theta^2 $
p_2, p_3, p_4	0
p_2, p_3, p_5	$(p_0 - p) -a_{1,0}a_{1,1} + 2a_{1,0}(a_{2,2} - a_{1,2})\theta + a_{1,1}(a_{2,2} - a_{5,2})\theta^2 $
p_2, p_4, p_5	0
p_3, p_4, p_5	$(p_0 - p) -a_{1,0}a_{1,1} + 2a_{1,0}(a_{2,2} - a_{1,2})\theta + a_{1,1}(a_{2,2} - a_{5,2})\theta^2 $

combinations, p_1, p_2, p_4 , p_2, p_3, p_4 , and p_2, p_4, p_5 , produced a determinant that was zero for all values of θ . The determinant of two combinations, p_1, p_2, p_3 and p_1, p_3, p_4 vanished when $\theta = 0$. The remaining five combinations all had nonzero determinants in the neighborhood of $\theta = 0$. Of these, the combination p_1, p_3, p_5 was the most

suitable to use for calibration. The magnitude of the determinant for this combination was twice as large as the remaining four combinations at $\theta = 0$.

Determining θ_0

To calculate the angle θ for each calibration measurement it was necessary to determine the total pitch difference angle $\theta_{0,k}$ for each k th Mach number at which calibration measurements were recorded. This was done numerically by calculating the value of α which satisfies $f_{1,k} = f_{3,k}$. This was accomplished by finding the least squares linear approximations given by Equation A.28.

$$f_{1,k,l} - f_{3,k,l} \approx c_{0,k} + c_{1,k}\alpha \quad (\text{A.28})$$

The coefficients $c_{0,k}$ and $c_{1,k}$ were calculated by solving the system of Equations A.29 and A.30. In these equations $f_{1,k,l}$, $f_{3,k,l}$ and $\alpha_{k,l}$ are determined from the l th measurements recorded at the k th Mach number.

$$c_{0,k}N_k + c_{1,k} \sum_{l=1}^{N_k} \alpha_{k,l} = \sum_{l=1}^{N_k} (f_{1,k,l} - f_{3,k,l}) \quad (\text{A.29})$$

$$c_{0,k} \sum \alpha_{k,l} + c_{1,k} \sum_{l=1}^{N_k} \alpha_{k,l}^2 = \sum_{l=1}^{N_k} (f_{1,k,l} - f_{3,k,l})\alpha_{k,l} \quad (\text{A.30})$$

$\theta_{0,k}$ was given by Equation A.31.

$$\theta_{0,k} = \frac{c_{0,k}}{c_{1,k}} \quad (\text{A.31})$$

Least squares approximation

To approximate the three pressure coefficients f_1 , f_3 and f_5 with the first three terms of their Taylor's series, only four of the nine coefficients must be determined; $a_{1,0}$, $a_{1,1}$, $a_{1,2}$ and $a_{5,2}$. This was done using a least squares procedure. The error

of the approximation, for all N_k experimental measurements recorded at all N_{Mach} Mach numbers, was defined by Equation A.32.

$$\begin{aligned}
E = & \sum_{k=1}^{N_{\text{Mach}}} \sum_{l=1}^{N_k} [f_{1,k,l} - (a_{1,0} + a_{1,1}\theta_{k,l} + a_{1,2}\theta_{k,l}^2)]^2 \\
& + \sum_{k=1}^{N_{\text{Mach}}} \sum_{l=1}^{N_k} [f_{3,k,l} - (a_{1,0} - a_{1,1}\theta_{k,l} + a_{1,2}\theta_{k,l}^2)]^2 \\
& + \sum_{k=1}^{N_{\text{Mach}}} \sum_{l=1}^{N_k} [f_{5,k,l} - (1 + a_{5,2}\theta_{k,l}^2)]^2
\end{aligned} \tag{A.32}$$

The least squares procedure required finding the four coefficients which minimize this error. These four coefficients satisfy Equation A.33. The four coefficients were found by solving Equations A.34 through A.37. Equations A.35 and A.37 were solved independently, Equations A.34 and A.36 were solved simultaneously.

$$\frac{\partial E}{\partial a_{1,0}} = \frac{\partial E}{\partial a_{1,1}} = \frac{\partial E}{\partial a_{1,2}} = \frac{\partial E}{\partial a_{5,2}} = 0 \tag{A.33}$$

$$a_{1,0} \sum_{k=1}^{N_{\text{Mach}}} N_k + a_{1,2} \sum_{k=1}^{N_{\text{Mach}}} \sum_{l=1}^{N_k} \theta_{k,l}^2 = \frac{1}{2} \sum_{k=1}^{N_{\text{Mach}}} \sum_{l=1}^{N_k} (f_{1,k,l} + f_{3,k,l}) \tag{A.34}$$

$$a_{1,1} \sum_{k=1}^{N_{\text{Mach}}} \sum_{l=1}^{N_k} \theta_{k,l}^2 = \frac{1}{2} \sum_{k=1}^{N_{\text{Mach}}} \sum_{l=1}^{N_k} (f_{1,k,l} - f_{3,k,l})\theta_{k,l} \tag{A.35}$$

$$a_{1,0} \sum_{k=1}^{N_{\text{Mach}}} \sum_{l=1}^{N_k} \theta_{k,l}^2 + a_{1,2} \sum_{k=1}^{N_{\text{Mach}}} \sum_{l=1}^{N_k} \theta_{k,l}^4 = \frac{1}{2} \sum_{k=1}^{N_{\text{Mach}}} \sum_{l=1}^{N_k} (f_{1,k,l} + f_{3,k,l})\theta_{k,l}^2 \tag{A.36}$$

$$\sum_{k=1}^{N_{\text{Mach}}} \sum_{l=1}^{N_k} \theta_{k,l}^2 + a_{5,2} \sum_{k=1}^{N_{\text{Mach}}} \sum_{l=1}^{N_k} \theta_{k,l}^4 = \sum_{k=1}^{N_{\text{Mach}}} \sum_{l=1}^{N_k} f_{5,k,l}\theta_{k,l}^2 \tag{A.37}$$

Data Reduction

The data reduction procedure used the truncated Taylor's series approximations of the pressure coefficients determined in the calibration procedure to calculate the flow field total pressure, static pressure, and direction from the probe pressures and yaw angle measured during an experiment. This required finding the inverse function, A.6, whose existence was established in the previous section.

Equation A.38, a ratio of differences of measured pressures, was used to determine θ . Any ratio of differences of measured pressures is equivalent to the corresponding ratio of differences of pressure coefficients, making the ratio of differences of measured pressures independent of total and static pressure and dependent on θ only. For a ratio of differences of pressure coefficients, the denominator of each pressure coefficient, $p_0 - p$, appears in both the numerator and denominator of the ratio of differences and cancel. The static pressure term which appears in the numerator of each pressure coefficient, $p_i - p$, is cancelled by the difference operations in the ratio of differences. These cancellations leave only the measured pressures, p_i , in the ratio of differences of pressure coefficients.

$$\frac{\frac{1}{2}(p_1 - p_3)}{p_5 - \frac{1}{2}(p_1 + p_3)} = \frac{\frac{1}{2}(f_1 - f_3)}{f_5 - \frac{1}{2}(f_1 + f_3)} = \frac{a_{1,1}\theta}{(a_{5,2} - a_{1,2})\theta^2 + 1 - a_{1,0}} \quad (\text{A.38})$$

Equation A.38 is a quadratic in θ , which appears contrary to the conclusion based on the inverse function theorem that the function A.5 was single valued. However, the function A.5 was single valued within the range of pitch angles used for calibration. Experience has shown that one root of Equation A.38 lies within the range of pitch angles while the second root lies well outside the range of pitch angles. In practice there has been no difficulty deciding which root of Equation A.38 is correct.

The value of θ found using A.38 was used in Equation A.39 to calculate the total and static pressure.

$$\begin{bmatrix} a_{1,0} + a_{1,2}\theta^2 & 1 - a_{1,0} - a_{1,2}\theta^2 \\ 1 + a_{5,2}\theta^2 & -a_{5,2}\theta^2 \end{bmatrix} \begin{bmatrix} p_0 \\ p \end{bmatrix} = \begin{bmatrix} \frac{1}{2}(p_1 + p_3) \\ p_5 \end{bmatrix} \quad (\text{A.39})$$

These values were then used in Equation A.40 to determine the Mach number.

$$M = \sqrt{\left[\left(\frac{p_0}{p} \right)^{\frac{\gamma-1}{\gamma}} - 1 \right] \frac{2}{\gamma-1}} \quad (\text{A.40})$$

Figure A.4 shows a nulled five-hole probe and the flow direction relative to the probe coordinate system. In this coordinate system the z' -axis is parallel with the probe shaft. The x' -axis is parallel to the probe pitch plane when $\psi = \psi_0$. The angle ψ_0 is the yaw reference angle. The components of a unit length vector in the flow direction relative to the probe coordinate system are given by Equation A.41.

$$\begin{bmatrix} u_{x'} \\ u_{y'} \\ u_{z'} \end{bmatrix} = \begin{bmatrix} \cos(\psi - \psi_0) \cos(\theta - \theta_0) \\ \sin(\psi - \psi_0) \cos(\theta - \theta_0) \\ \sin(\theta - \theta_0) \end{bmatrix} \quad (\text{A.41})$$

To determine the flow direction relative to the probe coordinate system required knowing the total pitch difference angle θ_0 and the yaw reference angle ψ_0 . Two ways of finding the angle θ_0 are:

1. Make a reference flow measurement at a location where the flow direction is known relative to the probe coordinate system.
2. Use the values of θ_0 found during calibration to estimate the value of θ_0 in the survey.

If a reference measurement was used to obtain θ_0 the measurement should be made under conditions where the Mach number and probe length-to-diameter ratio are nearly equal to the conditions expected in the survey. Usually, this reference measurement is made at a location in the experiment where the flow direction is known *a priori*, or in a different facility where the flow direction is known. The pitch angle θ , calculated from the reference pressure measurements, and the known pitch angle α are used to calculate θ_0 .

Estimating the angle θ_0 from calibration data was difficult because the angle θ_0 can change if the probe has been bent slightly after calibration. The reference

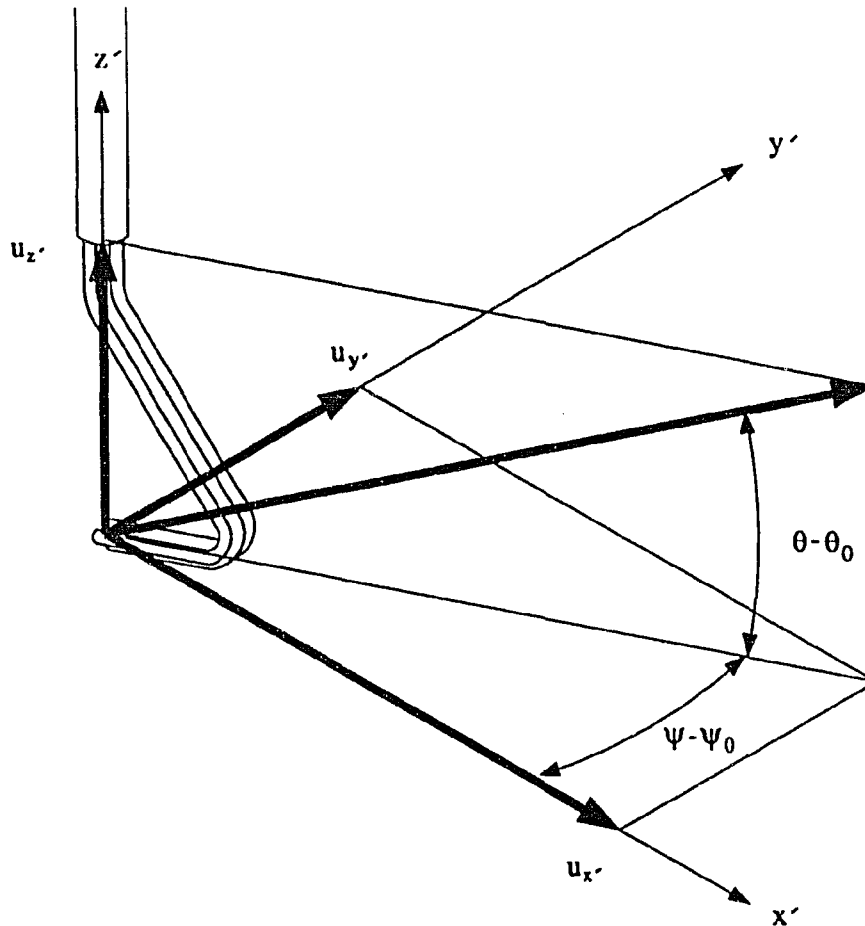


Figure A.4 Flow direction relative to the probe coordinate system measurement method was unaffected by any changes in the angle θ_0 occurring prior to the reference measurement.

The yaw reference angle ψ_0 was necessary for practical considerations. Typically, yaw angles are measured from an arbitrary origin. When the reference measurement was recorded, ψ_0 was assigned the value of the yaw angle at which the probe nulled. This allowed all future yaw angles to be referred to this angle.

To determine the flow direction relative to the experiment coordinate system required knowing the orientation of the probe relative to the experiment coordinate system. This orientation was determined by three angles, ϕ_1 , ϕ_2 , and ϕ_3 , shown in Figure A.5. The first angle, ϕ_1 , is a rotation about the z -axis, the second angle, ϕ_2 , is

a rotation about the new y -axis, the third angle, ϕ_3 , is a rotation about the new x -axis. Equation A.42 was used to transform the flow direction from probe coordinates to experiment coordinates.

$$\begin{bmatrix} u_x \\ u_y \\ u_z \end{bmatrix} = \begin{bmatrix} \cos \phi_1 & -\sin \phi_1 & 0 \\ \sin \phi_1 & \cos \phi_1 & 0 \\ 0 & 0 & 1 \end{bmatrix} \begin{bmatrix} \cos \phi_2 & 0 & -\sin \phi_2 \\ 0 & 1 & 0 \\ \sin \phi_2 & 0 & \cos \phi_2 \end{bmatrix} \begin{bmatrix} 1 & 0 & 0 \\ 0 & \cos \phi_3 & -\sin \phi_3 \\ 0 & \sin \phi_3 & \cos \phi_3 \end{bmatrix} \begin{bmatrix} u_{x'} \\ u_{y'} \\ u_{z'} \end{bmatrix} \quad (\text{A.42})$$

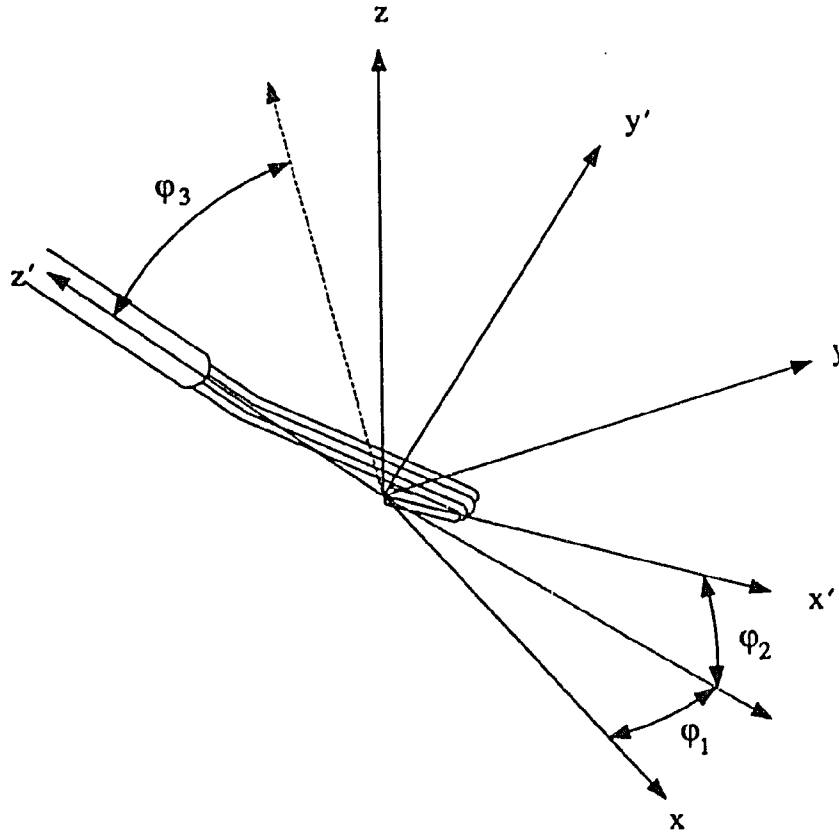


Figure A.5 The relation between the probe coordinate system and the experiment coordinate system

A Fortran Program For Five-Hole Probe Calibration

```

c-----|-----|-----|-----|-----|-----|-----|c
c
c          PCAL 1.1 (03/09/90)
c
c          Bruce Reichert
c          Mail Stop 5-11
c          NASA Lewis Research Center
c          21000 Brookpark Road
c          Cleveland OH 44135
c          (216) 433-8397
c
c-----|-----|-----| Purpose |-----|-----|-----|c
c
c The purpose of this program is to determine the four coefficients
c required to approximate the nondimensional pressures measured
c during the five-hole probe calibration procedure.
c
c-----|-----|----- Input - Output -----|-----|-----|c
c
c The input file is the calibration data. This is an ASCII file
c named WW_XX.MM_DD_YY where the WW_XX is the probe serial number
c and MM_DD_YY is the date of the calibration. The first record is
c an integer equal to the number of different Mach numbers for which
c calibration data were recorded. The calibration data follows
c grouped by Mach number. The first record is the number of different
c pitch angles recorded at the particular Mach number followed by the
c Mach number. This is followed by the data recorded for each pitch
c angle. The format for this data is (2(2x, f6.2), 7(2x, f7.3)) and
c is written in the order alpha, psi, p1, p2, p3, p4, p5, p0, p.
c
c The output file contains the four calibration coefficients. Their
c format is (4f) and are written in the order a10, a11, a12, a52.
c
c-----|-----|----- Variables -----|-----|-----|c
c

```

```

c Real
c
c a10, a11, a12, a52 - The coefficients of the third order
c approximation of the nondimensional pressures as
c functions of theta.
c alpha - The pitch angle relative to the probe shaft.
c amat - A matrix used to calculate least square coefficients.
c bvec - A vector used to calculate least square coefficients.
c c0, c1 - The coefficients used to calculate theta0.
c mach - An array containing each flow field Mach number.
c p - Flow field static pressure.
c p0 - Flow field total pressure.
c p1, p2, p3, p4, p5 - The five measured probe pressures.
c theta - The pitch angle relative to the probe openings.
c theta0 - An array containing the total pitch difference angle for
c each Mach number.
c
c Integer
c
c n - An array containing the number of different pitch angles
c recorded for each Mach number.
c nmach - The number of different Mach numbers.
c
c Character
c
c date - The character representation of the five-hole probe
c calibration date.
c infile - The name of the input file
c outfile - The name of the output file
c serial - The character representation of the five-hole probe serial
c number.
c
c-----|-----|-----|-----|-----|-----|-----|c

```

```

real amat(4,4), bvec(4), theta0(10), mach(10)

```

```

integer n(10)

```

```

character*5 serial*5, date*8
character*80 infile, outfile

gamma = 1.40

write(*, '(a)') ' Enter probe serial number'
read(*, '(a)') serial

write(*, '(a)') ' Enter probe calibration date'
read(*, '(a)') date

infile = '/home1/fsreich/calibration/original/'
1      //serial//'. '//date
outfile = '/home1/fsreich/calibration/parameter/'
1      //serial//'. '//date

open(unit = 1, file = infile, status = 'old')
read(1, '(i)') nmach

c For each Mach number find the difference between the
c pitch angle relative to the probe shaft, alpha, and the pitch angle
c relative to the probe openings, theta. This is the total pitch
c difference angle, theta0.

do 10 k = 1, nmach

    read(1, '(i)') n(k)
    read(1, '(f)') mach(k)

    do 20 l = 1, n(k)

        read(1, '(2(2x, f6.2), 7(2x, f7.3))') alpha, psi, p1, p2, p3,
1          p4, p5, p0, p
        f1 = (p1 - p) / (p0 - p)
        f3 = (p3 - p) / (p0 - p)
        amat(1, 1) = amat(1, 1) + alpha
        amat(1, 2) = amat(1, 2) + 1.0
        amat(2, 1) = amat(2, 1) + alpha ** 2.0

```

```

    amat(2, 2) = amat(1, 1)
    bvec(1)    = bvec(1) + (f1 - f3)
    bvec(2)    = bvec(2) + (f1 - f3) * alpha
20  continue

    det = amat(1, 1) * amat(2, 2) - amat(2, 1) * amat(1, 2)
    c0  = (amat(1,1) * bvec(2) - amat(2, 1) * bvec(1)) / det
    c1  = (bvec(1) * amat(2,2) - bvec(2) * amat(1, 2)) / det
    theta0(k) = c0 / c1

    amat(1, 1) = 0.0
    amat(1, 2) = 0.0
    amat(2, 1) = 0.0
    amat(2, 2) = 0.0
    bvec(1)    = 0.0
    bvec(2)    = 0.0

10  continue

    rewind(unit = 1)

c Curve fit the three dimensionless pressures as a function
c of true pitch angle.

    read(1, '(i)') nmach
    do 30 k = 1, nmach

        read(1, '(i)') n(k)
        read(1, '(f)') mach(i)

        do 40 l = 1, n(k)
            read(1, '(2(2x, f6.2), 7(2x, f7.3))') alpha, psi, p1, p2, p3,
1            p4, p5, p0, p
            f1 = (p1 - p) / (p0 - p)
            f3 = (p3 - p) / (p0 - p)
            f5 = (p5 - p) / (p0 - p)
            theta = alpha + theta0(k)
            amat(1, 1) = amat(1, 1) + 1.0

```

```

amat(1, 2) = amat(1, 2) + theta ** 2.0
amat(2, 2) = amat(2, 2) + theta ** 4.0
bvec(1)    = bvec(1) + 0.5 * (f1 + f3)
bvec(2)    = bvec(2) + 0.5 * (f1 + f3) * theta ** 2.0
bvec(3)    = bvec(3) + 0.5 * (f1 - f3) * theta
bvec(4)    = bvec(4) + f5 * theta ** 2.0

40    continue
30    continue

amat(2, 1) = amat(1, 2)
amat(3, 3) = amat(1, 2)
amat(4, 4) = amat(2, 2)

det = amat(1, 1) * amat(2, 2) - amat(2, 1) * amat(1, 2)
a10 = (bvec(1) * amat(2,2) - bvec(2) * amat(1, 2)) / det
a11 = bvec(3) / amat(3, 3)
a12 = (amat(1,1) * bvec(2) - amat(2, 1) * bvec(1)) / det
a52 = (bvec(4) - amat(1,2)) / amat(4, 4)

open(unit = 2, file = outfil, status = 'new')
write(2, '(4f)') a10, a11, a12, a52

stop
end

```

A Fortran Program For Five-Hole Probe Data Reduction

```

c-----|-----|-----|-----|-----|-----|-----|-----|c
c
c                      PDATA 1.1 (03/09/90)
c
c                      Bruce Reichert
c                      Mail Stop 5-11
c

```



```

c Real c
c
c amat - The matrix used to calculate total and static pressure. c
c bvec - The vector used to calculate total and static pressure. c
c gamma - The specific heat ratio. c
c h - The distance from the probe to the origin of the probe c
c coordinate system. c
c mach - The Mach number. c
c p - The static pressure. c
c phi1,phi2,phi3 - The three angles which determine the orientation c
c of the probe coordinate system with respect to the c
c experiment coordinate system. c
c p0 - The total pressure. c
c ux,uy,uz - The direction cosines of the flow direction with respect c
c to the experiment coordinate system. c
c ux1,uy1,uz1 - Intermediate results used in transforming the c
c ux2,uy2,uz2 direction cosines from the probe coordinate system c
c to the experiment coordinate system. c
c ux3,uy3,uz3 - The direction cosines of the flow direction with c
c respect to the probe coordinate system. c
c x,y,z - The cartesian coordinates with respect to the experimental c
c coordinate system of the location at which the data were c
c recorded. c
c x0,y0,z0 - The location of the origin of the probe coordinate c
c system with respect to the experiment coordinate system. c
c x1,y1,z1 - Intermediate results used in transforming the data c
c x2,y2,z2 location coordinates from the probe coordinate system c
c to the experiment coordinate system. c
c x3,y3,z3 - The cartesian coordinates with respect to the probe c
c coordinate system of the location at which the data were c
c recorded. c
c
c Integer c
c
c ndata - The number of locations at which data were recorded. c
c plane - The number of the data plane at which the data were c
c recorded. c
c slot - The number of the probe opening at which the data were c

```

```

c          recorded.
c
c Character
c
c date - The character representation of the five-hole probe
c        calibration date.
c
c machno - The character representation of the freestream Mach number
c          at which data were taken.
c
c outfil - The name of the output file.
c
c planno - The character representation of the number of the data
c          plane at which the data were recorded.
c
c serial - The character representation of the five-hole probe serial
c          number.
c
c slotno - The character representation of the number of the probe
c          opening at which the data were recorded.
c
c-----|-----|-----|-----|-----|-----|-----|-----|c
      real amat(2,2), bvec(2), mach

      integer plane, slot

      character serial*5, date*8, machno*7, planno*7, slotno*6
      character*80 infile(2), outfil

      pi = atan2(0.0, -1.0)
      gamma = 1.40

      write(*, '(a)') ' Enter probe serial number'
      read(*, '(a)') serial

      write(*, '(a)') ' Enter probe calibration date'
      read(*, '(a)') date

      write(*, '(a)') ' Enter Mach number'
      read(*, '(f)') mach
      if (mach .eq. 0.20) machno = 'mach20/'
      if (mach .eq. 0.35) machno = 'mach35/'
      if (mach .eq. 0.50) machno = 'mach50/'

```

```

write(*, '(a)') ' Enter plane number'
read(*, '(i)') plane
if (plane .eq. 1) planno = 'plane1/'
if (plane .eq. 2) planno = 'plane2/'
if (plane .eq. 3) planno = 'plane3/'
if (plane .eq. 4) planno = 'plane4/'

write(*, '(a)') ' Enter slot number'
read(*, '(i)') slot
if (slot .eq. 1) slotno = 'slot01'
if (slot .eq. 2) slotno = 'slot02'
if (slot .eq. 3) slotno = 'slot03'
if (slot .eq. 4) slotno = 'slot04'
if (slot .eq. 5) slotno = 'slot05'
if (slot .eq. 6) slotno = 'slot06'
if (slot .eq. 7) slotno = 'slot07'
if (slot .eq. 8) slotno = 'slot08'
if (slot .eq. 9) slotno = 'slot09'
if (slot .eq. 10) slotno = 'slot10'
if (slot .eq. 11) slotno = 'slot11'
if (slot .eq. 12) slotno = 'slot12'
if (slot .eq. 13) slotno = 'slot13'
if (slot .eq. 14) slotno = 'slot14'
if (slot .eq. 15) slotno = 'slot15'

infile(1) = '/home1/fsreich/calibration/parameter/' // serial
1          // '.' // date
infile(2) = '/home1/fsreich/pressure/original/' // machno
1          // planno // slotno
outfil    = '/home1/fsreich/pressure/reduced/' // machno
1          // planno // slotno

open(unit = 1, file = infile(1), status = 'old')
open(unit = 2, file = infile(2), status = 'old')
open(unit = 3, file = outfil, status = 'new')

write(*, '(a)') ' Enter x reference location, x0'
read(*, '(f)') x0

```

```
write(*, '(a)') ' Enter y reference location, y0'
read(*, '(f)') y0
```

```
write(*, '(a)') ' Enter z reference location, z0'
read(*, '(f)') z0
```

```
write(*, '(a)') ' Enter first transformation angle, phi1'
read(*, '(f)') phi1
```

```
write(*, '(a)') ' Enter second transformation angle, phi2'
read(*, '(f)') phi2
```

```
write(*, '(a)') ' Enter third transformation angle, phi3'
read(*, '(f)') phi3
```

c Read the calibration coefficients.

```
read(1, '(4f)') a10, a11, a12, a52
```

```
read(2, '(i)') ndata
write(3, '(i)') ndata - 1
```

c The first reading is expected to be the reference reading.

```
read(2, '(2x,f7.3,2x,f5.1,7(2x,f7.3))') h, psi0, p1, p2, p3, p4,
1      p5, ptotal, pstatic
```

c Calculate the reference pitch angle, theta0, and the reference
c yaw angle, psi0.

```
g = 0.5 * (p1 - p3) / (p5 - 0.5 * (p1 + p3))
a = g * (a52 - a12)
b = - a11
c = g * (1.0 - a10)
if (abs(g) .lt. 1.0e-008) then
  theta0 = 0.0
else
  thetal = (- b + sqrt(b * b - 4.0 * a * c)) / (2.0 * a)
```

```

theta2 = (- b - sqrt(b * b - 4.0 * a * c)) / (2.0 * a)
if (abs(theta1) .lt. abs(theta2)) then
  theta0 = theta1
else
  theta0 = theta2
end if
end if

theta0 = theta0 * pi / 180.0
psi0   = -psi0 * pi / 180.0

do 20 i = 1, ndata - 1

  read(2, '(2x,f7.3,2x,f5.1,5(2x,f7.3))') h, psi, p1, p2, p3, p4,
c      p5

```

c Calculate the pitch angle, theta.

```

g = 0.5 * (p1 - p3) / (p5 - 0.5 * (p1 + p3))
a = g * (a52 - a12)
b = - a11
c = g * (1.0 - a10)
if (abs(g) .lt. 1.0e-008) then
  theta = 0.0
else
  theta1 = (- b + sqrt(b * b - 4.0 * a * c)) / (2.0 * a)
  theta2 = (- b - sqrt(b * b - 4.0 * a * c)) / (2.0 * a)
  if (abs(theta1) .lt. abs(theta2)) then
    theta = theta1
  else
    theta = theta2
  end if
end if

```

c Use the pitch angle, theta, to determine the coefficients of the
c linear equation used to determine the total and static pressure.

```

amat(1, 1) = a10 + a12 * theta ** 2.0

```

```

amat(1, 2) = 1.0 - a10 - a12 * theta ** 2.0
amat(2, 1) = 1.0 + a52 * theta ** 2.0
amat(2, 2) = -a52 * theta ** 2.0
bvec(1)    = 0.5 * (p1 + p3)
bvec(2)    = p5

```

c Calculate the total and static pressure by solving the linear
c equation.

```

det = amat(1, 1) * amat(2, 2) - amat(2, 1) * amat(1, 2)
p0  = (bvec(1) * amat(2, 2) - bvec(2) * amat(1, 2)) / det
p   = (amat(1, 1) * bvec(2) - amat(2, 1) * bvec(1)) / det

```

c Calculate the Mach number from the total and static pressure.

```

mach = sqrt( (2.0 / (gamma - 1.0)) * (((p0/p) ** ((gamma - 1.0)
1      / gamma)) - 1.0))

```

c Convert the pitch and yaw angles from degrees to radians.

```

theta = theta * pi / 180.0
psi    = -psi * pi / 180.0

```

c Calculate the direction cosines and data location relative to
c the probe coordinate system.

```

ux3 = cos(psi - psi0) * cos(theta - theta0)
uy3 = sin(psi - psi0) * cos(theta - theta0)
uz3 =                    sin(theta - theta0)

x3 = 0
y3 = 0
z3 = h

```

c Transform the direction cosines and data location from the probe
c coordinate system to the experiment coordinate system. This is
c done in three transformations corresponding to the three angles,
c phi1, phi2, phi3, which define the orientation of the probe

c coordinate system relative to the experiment coordinate system.

```

ux2 = ux3
uy2 = uy3 * cos(phi3) - uz3 * sin(phi3)
uz2 = uy3 * sin(phi3) + uz3 * cos(phi3)

x2 = x3
y2 = y3 * cos(phi3) - z3 * sin(phi3)
z2 = y3 * sin(phi3) + z3 * cos(phi3)

ux1 = ux2 * cos(phi2) - uz2 * sin(phi2)
uy1 = uy2
uz1 = ux2 * sin(phi2) + uz2 * cos(phi2)

x1 = x2 * cos(phi2) - z2 * sin(phi2)
y1 = y2
z1 = x2 * sin(phi2) + z2 * cos(phi2)

ux = ux1 * cos(phi1) - uy1 * sin(phi1)
uy = ux1 * sin(phi1) + uy1 * cos(phi1)
uz = uz1

x = x0 + x1 * cos(phi1) - y1 * sin(phi1)
y = y0 + x1 * sin(phi1) + y1 * cos(phi1)
z = z0 + z1

write(3, '(9(2x,f7.3))') x, y, z, p0, p, mach, ux, uy, uz

```

20 continue

stop

end

APPENDIX B. A NUMERICAL PROCEDURE FOR INTERPOLATION OF IRREGULARLY DISTRIBUTED DATA

This appendix describes the procedure used to interpolate data known at locations that are irregularly distributed throughout a plane. Given the finite set of known data values (x_i, y_i, z_i) the interpolating function $f(x, y)$ satisfies $z_i = f(x_i, y_i)$ for all known values. The interpolating function is used to calculate interpolated values at the desired (x, y) coordinates. The term irregularly distributed means that it is not possible to construct a quadrilateral grid using the known data coordinates as the vertices of the quadrilaterals.

Bivariate interpolation procedures can be categorized as global methods or local methods. Global interpolation methods use all the known data to calculate the interpolated value at the desired coordinate. Global methods can become excessively cumbersome when the number of known data points is large and can lead to unwanted oscillations in the interpolating function. Local interpolation methods offer an improvement to the problems of global methods by only using a subset of the known data to calculate the interpolated value at the desired coordinate. This requires a rational procedure to determine which of the known data are used to calculate the interpolated value. Often, this is done by partitioning the irregularly distributed data into a triangular grid using the known data coordinates as the vertices of the triangles. The procedure of constructing a triangular grid from the irregularly distributed data is referred to as triangulation.

There is available in the IMSL library of Fortran subroutines a local bivariate interpolation program for irregularly distributed data. This program was written by Akima and is described in References 68, 69. Akima's program constructs a triangular grid and calculates local interpolating functions that possess continuous first derivatives. This procedure was not used for two reasons. First, because the interpolating functions have continuous first derivatives there will be some oscillation,

although much less severe than global methods. Second, and more importantly, the numerical procedure described in Appendix C requires an intermediate result of the interpolation procedure, the triangular grid. This information cannot be obtained from the IMSL subroutine and the Akima program is copyrighted and the source code is unavailable. For these two reasons a new interpolation program was written.

The procedure described in this appendix to interpolate irregularly distributed data was divided into two parts. The first part involves constructing the triangular grid from the irregularly distributed data. The second part is the actual interpolation. In practice, the triangulation requires more sophisticated programming while the interpolation requires more computational effort. Each part is described in a separate section.

Triangulation

The triangulation procedure used was based on the methods described by Akima [68] and Lawson [70]. Triangular grids constructed from irregularly distributed data are not unique. Therefore, an optimizing criterion was used to determine which triangles are constructed. The optimizing criterion was designed to avoid creating long and thin triangles whenever possible.

The set of known data is arranged in ascending order according to Euclidian distance from an arbitrary reference point. The first data point was used here as the reference point. Lawson used the point having the smallest x coordinate and Akima used the midpoint of the two nearest points. The first two data points of the ordered data are always vertices of the first triangle constructed. The third vertex of the first triangle is found by examining the ordered data sequentially for the first noncolinear point. The data are then reordered by placing the point used as the third vertex of the first triangle in the third position of the ordered data and increasing by one the indices of all points from the previous location of the third point to the previous location of the point used as the third vertex.

Each triangle is recorded by the three indices associated with the points forming the vertices. All triangles are recorded in counter-clockwise order. Additionally, a record is made of the indices of the points which form the perimeter of the region of all constructed triangles. The perimeter record is also maintained in counter-clockwise order proceeding successively around the perimeter. The program proceeds sequentially through the ordered data from the fourth through the last point constructing all possible new triangles using the new point as one vertex and points on the perimeter as the other two vertices of each new triangle. Proceeding sequentially through the ordered data insures that new points will lie outside the perimeter of the triangularized region. Creating all possible triangles using the new point and perimeter points insures the triangularized region will remain convex.

For a new point, the test used to determine which points on the perimeter are used to construct new triangles can be visualized by drawing a line from the new point to each point on the perimeter. If this line cuts through the perimeter then that particular perimeter point is not used. The actual procedure used involves calculating the angles formed by the new point and successive pairs of adjacent points on the perimeter.

After all new triangles have been constructed for a new point, each new triangle and the neighboring triangle which shares a common edge are examined according to the local optimizing criterion. If the criterion requires rearranging the new triangle and its neighbor then two new triangles are constructed and each are examined for rearrangement. This process continues until all new triangles have been examined and all satisfy the local optimizing criterion.

The local optimizing criterion decides which of two possible triangles is constructed from the quadrilateral formed by two triangles sharing a common edge. The criterion used here calculates the four interior angles of the quadrilateral. The optimized triangles are constructed by placing the common edge through the point on the quadrilateral with the largest interior angle. The criterion used by Akima [68] and Lawson [70] is referred to as the max-min angle criterion which creates the pair of triangles with the greatest least interior angle.

Linear Interpolation

In this program the interpolated value is calculated at the desired point (x, y) . This is done by first determining which triangle the desired point is a member of and then calculating the interpolated value for the point. If the point lies outside the convex hull containing all the known points, and therefore is not a member of any triangle, an arbitrary value (here zero) is recorded for the interpolated value.

A method suggested by Akima [68] was used to accelerate the procedure which determines of which triangle the desired point is a member. This method is most useful when interpolated values are desired at many locations. This method avoids testing the entire set of triangles by dividing the region in which the interpolation is desired into four quadrants. A list is prepared for each quadrant of the triangles that have a nonempty intersection with that quadrant. For each point where interpolation is desired it is first determined to which quadrant the point is a member. Then, only the list of triangles for that quadrant is tested to determine of which triangle the point is a member.

After the correct triangle is found for the desired point the linear interpolation is calculated. To calculate the interpolation in the i th triangle, a basis B , given by Equation B.1, is first calculated from the three points $(x_{i,1}, y_{i,1})$, $(x_{i,2}, y_{i,2})$, $(x_{i,3}, y_{i,3})$ which are the vertices of the triangle. The coordinates (α, β) of the point (x, y) with respect to the basis B are then calculated using Equation B.2. This result is used to calculate the interpolation using Equation B.3.

$$B = \{(x_2 - x_1, y_2 - y_1), (x_3 - x_1, y_3 - y_1)\} \quad (\text{B.1})$$

$$\begin{bmatrix} \alpha \\ \beta \end{bmatrix} = \begin{bmatrix} x_{i,2} - x_{i,1} & x_{i,3} - x_{i,1} \\ y_{i,2} - y_{i,1} & y_{i,3} - y_{i,1} \end{bmatrix}^{-1} \begin{bmatrix} x - x_{i,1} \\ y - y_{i,1} \end{bmatrix} \quad (\text{B.2})$$

$$z = z_{i,1} + \alpha(z_{i,2} - z_{i,1}) + \beta(z_{i,3} - z_{i,1}) \quad (\text{B.3})$$

A Fortran Program For Triangulation

```

c-----|-----|-----|-----|-----|-----|-----|c
c
c          TRIANGLE 2.0 (08/07/89)
c
c          Bruce Reichert
c          Mail Stop 5-11
c          NASA Lewis Research Center
c          2100C Brookpark Road
c          Cleveland, Ohio 44135
c          (216) 433-8397
c
c-----|-----|-----| Purpose |-----|-----|-----|c
c
c The purpose of TRIANGLE is to triangulate the x-y plane (divide
c the x-y plane into triangular cells) using the supplied set of
c irregularly distributed 2D data points as the vertices of the
c triangular cells. These triangles can be used later for analysis
c of the data (e.g. interpolation, graphical display, statistical
c analysis).
c
c-----|-----|----- Input - Output -----|-----|-----|c
c
c The input to TRIANGLE is a file containing the set of 2D data
c points to triangulate. The first record must be the number of
c points in the dataset. The following records must contain the
c the x and y values in the first and second fields. Only the first
c two fields of each record are read, subsequent fields are
c ignored.
c
c The first record of the output file is the number of triangles
c constructed. The following records each have three fields
c containing the three vertices of a triangle. The vertices are
c written not as x-y coordinates but as the integer number of the
c datapoint (the order of the data points occurrence in the input
c file).

```

```

c
c-----|-----|----- Variables -----|-----|-----|c
c
c Real
c
c xydata - The array of data points used to construct the triangles. c
c         xydata is arranged in order from least to greatest c
c         distance from the the first data point. c
c distan - The array containing the distance from the first data c
c         point. This is used only to arrange the order of xydata. c
c
c Integer
c
c index - The array that contains the original location of the data c
c         points in the input file. c
c irow - The current data point in the array xydata. c
c ldata - The total number of data points in the array xydata. c
c triang - The array containing the vertices of the triangles. c
c mdata - The current number of triangles in the array triang. c
c ntri - The number of new triangles constructed using the current c
c         data point. c
c perim - The array containing the vertices of the triangles that c
c         lie on the perimeter of the triangulated domain. c
c ndata - The current number of vertices in the array perim. c
c
c Character
c
c file1 - The name of the input file containing the set of data c
c         points. c
c file2 - The name of the ouput file containing the vertices of the c
c         triangles. c
c
c-----|-----|-----| Method -|-----|-----|-----|c
c
c To triangulate the x-y plane the data set is first ordered from c
c least to greatest distance from the first point of the data set. c
c Triangles are then constructed by proceeding sequentially through c
c this ordered array. Ordering the data points from least to c

```

```

c greatest distance insures that the new data point will lie outside c
c the domain of existing triangles. c
c c
c New triangles are constructed by determining what vertices of c
c existing triangles the new data point can "see". Only points on c
c the perimeter of the domain of the existing triangles need to be c
c considered. c
c c
c The newly constructed triangles are then inspected to determine c
c if they need rearranged. This is done by finding the existing c
c triangle that lies adjacent to the new triangle. The four c
c vertices of these two adjacent triangles form a quadrilateral. c
c By constructing a diagonal line between opposite vertices of the c
c quadrilateral two possible sets of triangles can be formed. c
c The triangles which are constructed are those formed by placing c
c the diagonal through the largest interior angle of the c
c quadrilateral. The vertices of triangles are always written in c
c counter-clockwise order. c
c c
c-----|-----|-----|-----|-----|-----|-----|-----|c

```

```

common      xydata,          triang,          perim
common      pi,            twopi,          ntri
common      ldata,         mdata,         ndata
common      irow

```

```

real        xydata(10000,2),  distan(10000)
integer     triang(20000,3),  perim(10000),  index(10000)
character*80 file1, file2

```

```

pi = atan2(0.0, -1.0)
twopi = 2 * pi

```

```

write (*, '(a)') ' Enter the cartesian data file name'
read (*, '(a)') file1
open (unit = 1, file = file1, status = 'old')

```

```

write (*, '(a)') ' Enter the triangle data file name'

```

```

read (*, '(a)') file2
open (unit = 2, file = file2, status = 'new')

read (1, '(i)') ldata

c Order the data from the file file1 into the array xydata from
c least to greatest distance from the first point in the file
c file1.

read (1, '(2f)') x, y
xydata(1, 1) = x
xydata(1, 2) = y
index(1)     = 1
distan(1)    = 0.0

c Read the ith row of data from file1 and calculate its distance
c from the first point.

do 10 i = 2, ldata

read (1, '(2f)') x, y
r = (x - xydata(1, 1)) ** 2 + (y - xydata(1, 2)) ** 2

c Compare the distance of the point in the jth row of the array
c xydata (which currently has values in rows 1 to i - 1) with the
c distance of the point in the ith row of the file file1. If the
c distance of the point in the ith row from file1 is less than the
c distance of the point in the jth row of the array xydata then
c move all the values of the array xydata from rows j+1 to the end
c (row i - 1) ahead one row to make room in the array xydata for
c the new row. If the distance of the point in the jth row of the
c array xydata is greater than or equal to the distance of all the
c points in the rows of the array work than j will exit the
c comparison loop with a value j = 1 and row shifting loop will
c not execute.

do 20 j = 1, i - 1
  if (r .lt. distan(j)) goto 30

```

```
20   continue
```

```
30   do 40 k = i, j + 1, -1
      xydata(k, 1) = xydata(k-1, 1)
      xydata(k, 2) = xydata(k-1, 2)
      index(k)     = index(k-1)
      distan(k)    = distan(k-1)
```

```
40   continue
```

```
c   Now add the ith row of from file file1 into the proper kth row
c   of the array xydata.
```

```
      xydata(j, 1) = x
      xydata(j, 2) = y
      index(j)     = i
      distan(j)    = r
```

```
10   continue
```

```
      irow = 2
50   irow = irow + 1
```

```
c   Calculate the angle formed by the first two points seen from the
c   irow-th data point. Use this to determine if the three points can
c   form a triangle.
```

```
      theta = atan2(xydata(2, 1) - xydata(irow, 1),
1             xydata(2, 2) - xydata(irow, 2))
2      - atan2(xydata(1, 1) - xydata(irow, 1),
3             xydata(1, 2) - xydata(irow, 2))
```

```
      if (theta .le. 0.0) theta = theta + twopi
      if (theta .eq. twopi) goto 50
      if (theta .le. pi) then
```

```
c   Construct the first triangle and perimeter in the proper counter-
c   clockwise order.
```

```

    triang(1, 1) = 1
    triang(1, 2) = 3
    triang(1, 3) = 2
    perim(1) = 1
    perim(2) = 3
    perim(3) = 2

```

```

else

```

```

    triang(1, 1) = 2
    triang(1, 2) = 3
    triang(1, 3) = 1
    perim(1) = 2
    perim(2) = 3
    perim(3) = 1

```

```

end if

```

```

c Remove the irow-th values from the array xydata and index and move
c rows 3 to irow - 1 ahead one position. Place the original irow-th
c values in row 3.

```

```

    x = xydata(irow, 1)
    y = xydata(irow, 2)
    n = index(irow)

```

```

do 60 j = irow, 4, -1
    xydata(j, 1) = xydata(j - 1, 1)
    xydata(j, 2) = xydata(j - 1, 2)
    index(j)    = index(j - 1)

```

```

60 continue

```

```

xydata(3, 1) = x
xydata(3, 2) = y
index(3)    = n

```

```

mdata = 1
ndata = 3

```

```
c Continue sequentially through the array xydata adding new triangles
c and then rearranging them if necessary.
```

```
do 70 irow = 4, ldata
  call newtri
  call arrang
```

```
70 continue
```

```
c Write the results to the output file.
```

```
write (2, '(i)') mdata
do 80 i = 1, mdata
  write (2, '(3(i))') index(triang(i, 1)), index(triang(i, 2)),
1      index(triang(i, 3))
80 continue
```

```
stop
end
```

```
subroutine newtri
```

```
c-----|-----|-----| Purpose |-----|-----|-----|-----|c
c
c This subroutine determines what points on the perimeter the
c new data point can "see" and then creates new triangles with
c those points. After this is complete the perimeter array
c is updated.
c
c-----|-----|-----| Variables -----|-----|-----|-----|c
c
c Real
c
c angle - An array that contains the angle between the new data
c point and each point on the perimeter.
c theta - The angle formed formed by two adjacent points on the
c perimeter as seen from the new data point.
c
```

```

c
c Integer
c
c ifalse - The location preceeding the first occurrence of the logical
c          value true in the array see.
c itrue  - The location preceeding the first occurrence of the logical
c          value false in the array see.
c ntrue  - The total number of occurrences of the logical value true
c          in the array see.
c work   - An array used as a work space to update the array perim.
c
c Logical
c
c see    - An array that contains a logical value of true for each
c          point on the perimeter if it can be seen from the new
c          data point.
c
c-----|-----|-----|-----|-----|-----|-----|-----|c

      common      xydata,          triang,          perim
      common      pi,              twopi,          ntri
      common      ldata,          mdata,          ndata
      common      irow

      real        xydata(10000,2),  angle(10000)
      integer     triang(20000, 3), perim(10000), work(10000)
      logical     see(10000)

c Calculate the angle from the new data point to the points
c on the perimeter

      do 10 i = 1, ndata
         j = perim(i)
         angle(i) = atan2(xydata(j, 1) - xydata(irow, 1),
1             xydata(j, 2) - xydata(irow, 2))
10 continue

      ntrue = 0

```

```

ntri = 0

do 20 i = 1, ndata - 1

c Calculate the angle formed by two adjacent points on the
c perimeter as seen from the new data point. Use this to
c determine if the two points can be seen from the new data
c point.

theta = angle(i + 1) - angle(i)
if (theta .le. 0.0) theta = theta + twopi
if (theta .le. pi) then

c Construct the new triangle.

ntri = ntri + 1
mdata = mdata + 1
triang(mdata, 1) = perim(i)
triang(mdata, 2) = irow
triang(mdata, 3) = perim(i + 1)

ntrue = ntrue + 1
see(i) = .true.

else

see(i) = .false.

end if

20 continue

theta = angle(1) - angle(ndata)
if (theta .le. 0.0) theta = theta + twopi
if (theta .le. pi) then

ntri = ntri + 1
mdata = mdata + 1

```

```

triang(mdata, 1) = perim(ndata)
triang(mdata, 2) = irow
triang(mdata, 3) = perim(1)

```

```

ntrue          = ntrue + 1
see(ndata)     = .true.

```

```

else

```

```

    see(ndata)     = .false.

```

```

end if

```

c Place the new perimeter points into the array work.

```

if (see(1)) then

```

```

    do 30 i = 2, ndata
        if (.not.see(i)) goto 40
30    continue

    40    itrue = i - 1

        do 50 i = 1, ndata - ntrue
            work(i) = perim(i + itrue)
50    continue

        if (itrue .lt. ntrue) then
            work(i) = perim(i + itrue)
        else
            work(i) = perim(1)
        end if

```

```

    i = i + 1

```

```

else

```

```

    do 60 i = 2, ndata

```

```

        if (see(i)) goto 70
60    continue

70    ifalse = i - 1

        do 80 i = 1, ndata - (ifalse + ntrue)
            work(i) = perim(i + (ifalse + ntrue))
80    continue

        do 90 i = ndata - (ifalse + ntrue) + 1, ndata - ntrue + 1
            work(i) = perim(i - (ndata - (ifalse + ntrue)))
90    continue

    end if

    work(i) = irow
    ndata = ndata - ntrue + 2

c Write the results of the new perimeter contained in the array
c work into the array perim.

    do 100 i = 1, ndata
        perim(i) = work(i)
100    continue

    return
    end

subroutine arrang

c-----|-----|-----| Purpose |-----|-----|-----|-c
c
c This subroutine inspects the newly constructed triangles and
c rearranges them if necessary. If triangles are rearranged
c they are listed as new triangles and inspected for rearrangement.
c
c
c-----|-----|----- Variables -----|-----|-----|-c

```

```

c
c Real
c
c alphax - This is the angle from the xth vertex to adjacent vertex
c           moving in the counter-clockwise direction
c betax  - This is the interior angle of the the xth vertex of the
c           quadralateral.
c
c Integer
c
c pointx - This is the xth point of the quadralateral.
c
c-----|-----|-----|-----|-----|-----|-----|-----|c

      common      xydata,      triang,      perim
      common      pi,          twopi,       ntri
      common      ldata,      mdata,      ndata
      common      irow

      real        xydata(10000, 2)
      integer     triang(20000, 3), perim(10000)
      integer     point1, point2, point3, point4

c Select the new triangle.

10   do 20 i = mdata - ntri + 1, mdata

      point1 = triang(i, 1)
      point2 = triang(i, 2)
      point3 = triang(i, 3)

c Find the adjacent triangle.

      do 30 j = mdata - ntri, 1, -1

          do 40 k = 1, 3

              if (point1 .eq. triang(j, k)) then

```

```

do 50 l = 1, 3

    if (point3 .eq. triang(j, 1)) then

c Form the quadralateral with the adjacent triangle.

        point4 = triang(j, 6 - k - 1)

c Calculate the angles between the vertices of quadralateral.

        alpha1 = atan2(xydata(point2, 1) - xydata(point1, 1),
1                xydata(point2, 2) - xydata(point1, 2))

        alpha2 = atan2(xydata(point3, 1) - xydata(point2, 1),
1                xydata(point3, 2) - xydata(point2, 2))

        alpha3 = atan2(xydata(point4, 1) - xydata(point3, 1),
1                xydata(point4, 2) - xydata(point3, 2))

        alpha4 = atan2(xydata(point1, 1) - xydata(point4, 1),
1                xydata(point1, 2) - xydata(point4, 2))

c Calculate the interior angles of the quadralateral.

        beta1 = alpha1 - alpha4 + pi
        if (beta1 .lt. 0.0) beta1 = beta1 + twopi
        if (beta1 .ge. twopi) beta1 = beta1 - twopi

        beta2 = alpha2 - alpha1 + pi
        if (beta2 .lt. 0.0) beta2 = beta2 + twopi
        if (beta2 .ge. twopi) beta2 = beta2 - twopi

        beta3 = alpha3 - alpha2 + pi
        if (beta3 .lt. 0.0) beta3 = beta3 + twopi
        if (beta3 .ge. twopi) beta3 = beta3 - twopi

        beta4 = alpha4 - alpha3 + pi
        if (beta4 .lt. 0.0) beta4 = beta4 + twopi

```

```
if (beta4 .ge. twopi) beta4 = beta4 - twopi
```

c Rearrange the triangles if necessary.

```
if (max(beta2, beta4) .gt. max(beta1, beta3)) then
  triang(j, 1) = triang(mdata - ntri, 1)
  triang(j, 2) = triang(mdata - ntri, 2)
  triang(j, 3) = triang(mdata - ntri, 3)
  triang(mdata - ntri, 1) = point1
  triang(mdata - ntri, 2) = point2
  triang(mdata - ntri, 3) = point4
  triang(i, 1) = point4
  triang(i, 2) = point2
  triang(i, 3) = point3
  ntri = ntri + 1
  goto 10
end if
```

```
goto 20
```

```
end if
```

```
50      continue
```

```
end if
```

```
40      continue
```

```
30      continue
```

```
20      continue
```

```
return
```

```
end
```

A Fortran Program for Linear Interpolation

```

c-----|-----|-----|-----|-----|-----|-----|c
c
c          LINEAR 2.1 (02/19/90)
c
c          Bruce Reichert
c          Mail Stop 5-11
c          NASA Lewis Research Center
c          21000 Brookpark Road
c          Cleveland, Ohio 44135
c          (216) 433-8397
c
c-----|-----|-----| Purpose |-----|-----|-----|c
c
c The purpose of LINEAR is provide a 2D linear interpolation between
c irregularly distributed 2D data points.
c
c-----|-----|-----| Input - Output |-----|-----|-----|c
c
c The inputs to LINEAR are a file containing the set of 2D data
c points, the file produce by TRIANGLE containing the triangles
c constructed from the set of 2D data points, and the file
c containing the x and y coordinates of the points where the
c interpolation is desired.
c
c The output is the interpolated value for the given location. It
c is written in the output file as f(i) for the point x(i), y(i).
c
c-----|-----|-----| Variables |-----|-----|-----|c
c
c Real
c
c xydata - The array of 2D data points and their function value to
c          interpolate between.
c
c x, y   - Two arrays that contain the x and y coordinates of the
c          points where interpolation is desired.

```

```

c  rx, ry - Arrays that define the x and y coordinates of the corners c
c          of the four regions. c
c  f      - The interpolated value at the point x(i), y(i). c
c c c c
c  Integer c
c c c c
c  ldata - The total number of data points in the array xydata. c
c  mdata - The total number of triangles in the array triang. c
c  ndata - An array containing the number of triangles in each region c
c  triang - The array containing the vertices of the triangles. c
c  nxy    - The total number of x and y coordinates in the arrays c
c          x and y. c
c  nreg   - The array that contains which region the triangles are c
c          members of. c
c  ntri   - The number of the triangle that the point x(i), y(i) c
c          lies within. c
c  region - An array that contains which triangles are members of each c
c          region. c
c c c c
c  Character c
c c c c
c  file1 - The name of the input file containing the set of 2D data c
c          points. c
c  file2 - The name of the input file containing the set of triangles c
c          constructed from the set of 2D data points. c
c  file3 - The name of the input file containing the set of x c
c          coordinates where interpolation is desired. c
c  file4 - The name of the output file containing the interpolated c
c          values. c
c c c c
c-----|-----|-----| Method -|-----|-----|-----|c
c c c c
c  The interpolation domain is first partitioned into four rectangular c
c  regions. The list of triangles is searched to find which triangles c
c  the points defining the corners of the four regions are members of. c
c  Then it is determined to which region the points that define the c
c  triangles are members. This produces a list of triangles that c
c  are members of each region. For the given point x(i), y(i) where c

```

```

c interpolation is desired it is first determined in which region the c
c point lies. Then the list of triangles that are members of that c
c region are searched to find to which triangle the point is a member.c
c A linear interpolation is then calculated using the three c
c vertices of the correct triangle. If the point lies outside the c
c data domain the interpolated value is recorded as 0. c
c c
c-----|-----|-----|-----|-----|-----|-----|-----|c

```

```

common xydata, triang, region
common ldata, mdata, ndata

real xydata(10000,3)
integer triang(20000,3), region(20000,5), ndata(5)
real x(1000), y(1000), rx(4, 2), ry(4,2)
character*80 file1, file2, file3, file4, file5
logical member

write (*, '(a)') 'Enter the irregularly distributed
+ cartesian data file name'
read (*, '(a)') file1
open (unit = 1, file = file1, status = 'old')
read (1, '(i)') ldata

write (*, '(a)') 'Enter the triangle data file name'
read (*, '(a)') file2
open (unit = 2, file = file2, status = 'old')
read (2, '(i)') mdata

write (*, '(a)') 'Enter the grid data file name'
read (*, '(a)') file3
open (unit = 3, file = file3, status = 'old')
read (3, '(i)') nxy

write (*, '(a)') 'Enter interpolation data file name'
read (*, '(a)') file5
open (unit = 4, file = file4, status = 'new')

```

```

do 10 i = 1, nxy
  read (3, '(1x,2(f10.5))') x(i), y(i)
10 continue

do 20 i = 1, ldata
  read (1, '(f14.6,f12.6,f13.6)') xx, yy, ff
  xydata(i, 1) = xx
  xydata(i, 2) = yy
  xydata(i, 3) = ff
20 continue

do 40 i = 1, mdata
  read (2, '(3i)') l1, l2, l3
  triang(i, 1) = l1
  triang(i, 2) = l2
  triang(i, 3) = l3
  region(i, 5) = i
40 continue
ndata(5) = mdata

```

c Determine the min and max of the new grid.

```

xmin = x(1)
xmax = x(1)
ymin = y(1)
ymax = y(1)

do 45 i = 2, nxy

  if (xmin .gt. x(i)) xmin = x(i)
  if (xmax .lt. x(i)) xmax = x(i)
  if (ymin .gt. y(i)) ymin = y(i)
  if (ymax .lt. y(i)) ymax = y(i)

45 continue

```

c Determine the boundaries for the four regions.

```

xmid = (xmin + xmax) / 2.0
ymid = (ymin + ymax) / 2.0

```

```

rx(1, 1) = xmin
ry(1, 1) = ymin
rx(1, 2) = xmid
ry(1, 2) = ymid

```

```

rx(2, 1) = xmid
ry(2, 1) = ymin
rx(2, 2) = xmax
ry(2, 2) = ymid

```

```

rx(3, 1) = xmin
ry(3, 1) = ymid
rx(3, 2) = xmid
ry(3, 2) = ymax

```

```

rx(4, 1) = xmid
ry(4, 1) = ymid
rx(4, 2) = xmax
ry(4, 2) = ymax

```

c Find which triangles the 16 points that define the
c four regions belong to.

```

do 50 i = 1, 4

```

```

    call which(rx(i, 1), ry(i, 1), 5, ntri)
    if (ntri .ne. 0) then
        call check(ntri, i, member)
        if (member .eq. .false.) then
            ndata(i) = ndata(i) + 1
            region(ndata(i), i) = ntri
        endif
    endif
endif

```

```

    call which(rx(i, 2), ry(i, 1), 5, ntri)

```

```

if (ntri .ne. 0) then
  call check(ntri, i, member)
  if (member .eq. .false.) then
    ndata(i) = ndata(i) + 1
    region(ndata(i), i) = ntri
  endif
endif

call which(rx(i, 1), ry(i, 2), 5, ntri)
if (ntri .ne. 0) then
  call check(ntri, i, member)
  if (member .eq. .false.) then
    ndata(i) = ndata(i) + 1
    region(ndata(i), i) = ntri
  endif
endif

call which(rx(i, 2), ry(i, 2), 5, ntri)
if (ntri .ne. 0) then
  call check(ntri, i, member)
  if (member .eq. .false.) then
    ndata(i) = ndata(i) + 1
    region(ndata(i), i) = ntri
  endif
endif

```

50 continue

c Find to which regions the three points that define each
c triangle belong to.

```

do 60 i = 1, ndata(5)
  do 70 j = 1, 3
    l = triang(i, j)
    xtri = xydata(l, 1)
    ytri = xydata(l, 2)
    do 80 k = 1, 4
      if (xtri .ge. rx(k, 1)) then

```

```

      if (xtri .le. rx(k, 2)) then
        if (ytri .ge. ry(k, 1)) then
          if (ytri .le. ry(k, 2)) then
            call check(i, k, member)
            if (member .eq. .false.) then
              ndata(k) = ndata(k) + 1
              region(ndata(k), k) = i
            endif
          end if
        end if
      end if
    end if
  end if
80   continue
70   continue
60   continue

```

```

do 90 i = 1, nxy
  do 100 j = 1, 4

```

c Find which region the point belongs.

```

      if (x(i) .ge. rx(j, 1)) then
        if (x(i) .le. rx(j, 2)) then
          if (y(i) .ge. ry(j, 1)) then
            if (y(i) .le. ry(j, 2)) then

```

c Find which triangle in this region the point belongs to

```

          call which (x(i), y(i), j, ntri)

```

c Calculate the linear interpolation.

```

          if (ntri .ne. 0) then
            call linint (x(i), y(i), f, ntri)
          else
            f = 0.0
          end if

```

```

        end if
        end if
        end if
        end if
100    continue

        write(5, '(f)') f

90    continue

    stop
    end

    subroutine which (x, y, nreg, j)

c This subroutine determines which triangle the point (x,y) lies within.

    common  xydata, triang, region
    common  ldata, mdata, ndata

    real    xydata(10000,3)
    integer triang(20000,3), region(20000,5), ndata(5)

    pi = atan2(0.0, -1.0)
    twopi = 2 * pi

    do 10 i = 1, ndata(nreg)

        j = region(i, nreg)
        x1 = xydata(triang(j,1), 1)
        y1 = xydata(triang(j,1), 2)
        x2 = xydata(triang(j,2), 1)
        y2 = xydata(triang(j,2), 2)
        x3 = xydata(triang(j,3), 1)
        y3 = xydata(triang(j,3), 2)

c Check to see if the point (x,y) coincides with a vertex.

```

```

if ((x.eq.x1).and.(y.eq.y1)) go to 20
if ((x.eq.x2).and.(y.eq.y2)) go to 20
if ((x.eq.x3).and.(y.eq.y3)) go to 20

```

c Check to see if the point (x,y) lies within the interior.

```

thetal = atan2(x1-x, y1-y)
theta2 = atan2(x2-x, y2-y)
theta3 = atan2(x3-x, y3-y)

```

```

phi12 = thetal-theta2
phi23 = theta2-theta3
phi31 = theta3-thetal

```

```

if (phi12.lt.0.0) phi12 = phi12 + twopi
if (phi23.lt.0.0) phi23 = phi23 + twopi
if (phi31.lt.0.0) phi31 = phi31 + twopi

```

```

if (((phi12.le.pi).and.(phi23.le.pi)).and.(phi31.le.pi)) goto 20

```

```

10  continue
    j = 0

```

```

20  return
    end

```

```

subroutine linint (x, y, f, i)

```

c This subroutine calculates a linear interpolation at the point x,y using
c the vertices of the ith triangle.

```

common  xydata,  triang,  region
common  ldata,  mdata,  ndata

```

```

real    xydata(10000,3)
integer triang(20000,3), region(20000,5), ndata(5)

```

```

real    bv1(3), bv2(3)

```

```

x1 = xydata(triang(i,1), 1)
y1 = xydata(triang(i,1), 2)
f1 = xydata(triang(i,1), 3)
x2 = xydata(triang(i,2), 1)
y2 = xydata(triang(i,2), 2)
f2 = xydata(triang(i,2), 3)
x3 = xydata(triang(i,3), 1)
y3 = xydata(triang(i,3), 2)
f3 = xydata(triang(i,3), 3)

```

c Create a basis for the plane.

```

bv1(1) = (x2 - x1)
bv1(2) = (y2 - y1)
bv1(3) = (f2 - f1)
bv2(1) = (x3 - x1)
bv2(2) = (y3 - y1)
bv2(3) = (f3 - f1)

```

c Calculate the coordinate of the point (x, y) with respect
c to the new basis.

```

det = bv1(1) * bv2(2) - bv2(1) * bv1(2)
c1 = ((x - x1) * bv2(2) - (y - y1) * bv2(1)) / det
c2 = ((y - y1) * bv1(1) - (x - x1) * bv1(2)) / det

f = f1 + c1 * bv1(3) + c2 * bv2(3)

return
end

```

```

subroutine check(ntri, nreg, member)

```

c This subroutine checks if triangle ntri is already
c listed with the triangles belonging to region nreg.

```

common xydata, triang, region
common ldata, mdata, ndata

```

```
real    xydata(10000,3)
integer triang(20000,3), region(20000,5), ndata(5)
logical member

do 10 i = 1, ndata(nreg)

    if (ntri .eq. region(i, nreg)) then
        member = .true.
        return
    end if

10 continue

member = .false.
return

end
```

APPENDIX C. A NUMERICAL PROCEDURE FOR CALCULATING MOMENTS OF A BIVARIATE DISTRIBUTION

This appendix describes the procedures used to calculate the moments of a bivariate distribution. In practice the distribution is not known, only values of the distribution at a finite number of points are known. In the first section the integrals used to determine the moments are examined by first considering the case where the distribution is known explicitly and then considering the actual case where the distribution is only known at discrete locations. The second section includes the Fortran source code which implements the algorithms derived in the first section.

The Calculation of Moments

The moments of the distribution f which were calculated are defined by Equation C.1. The integrals are over the domain Ω which contains the support of the distribution f . The integral of the distribution over Ω does not necessarily equal one and therefore appears in the denominator of Equation C.1.

$$E[\phi] = \frac{\int_{\Omega} \phi f dA}{\int_{\Omega} f dA}, \quad \phi = x, y, x^2, xy, y^2 \quad (\text{C.1})$$

From these moments the means, variances and covariance of the distribution are found using Equations C.2 through C.6

$$\mu_x = E[x] \quad (\text{C.2})$$

$$\mu_y = E[y] \quad (\text{C.3})$$

$$\sigma_x^2 = E[(x - \mu_x)^2] = E[x^2] - E^2[x] \quad (\text{C.4})$$

$$\sigma_y^2 = E[(y - \mu_y)^2] = E[y^2] - E^2[y] \quad (\text{C.5})$$

$$\sigma_{xy} = E[(x - \mu_x)(y - \mu_y)] = E[xy] - E[x]E[y] \quad (\text{C.6})$$

The distribution must be known to evaluate these moments. In practice, f is only known at a finite number of points, corresponding with the locations of experimental measurements. Because of the limited knowledge of the distribution, the calculations described are actually estimates of the moments. However, the calculated values approach the moments, with some restrictions on f , after sufficient refinement of the partition.

For a partition $\{\Delta_i\}_{i=1}^n$ of the domain Ω which satisfies the conditions C.7, the moments may be calculated as shown in Equation C.8. The partition used in calculating the moments is the one determined by the triangulation procedure described in Appendix B. The elements of the partition are the sets of points Δ_i which are the interior of the i th triangle whose vertices are the three points $(x_{i,1}, y_{i,1}), (x_{i,2}, y_{i,2}), (x_{i,3}, y_{i,3})$. Values of f are known only at the vertices.

$$\Omega = \bigcup_{i=1}^n \overline{\Delta_i}, \quad \Delta_i \cap \Delta_j = \begin{cases} \emptyset & i \neq j \\ \Delta_i & i = j \end{cases} \quad (\text{C.7})$$

$$E[\phi] = \frac{\int_{\Omega} \phi f dA}{\int_{\Omega} f dA} = \frac{\sum_{i=1}^n \int_{\Delta_i} \phi f dA}{\sum_{i=1}^n \int_{\Delta_i} f dA} \quad (\text{C.8})$$

To calculate the integrals used in evaluating the moments the change of variables shown in Equation C.9 was used. These change of variables have the beneficial effect of changing the integration from the elements of the partition Δ_i to the set D shown in Figure C.1

$$\begin{bmatrix} \alpha \\ \beta \end{bmatrix} = \begin{bmatrix} x_{i,2} - x_{i,1} & x_{i,3} - x_{i,1} \\ y_{i,2} - y_{i,1} & y_{i,3} - y_{i,1} \end{bmatrix}^{-1} \begin{bmatrix} x - x_{i,1} \\ y - y_{i,1} \end{bmatrix} \quad (\text{C.9})$$

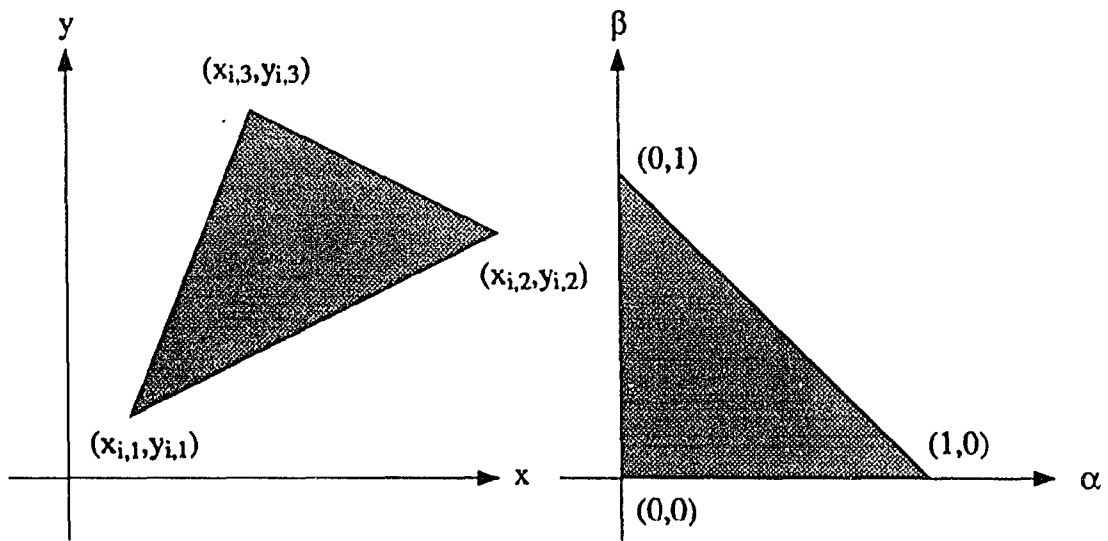


Figure C.1 The change of variables from Δ_i to D

A reasonable approximation of f to use in evaluating the integrals is the linear interpolation described in Appendix B. Using the change of variables described in the preceding paragraph, the linear approximation of the distribution is determined by Equation C.10.

$$f = f_{i,1} + \alpha(f_{i,2} - f_{i,1}) + \beta(f_{i,3} - f_{i,1}) \quad (\text{C.10})$$

By using the change of variables it was possible to calculate the integrals exactly for the linear interpolation of f . Equation C.11 is a result of the change of variable theorem of integration of a function of several variables.

$$dA = dx dy = \left| \frac{\partial(x, y)}{\partial(\alpha, \beta)} \right| d\alpha d\beta \quad (\text{C.11})$$

The Jacobian was evaluated using Equation C.12, where A_i is the area of the element of the partition Δ_i .

$$\begin{aligned} \left| \frac{\partial(x, y)}{\partial(\alpha, \beta)} \right| &= \begin{vmatrix} x_{i,2} - x_{i,1} & x_{i,3} - x_{i,1} \\ y_{i,2} - y_{i,1} & y_{i,3} - y_{i,1} \end{vmatrix} \\ &= \begin{bmatrix} x_{i,1} \\ x_{i,2} \\ x_{i,3} \end{bmatrix}^T \begin{bmatrix} 0 & 1 & -1 \\ -1 & 0 & 1 \\ 1 & -1 & 0 \end{bmatrix} \begin{bmatrix} y_{i,1} \\ y_{i,2} \\ y_{i,3} \end{bmatrix} \\ &= 2A_i \end{aligned} \quad (\text{C.12})$$

Since the points $(x_{i,1}, y_{i,1})$, $(x_{i,2}, y_{i,2})$, $(x_{i,3}, y_{i,3})$ and the values of the distribution at those points $f_{i,1}$, $f_{i,2}$, $f_{i,3}$ are constant, only products of α and β up to second order remain within the integral. Thus, the integrals were evaluated in advance without the specific knowledge of the partition or the distribution. All that remains is algebraic operations involving the points $(x_{i,1}, y_{i,1})$, $(x_{i,2}, y_{i,2})$, $(x_{i,3}, y_{i,3})$ and the values of the distribution at those points $f_{i,1}$, $f_{i,2}$, $f_{i,3}$.

An example calculation of the integral used to evaluate the moment $E[x]$ is shown in Equation C.13. The results of calculations for the remaining integrals are given in Equations C.14 through C.18. The coefficients a_j , $b_{j,k}$ and $c_{j,k,l}$ are given in Table C.2

$$\begin{aligned}
\int_{\Delta_i} x f dA &= \int (x_{i,1} + \alpha(x_{i,2} - x_{i,1}) + \beta(x_{i,3} - x_{i,1})) \\
&\quad (f_{i,1} + \alpha(f_{i,2} - f_{i,1}) + \beta(f_{i,3} - f_{i,1})) \left| \frac{\partial(x, y)}{\partial(\alpha, \beta)} \right| d\alpha d\beta \\
&= 2A_i \begin{bmatrix} x_{i,1} \\ x_{i,2} \\ x_{i,3} \end{bmatrix}^T \int_{\Delta} \begin{bmatrix} (1-\alpha-\beta)^2 & \alpha(1-\alpha-\beta) & \beta(1-\alpha-\beta) \\ \alpha(1-\alpha-\beta) & \alpha^2 & \alpha\beta \\ \beta(1-\alpha-\beta) & \alpha\beta & \beta^2 \end{bmatrix} d\alpha d\beta \begin{bmatrix} f_{i,1} \\ f_{i,2} \\ f_{i,3} \end{bmatrix} \\
&= A_i \begin{bmatrix} x_{i,1} \\ x_{i,2} \\ x_{i,3} \end{bmatrix}^T \begin{bmatrix} 1/6 & 1/12 & 1/12 \\ 1/12 & 1/6 & 1/12 \\ 1/12 & 1/12 & 1/6 \end{bmatrix} \begin{bmatrix} f_{i,1} \\ f_{i,2} \\ f_{i,3} \end{bmatrix} \\
&= A_i \sum_{j=1}^3 \sum_{k=1}^3 b_{j,k} x_j f_k
\end{aligned} \tag{C.13}$$

$$\int_{\Delta_i} f dA = A_i \sum_{j=1}^3 a_j f_{i,j} \tag{C.14}$$

$$\int_{\Delta_i} y f dA = A_i \sum_{j=1}^3 \sum_{k=1}^3 b_{j,k} y_j f_k \tag{C.15}$$

$$\int_{\Delta_i} x^2 f dA = A_i \sum_{l=1}^3 \sum_{k=1}^3 \sum_{j=1}^3 c_{j,k,l} x_j y_k f_l \tag{C.16}$$

$$\int_{\Delta_i} y^2 f dA = A_i \sum_{l=1}^3 \sum_{k=1}^3 \sum_{j=1}^3 c_{j,k,l} y_j x_k f_l \tag{C.17}$$

$$\int_{\Delta_i} x y f dA = A_i \sum_{l=1}^3 \sum_{k=1}^3 \sum_{j=1}^3 c_{j,k,l} y_j x_k f_l \tag{C.18}$$

Table C.1 The values of the coefficients a_j , $b_{j,k}$ and $c_{j,k,l}$

a_j	$j = 1$	$j = 2$	$j = 3$
	1/3	1/3	1/3
$b_{j,k}$	$k = 1$	$k = 2$	$k = 3$
$j = 1$	1/6	1/12	1/12
$j = 2$	1/12	1/6	1/12
$j = 3$	1/12	1/12	1/6
$c_{1,k,l}$	$l = 1$	$l = 2$	$l = 3$
$k = 1$	1/10	1/30	1/30
$k = 2$	1/30	1/30	1/60
$k = 3$	1/30	1/60	1/30
$c_{2,k,l}$	$l = 1$	$l = 2$	$l = 3$
$k = 1$	1/30	1/30	1/60
$k = 2$	1/30	1/10	1/30
$k = 3$	1/60	1/30	1/30
$c_{3,k,l}$	$l = 1$	$l = 2$	$l = 3$
$k = 1$	1/30	1/60	1/30
$k = 2$	1/60	1/30	1/30
$k = 3$	1/30	1/30	1/10

A Fortran Program For Two-Dimensional Moments Calculation

```

c-----|-----|-----|-----|-----|-----|-----|c
c
c          STATISTIC 1.1  (08/17/89)
c
c          Bruce A. Reichert
c          Mail Stop 5-11
c          NASA Lewis Research Center
c          21000 Brookpark Road
c          Cleveland, Ohio 44111
c          (216) 433-8397
c

```

```

c
c-----|-----|-----| Purpose |-----|-----|-----|c
c
c The purpose of STATISTIC is to calculate the means, variances,
c and covariance of a continuous bivariate distribution. The set
c of data are discrete values of the distribution which may be
c located irregularly throughout the plane.
c
c-----|-----|----- Input - Output -----|-----|-----|c
c
c There are two files required as input to STATISTIC. The first
c is a file containing the set of data. The first record must be
c the number of points in the data set. The following records must
c contain the x and y values in the first and second fields and the
c function value in the third field. Any remaining fields are
c ignored.
c
c The second input file required is the output of the program
c TRIANGLE. The first record is the number of triangles constructed
c from the data set. The following records each have three
c fields containing the three vertices of a triangle. The vertices
c are written as the integer number of the datapoint (the order
c of the data points occurrence in the input file).
c
c The output of STATISTIC is a file containing the mean of x, mean
c of y, variance of x, variance of y and covariance.
c
c-----|-----|----- Variables -----|-----|-----|c
c
c Real
c
c xydata - The array of data points taken from the first input file.
c cX      - Arrays that are used to calculate the integrals for each
c          individual triangle.
c area    - The areal of the current triangle.
c e1      - The integral E[1] for the current triangle.
c ex      - The integral E[X] for the current triangle.
c ey      - The integral E[Y] for the current triangle.

```

```

c  exx   - The integral E{X*X} for the current triangle.      c
c  exy   - The integral E{X*Y} for the current triangle.      c
c  eyy   - The integral E{Y*Y} for the current triangle.      c
c  sumel - The sum of each integral E{1} for all triangles.    c
c  sumex - The sum of each integral E{X} for all triangles.    c
c  sumey - The sum of each integral E{Y} for all triangles.    c
c  sumexx - The sum of each integral E{X*X} for all triangles. c
c  sumexy - The sum of each integral E{X*Y} for all triangles. c
c  sumeyy - The sum of each integral E{Y*Y} for all triangles. c
c  xmean - The mean x value of the distribution.                c
c  ymean - The mean y value of the distribution.                c
c  xvar  - The x variance of the distribution.                  c
c  xycov - The xy covariance of the distribution.                c
c  yvar  - The y variance of the distribution.                  c
c
c  Integer
c
c  ldata - The total number of data points in the array xydata. c
c  mdata - The total number of triangles.                       c
c  point - The array containing the three points the current   c
c          triangle.                                           c
c
c  Character
c
c  file1 - The name of the input file containing the set of data c
c          points.                                              c
c  file2 - The name of the input file containing the vertices of the c
c          triangles.                                           c
c  file3 - The name of the output file containing the statistics of c
c          the data set.                                         c
c
c-----|-----|-----| Method -|-----|-----|-----|c
c
c  This program calculates the statistics for each individual triangle c
c  and then sums each statistic for all triangles. For each triangle c
c  a linear approximation is assumed and the statistic is calculated c
c  exactly.
c
c

```

```
c-----|-----|-----|-----|-----|-----|-----|-----|c
```

```
real xydata(10000, 3), x(3), y(3), f(3)
real c1(3), c2(3,3), c3(3,3), c4(3,3,3)
integer point(3)
character*80 file1, file2, file3
```

c Establish some parameters to save some writting.

```
parameter ( p1 = 1.0 / 3.0, p2 = 1.0 / 6.0 )
parameter ( p3 = 1.0 / 10.0, p4 = 1.0 / 12.0 )
parameter ( p5 = 1.0 / 30.0, p6 = 1.0 / 60.0 )
```

c Create the arrays used to calculate the integrals.

```
data c1 / p1, p1, p1 /
data c2 / 0.0, 0.5, -0.5, -0.5, 0.0, 0.5, 0.5, -0.5, 0.0 /
data c3 / p2, p4, p4, p4, p2, p4, p4, p4, p2 /
data c4 / p3, p5, p5, p5, p5, p6, p5, p6, p5,
1      p5, p5, p6, p5, p3, p5, p6, p5, p5,
2      p5, p6, p5, p6, p5, p5, p5, p5, p3 /
```

```
write (*, '(a)') ' Enter cartesian data file name'
read (*, '(a)') file1
open (unit = 1, file = file1, status = 'old')
```

```
write (*, '(a)') ' Enter triangle data file name'
read (*, '(a)') file2
open (unit = 2, file = file2, status = 'old')
```

```
write (*, '(a)') ' Enter statistic file name'
read (*, '(a)') file3
open (unit = 3, file = file3, status = 'new')
```

c Load the data set from the first input file into the array xydata.

```
read (1, '(i)') ldata
do 10 i = 1, ldata
```

```

        read(1, '(3f)') xydata(i, 1), xydata(i, 2), xydata(i, 3)
10    continue

```

c Proceed sequentially through the list of triangles calculating
c the necessary integrals.

```

        read (2, '(i)') mdata
        do 20 i = 1, mdata

            read(2, '(3i)') point(1), point(2), point(3)

            do 30 j = 1, 3

                x(j) = xydata(point(j), 1)
                y(j) = xydata(point(j), 2)
                f(j) = xydata(point(j), 3)

30    continue

```

c Set the integrals for the new triangle to zero

```

        area = 0.0
        e1   = 0.0
        ex   = 0.0
        ey   = 0.0
        exx  = 0.0
        exy  = 0.0
        eyy  = 0.0

```

c Calculate the integrals for one triangle.

```

        do 40 j = 1, 3
            e1 = e1 + f(j) * c1(j)

            do 50 k = 1, 3

                area = area + x(j) * y(k) * c2(j, k)
                ex   = ex + x(j) * f(k) * c3(j, k)

```

```
    ey = ey + y(j) * f(k) * c3(j, k)

    do 60 l = 1, 3

        exx = exx + x(j) * x(k) * f(l) * c4(j, k, l)
        exy = exy + x(j) * y(k) * f(l) * c4(j, k, l)
        eyy = eyy + y(j) * y(k) * f(l) * c4(j, k, l)

60    continue

50    continue

40    continue

    area = abs(area)

    el = el * area
    ex = ex * area
    ey = ey * area
    exx = exx * area
    exy = exy * area
    eyy = eyy * area

c Sum the integrals for all triangles.

    sumel = sumel + el
    sumex = sumex + ex
    sumey = sumey + ey
    sumexx = sumexx + exx
    sumexy = sumexy + exy
    sumeyy = sumeyy + eyy

20    continue

c Normalize the resulting sum of integrals.

    xmean = sumex / sumel
    ymean = sumey / sumel
```

```
xvar = sumexx / sumel - xmean * xmean
xycov = sumexy / sumel - xmean * ymean
yvar = sumeyy / sumel - ymean * ymean

write (3, '(6f)') xmean, ymean, xvar, xycov, yvar, sumel

stop
end
```

BIBLIOGRAPHY

- 1 Stevens, H., Thayer, E. B., and Fullerton, J. F., "Development of the Multi-Function 2-D/C-D Nozzle," AIAA Paper 81-1491, 1981.
- 2 Anderson, B. H., "Three-Dimensional Viscous Design Methodology of Supersonic Inlet Systems for Advanced Technology Aircraft," in *Numerical Methods for Engine-Airframe Integration* (Murthy, S. N. B. and Paynter, G. C., eds.), pp. 431-480, AIAA, 1986.
- 3 Taylor, A. M. K. P., Whitelaw, J. H., and Yianneskis, M., "Measurement of Laminar and Turbulent Flow in a Curved Duct With Thin Inlet Boundary Layers," Imperial College of Science and Technology NASA Contractor Report 3367, 1981.
- 4 Taylor, A. M. K. P., Whitelaw, J. H., and Yianneskis, M., "Turbulent Flow in a Square-to-Round Transition," Imperial College of Science and Technology NASA Contractor Report 3447, 1981.
- 5 Taylor, A. M. K. P., Whitelaw, J. H., and Yianneskis, M., "Developing Flow in S-Shaped Ducts I - Square Cross-Section Duct," Imperial College of Science and Technology NASA Contractor Report 3550, 1982.
- 6 Taylor, A. M. K. P., Whitelaw, J. H., and Yianneskis, M., "Developing Flow in S-Shaped Ducts II - Circular Cross-Section Duct," Imperial College of Science and Technology NASA Contractor Report 3759, Feb. 1984.
- 7 Enayet, M. M., Gibson, M. M., Taylor, A. M. K. P., and Yianneskis, M., "Laser Doppler Measurements of Laminar and Turbulent Flow in a Pipe Bend," Imperial College of Science and Technology NASA Contractor Report 3551, 1982.
- 8 Vakili, A., Wu, J. M., Liver, P., and Bhat, M. K., "An Experimental Investigation of Secondary Flows in a S-Shaped Circular Duct," The University of Tennessee Space Institute Final Report for NASA Contract NAG3 233, June 1983.

- 9 Vakili, A., Wu, J. M., Liver, P., and Bhat, M. K., "Measurements of Compressible Secondary Flow in a Circular S-Duct," AIAA Paper 83-1739, 1983.
- 10 Vakili, A., Wu, J. M., Hingst, W. R., and Towne, C. E., "Comparison of Experimental and Computational Compressible Flow in a S-Duct," AIAA Paper 84-0033, 1984.
- 11 Vakili, A. D., Wu, J. M., Liver, P., and Bhat, M. K., "Experimental Investigation of Secondary Flows in a Diffusing S-Duct," The University of Tennessee Space Institute Preliminary Copy Final Report for NASA Contract NAG3 233, Sept. 1984.
- 12 Vakili, A. D., Wu, J. M., Liver, P., and Bhat, M. K., "Experimental Investigation of Secondary Flows in a Diffusing S-Duct with Vortex Generators," The University of Tennessee Space Institute Preliminary Copy Final Report for NASA Contract NAG3 233, July 1986.
- 13 Vakili, A. D., Wu, J. M., Bhat, M. K., and Liver, P., "Compressible Flow in a Diffusing S-Duct with Flow Separation," in *Heat Transfer and Fluid Flow in Rotating Machinery* (Yang, W.-J., ed.), pp. 201–211, Hemisphere Publishing Corporation, 1987. First International Symposium on Transport Phenomena, April 28 - May 3, 1985, Honolulu, Hawaii.
- 14 Patrick, W. P. and McCormick, D. C., "Laser Velocimeter and Total Pressure Measurements in Circular-to-Rectangular Transition Ducts," United Technologies Research Center Report 87-41, June 1988.
- 15 Patrick, W. P. and McCormick, D. C., "Circular-to-Rectangular Duct Flows - A Benchmark Experimental Study," Society of Automotive Engineers Paper 871776, 1988.
- 16 Miao, J. J., Lin, S. A., Chou, J. H., Wei, C. Y., and Lin, C. K., "An Experimental Study of Flow in a Circular-Rectangular Transition Duct," AIAA Paper 88-3029, 1988.
- 17 Miao, J. J., Leu, T. S., Chou, J. H., Lin, S. A., and Lin, C. K., "Flow Distortion in a Circular-to-Rectangular Transition Duct," *AIAA Journal*, Vol. 28, Aug. 1990,

pp. 1447–1456.

18 Davis, D. O. and Gessner, F. B., “Experimental Investigation of Turbulent Flow Through a Circular-to-Rectangular Transition Duct,” AIAA Paper 90-1505, 1990.

19 Whitney, W. J., Schum, H. J., and Behning, F. P., “Cold-Air Investigation of a Turbine for High-Temperature-Engine Application IV - Two-Stage Turbine Performance,” NASA TN D-6960, 1972.

20 Szanca, E. M., Schum, H. J., and Hotz, G. M., “Research Turbine for High-Temperature Core Engine Application I - Cold-Air Overall Performance of Solid Scaled Turbine,” NASA TN D-7557, 1974.

21 Schwab, J. R., Stabe, R. G., and Whitney, W. J., “Analytical and Experimental Study of Flow Through Axial Turbine Stage With a Nonuniform Inlet Radial Temperature Profile,” AIAA Paper 83-1175, 1983.

22 Burley, J. R. and Carlson, J. R., “Circular-to-Rectangular Transition Ducts for High-Aspect Ratio Nonaxisymmetric Nozzles,” AIAA Paper 85-1346, 1985.

23 Burley, J. R., Bangert, L. S., and Carlson, J. R., “Investigation of Circular-to-Rectangular Transition Ducts for High-Aspect Ratio Nonaxisymmetric Nozzles,” NASA TP 2534, Mar. 1986.

24 Ahmed, M., Wigeland, R. A., and Nagib, H. M., “Generation and Management of Swirling Flows in Confined Streams,” Illinois Institute of Technology Interim Technical Report ARO-ITR-76-1, June 1976.

25 Hallet, W. L. H., “Swirl Generator for Independent Variation of Swirl and Velocity Profile,” *AIAA Journal*, Vol. 24, July 1986, pp. 1212–1213.

26 Weske, D. R. and Sturov, G. Y., “Experimental Study of Turbulent Swirled Flows in a Cylindrical Tube,” *Fluid Mechanics-Soviet Research*, Vol. 3, July 1974, pp. 77–82.

27 Kerrebrock, J. L. and Mikolajczak, A. A., “Intra-Stator Transport of Rotor Wakes and Its Effect on Compressor Performance,” *ASME Journal of Engineering for Power*, Vol. 92, Oct. 1970, pp. 359–386.

- 28 Denton, J. D. and Usui, S., "Use of a Tracer Gas Technique to Study Mixing in a Low Speed Turbine," ASME Paper 81-GT-86, 1981.
- 29 Smith, B. L., "Detection of Secondary Flow in a Turbine Cascade Using a Tracer Gas Technique," Master's thesis, Virginia Polytechnic Institute and State University, Blacksburg, Virginia, Feb. 1983.
- 30 Moore, J., "Flow Trajectories, Mixing, and Entropy Fluxes in a Turbine Cascade," in *Viscous Effects in Turbomachinery*, pp. 5-1 – 5-14, AGARD, 1983. AGARD CP-351.
- 31 Moore, J. and Smith, B. L., "Flow in a Turbine Cascade: Part II-Measurements of Flow Trajectories by Ethylene Detection," *ASME Journal of Engineering for Gas Turbines and Power*, Vol. 106, Apr. 1984, pp. 409-413.
- 32 Gallimore, S. J., *Spanwise Mixing in Multi-Stage Axial Compressors*. PhD thesis, University of Cambridge, Cambridge, England, Sept. 1985.
- 33 Gallimore, S. J. and Cumpsty, N. A., "Spanwise Mixing in Multistage Axial Flow Compressors: Part 1 - Experimental Investigations," ASME Paper 86-GT-20, 1986.
- 34 Bauer, R. C., "Fluid Migration and Mixing in a Multistage, Axial-Flow Compressor," Master's thesis, Iowa State University, Ames, Iowa, 1987.
- 35 Wisler, D. C., Bauer, R. C., and Okiishi, T. H., "Secondary Flow, Turbulent Diffusion and Mixing in Axial-Flow Compressors," *ASME Journal of Turbomachinery*, Vol. 109, Oct. 1987, pp. 455-482.
- 36 Hallett, W. L. H. and Guenther, R., "The Turbulent Structure of Swirling Flows in a Sudden Expansion," in *Symposium on Turbulent Shear Flows, 4th, Karlsruhe, West Germany, September 12-14, 1983, Proceedings*, (College Park, Pennsylvania), pp. 19.25-19.31, Pennsylvania State University, 1984.
- 37 McGreehan, W. F., Haaser, F. G., and Sherwood, L. T., "Labyrinth Seal Flow Measurements by Tracer Gas Injection," ASME Paper 87-GT-187, 1987.
- 38 Joslyn, H. D. and Dring, R. P., "A Trace Gas Technique to Study Mixing in a Turbine Stage," ASME Paper 87-GT-118, 1987.

- 39 Folayan, C. O. and Whitelaw, J. H., "The Effectiveness of Two-Dimensional Film-Cooling Over Curved Surfaces," ASME Paper 76-HT-31, 1976.
- 40 Humphrey, J. A. C. and Whitelaw, J. H., "Measurements in Curved Flows," in *Turbulence in Internal Flows* (Murthy, S. N. B., ed.), (Washington, D.C.), pp. 407–437, Hemisphere Publishing Corporation, 1977.
- 41 Davis, D. O., Hingst, W. R., and Porro, A. R., "Experimental Investigation of a Single Flush-Mounted Hypermixing Nozzle," AIAA Paper 90-5240, 1990.
- 42 Moore, J., Moore, J. G., and Adhye, R. Y., "Testing Numerical Methods for Turbomachinery Flows Using Ethylene Injection Studies," in *Numerical Methods in Laminar and Turbulent Flows* (Taylor, C., Habashi, W. G., and Hafez, M. M., eds.), (Swansea, U. K.), pp. 1675–1686, Pineridge Press, 1987.
- 43 Leylek, J. H. and Wisler, D. C., "Mixing in Axial-Flow Compressors: Conclusions Drawn from 3-D Navier-Stokes Analyses and Experiments," ASME Paper 90-GT-, 1990.
- 44 Schieman, J., "Comparison of Experimental and Theoretical Turbulence Reduction Characteristics for Screens, Honeycomb, and Honeycomb-Screen Combinations," NASA TP 1958, 1981.
- 45 Loehrke, R. I. and Nagib, H. M., "Experiments on Management of Free-Stream Turbulence," AGARD Report R-598, 1972.
- 46 Schubauer, G. B., Spangenberg, W. G., and Klebanoff, P. S., "Aerodynamic Characteristics of Damping Screens," NACA TN 2001, Jan. 1950.
- 47 Morel, T., "Comprehensive Design of Axisymmetric Wind Tunnel Contractions," *Journal of Fluids Engineering*, June 1975, pp. 225–233.
- 48 Wilson, D. G., *The Design of High-Efficiency Turbomachinery and Gas Turbines*. Cambridge, Massachusetts: MIT Press, 1984.
- 49 Taylor, G. I., "Stability of a Viscous Liquid Contained Between Two Rotating Cylinders," *Philosophical Transactions*, Vol. 223, 1923, pp. 289–343.

- 50 Glassman, A. J., ed., *Turbine Design and Application*, Vol. 1. Washington, D. C.: NASA, 1972. NASA SP-290.
- 51 Squire, L. C., Maltby, R. L., Keating, R. F. A., and Stanbrook, A., "The Surface Oil Flow Technique," in *Flow Visualization in Wind Tunnels Using Indicators* (Maltby, R. L., ed.), pp. 1–28, AGARD, Apr. 1962. AGARDograph 70.
- 52 Gessner, F. B. and Chen, Y. L., "Flow in a Rectangular Diffuser With Local Flow Detachment in the Corner Region," *Journal of Fluids Engineering*, Vol. 105, June 1983, pp. 204–211.
- 53 Jurkovich, M. S., Greber, I., and Hingst, W. R., "Flow Visualization Studies of a 3-D Shock/Boundary Layer Interaction in the Presence of a Non-Uniform Approach Boundary Layer," AIAA Paper 84-1560, 1984.
- 54 Roshko, A., "On the Development of Turbulent Wakes From Vortex Streets," NACA RP 1191, 1954.
- 55 Datametrics - Dresser Industries, Inc., Wilmington, Massachusetts, *Instruction Manual - Type 825 Mass Flow Controller*, Oct. 1984.
- 56 Braker, W. and Mossman, A. L., *Matheson Gas Data Book*. Lyndhurst, New Jersey: Matheson, Inc., 6 ed., 1987.
- 57 Wagner, J. H., Dring, R. P., and Joslyn, H. D., "Inlet Boundary Layer Effects in an Axial Compressor Rotor: Part II-Throughflow Effects," *ASME Journal of Engineering for Gas Turbines and Power*, Vol. 107, July 1984, pp. 382–386.
- 58 Dong, Y., Gallimore, S. J., and Hodson, H. P., "Three-Dimensional Flows and Loss Reduction in Axial Compressors," ASME Paper 86-GT-193, 1986.
- 59 Gow-Mac Instrument Company, Bound Brook, New Jersey, *Operating Manual Model 23-500 Total Hydrocarbon Analyzer*, Aug. 1987.
- 60 Pressure Systems Incorporated, Hampton, Virginia, *Model 780BIT Pressure Measurement System Users Manual*, 1 ed., Sept. 1983.
- 61 TSI Incorporated, St. Paul, Minnesota, *Instruction Manual - IFA 100 System Intelligent Flow Analyzer*, 1987.

- 62 TSI Incorporated, St. Paul, Minnesota, *Hot Film and Hot Wire Anemometry Theory and Application*. Technical Bulletin 5.
- 63 Bradshaw, P., *An Introduction to Turbulence and its Measurement*. Oxford, England: Pergamon Press, 1971.
- 64 Hinze, J. O., *Turbulence*. New York: McGraw-Hill, Inc., 2 ed., 1975.
- 65 Klebanoff, P. S., "Characteristics of Turbulence in a Boundary Layer with Zero Pressure Gradient," NACA Technical Note 3178, 1954.
- 66 Bradshaw, P., "Turbulent Secondary Flows," *Annual Review of Fluid Mechanics*, Vol. 19, 1987, pp. 53–74.
- 67 Huang, D. Private communications, 1990.
- 68 Akima, H., "A Method of Bivariate Interpolation and Smooth Surface Fitting for Irregularly Distributed Data Points," *ACM Transactions on Mathematical Software*, Vol. 4, June 1978, pp. 148–159.
- 69 Akima, H., "ALGORITHM 526 Bivariate Interpolation and Smooth Surface Fitting for Irregularly Distributed Data Points [E1]," *ACM Transactions on Mathematical Software*, Vol. 4, June 1978, pp. 160–164.
- 70 Lawson, C. L., "Software for C1 Surface Interpolation," Jet Propulsion Laboratory, California Institute of Technology JPL Publication 77-30, Aug. 1977.